Tailoring the Features of Covalent Organic Frameworks

Sabrina Maria Inge Rager

2019

Dissertation zur Erlangung des Doktorgrades

der Fakultät für Chemie und Pharmazie

der Ludwig-Maximilians-Universität München

Tailoring the Features of Covalent Organic Frameworks

Sabrina Maria Inge Rager

aus

München, Deutschland

2019

Erklärung

Diese Dissertation wurde im Sinne von § 7 der Promotionsordnung vom 28. November 2011 von Herrn Prof. Dr. Thomas Bein betreut.

Eidesstattliche Versicherung

Diese Dissertation wurde eigenständig und ohne unerlaubte Hilfe bearbeitet.

München, den 10.07.2019

_____

Sabrina Rager

Dissertation eingereicht am 03.05.2019

1. Gutachter: Prof. Dr. Thomas Bein
2. Gutachter: Senior Lecturer Dr. Stefan Wuttke

Mündliche Prüfung am 05.06.2019

“ It always seems impossible

until it’s done. ”

- Nelson Mandela -

Danksagung

Nach vier Jahren Doktorarbeit und insgesamt zehn Jahren an der LMU ist es nun Zeit Danke zu sagen. Viele Menschen sind mir auf diesem Weg begegnet, haben mich begleitet und dazu beigetragen, dass ich mich fachlich, wie auch persönlich weiterentwickeln konnte.

Mein erster großer Dank geht an meinen Doktorvater Prof. Thomas Bein. Danke dir Thomas, dass du mir die Möglichkeit gegeben hast, in deiner Arbeitsgruppe an einem interessanten Forschungsthema zu arbeiten. Vielen Dank für die Freiheiten, die ich während der Bearbeitung meiner verschiedenen Projekte von dir erhalten habe. Außerdem möchte ich mich für die Möglichkeit bedanken, dass ich viele nationale und internationale Konferenzen besuchen durfte. Vielen Dank auch, dass wir uns immer in Subgroup-, sowie Groupmeetings austauschen konnten und viele gute und weiterbringende Diskussionen hatten.

Desweiteren möchte ich mich bei Stefan Wuttke bedanken. Danke Stefan, dass du mich als deine Masterstudentin angenommen hast, mich mit der physikalischen Chemie vertraut gemacht hast und mir den Weg eröffnet hast auch meine Doktorarbeit in der Arbeitsgruppe anzufertigen. Vielen Dank auch, dass du das Zweitgutachten für meine Arbeit erstellt hast und nach München für meine Prüfung kommst, denn das bedeutet mir viel.

Weiterhin möchte ich Dana danken, dass sie viele Projekte mit mir zusammen gemacht hat, immer ein offenes Ohr hatte und vor allem mir in der Anfangsphase der Doktorarbeit geholfen hat.

Vielen lieben Dank auch an Andi Jakowetz, mit dem ich in der zweiten Hälfte der Arbeit erfolgreiche Kooperationen gestartet habe und wir wirklich sehr gut zusammen gearbeitet haben. Nicht nur die morgendlichen Kaffeepausen, auch deine Geduld mir immer wieder Physik zu erklären und vor allem das ewige Korrekturlesen meiner Dissertation habe ich dir zu verdanken!

Meinen Kooperationspartnern aus der Uni Würzburg möchte ich für eine erfolgreiche Zusammenarbeit danken. Danke vor allem an Bappaditya Gole und Florian Beuerle für

die wissenschaftlichen Diskussionen, welche dazu führten, dass wir zwei Manuskripte gemeinsam veröffentlichen konnten.

Für die administrativen Dinge möchte ich Regina und vor allem später Corinna danken. Danke, dass ihr beide euch um Papierkram kümmert, dafür sorgt, dass wir unsere Termine einhalten und für immer ein offenes Ohr! Vielen Dank auch an Tina, Markus und meinen Praktikanten (Stefan, Maria, Irina, Marina) für die tatkräftige Unterstützung bei der Arbeit, welche dazu beigetragen hat, dass wir alle effizienter arbeiten konnten und ohne die die Arbeit nie so einfach gewesen wäre.

Vielen Dank auch an Steffen für sämtliche SEM und TEM Messungen. Vor allem auch unsere langen Diskussionen um die bestmöglichen Ergebnisse zu erhalten. Ganz besonders fand ich auch, dass du dir die Mühe gemacht hast viele FIB Proben zu messen und um schöne Bilder zu erhalten.

Vor allem möchte ich auch der kompletten Arbeitsgruppe und vor allem meiner Subgroup danken für die tolle Atmosphäre während der letzten Jahre, auch, wenn viele fertig geworden sind und andere Wege eingeschlagen haben. Danke an meine Bürokollegen Andi, Noggi, Stef, Bini, Andre und Pät, welche mir immer das Gefühl gegeben haben gerne ins Office zu gehen und auch Spaß an der Arbeit zu haben. Vielen lieben Dank für die ganzen Kaffeepausen, Grillfeiern, Ausflüge und 1543-Runden, welche mir mein Mentor Fabi sehr stark ans Herz legte.

Weiterhin habe ich in der Zeit in der Arbeitsgruppe nicht nur nette Kollegen kennenlernen dürfen sondern auch richtig gute Freunde! Fabi, Noggi, Stef, Dodo, Niklas, Pät, Wascht, Ed, Peter, Jakowetz, Lisa, Erika, Danni B., Krissi und Zimpel! Danke für die tolle Zeit und die vielen Sachen, die wir gemeinsam erlebt haben!

Mein letzter großer Dank geht an meine Freunde und meine Familie! Vor allem Amelie und Mama möchte ich für die ganzen letzten Jahre danken, in denen sie mich immer psychisch und finanziell unterstützt haben. Danke Amelie, dass du mich die ganzen WG-Jahre ausgehalten hast, mir immer wieder Mut zugesprochen hast, dich immer mit mir gefreut hast, wenn es was zu feiern gab und du immer für mich da bist! Danke Mama, dass du immer an mich geglaubt hast und immer hinter mir stehst! ♥

Abstract

Covalent organic frameworks (COFs) represent a new and emerging class of functional materials built from organic subunits. These networks are formed *via* reversible co-condensation reactions resulting in covalent bonds based on diverse binding motifs. Due to the great variety and large number of accessible building blocks, structural and functional diversity can be achieved easily. By combining desired subunits, crystalline and porous two- or three-dimensional frameworks can be synthesized exhibiting a defined pore size and a high surface area. Crystallinity and porosity are of central importance for many characteristics of COFs such as adsorption, diffusion, and electronic transport. The possible role of COF materials applied for sensing, catalysis, and optoelectronic applications is based on their tunable characteristics which can be tailored by implementing suitable subunits. Furthermore, postsynthetic modifications can be used to adjust properties of the framework while maintaining the main aspects. In general, COFs can be synthesized during solvothermal reaction conditions followed by diverse work-up steps which have to be adapted and optimized for each system. Therefore, finding the right parameters is key for the successful synthesis of crystalline materials and mastering them enables the formation of thin films on suitable substrates. This is particularly important for device applications in the optoelectronic area.

This thesis focuses on the synthesis of novel two-dimensional COFs, introducing new characteristic features into such frameworks. The different COF materials were fully characterized by various methods to ensure high crystallinity and porosity as well as elucidating their morphology and structure. Next to neat bulk and film materials, also full electronic devices were fabricated for further analysis. In addition, postsynthetic treatments concerning structural improvement and pore wall modifications were investigated. The possible applications arising from introducing additional functionality after the synthesis were a substantial part of this work. The experimental results of this thesis can be separated into three main parts: structural control as well as implementation of dyes and electroactive subunits, electrical characterization, and postsynthetic treatment methods.

In general, while Chapter 1 of this thesis is introducing the main aspects of COFs and the theoretical background, Chapter 2 contains descriptions of the methods used for materials characterization. The first part of the experimental results (Chapter 3 and 4) deals with structural control including the implementation of dyes and the comparison of imine and boronate ester binding motifs.

Chapter 3 is focused on the precise construction of template-free nano- and microstructures of dye-containing porous materials. The implemented organic dye diketopyrrolopyrrole was functionalized with accessible aldehyde groups. After reaction with a tetra amine-functionalized porphyrin building block the resulting DPP-TAPP-COF showed enhanced absorption capabilities. Regarding structural control, the obtained COF exhibited spontaneous aggregation into hollow microtubular assemblies with well-defined and controllable outer and inner tube diameters. A detailed mechanistic morphology investigation revealed that the whole process is time-dependent and undergoes a traceable transformation starting with sheet-like agglomerates into stable tubular microstructures *via* a rolling-up mechanism.

As already mentioned in the third chapter (the implementation of sterically demanding dyes as building blocks for COF systems), the integration of diketopyrrolopyrrole molecules is still hampered by limited control of the binding motif in combination with the size of the backbone. In Chapter 4, the results of using a flat, rigid, and non-conjugated boronate ester bond combined with the dye and a suitable counterpart are reported. Here, structural control was achieved and led to enhanced properties and enforced specific stacking behavior. The COF was successfully synthesized and crystallinity as well as porosity could be improved as compared to the imine-connected counter-part, with even shorter reaction times. The boronate ester coupling motif guides the formation of a planar and rigid backbone and long-range molecular stacks. Furthermore, the COF exhibits application-relevant optical properties including strong absorption over the visible spectral range, broad emission into the near infrared region (NIR), and a long singlet lifetime. All the findings can be attributed to the controlled formation of molecular stacks with *J*-type interactions between the subcomponents in the COF. In addition, these molecular stacks showed an influence on the electronic behavior revealing electrical conductivity values of crystalline COF pellets up to 10^{-6} Scm^{-1}.

Further investigations on electrical conductivity and charge carrier mobility studies on different COF systems are described in Chapter 5. Here, a series of acene-based building blocks was implemented into a scaffold, i.e. benzene and anthracene dialdehyde-functionalized subunits, which show high charge carrier mobilities comparable to organic materials in single crystals. The building blocks were designed in a way to tailor the length of the resulting aromatic backbone pointing into the pore of the framework without changing the overall unit cell dimensions, i.e. the molecules

were inserted perpendicular to the binding direction. This allows for a better comparison of the structures and the resulting properties. The measurements revealed that the length of the backbone has a strong influence on the achieved electrical conductivity and mobility values. Moreover, different measurement methods for conductivity in combination with mobility are compared due to the diverse theoretical backgrounds each method is based on, yielding technique-specific values. In addition, all COF samples revealed surprisingly high Hall mobility values for pressed powder pellets as well as for thin films and devices. The measured hole-only devices exhibited up to 10^{-3} $cm^2V^{-1}s^{-1}$ for the anthracene COF, which is one of the largest values of intrinsic mobility for COFs so far. The results point towards the importance of π-overlap and hence the length of the acene unit. Further extension of the series towards the even longer pentacene unit was initiated but will be part of future studies.

The third part of the experimental results deals with the different possibilities of postsynthetic treatments. In Chapter 6, a new postsynthetic treatment for covalent organic frameworks is introduced. Here, a newly synthesized anthracene-based COF (from Chapter 5) is reported followed by a postsynthetic treatment based on light-induced defect reduction. The applied laser light apparently leads to opening and reformation of imine bonds resulting in a significant decrease of defect sites and therefore a striking increase in photoluminescence. This effect was further supported by IR investigations showing a reduced intensity of aldehyde and amine vibrations and a gain of imine vibration intensity upon laser irradiation of a stoichiometric precursor mix.

Another approach regarding postsynthetic treatment is presented in Chapter 7, based on chemical modification after successful COF synthesis. A novel terphenyldiboronic acid-based COF is reported which features accessible hydroxyl groups at the inner and outer pore wall environment. These functional groups serve as anchor sites for a fluorescence label which can be installed by a postsynthetic modification approach. By forming *o*-thiocarbamate bonds, fluorescein molecules were immobilized on the inner as well as at the outer surface of the pore system. This reaction was further extended to another COF system and to other grafting moieties.

In conclusion, this thesis mainly focused on the fundamental synthetic, structural, and functional characteristics of new optoelectronic COF materials. Next to synthesis and morphology control, electrical and optical characterization was performed, giving insights on the stacking behavior and electronic landscape within the framework. The

COF was used as a new tool for directed structural control and stacking of molecular chromophore units. Furthermore, exceptionally high intrinsic charge carrier mobilities were found even on the macroscopic scale of devices, possibly enabling new applications in sensing and optoelectronic devices. Additionally, postsynthetic processes were developed to extend the portfolio of applications for synthesized COFs through modification or to improve the performance of materials through defect reduction, which is of particular interest for optoelectronic thin film-based devices.

Table of Contents

1 Introduction

The enormous and still rising demand for energy is a big issue in our society today. Fossil fuels are getting rare and, upon burning, greenhouse gases are released which contribute to changing the climate on our planet. Figure 1-1 illustrates the electrical energy consumption and underlines the importance of permanent generation and efficient storage of clean and sustainable energy. The high energy demand of all nations combined is constantly growing with further spread of mobile devices as well as electrical cars and bikes.[1]

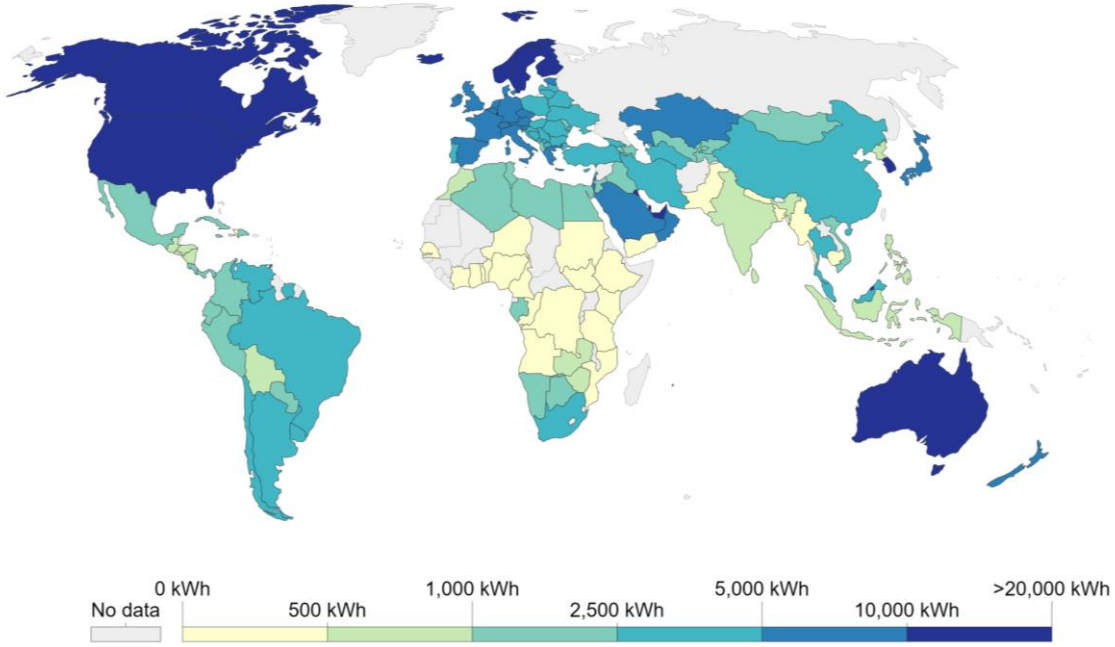

Figure 1-1: Worldwide overview of the electrical power consumption per capita, measured in kWh per capita depicting the enormous demand of electrical energy required on our planet.[2] Figure adapted from Ref. 2.

To meet this growing energy consumption, we are always looking for other energy sources, especially renewable and sustainable ones. Next to wind and water as natural forces, this also includes the sun. The sunlight reaching earth on one day would be sufficient to cover the energy needs of mankind for one year.[1] So far, silicon wafer-based photovoltaic (PV) technology is most commonly used for solar energy generation, covering about 92% of the market. These solar cells exhibit good power conversion efficiencies and long life times.[3] However, they feature a slow production and require a supply of highly purified and clean chemicals and materials, hence

requiring a large energy input for solar cell production and therefore a rather long energy payback time. For a sustainable energy future, a new way has to be developed which includes an efficient and low-cost alternative to the already existing and studied PV technologies and preserving the required stability. One way to overcome these limitations is the use of organic compounds which can act as active materials in solar cell devices due to their attractive optical and physical characteristics. Moreover, compared to inorganic solar cells, they can be easily transferred on flexible substrates using fast and facile wet-chemistry deposition processes.[4] In principle, this allows for cheap production of solar cells and opens up new application areas from small to large scale solar light harvesting.

1.1 Organic Photovoltaic Devices

In organic photovoltaic (OPV) devices, conductive organic compounds such as polymers or small molecules are used for light absorption and charge transport leading to the generation of electricity from sunlight. The used organic molecules are often solution-processable and relatively cheap which results in low production costs per power output.[5]

The basic principle of a photovoltaic device is based on the effects which take place in a semiconducting diode which converts light into direct current electricity. The available band gap of photovoltaic devices is determining the energy of absorbed photons ranging from low-energy (IR) to high-energy (UV), which can be further converted into electricity.[6] The main characteristic of the applied materials depends on the existence of free charge carriers, i.e. electrons and holes, within large conjugated systems. The conjugated system is accomplished when organic atoms are covalently bond and conjugation takes place. Here, the electrons in atomic p_z orbitals form a delocalized bonding π-orbital (HOMO) with an antibonding π*-orbital (LUMO). The energy separation between the HOMO and the LUMO level is considered to be the band gap of the material and often lies between around 1 and 4 eV, depending on the desired absorption properties.[7] Due to the fairly low dielectric constant of organic materials and the considerable exciton binding energy, OPV devices are generally based on a heterojunction of electron donor and electron acceptor material phases. Often, the donor is excited upon light illumination which causes an electron to be transferred to the acceptor phase. The generated electron-hole pairs are then separated and transported to opposite electrodes to be utilized before recombination can occur.[8, 9] If the charge

carrier mobility is insufficient, the carriers will not be able to reach the contacts and will recombine in trap sites or remain in the device, which opposes the flow of new carriers. This latter problem can lead to a limited device performance.[10]

The composition of a common organic polymer-based photovoltaic device is shown in Figure 1-2. For better direct transport, an electron or hole blocking layer is coated on top of an indium tin oxide (ITO) conductive substrate. These first layers are further covered with an active layer comprising electron donor and acceptor materials, followed by a hole or electron blocking layer for "normal" or "inverted" devices, respectively. The sequence of layers is finally covered with a metal electrode.[11]

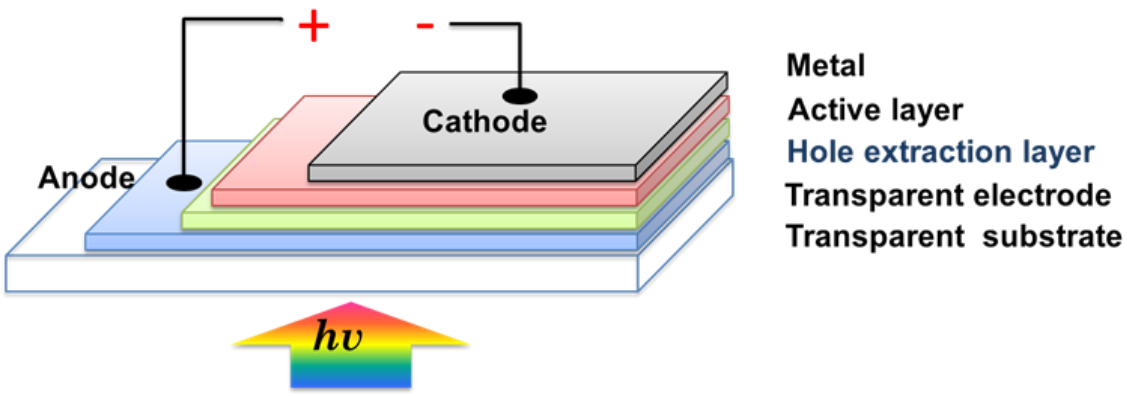

Figure 1-2: Architecture of a basic organic photovoltaic device with a normal geometry.[12] Figure adapted from Ref. 12.

The most-studied polymer photovoltaic cell is built up from poly(3-hexylthiophene) (P3HT) and [6,6]-phenyl-C_{61}-butyric acid methyl ester (PCBM) in a bulk-heterojunction structure (chemical structures are illustrated in Figure 1-3).[13] The P3HT absorption spectrum reaches up to 650 nm, which means that the solar spectrum is not used effectively.[14] Consequently, the development of new polymers and materials with a broader absorption range has attracted much recent research activity. For example, this can be achieved with alternating donor-acceptor units in the polymer chains caused by intramolecular charge transfer.[15]

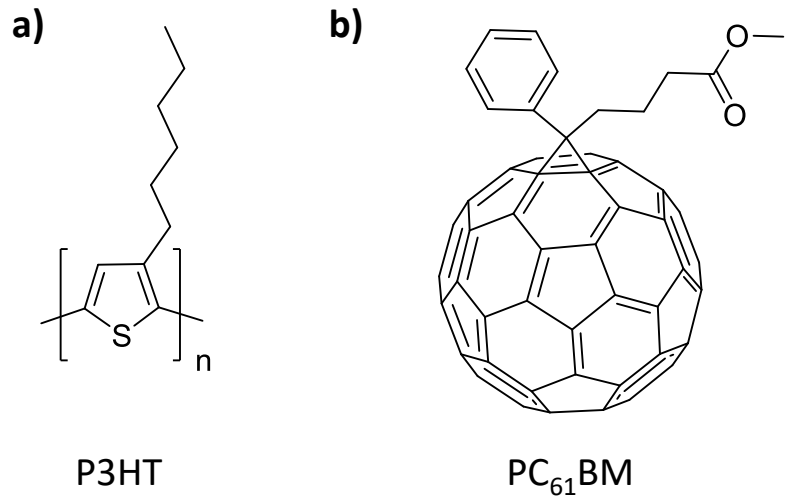

Figure 1-3: Molecular structure of a) electron donor P3HT and b) electron acceptor $PC_{61}BM$.

1.2 Covalent Organic Frameworks

Covalent organic frameworks (COFs) are a new class of materials based on light-weight elements such as carbon, hydrogen, sulfur, nitrogen, oxygen, and boron. The framework is usually built up from at least two different molecules (although there are a few examples of molecular self-condensation), which can be designed on an atomically precise basis. The first COF was developed and reported in 2005 by Coté *et al.*.[16] COFs are defined by their main characteristics crystallinity and porosity. The latter includes accessible pores and a large surface area which can be used for several applications.[17] By modifying the metrics as well as the composition of the compounds, meaning the atomic composition, the physical and chemical properties of the desired product can be designed. This leads to the possibility of synthesizing new materials with a desired structural design in combination with tailoring their properties for a targeted application. The construction of COFs is based on a slightly reversible co-condensation of two (or more) organic linker molecules which are connected *via* covalent bonds. This new type of material allows for the integration of numerous desired organic building blocks into an ordered structure with atomic precision.[18] In general, porous crystalline solids can be described as consisting of secondary building units (SBUs) which assemble and form a periodic and porous framework. The forerunners of COFs were metal organic frameworks (MOFs), which are based on similar principles but with coordinative bonds instead of covalent bonds. In both cases, the synthesis route is based on reticular synthesis which can be described as the process of assembling judiciously designed rigid SBUs or building blocks into predetermined ordered structures.[16, 19]

As mentioned above, the scientific discovery of COFs started in Yaghi´s group reporting the successful synthesis and design of COF-1 and COF-5. The COF-1 framework is based on the self-condensation of phenyldiboronic acid whereas the COF-5 network results from the condensation of phenyldiboronic acid and hexahydroxytriphenylene. Both systems offer a two-dimensional crystalline material with a high thermal stability, a low mass density and permanent porosity.[16] The reaction schemes are displayed in Figure 1-4.

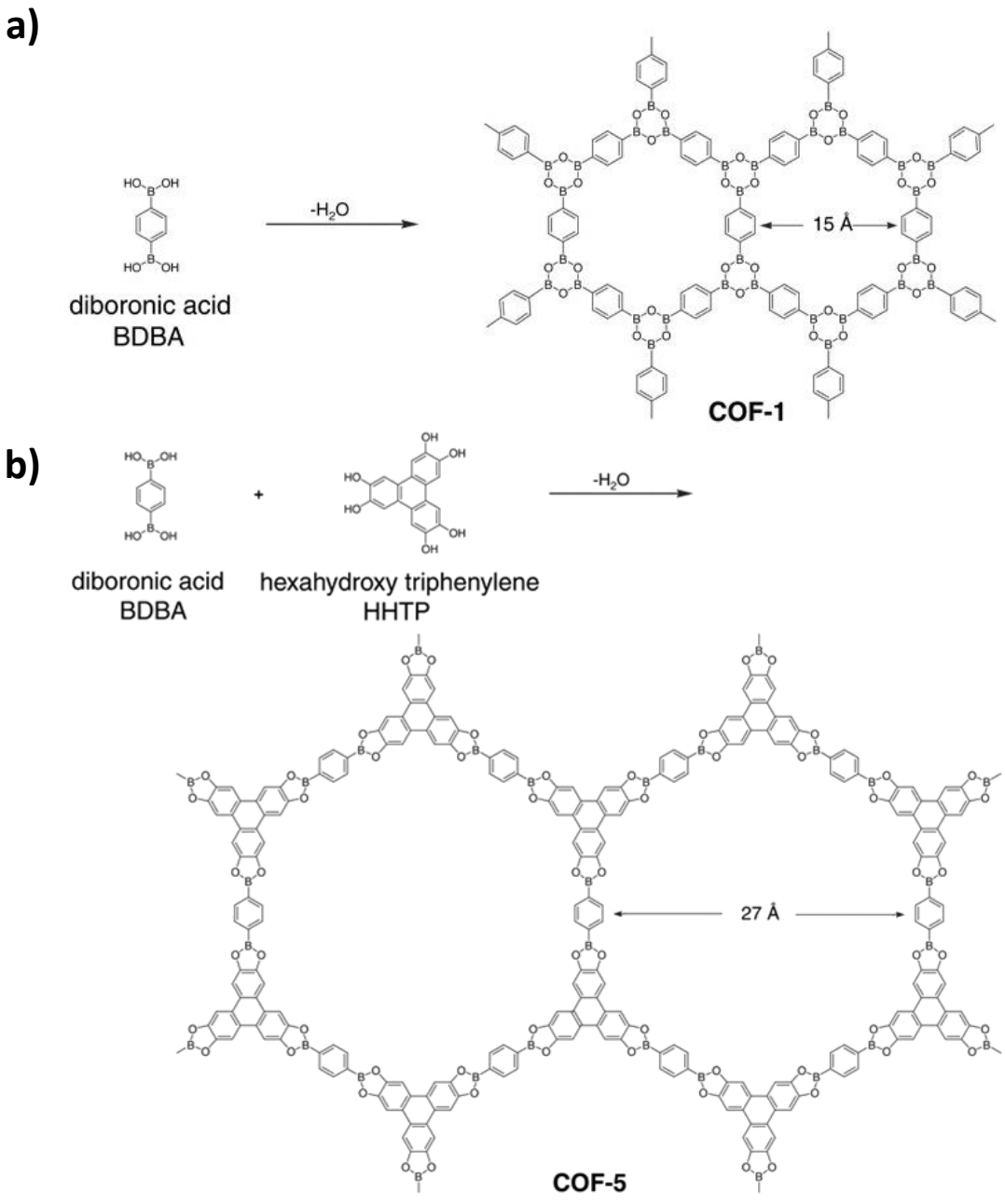

Figure 1-4: a) Self-condensation of diboronic acid forming COF-1; b) co-condensation reaction between phenyldiboronic acid with hexahydroxytriphenylene resulting in COF-5.[16] Figure adapted from Ref. 16.

As already mentioned, the condensation reaction is slightly reversible, which means that the network can undergo a self-healing process during reaction which promotes high crystallinity. For certain applications, in particular in optoelectronics, aromatic building blocks are often preferred to be implemented due to their delocalized π-electron systems. These systems can assemble into conjugated two-dimensional sheets that are held together by π-π-interactions. Here, the 2D sheets are stacked in the third dimension resulting in accessible channels with open pores in one direction.

Depending on the geometry, size and characteristics of the organic building blocks, new COF structures can be realized. The networks can be tuned with regard to the pore shape through targeted selection of linker design. As an example, a trigonal linker combined with a linear linker results in a hexagonal pore (see Figure 1-5). In addition to two-dimensional (2D) COFs, also three-dimensional (3D) frameworks can be synthesized by the judicious choice of the appropriate linker [20, 21]

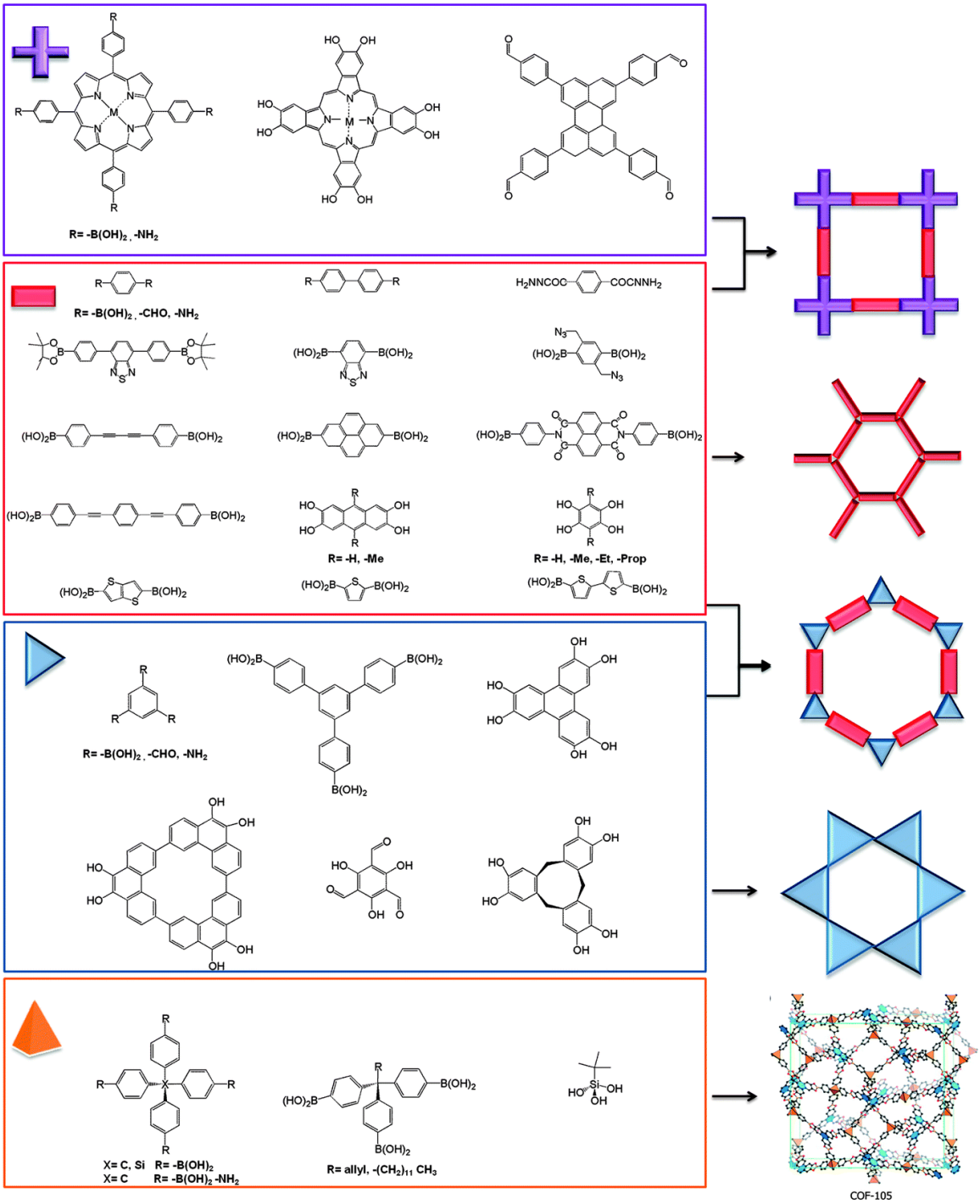

Figure 1-5: Examples of different linker molecules, resulting in a series of COF geometries, from tetragonal to hexagonal and star-shaped pores to 3D-frameworks.[22] Figure adapted from Ref. 22.

1.3 Choosing the Ideal Building Block – Tailoring the Properties of COFs

The first attempts at COF synthesis were performed with regard to boronic acid-based linkers. COF-1 was produced *via* self-condensation whereas COF-5 could be accessed by a co-condensation with a poly-ol. Both systems feature the ability of the already mentioned self-healing process due to reversibility of the condensation reaction.[16] In 2009, Yaghi´s group introduced a new linkage motif based on the co-condensation of amines with aldehydes in the presence of an acid as catalyst to obtain fully conjugated imine bonds between the organic linker molecules.[23] This Schiff base reaction has become the state of the art in COF synthesis in the recent years due to its stability and facile handling.[24] Since then, further linkage motifs have been developed like imide bonds [25], triazine [26], borazine [27], and hydrazine [28] formation. The choice depends on the desired electroactive influence of the binding motif and the geometry of the resulting framework including the anticipated application.

Next to the choice of the electronically-requested binding motif, the selection of the appropriate building block has an enormous influence on the COF structure. Tailoring the properties of the network includes transferring the optoelectronic characteristics of the building blocks to the framework. This leads to the possibility to directly target the material and further effect future applications. Subsequently, the most used building blocks in this work will be depicted and discussed.

1.3.1 Terphenyl Building Block

Terphenyl molecules are a class of substances which are consisting of one benzene ring functionalized with two additional phenyl rings resulting in three possibilities of their arrangement. The three different constitutional isomers are shown in Figure 1-6.

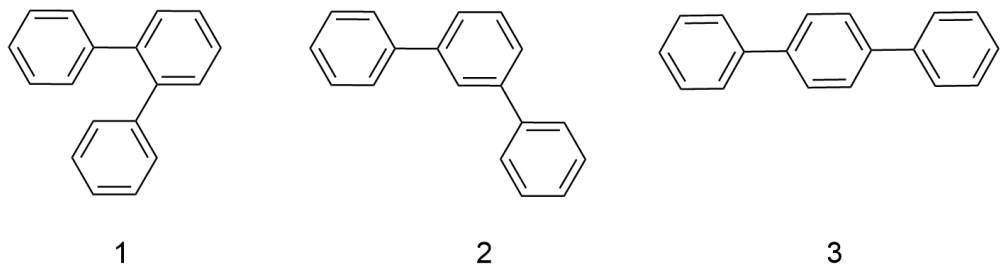

Figure 1-6: Three different constitution isomers of terphenyl molecule (1) *o*-terphenyl, (2) *m*-terphenyl, (3) *p*-terphenyl.

The mostly used molecule is *p*-terphenyl which is a common dye, used in lasers or in sunscreen. For the use as building block in COF materials, *p*-terphenyl is mostly applied due to its linear nature. The three benzene containing molecule exhibits a great delocalized π-system which can influence the stacking behavior of the 2D sheets. Functional groups can be installed in para position at the first and last benzene unit to be linked to the other building blocks, respectively. In this work, boronic acids have been added as anchor points to build a non-conjugated system.

1.3.2 Diketopyrrolopyrrole Building Block

Diketopyrrolopyrrole (DPP)-based molecules are pigments which are often used in diverse lacquers or in the production of colorful plastics. These resistant dyes were first synthesized in 1974 in small amounts in CH-Basel. After extensive screening of the reaction conditions, the product was first sold in 1986 before the patent ran out in 2004.[29] During the next years, a lot of business competition emerged, leading to many different suppliers and crumbling prices.

DPP molecules are predicated on the heterocyclic nitrogen-based DPP unit existing of two five-membered rings with nitrogen and carbonyl functional groups in α-position. For applications, the skeletal structure of DPP (see Figure 1-7) is functionalized at the 3- and 6-positions whereas also the nitrogen position can be reacted with alkyl chains for a better solubility in organic solvents. In addition these representatives are exhibiting orange to reddish fluorescence.[30, 31]

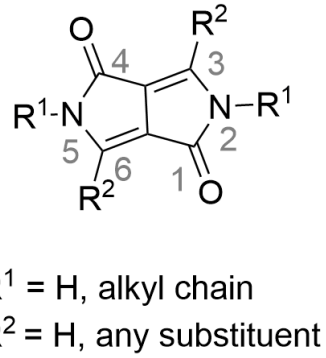

Figure 1-7: Skeletal structure of 2,5-Dihydropyrrolo[3,4]pyrrol-1,4-dion named after IUPAC illustrating the different possibilities of functionalization of the backbone.

Due to their strong delocalization of π-electrons, DPP dyes possess colors ranging from orange to dark violet and consequently covering the whole visible spectrum. They are

very resistant against light and moisture as well as heat and chemicals in general, which makes them very good candidates for high performance applications. Furthermore, suitable substituents can lead to a better fluorescence quantum yield due to their large Stokes shift resulting in possible applications in lasers or solar-based devices.
The most popular field of applications is in the motor industry as red car paint, also known as "*Ferrari-red*". Due to their high stability DPP pigments are more used in high-quality areas and for outside coverings, whereas cheaper pigments are used for internal decoration.[29, 30]

1.3.3 Porphyrin Building Block

Porphyrins are organic dyes with a broad absorption in the visible light range leading to an intensive color of these species. The elementary construction of this family of molecules is based on four pyrrole subunits which are interconnected at their α-carbon atoms by methine bridges (see Figure 1-8). The parent porphyrin is porphine without any other functionalization attached to the compound. The great interest in this class of dyes is focused on the unique electronic behavior. The whole ring consists of 26 π-electrons, of which 18 π-electrons are forming a planar and continuous cycle leading to an aromatic structure.[32, 33]

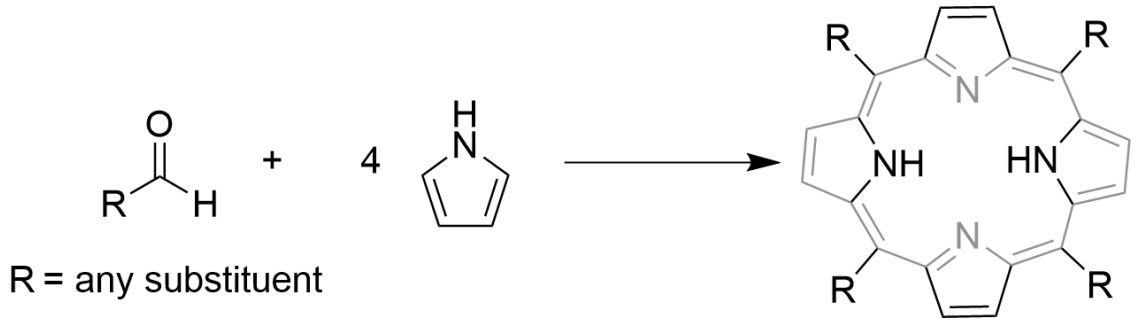

Figure 1-8: Reaction scheme of the condensation and oxidation of pyrrole and an aldehyde component leading to the functionalized porphyrin-based compound. The 18 π-electron aromatic system is highlighted in grey.

Porphyrin-based molecules often occur in nature. Apart from being an important part in light-harvesting complexes of plants, porphyrins can be found in metal complexes. Here, the best-known material is heme, the pigment in red blood cells and a cofactor of the protein hemoglobin. Moreover, they appear in several enzymes in the human

metabolism and are responsible for the color of some decomposition products in our body.[34]

Next to biosynthesis, porphyrins can also be obtained synthetically. One of the most common synthesis routes was established by the work by Paul Rothemund.[35, 36] This procedure is a condensation and oxidation with pyrrole and any aldehyde as precursor molecules yielding components that are easy to purify. Nowadays, porphyrins are also used in photodynamic therapy due to their ability to strongly absorb light and transform common triplet oxygen into reactive singlet oxygen.[37] Moreover, they are used in the field of organic geochemistry and as biomarker in environmental toxicology studies.[38] Porphyrin-based compounds are also of interest as possible components for molecular electronics and photonics,[39] as building blocks for supramolecular chemistry [40] or as complexes for catalysis for the oxidation of organic compounds.[41]

1.3.4 Anthracene Building Block

Anthracene is a polycyclic aromatic molecule based on carbon and hydrogen. The solid is colorless and crystalline and is used as organic semiconductor material. Naturally, anthracene can be found in coal tar and the oxidized species, such as quinones, are present in several organisms. The industrial production is consequently based on the extraction from coal tar.[42] Anthracene is mainly used as precursor for several dyes but also possesses interesting characteristics concerning conducting materials or future solar devices. Basically, anthracene crystallizes in colorless to yellowish leafs with a strong violet fluorescence.[43] Due to its aromaticity, only one six-membered ring contains 6 π-electrons leading to a great reactivity against other reactants, especially oxidation.[44] Furthermore, the molecule is able to dimerize by illuminating with UV light (see Figure 1-9). However, the dimer easily undergoes decomposition *via* thermal activation.[45, 46]

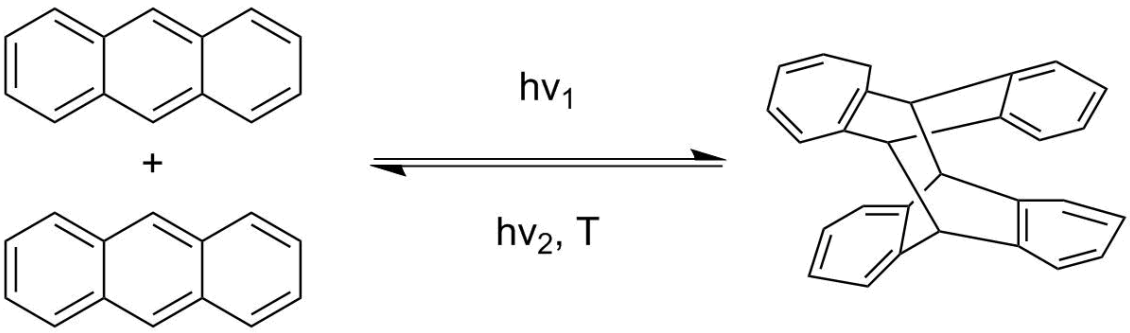

Figure 1-9: Reaction scheme of the photodimerization of two anthracene molecules by the action of UV light and the decomposition reaction of the anthracene dimer after thermal activation.

The non-functionalized material is also known to be a good candidate as a wide band-gap semiconductor and is utilized as scintillator for detectors of high energy photons, electrons as well as alpha particles. Several plastics can also be doped with anthracene for the production of plastic scintillators which are approximately water-equivalent for the general use in radiation therapy dosimetry.[47] Due to its high fluorescence, the molecule is further applied as UV tracer in conformal coatings on printed wiring boards. Here, the implemented dye can be inspected under UV light in the coating material.[48] Anthracene derivatives are widely used as emitting materials in the production of efficient and stable blue emission for full color organic electroluminescence devices.[49, 50] Here, the fluorescent material is utilized as an emitting layer producing blue emission with good chromaticity and high luminous efficiency. Another notable property of anthracene crystals is their high charge carrier mobility at room temperature which is strongly depending on the crystal structure.[51] Anthracene has already been implemented in metal-organic frameworks resulting in crystalline and porous materials for applications such as gas storage, gas uptakes or materials for catalytic reactions.[52] In general, anthracenes have not been widely used as linkers in COF synthesis so far. Therefore, this study deals with the incorporation of anthracene with a new orientation to harness the high mobility properties of the bulk material.

1.3.5 Pentacene Building Block

Similar to anthracene as building block for COFs, pentacene also attracts attention with promising electrical and optical characteristics. The basic construction is similar to anthracene but it is elongated by two more benzene rings. This leads to five linearly fused polycyclic aromatic benzene rings. Due to this extended aromaticity the

compound is highly conjugated and can be applied as an organic semiconductor. The non-functionalized material shows absorption of UV and visible light. As also mentioned for the anthracene compound, due to the high reactivity in the molecule center pentacene is very sensitive against other reactants and especially oxidation. The material exhibits a purple color and degrades when exposed to air and light. The first synthesis route was published and performed by William Hobson Mills and Mildred May Gostling [53] in 1912 and further developed to an extrusion of carbon monoxide from a suitable precursor at 150 °C. Several derivatives of pentacene are also accessible through the precursor pentacenequinone, including the functionalization with side groups at any part of the skeleton.[54] Additional interest is focused on diverse oligomers and polymers of pentacene (see Figure 1-10).

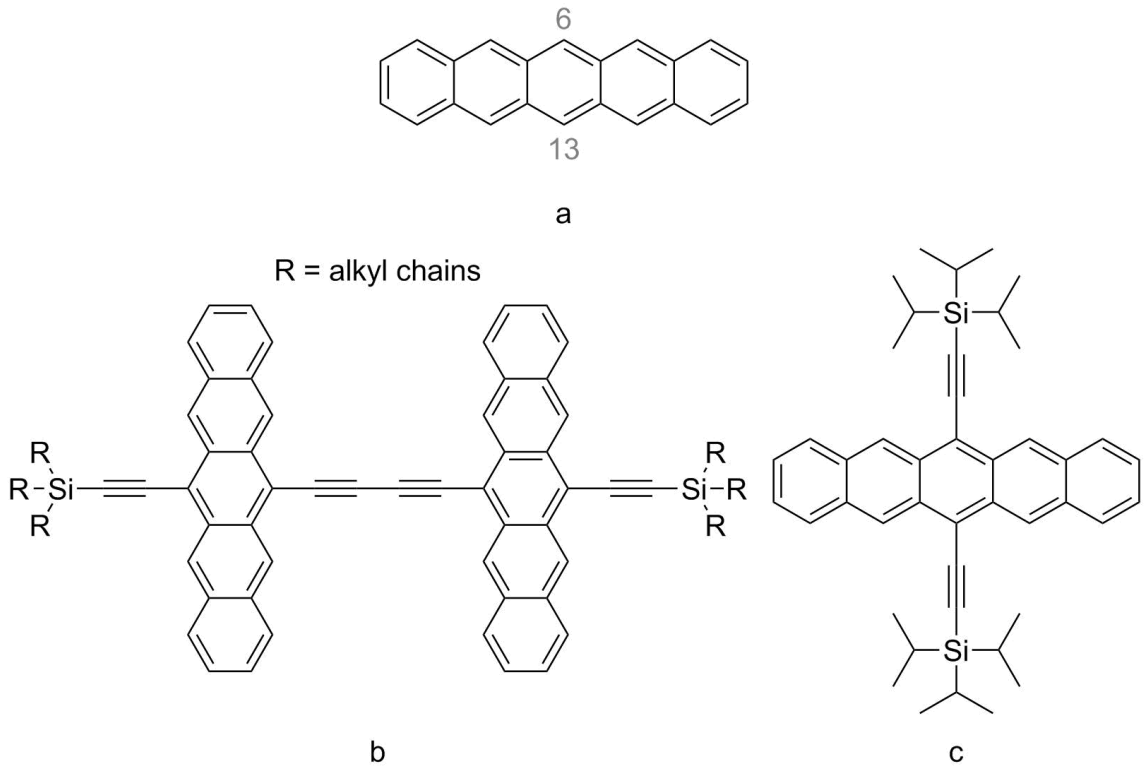

Figure 1-10: a) Non-functionalized pentacene with the reactive sites 6 and 13, b) example for a pentacene dimer, c) TIPS-pentacene (6,13-bis(triisopropylsilylethinyl)pentacene) as a commonly used material for OFETs.

Next to demanding synthesis routes, various device applications have been explored. Light emitting diodes (LEDs) based on pentacene oligomers and polymers (PLED) have been constructed using conjugated copolymers. In materials research, pentacene was examined as potential dichroic dye due to its quinone nature as quinone derivative mixed with liquid crystals.[55] Furthermore, applications of pentacene as material for

organic photovoltaics (OPVs) and hybrid devices have been demonstrated.[56-60] Due to the lower cost and the greater flexibility of the constructed devices, as compared to traditional inorganic cells, organic materials have been attracting high attention over the last years. Also organic thin-film transistors and organic field-effect transistors (OFETs) based on pentacene have been investigated as it exhibits high application potential with charge carrier mobilities exceeding those of amorphous silicon.[61-63] For OFETs it is essential to assemble a semiconducting layer with favorable molecular orientation and uniform morphology to achieve devices with high performance.[64] While one of the best reported performances for this device is based on pure pentacene functionalized pentacene molecules have been demonstrated to be able to even improve the efficiency of these devices. The best positions for this purpose are the 6,13-positions on the molecule (see Figure 1-10a) because of the reduction of the edge-to-face molecular interactions resulting in modified molecular ordering and improved π-overlap. One of the best known and most efficient functionalized derivatives is TIPS-pentacene (6,13-bis(triisopropylsilylethinyl)pentacene) (Figure 1-10c).[65]

Pentacene and other acenes are known to be prominent candidates for the uncommon and intriguing effect of singlet fission. Singlet fission is a spin-allowed process whereby one singlet excited state is converted into two triplet states (see Figure 1-11). The resulting triplet excitions are coupled and their overall spin is conserving the singlet spin, hence making this process possible. Consequently, singlet fission can be seen as a kind of internal conversion with a radiationless transition between two electronic states of equal multiplicity. This phenomenon can be observed for materials where the implemented chromophores are oriented such that the electronic coupling between the singlet and the double triplet state is large. If the process is spin-allowed it can occur very rapidly on pico- or even femtosecond timescales, competing with vibrational relaxation and prompt fluorescence.[66] With triplet decay normally occurring on the nano- to microsecond timescale, this process results in two triplet states exhibiting the possibility for highly efficient charge generation.[67-69] It has to be mentioned that singlet fission does not occur in single small-molecule chromophores and is constrained to multichromophoric systems, because there have to be at least two excitation states to accommodate the two triplet excitations. The two different chromophores can occur in one molecule or even in two different ones. Singlet fission has already been observed for molecules which contain covalently linked pentacenes and tetracenes, underlining

the outstanding importance of this class of molecules in the field of solar devices and optoelectronics.[67, 70, 71]

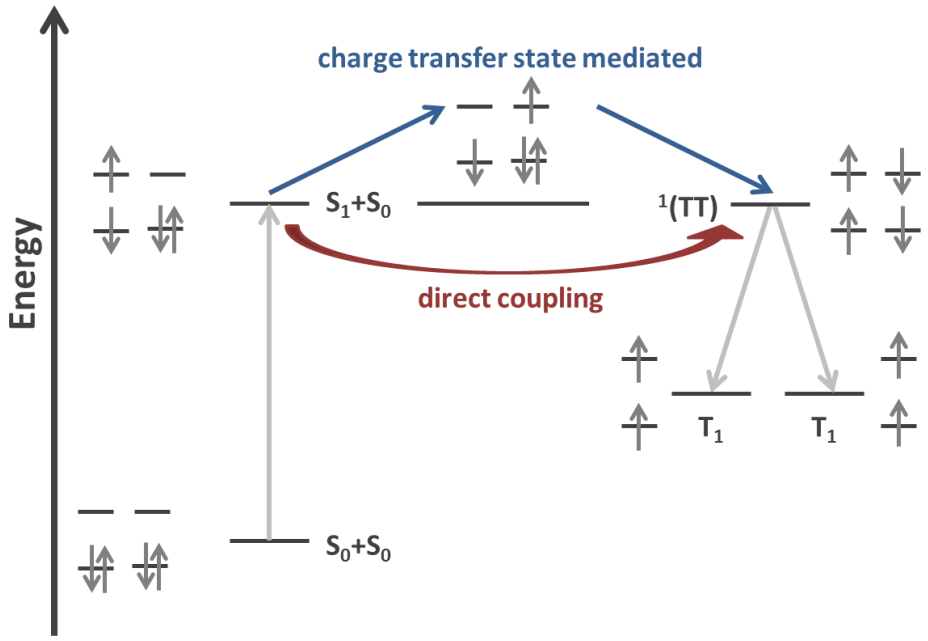

Figure 1-11: Singlet fission mechanisms and according electronic states; one chromophore undergoes an initial excitation to S_1; followed by the excited chromophore sharing its energy with the other available chromophore creating a T_1 state each.[67]

1.4 Synthesis of COFs as Bulk and Film Materials

The synthesis of COFs is based on reticular chemistry, meaning linking molecular building blocks into predetermined periodic structures using strong bonds. By now, it is often possible to crystallize COF materials in a good quality and to overcome crystallization problems for these covalent solids. This is accomplished by striking a balance between the kinetic and thermodynamic factors in the synthesis. These factors play an important role in the reversible covalent bond formation, which is a necessary criterion for crystallization of extended structures.[72] In general, the co-condensation reactions are carried out in reaction vessels using solvothermal conditions, resulting in crystalline COF bulk powders with yields of up to 80%. The reaction vessels have to be closed containers such as sealed pyrex tubes, steel autoclaves or glass vials sealed with a plastic cap.[24] In this work, the molecular building blocks are mixed in a small glass vial to extend the reactive surface of the mixture and different solvent combinations are added. Here, the latter strongly depends on the solubility of the linkers. Furthermore, finding the right solvent mixture and reactant ratio has a great influence on the crystallinity and porosity of the synthesized material. The most commonly used solvents

for COF synthesis are dioxane, mesitylene and diverse alcohols but also chloroform and dichloromethane. Depending on the applied binding-motif, catalysts have to be added to the reaction mixture to enable bond formation. For forming imine bonds, acetic acid at different concentrations and different volumes added to the reaction vials is often applied. The other reaction parameters such as temperature and reaction time have a significant influence on the crystallinity and quality of the COFs as well. The prepared reaction mixture in the closed glass vial can be heated above the boiling point at autogenous pressure of the solvent mixture, which allows for an increased solubility of the precursors and consequently improved kinetics of the reaction.[24] Another way to create crystalline networks is the microwave reaction under ambient pressure. One advantage of this procedure is the relatively short reaction time compared to the solvothermal method.[73] It has to be mentioned that for every new COF system, the reaction conditions as well as the procedure have to be developed henceforward.

After successful synthesis, the obtained material is cleaned from non-reacted precursors and solvent residues in the open pores to gain accessibility. In general, the bulk material is filtrated and washed with a suitable solvent, normally the applied solvent or solvent mixture of the reaction, which is not degrading the COF.

To fully extract residues from the pores, Soxhlet extraction is an appropriate method. Here, the pure solvent is heated up to boiling temperature and the solvent vapor condenses in a reflux condenser. The condensed solvent gets in contact with the material to be purified and extracts non-bound materials. This procedure allows always freshly distilled solvent to contact and purify the powder and is a fast, complete, and automatic way to work-up synthesized COFs.

Supercritical (sc) CO_2-extraction can also be applied to purify materials in a gentle way. Here, CO_2 is used in its sc form to extract the components. The COF material is placed in a sealed steel autoclave and the sc-conditions for CO_2 are set to exceed the critical temperature of 30.98 °C and the critical pressure of 73.75 bar (see Figure 1-12).[74] The material is allowed to be extracted for several hours under these conditions yielding clean, porous and crystalline materials. As well as for the synthesis conditions and procedures, parameters for the purification methods have to be optimized for every new COF with its diverse building blocks.

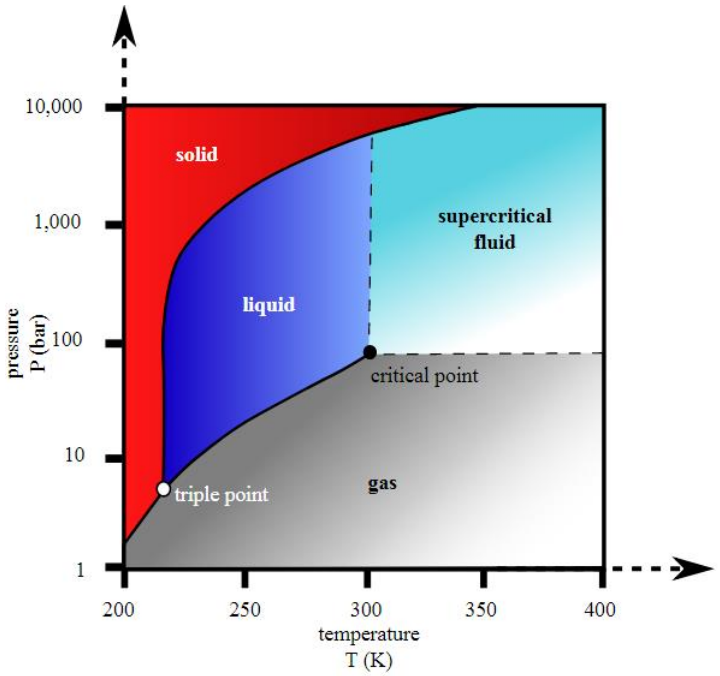

Figure 1-12: CO_2 pressure-temperature phase diagram illustrating the conditions for supercritical reaction conditions.[75] Figure adapted from Ref. 75.

Next to the synthesis of COFs as bulk material, they can also be prepared as films to further build devices. Basically, the film synthesis is established along the synthesis conditions of the powder. Normally, the same reaction conditions are applied in a lower reaction mixture concentration.

Another way for film production is the vapor-assisted conversion method, where the COF precursors are dissolved in a suitable solvent and dropcast onto a substrate. The choice of the substrate depends on the desired future application and is usually between glass, quartz, ITO, FTO or even silicon. This substrate is further placed into a desiccator together with a reservoir of the solvent mixture (or a similar one) leading to the COF in bulk material synthesis. After a specific reaction time at room temperature a smooth and homogeneous COF film can be obtained. Thereby, a strong influence of the applied solvent in the reservoir on crystallinity can be observed. One great advantage of this procedure is that the film thickness can be controlled very easily by adjusting the amount of dissolved precursors in the liquid but at the same time, directed orientation of the films cannot be easily achieved.[76]

The formation of oriented thin films can be realized with a different construction of the reaction vessel. In this case, the desired substrate is placed upside down in the reaction mixture and solvothermal reaction conditions are applied. During the reaction time, bulk COF material is formed at the bottom of the vessel and an oriented film is able to grow

on the bottom side of the substrate. When removing the substrate out of the reaction mixture the top side can be cleaned from bulk material, leaving only the thin, well-orientated, and porous films on the bottom. The according film synthesis is illustrated in Figure 1-13.[77, 78]

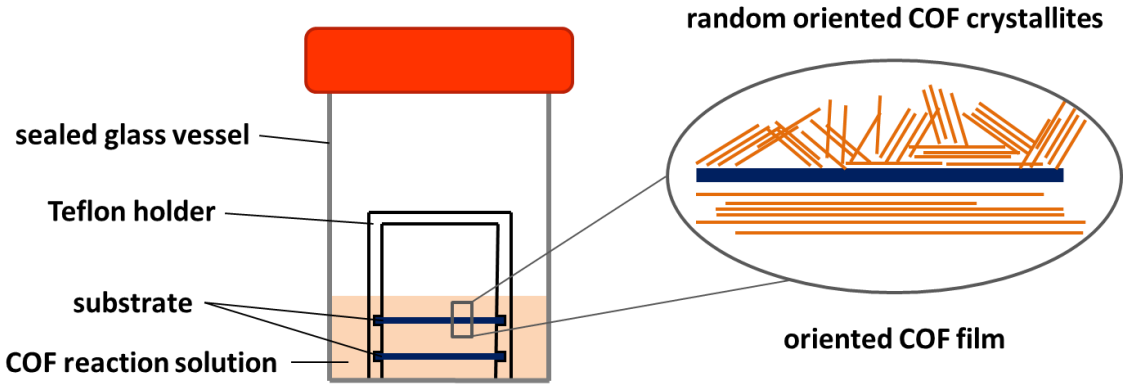

Figure 1-13: COF film synthesis under solvothermal reaction conditions resulting in an oriented, thin, and porous film at the bottom of the substrate, whereas on the top formation of randomly oriented crystallites can be observed.

1.5 Postsynthetic Modification

By applying reticular synthesis based on the different linker geometries for COF synthesis, COFs possess open pores with diverse shapes. The resulting environment of the pore strongly depends on the implemented linkers and their decoration such as sterically demanding side chains or different functional groups at their backbones. However, the range of variation of decorated linkers which can be established during the COF synthesis is limited due to geometry reasons. To overcome this problem and to be able to implement even large side or functional groups which would inhibit the COF formation, a postsynthetic modification (PSM) process can be performed after the crystalline framework has already been formed. This process allows for the introduction of desired functionalization into the pores and to the outer surface of the COF network.[24] One precondition for this approach is that the implemented linkers within the network are decorated with functional groups which can later be modified in the process of attaching other anticipated molecules. On the other side, the desired function or molecule has also to be assigned with a corresponding functional group to make sure that bonds, such as covalent or complex bonds, can be formed.

Postsynthetic intercalation is one of the most straight-forward PSM approaches on COFs. Here, molecules are introduced in the COF pores by adsorption, influencing the

characteristics. For example pyridine moieties were intercalated into COF-10 based on boronate ester bonds showing a drastically improvement of the network stability against hydrolysis.[79] When using imine-linked COFs the nitrogen of the bond can serve as anchor point for metal ions. Consequently, the postsynthetic introduction of metal ions leads to a fixation of the metal centers within the porous framework. These can serve as defined and separate reaction centers which could be favorable for applications concerning catalysis and sorption.[24, 80] Also hydroxyl groups intruding into the pores can serve as anchor points for several metal ions like vanadium, copper or cobalt, improving the overall catalytic performances.[81] Another possibility to insert metal ions is the implementation of porphyrin units and intercalating metals directly into the center of these building blocks leading to improved catalysis and different stacking behavior between the 2D sheets.[24]

First investigations on covalent attachments of functional groups were performed again on boronate ester-based COFs and different fractions of azides were introduced in the network.[82] The azide moieties were able to react with various alkynes *via* copper-catalyzed click reactions. Using this reaction mechanism, even large functionalities could be attached to the framework. Moreover, the amount of azides within the framework had an influence on the possible amount of introduced groups.[82] This click chemistry approach also enabled the incorporation of electroactive functionalized fullerenes into the pores of a boronate ester phthalocyanine COF by covalent binding.[83] On the other hand, the click reaction can also be used starting from an alkyne-functionalized COF resulting in postsynthetically introduced functional groups. For example, this approach was applied for tuning the capacity for carbon dioxide storage.[84] Apart from one-step reactions, more complicated two-step reactions are also used for modification approaches. Pendant nitro groups in ketoenamine-based COFs can be reduced to primary amines in a first step. This leads to accessible amino-decorated pores which cannot be obtained directly during the COF synthesis due to their high reactivity. In a second step these free amino groups can now be modified with any suitable functionalization. This approach is an option if amino pore wall functionalization is desired in imine-based COFs, due to amines being the reactive parts of the starting material in COF synthesis.[85] As well as for the intercalation and complexation approach, hydroxyl groups can also be an anchor point for covalently attaching molecules postsynthetically. They are a very suitable type of functional groups due to their small size and their wide-spread use on linkers for COF synthesis. Furthermore,

hydroxyl groups can form covalent bonds with diverse functional groups. Next to bond formation they can also be transformed into free carboxylic acid groups to improve gas storage in general.[86]

Apart from forming complex and covalent bonds, there are other approaches for PSM. A connection between adjacent COF layers was reported, exploiting the ability of anthracene to dimerize under UV illumination. Here, anthracene was implemented into a boronate ester-based COF as a linear linker. The crystalline COF was then exposed to UV irradiation at 360 nm and the anthracene units of adjacent COF layers underwent a [4+4] cycloaddition resulting in a connection between two neighboring COF layers. As known for pure anthracene (see Section 1.3.4), the cycloaddition was reversible and repeatable for several cycles.[87] This process has to be carefully selected though since some cycloadditions on anthracene result in a delamination of the COF layers when the implemented moiety is too sterically demanding.[88] In addition, stable functional groups such as methyl groups can be postsynthetically modified by bromination to further establish quaternary ammonium units at the pore walls.[89] All in all, the great variety of linkers in COF synthesis in combination with vast range of linker functionalization with different groups offers a great way to postsynthetically modify COFs in order to achieve the desired properties. This further extends the structural and functional diversity of COFs for applications and devices.

One common application is functionalization with dyes. Due to their optical characteristics they are very easy to detect and to locate. In biomedical research, fluorescent dyes are frequently used for imaging biological structures and processes. This includes cell signaling, live-cell imaging, photoswitching, as well as transcription and replication.[90] Fluorescent sensors have attracted much attention directed towards real-time monitoring and the possibility of imaging deep structures. These fluorophores are often compounds which can re-emit light upon photoexcitation due to their aromaticity arising from several combined aromatic groups. Fluorophores can be used on their own as tracers in fluids or as a substrate for enzymes but more generally they are covalently bonded to macromolecules where they can serve as marker.[91] One of the most popular fluorophores is fluorescein with its most reactive fluorescein isothiocyanate (FITC) (see Figure 1-14). This molecule exhibits its absorption maximum at around 490 nm and its emission maximum at approximately 520 nm.[92] Due to its highly fluorescent character, it can be easily detected with microscopes or in

fluorescence spectroscopy. Especially, in biochemical research, fluorescein and its derivatives are used to label and track cells in fluorescence microscopy applications. In addition, the fluorophore can be attached to biologically active molecules, such as antibodies, which allows for the targeting of specific proteins or structures within cells.[93] This attachment can also be used for marking oligonucleotides for the same purpose.[94]

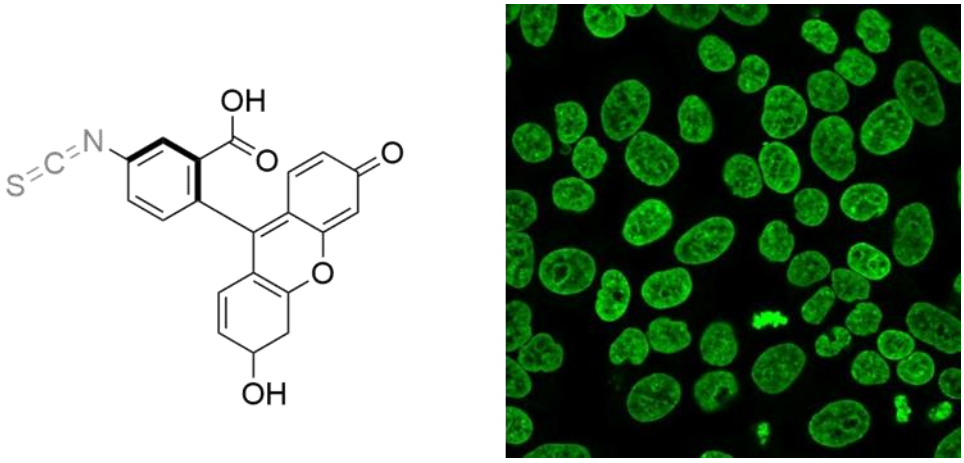

Figure 1-14: Illustration of the fluorescein isothiocyanate molecule which can be used for cell labeling; here formaldehyde-fixed, Triton X-100-permeabilized HeLa cancer cells.[95] Figure adapted from Ref. 95.

One great advantage of applying such fluorescent dyes for modification approaches is the possibility to visualize the dye-labeled location using super-resolution microscopy. Several methods have already been developed to detect fluorescence signals from molecules even in small amounts and spatial resolutions which break the limits of conventional microscopies.[96-98]

1.6 Electroactive and Photoactive Materials

Due to the well-defined geometry of COFs the material is able to form well-ordered conjugated π-systems which result in 2D sheets. As already mentioned these sheets can stack on top of each other, directed by π-π interactions and leading to 3D materials. The stacking behavior influences and defines the electronic performance and makes COFs promising candidates for electroactive materials. The optical and electrical properties of the desired framework can be tailored by the careful choice of the integrated building blocks. The implementation of the desired molecules strongly influences the interactions between the 2D layers. The layers usually avoid stacking directly on top of each other but rather show a slight offset of less than 2 Å which is driven through energy minimization.[99]

One of the most important and basic characteristics of electroactive materials is their electrical conductivity and charge carrier mobility, defining their charge transport ability.[100]

Enhancing the mobility can be achieved by using crystalline materials instead of amorphous organic polymer chains because they exhibit close interactions between the internal segments.[101] In the case of polymers, only few materials have shown high charge carrier mobilities due to the small overlap of the short effectively-conjugated segments, even in a face-to-face stacking mode.[102, 103] Consequently, 2D sheets offer an ideal basis for a large number of molecular interactions. Due to the periodicity of the sheets and the π-π interactions between them, a broad path for charge carriers moving along the stack of the layers is created.[104] With this background in mind, COFs with a relatively short interlayer distance allowing for stronger electronic interactions between the different sheets can be designed.

In principle, the in-plane conductivity values strongly depend on the applied bonding motif. Concerning only bulk material, mainly the well-established boronate ester and imine bond linkages, were established. Comparing these two types of linkages, the boronate ester bond exhibits limited electronic coupling within the layer because of the non-conjugated connection. This allows for the formation of a continuous pattern in one (*z*-) direction. In contrast, the imine bond offers a path towards extended conjugation also within the layer due to the full (although polarized) conjugation also across the bonds. This ultimately results in charge transport expected to occur mainly along the stacking direction in boronate ester-based COFs whereas imine-based COFs can exhibit additional transport in the lateral directions.[105]

The boronate ester-based COF platform can show great promise for charge-carrier separation and collection, respectively. Diimide linear chromophores were implemented in boronate ester-based COFs showing a charge transfer (CT) state lifetime of 2.5 μs indicating the presence of long-lived radicals.[106] In addition, a COF based on diimide and metallo-phtalocyanine chromophores showed a so called superheterojunction. Here, an electron donor and an electron acceptor subunit are implemented at the same time in the same framework.[107] Due to the well-defined distribution of the acceptor and donor within the framework a stack can be achieved, in which the chemical and physical environment supports electron transfer and charge separation leading to enhanced excited state lifetimes.

COF charge carrier mobilities have so far usually been obtained through laser flash-photolysis time-resolved microwave conductivity measurements (FP-TRMC). Here, for the two boronate ester-based COF-366 and COF-66 high charge carrier mobilities of 8.1 and 3.0 $cm^2V^{-1}s^{-1}$ have been reported.[104] Furthermore, the charge carrier mobility was studied on imine-linked COFs containing tetrathiafulvalene and -arene as well as phenyl pyrene subunits, obtaining mobilities of 0.08 and 0.2 $cm^2V^{-1}s^{-1}$, respectively.[104] The higher mobility of the arene-based framework was attributed to the shorter stacking distance in the arene-based COF with more planar conformation of the layers and a stronger overlap of the π-electrons between the 2D sheets.[108] In order to measure their electrical conductivity, the COF bulk material was chemically oxidized by exposure to iodine vapor and further transferred on a substrate with gold electrode patterns, reaching conductivity values up to 10^{-6} Scm^{-1}.[109] Other tetrathiafulvalene COFs exhibit conductivities as high as 10^{-3} Scm^{-1} for iodine doped films.[109]

It has to be noted that FP-TRMC measurements are probing the charge carrier mobilities only within a small, few nanometer wide volume. The extracted values can be orders of magnitude larger than long-range mobilities of the same material.[110] Therefore, to assess the macroscopic charge carrier mobility, complementary measurement techniques should be applied as well.

Using hole-only devices (HODs), mobilities of an oriented BDT thin COF film were reported.[111] Here, the HODs were constructed in the following architecture: glass/ITO/MoO_x/BDT-COF/MoO_x/Au. (see Figure 1-15a). Measurements were performed in the dark and revealed that the thickness of the COF film strongly influences the mobility and charge transport of the system. Thinner films showed a higher hole mobility, reaching up to 10^{-7} $cm^2V^{-1}s^{-1}$. This effect can be attributed to intrinsic electronic defects within the stacks of the COF sheets. Furthermore, charge carrier mobilities could be increased under illumination, pointing to the photoactivity of the material.[111]

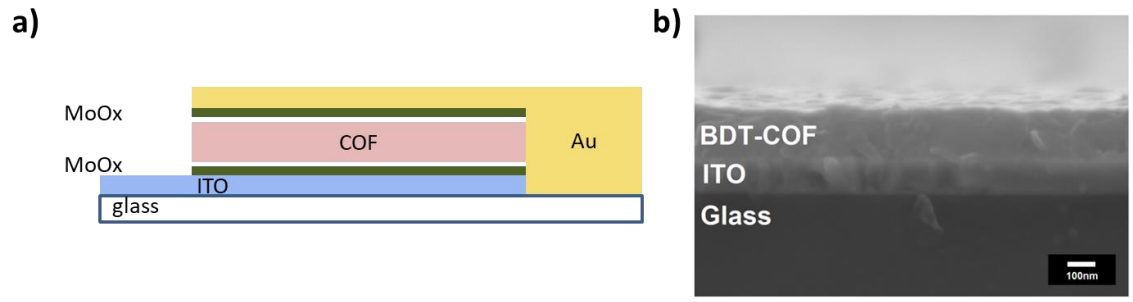

Figure 1-15: a) Device architecture for measuring the hole mobility based on glass/ITO/MoO_x/COF/MoO_x/Au, b) SEM cross-section micrographs of 90 nm BDT-COF film HOD imaged in backscattered electron mode.[111] Figure adapted from Ref. 111.

A different approach for electroactive COFs and in particular for photoactive systems is the formation of interpenetrating systems. In this case, the porosity of the crystalline framework is used by intercalating guest molecules into the open pores allowing for the formation of a second continuous phase in the COF. Here, the idea is to exploit photo-induced charge transfer from a semiconducting electron donating COF to a complementary guest phase located in the pores, which can accept the electrons. In previous work, a boronate ester TT-COF was interpenetrated with PCBM acting as electron acceptor showing efficient COF fluorescence quenching.[112] In addition, this framework was integrated into a photovoltaic device which was able to extract charge carriers from this interpenetrated COF system.[105]

Because of the relatively low conductivity of two-dimensional COFs developed so far, several methods have been explored to increase this property. Electropolymerization of 3,4-ethylenedioxythiophene (EDOT) in the pores of thin COF films showed an enhancement of conductivity followed by a drastic improvement of the electrochemical response. Another effort to leverage the structural features of these frameworks is the introduction of chalcogen-based materials as dopands due to their known ability to improve organic conductors. Here, narrow band gap polymers could be improved with regard to charge carrier mobility. Also the doped COF materials showed enhanced conductivity values when performing two-point probe measurements.[113]

For further optoelectronic applications, the deposition of COF materials as thin films opens the path for devices with a great range of functionalities. Hereby, the orientation of the network including its stacking behavior and stacking distance strongly influences the carrier transport and collection and can be controlled during film formation. Therefore, the film synthesis is very important for studying the physical properties of future devices.

The first COF solar cell device was based on a TT-COF network, where the network served as electron donor and PCBM was interpenetrated in the open pores serving as acceptor phase (see Figure 1-16a). The whole device was synthesized and built up from a 200 nm thick film and was able to show moderate power conversion efficiency.[112] Fully conjugated COF frameworks transferred on a thin film and used as solar cells were developed based on phenazine linkages. Interpenetrated systems were obtained *via* a sublimation under vacuum showing efficiencies of 0.9%.[114] Next to interpenetration of electron acceptors, electron donors and acceptors can also be implemented in a framework at the same time by separating the subunit stacks through non-conjugated boronate ester groups (see Figure 1-16b). A COF based on triphenylene and porphyrin led to an intrinsic type II heterojunction behavior. The overall device was built up from a 50 nm thick film grown on ITO/MoO_x with ZnO/Al as counter electrode. External quantum efficiency (EQE) measurements showed that the observed photoresponse was originating from both components of the framework.[78]

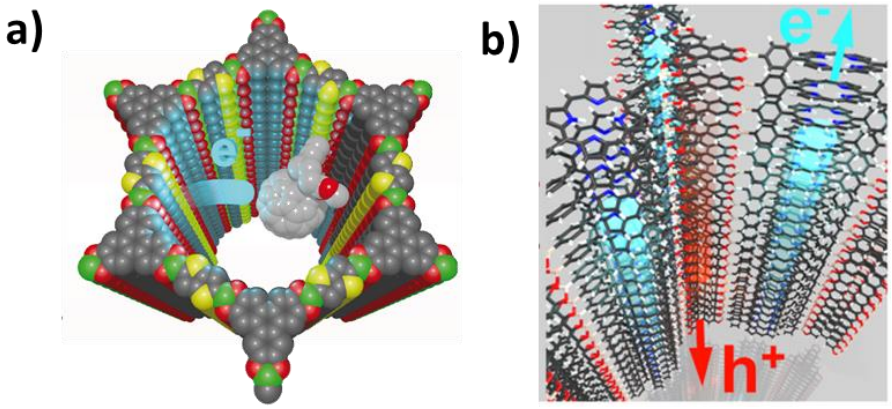

Figure 1-16: a) TT-COF interpenetrated with PCBM as electron acceptor,[112] b) schematic illustration of photo-induced charge transfer in a TP-Por-COF showing isolated subunits by boronate ester connection.[78] Figure adapted from Ref. 112 and 78, respectively.

1.7 References

1. D. Chandler, *Phys. Org.* **2011**, *4*, 2017.
2. IEA, International Energy Agency (IEA) via The World Bank, **2014**.
3. G. P. Smestad, F. C. Krebs, C. M. Lampert, C. G. Granqvist, K. Chopra, X. Mathew, and H. Takakura, Elsevier, **2008**.
4. B. Ecker, *Phy. Unserer Zeit* **2013**, *44*, 84-91.
5. M. Ramrakhiani, S. Dubey, H. Waxar, K. K. Kushwaha, and P. Singh, in *Recent Advances in Photovoltaics*, **2017**.
6. J. Nelson, *Mater. Today* **2011**, *14*, 462-470.
7. J. Luther, M. Nast, M. N. Fisch, D. Christoffers, F. Pfisterer, D. Meissner, J. Nitsch, and M. Becker, in *Ullmann's Encyclopedia of Industrial Chemistry*, **2012**.
8. M. Jørgensen, K. Norrman, and F. C. Krebs, *Sol. Energy Mater. Sol. Cells* **2008**, *92*, 686-714.
9. J. Nelson, *Curr. Opin. Solid State Mater. Sci.* **2002**, *6*, 87-95.
10. M. D. McGehee, and M. A. Topinka, *Nat. Mater.* **2006**, *5*, 675.
11. M. C. Scharber, D. Mühlbacher, M. Koppe, P. Denk, C. Waldauf, A. J. Heeger, and C. J. Brabec, *Adv. Mater.* **2006**, *18*, 789-794.
12. http://h2.gntech.ac.kr/index.php?mid=opv, Accessed 27.08.2018.
13. Y. Kim and E. Lim, *Polymers* **2014**, *6*, 382-407.
14. M. T. Dang, L. Hirsch, and G. Wantz, *Adv. Mater.* **2011**, *23*, 3597-3602.
15. S. Chizu, T. Yoshiaki, Y. Takeshi, K. Makoto, and D. Shuji, *Sci. Tech. Adv. Mater.* **2014**, *15*, 034203.
16. A. P. Côté, A. I. Benin, N. W. Ockwig, M. O'Keeffe, A. J. Matzger, and O. M. Yaghi, *Science* **2005**, *310*, 1166-1170.
17. C. J. Brabec, *Sol. Energy Mater. Sol. Cells* **2004**, *83*, 273-292.
18. L. El Chaar, L. A. Lamont, and N. El Zein, *Renew. Sust. Energ. Rev.* **2011**, *15*, 2165-2175.
19. S. Kitagawa, R. Kitaura, and S.-I. Noro, *Angew. Chem. Int. Ed.* **2004**, *43*, 2334-2375.
20. X. Feng, X. Ding, and D. Jiang, *Chem. Soc. Rev.* **2012**, *41*, 6010-6022.
21. A. Granzhan, T. Riis-Johannessen, R. Scopelliti, and K. Severin, *Angew. Chem. Int. Ed.* **2010**, *49*, 5515-5518.
22. M. Dogru and T. Bein, *Chem. Comm.* **2014**, *50*, 5531-5546.

23. F. J. Uribe-Romo, J. R. Hunt, H. Furukawa, C. Klöck, M. O'Keeffe, and O. M. Yaghi, *J. Am. Chem. Soc.* **2009**, *131*, 4570-4571.
24. M. S. Lohse and T. Bein, *Adv. Funct. Mater.* **2018**, *28*, 1705553.
25. Q. Fang, Z. Zhuang, S. Gu, R. B. Kaspar, J. Zheng, J. Wang, S. Qiu, and Y. Yan, *Nat. Commun.* **2014**, *5*, 4503.
26. P. Kuhn, M. Antonietti, and A. Thomas, *Angew. Chem. Int. Ed.* **2008**, *47*, 3450-3453.
27. K. T. Jackson, T. E. Reich, and H. M. El-Kaderi, *Chem. Comm.* **2012**, *48*, 8823-8825.
28. F. J. Uribe-Romo, C. J. Doonan, H. Furukawa, K. Oisaki, and O. M. Yaghi, *J. Am. Chem. Soc.* **2011**, *133*, 11478-11481.
29. W. Herbst and K. Hunger, *Industrielle Organische Pigmente*, John Wiley & Sons, **2009**.
30. H. Langhals, T. Potrawa, H. Noeth, and G. Linti, *Angew. Chem. Int. Ed.* **1989**, *28*, 478-480.
31. H. Langhals, T. Grundei, T. Potrawa, and K. Polborn, *Liebigs Ann.* **1996**, *1996*, 679-682.
32. A. S. Ivanov and A. I. Boldyrev, *Org. Biomol. Chem.* **2014**, *12*, 6145-6150.
33. T. D. Lash, *J. Porphyrins Phthalocyanines* **2011**, *15*, 1093-1115.
34. K. Kadish, K. M. Smith, and R. Guilard, *The Porphyrin Handbook*, Elsevier Science, **2000**.
35. P. Rothemund, *J. Am. Chem. Soc.* **1935**, *57*, 2010-2011.
36. P. Rothemund, *J. Am. Chem. Soc.* **1936**, *58*, 625-627.
37. F. Giuntini, R. Boyle, M. Sibrian-Vazquez, and M. Graça H. Vicente, in *Handbook of Porphyrin Science (Volume 27) With Applications to Chemistry, Physics, Materials Science, Engineering, Biology, and Medicine—Volume 27: Erythropoiesis, Heme, and Applications to Biomedicine*, World Scientific, **2014**, 303-416.
38. C. H. Walker, R. Sibly, S. P. Hopkin, and D. B. Peakall, *Principles of ecotoxicology*, CRC press, **2005**.
39. M. G. Walter, A. B. Rudine, and C. C. Wamser, *J. Porphyrins Phthalocyanines* **2010**, *14*, 759-792.
40. S. Anderson, H. L. Anderson, A. Bashall, M. McPartlin, and J. K. M. Sanders, *Angew. Chem. Int. Ed.* **1995**, *34*, 1096-1099.

41. P. Zucca, A. Rescigno, A. C. Rinaldi, and E. Sanjust, *J. Mol. Catal. A: Chem.* **2014**, *388-389*, 2-34.
42. in *Ullmann's Encyclopedia of Industrial Chemistry*.
43. J. Rouzaud and A. Oberlin, *Carbon* **1989**, *27*, 517-529.
44. K. D. M. Charleton and E. M. Prokopchuk, *J. Chem. Educ.* **2011**, *88*, 1155-1157.
45. B. Rickborn, *Org. React.* **1998**.
46. H. Bouas-Laurent, A. Castellan, J.-P. Desvergne, and R. Lapouyade, *Chem. Soc. Rev.* **2000**, *29*, 43-55.
47. J. K. Guillory, ACS Publications, **2009**.
48. https://www.smta.org/chapters/files/UpperMidwest_BTW_ Conformal_Coating_June_27th_2012.pdf, Accessed 07.11.2018.
49. J. Shi and C. W. Tang, *Appl. Phys. Lett.* **2002**, *80*, 3201-3203.
50. B. J. Chen, X. W. Sun, Y. Divayana, and B. K. Tay, *J. App. Phys.* **2005**, *98*, 046107.
51. R. Kepler, *Phy. Rev.* **1960**, *119*, 1226.
52. S. Ma, D. Sun, J. M. Simmons, C. D. Collier, D. Yuan, and H.-C. Zhou, *J. Am. Chem. Soc.* **2008**, *130*, 1012-1016.
53. W. H. Mills and M. Mills, *J. Chem. Soc., Trans.* **1912**, *101*, 2194-2208.
54. D. R. Maulding and B. G. Roberts, *J. Org. Chem.* **1969**, *34*, 1734-1736.
55. Z. Chen and T. M. Swager, *Org. Lett.* **2007**, *9*, 997-1000.
56. Georgia Institute Of Technology. "Efficiently Organic: Researchers Use Pentacene To Develop Next-generation Solar Power." ScienceDaily, Accessed 08.11.2018.
57. S. Yoo, B. Domercq, and B. Kippelen, *Appl. Phys. Lett.* **2004**, *85*, 5427-5429.
58. D. N. Congreve, J. Lee, N. J. Thompson, E. Hontz, S. R. Yost, P. D. Reusswig, M. E. Bahlke, S. Reineke, T. Van Voorhis, and M. A. Baldo, *Science* **2013**, *340*, 334-337.
59. M. Tabachnyk, B. Ehrler, S. Bayliss, R. H. Friend, and N. C. Greenham, *Appl. Phys. Lett.* **2013**, *103*, 153302.
60. B. Ehrler, K. P. Musselman, M. L. Böhm, R. H. Friend, and N. C. Greenham, *Appl. Phys. Lett.* **2012**, *101*, 153507.
61. N. Koch, *ChemPhysChem* **2007**, *8*, 1438-1455.
62. T. Hasegawa and J. Takeya, *Sci. Technol. Adv. Mater.* **2009**, *10*, 024314.

63. Y. Yamashita, *Sci. Tech. Adv. Mater.* **2009**, *10*, 024313.
64. S. K. Park, T. N. Jackson, J. E. Anthony, and D. A. Mourey, *Appl. Phys. Lett.* **2007**, *91*, 063514.
65. C. D. Sheraw, T. N. Jackson, D. L. Eaton, and J. E. Anthony, *Adv. Mater.* **2003**, *15*, 2009-2011.
66. M. W. B. Wilson, A. Rao, J. Clark, R. S. S. Kumar, D. Brida, G. Cerullo, and R. H. Friend, *J. Am. Chem. Soc.* **2011**, *133*, 11830-11833.
67. M. B. Smith and J. Michl, *Chem. Rev.* **2010**, *110*, 6891-6936.
68. https://science.energy.gov/~/media/bes/csgb/pdf/docs/Solar_ photochemistry_2004.pdf, Accessed 27.10.2018.
69. B. J. Walker, A. J. Musser, D. Beljonne, and R. H. Friend, *Nat. Chem.* **2013**, *5*, 1019.
70. J. Zirzlmeier, D. Lehnherr, P. B. Coto, E. T. Chernick, R. Casillas, B. S. Basel, M. Thoss, R. R. Tykwinski, and D. M. Guldi, *PNAS* **2015**, *112*, 5325-5330.
71. S. Lukman, K. Chen, J. M. Hodgkiss, D. H. P. Turban, N. D. M. Hine, S. Dong, J. Wu, N. C. Greenham, and A. J. Musser, *Nat. Commun.* **2016**, *7*, 13622.
72. A. P. Cote, H. M. El-Kaderi, H. Furukawa, J. R. Hunt, and O. M. Yaghi, *J. Am. Chem. Soc.* **2007**, *129*, 12914-12915.
73. N. L. Campbell, R. Clowes, L. K. Ritchie, and A. I. Cooper, *Chem. Mater.* **2009**, *21*, 204-206.
74. P. W. Atkins and J. De Paula, *Physikalische Chemie*, John Wiley & Sons, **2013**.
75. https://en.wikipedia.org/wiki/Supercritical_carbon_ dioxide#/media/File:Carbon_dioxide_pressure-temperature_phase_diagram.svg, Accessed 08.11.2018.
76. D. D. Medina, J. M. Rotter, Y. Hu, M. Dogru, V. Werner, F. Auras, J. T. Markiewicz, P. Knochel, and T. Bein, *J. Am. Chem. Soc.* **2015**, *137*, 1016-1019.
77. D. D. Medina, V. Werner, F. Auras, R. Tautz, M. Dogru, J. r. Schuster, S. Linke, M. Döblinger, J. Feldmann, and P. Knochel, *ACS Nano* **2014**, *8*, 4042-4052.
78. M. Calik, F. Auras, L. M. Salonen, K. Bader, I. Grill, M. Handloser, D. D. Medina, M. Dogru, F. Löbermann, D. Trauner, A. Hartschuh, and T. Bein, *J. Am. Chem. Soc.* **2014**, *136*, 17802-17807.
79. Y. Du, K. Mao, P. Kamakoti, P. Ravikovitch, C. Paur, S. Cundy, Q. Li, and D. Calabro, *Chem. Comm.* **2012**, *48*, 4606-4608.

80. S.-Y. Ding, J. Gao, Q. Wang, Y. Zhang, W.-G. Song, C.-Y. Su, and W. Wang, *J. Am. Chem. Soc.* **2011**, *133*, 19816-19822.
81. Q. Sun, B. Aguila, J. Perman, N. Nguyen, and S. Ma, *J. Am. Chem. Soc.* **2016**, *138*, 15790-15796.
82. A. Nagai, Z. Guo, X. Feng, S. Jin, X. Chen, X. Ding, and D. Jiang, *Nat. Commun.* **2011**, *2*, 536.
83. L. Chen, K. Furukawa, J. Gao, A. Nagai, T. Nakamura, Y. Dong, and D. Jiang, *J. Am. Chem. Soc.* **2014**, *136*, 9806-9809.
84. N. Huang, R. Krishna, and D. Jiang, *J. Am. Chem. Soc.* **2015**, *137*, 7079-7082.
85. M. S. Lohse, T. Stassin, G. Naudin, S. Wuttke, R. Ameloot, D. De Vos, D. D. Medina, and T. Bein, *Chem. Mater.* **2016**, *28*, 626-631.
86. N. Huang, X. Chen, R. Krishna, and D. Jiang, *Angew. Chem. Int. Ed.* **2015**, *54*, 2986-2990.
87. N. Huang, X. Ding, J. Kim, H. Ihee, and D. Jiang, *Angew. Chem. Int. Ed.* **2015**, *54*, 8704-8707.
88. M. A. Khayum, S. Kandambeth, S. Mitra, S. B. Nair, A. Das, S. S. Nagane, R. Mukherjee, and R. Banerjee, *Angew. Chem. Int. Ed.* **2016**, *128*, 15833-15837.
89. H. Guo, J. Wang, Q. Fang, Y. Zhao, S. Gu, J. Zheng, and Y. Yan, *CrystEngComm* **2017**, *19*, 4905-4910.
90. X. Liu, L. Yang, Q. Long, D. Weaver, and G. Hajnóczky, *Biophys. Rep.* **2017**, *3*, 64-72.
91. K. Rurack and M. Spieles, *Anal. Chem.* **2011**, *83*, 1232-1242.
92. E. Noga and P. Udomkusonsri, *Vet. Pathol.* **2002**, *39*, 726-731.
93. J. D. Marshall, W. C. Eveland, and C. W. Smith, *Proc. Soc. Exp. Miol. Med.* **1958**, *98*, 898-900.
94. F. Schubert, K. Ahlert, D. Cech, and A. Rosenthal, *Nucleic Acids Res.* **1990**, *18*, 3427.
95. https://biotium.com/technology/cellular-stains/, Accessed 08.11.2018.
96. M. Minoshima and K. Kikuchi, *J. Biol. Inorg. Chem.* **2017**, *22*, 639-652.
97. S. W. Hell and J. Wichmann, *Opti. Lett.* **1994**, *19*, 780-782.
98. E. Betzig, A. Lewis, A. Harootunian, M. Isaacson, and E. Kratschmer, *Biophys. J.* **1986**, *49*, 269-279.

99. E. L. Spitler, B. T. Koo, J. L. Novotney, J. W. Colson, F. J. Uribe-Romo, G. D. Gutierrez, P. Clancy, and W. R. Dichtel, *J. Am. Chem. Soc.* **2011**, *133*, 19416-19421.

100. F. Laquai, G. Wegner, and H. Bässler, *Philos. Trans. R. Soc. London, Ser. A* **2007**, *365*, 1473-1487.

101. V. Coropceanu, J. Cornil, D. A. da Silva Filho, Y. Olivier, R. Silbey, and J.-L. Brédas, *Chem. Rev.* **2007**, *107*, 926-952.

102. J. M. Warman, M. P. de Haas, G. Dicker, F. C. Grozema, J. Piris, and M. G. Debije, *Chem. Mater.* **2004**, *16*, 4600-4609.

103. I. McCulloch, M. Heeney, C. Bailey, K. Genevicius, I. MacDonald, M. Shkunov, D. Sparrowe, S. Tierney, R. Wagner, W. Zhang, M. L. Chabinyc, R. J. Kline, M. D. McGehee, and M. F. Toney, *Nat. Mater.* **2006**, *5*, 328.

104. S. Wan, F. Gándara, A. Asano, H. Furukawa, A. Saeki, S. K. Dey, L. Liao, M. W. Ambrogio, Y. Y. Botros, X. Duan, S. Seki, J. F. Stoddart, and O. M. Yaghi, *Chem. Mater.* **2011**, *23*, 4094-4097.

105. D. D. Medina, T. Sick, and T. Bein, *Adv. Energy Mater.* **2017**, *7*, 1700387.

106. S. Jin, K. Furukawa, M. Addicoat, L. Chen, S. Takahashi, S. Irle, T. Nakamura, and D. Jiang, *Chem. Sci.* **2013**, *4*, 4505-4511.

107. S. Jin, M. Supur, M. Addicoat, K. Furukawa, L. Chen, T. Nakamura, S. Fukuzumi, S. Irle, and D. Jiang, *J. Am. Chem. Soc.* **2015**, *137*, 7817-7827.

108. S. Jin, T. Sakurai, T. Kowalczyk, S. Dalapati, F. Xu, H. Wei, X. Chen, J. Gao, S. Seki, and S. Irle, *Chem. Eur. J.* **2014**, *20*, 14608-14613.

109. S.-L. Cai, Y.-B. Zhang, A. B. Pun, B. He, J. Yang, F. M. Toma, I. D. Sharp, O. M. Yaghi, J. Fan, S.-R. Zheng, W.-G. Zhang, and Y. Liu, *Chem. Sci.* **2014**, *5*, 4693-4700.

110. A. Saeki, Y. Koizumi, T. Aida, and S. Seki, *Acc. Chem. Res.* **2012**, *45*, 1193-1202.

111. D. D. Medina, M. L. Petrus, A. N. Jumabekov, J. T. Margraf, S. Weinberger, J. M. Rotter, T. Clark, and T. Bein, *ACS Nano* **2017**, *11*, 2706-2713.

112. M. Dogru, M. Handloser, F. Auras, T. Kunz, D. Medina, A. Hartschuh, P. Knochel, and T. Bein, *Angew. Chem. Int. Ed.* **2013**, *52*, 2920-2924.

113. S. Duhović and M. Dincă, *Chem. Mater.* **2015**, *27*, 5487-5490.

114. J. Guo, Y. Xu, S. Jin, L. Chen, T. Kaji, Y. Honsho, M. A. Addicoat, J. Kim, A. Saeki, and H. Ihee, *Nat. Commun.* **2013**, *4*, 2736.

2 Characterization Techniques

This chapter deals with the complete and detailed characterization of the produced materials, precursors, resulting effects, and possible applications. Next to the different characterization techniques, their theoretical background is briefly discussed.

The phase composition and crystallinity were determined by X-ray diffraction (XRD) and Infrared (IR) spectroscopy. Nitrogen sorption measurements were used to gain information about the porosity of the synthesized structure including surface area, pore size and pore size distribution. Thermogravimetric analysis (TGA) was applied to show the thermal stability in synthetic air. The topology and morphology as well as the pore shape and distribution within the material were obtained by using electron microscopy (SEM/TEM). Optical characterization was achieved by using ultraviolet-visible (UV-vis) spectroscopy, photoluminescence (PL) spectroscopy and time correlated single photon counting (TCSPC). Nuclear magnetic resonance (NMR) was applied to either check the successful synthesis of the precursors or to get a deeper insight in the composition of the produced materials. Fluorescence microscopy was used to determine the amount of fluorescent dyes in the functionalized COF whereas the fluorescence microscope can detect the successful functionalization optically. The electrical conductivity of bulk powder and thin film materials was studied by Hall conductivity measurements in the van der Pauw geometry. Hole-only devices were investigated to learn about the charge carrier mobility.

2.1 X-ray Diffraction (XRD)

XRD is an analytical technique which allows for the identification of the composition, crystallinity, purity of the different phases, crystal symmetry, particle size, and furthermore structure of crystalline substances. X-rays were first observed by Wilhelm Conrad Röntgen in 1895. They are a form of electromagnetic radiation having a wavelength between 10^{-8} and 10^{-12} m. X-rays are generated inside a high vacuum tube. Thus highly accelerated electrons from the cathode collide with the anode metal, such as Cu, Mo, Al or Mg, under a high voltage resulting in different X-ray wavelengths. The correlation between the atomic number Z and the wavelength λ of the emitted characteristic radiation is described by Moseley´s law.[1]

$$\frac{1}{\lambda} = \frac{K}{(Z-\sigma)^2} \tag{2.1}$$

Equation 2.1: Mosely´s law: wavelength λ, atomic number Z, K, σ: constants for spectral line.

In 1912, Max von Laue discovered the interference of X-rays, passing through crystals, acting as three-dimensional diffraction lattices. The scattering of electromagnetic waves in a small range (Å) on structure with the same dimension allows for structure determination by monitoring the diffraction maxima caused by constructive interference.[2]

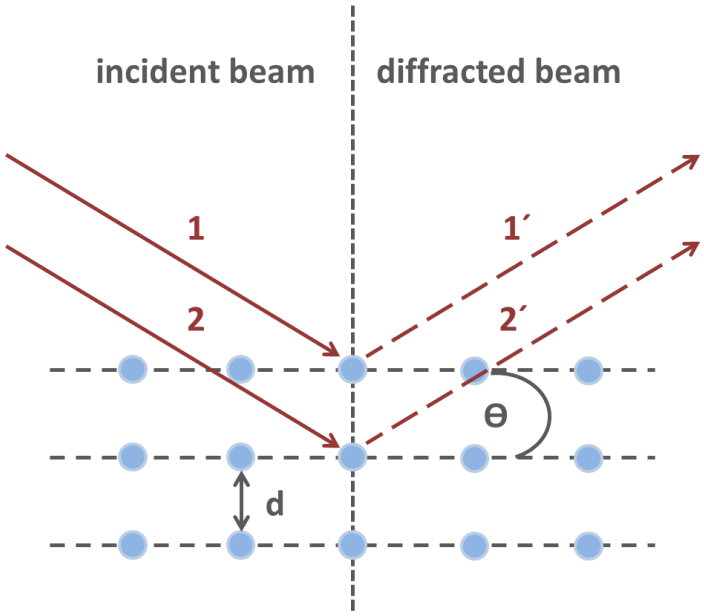

Figure 2-1: Schematic illustration of X-ray scattering according to Bragg´s relation; *d*: lattice plane spacing, *Θ*: angle of incident.

Figure 2-1 shows the diffraction geometry at different lattice planes of a crystal. Here, the originated characteristic monochromatic X-rays interact with the sample. These interactions can result in different effects such as scattering, reflection and absorption. Since the distances in the crystal lattice and the wavelength of X-rays are used by similar order of magnitude constructive interference phenomena occurs here. All lattice planes of a crystal are oriented in all directions at a certain distance in the space. The X-rays are diffracted at the material under specific, so called Bragg angles. This results in an angle-dependent intensity distribution, which is based on Bragg`s equation:

$$2dsin\theta = n\lambda$$

(2.2)

Equation 2.2: *d:* lattice spacing, *Θ:* angle of incidence, *n:* order of interference, λ: wavelength of X-rays.

Different effects like overlapping reflexes or certain preferred orientations of the crystallites can limit the information content of the resulting diffractogram. The angle-dependent exposition of the position of the reflexes can be used to draw conclusions from the structure. Equally, size and shape of the located reflexes can indicate parameters of the sample. For example the peak broadening of the diffraction peaks depends on the domain size of the crystalline phase.[1] The crystal size is related with the diffraction peak width using the form of full width at half maximum (FWHM) by the Scherrer equation:

$$D = \frac{k\lambda}{\beta \cos\theta}$$

(2.3)

Equation 2.3: *D*: crystallite size, λ: wavelength of the X-rays, β*:* full width at half maximum (FWHM) of diffraction peak, θ*:* diffraction angle, *k*: Scherrer constant.

In this work, PXRD measurements were performed on a Bruker D8 Discover diffractometer with Ni filtered Kα radiation (λ = 1.54060 Å) and a position-sensitive detector (LynxEye) in reflection mode.

2.2 Sorption Measurements

Sorption measurements are a significant technique to analyze materials regarding their porosity including surface area, pore size distribution and pore volume.[3] For porous materials used in this work, especially nitrogen physisorption was applied. Next to chemisorption, where chemical bonds are formed between two species, physisorption is the second classification concerning sorption in general. It occurs when only weak interactions, like van der Waals forces, are interacting between the porous material and gas molecules.[3]

During physisorption, the material is equilibrated with a specific amount of the applied gas molecules (e.g. nitrogen, argon, etc.). The amount of the adsorbed nitrogen is measured at different relative pressures p/p_0 (where p is the absolute pressure and p_0 is the saturated vapor pressure) with a constant temperature at 77 K (liquid nitrogen) to

obtain specific sorption isotherms. The resulting different types of isotherms (I-VI), classified by IUPAC, distinguish porous materials regarding their pore structure, pore size and the interactions of the adsorbed gas molecules with the adsorbent (see Figure 2-2).[4]

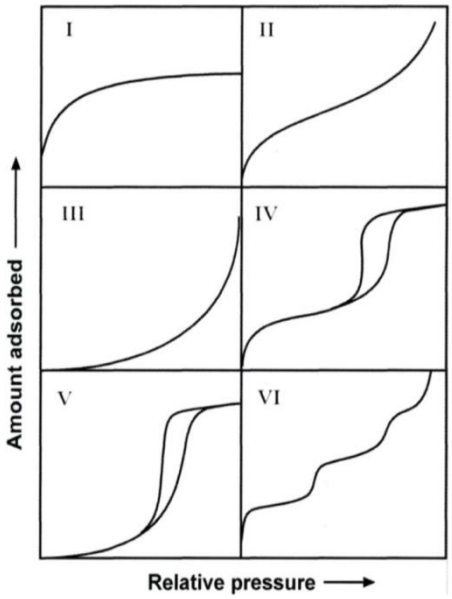

Figure 2-2: IUPAC classification of the six different isotherm types.[5] Figure adapted from Ref. 5.

Type I can be observed for microporous materials. It shows a steep increase of adsorbed volume at small relative pressures followed by a complete pore filling and reaching a constant value at high relative pressures.

Type II describes non-porous and macroporous solids with a low increase at the beginning indicating a monolayer adsorption followed by unrestricted multilayer condensation.

Type III also shows non-porous and macroporous materials but only with weak interactions between the adsorptive and the adsorbent.

Type IV and type V are observed for mesoporous materials with strong and weak interactions between the material and the gas molecule, respectively. The hysteresis loop is caused by capillary condensation within the mesopores.

Type VI describes non-porous materials with a stepwise multilayer adsorption.[6]

Covalent organic frameworks are classified as mesoporous materials due to their average pore size between 2 and maximum 6-7 nm and exhibit type IV isotherms. Specific for this kind of isotherm is the appearance of a hysteresis loop.

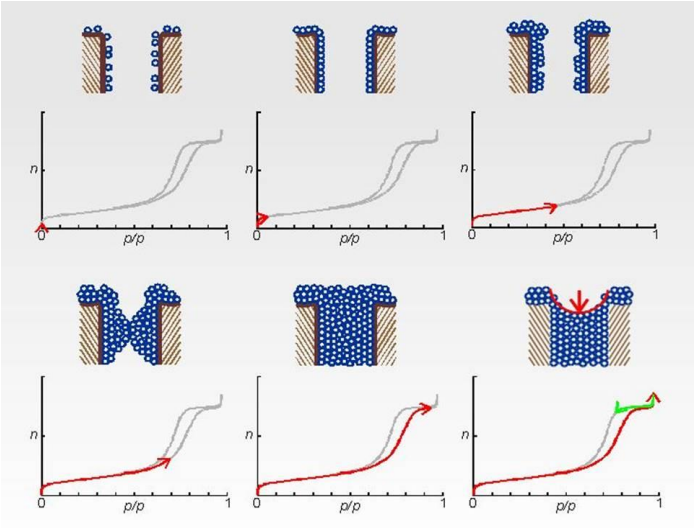

Figure 2-3: Adsorption and desorption process on mesoporous materials regarding capillary condensation and the origin of the hysteresis loop.[7] Figure adapted from Ref. 7.

Multilayers of the adsorbed gas molecules are formed during the adsorption process and condense at a certain relative pressure inside the pores. This process is favoured by a higher adsorption enthalpy occurring during this procedure. After a complete pore filling the isotherm reaches a constant value. When starting the desorption process, the relative pressures have to be reduced. Desorbing the adsorbens from the surface needs more energy to overcome the van der Waals forces which results consequently in the hysteresis loop. The shape of the specific hysteresis is proposed to be related to the different geometries of the liquid-gas interfaces during the adsorption process (cylindrical concave) and desorption process (semi-spherical concave). There are four different types of hysteresis classified by IUPAC bearing information about the pore shapes.[6]

The very steep hysteresis loop H1 describes cylindrical/slit-like pores. A delayed condensation can be observed due to a metastable pore fluid where the desorption branch reflects the equilibrium of the process.

H2, H3 and H4 hysteresis describe whole pore networks and ink-bottle pores. Here a delay in evaporation occurs in addition to a delayed condensation, potentially arisen by a blocking of the pores, cavitation or filtration phenomena.[6]

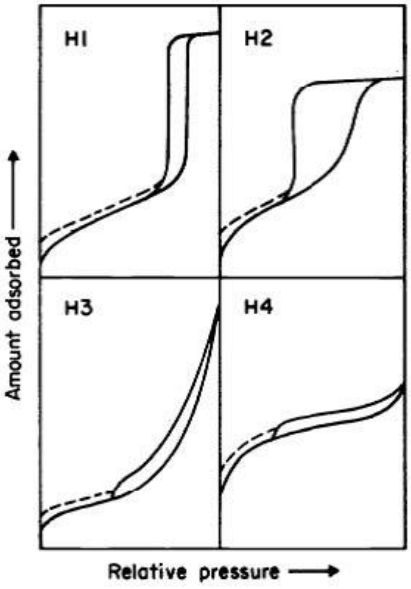

Figure 2-4: Different types of hysteresis loops classified by IUPAC.[6] Figure adapted from Ref. 6.

In this work, nitrogen sorption measurements were performed on a Quantachrome Instruments NOVA 4000e or Autosorb at 77 K. For the measurements approximately 10-30 mg of the desired sample were outgassed at different elevated temperatures and 10 mTorr for diverse times, according to the experiments and materials.

2.2.1 Specific Surface Area

The calculation of the specific surface area was described at first by Langmuir. This model is restricted to the formation of monolayers and assumes that the surface of the materials is homogeneous. In addition, all binding sites are equal and the interactions between the adsorbed molecules are neglected.[8]

$$\frac{n}{n_m} = \frac{Kp}{1 + Kp} \qquad \textbf{(2.4)}$$

Equation 2.4: Langmuir model: n: amount of adsorbate; n_m: capacity of one monolayer, p: pressure, $K=k_{ad}/K_{des}$.

This model was further extended by Brunauer, Emmett and Teller (BET) also including the formation of multilayers. The first monolayer serves as substrate for the following monolayer and results in a change in the adsorption enthalpy between the different layers.[9]

$$\frac{n_a}{n_m} = \frac{C\frac{p}{p_0}}{\left(1-\frac{p}{p_0}\right)\left(1+C-\frac{p}{p_0}\right)}$$

(2.5)

Equation 2.5: BET equation: n_a: amount of adsorbate, n_m: capacity of one monolayer, C: BET constant, p: equilibrium pressure, p_0: saturation vapor pressure of adsorbate.

This analysis method is used for determination of the surface area of porous materials. To determine n_m only the linear form of the BET in the positive region is used. This is in most cases only typical for low relative pressures (0.00-0.03). In addition, the cross-sectional area of the adsorbate molecules has to be considered for the calculation.[9]

$$A_s = n_m N_A \sigma_m$$

(2.6)

Equation 2.6: Calculation of the BET surface area A_s: N_A: Avogadro constant, σ_m: molecular cross-sectional area.

2.2.2 Pore Size Calculation

The specific pore sizes of the porous materials can also be calculated from the isotherm data. Especially the pore size distribution within the sample can be analyzed by using density functional theory (DFT) and Monte Carlo simulations. The calculations are based on statistical mechanics and describe also the attractive and repulsive interactions in the solid-fluid and fluid-fluid state.[10] Hence, different models for diverse pore shapes (slit, cylindrical, spherical) and diverse materials classes (zeolites, carbons, silica) are available. For silica materials and ordered homogeneous carbon materials a non-local density functional theory (NLDFT) method can be applied which allows an exact description of the local fluid structure at curved interfaces. For the analysis of heterogeneous carbon materials, such as COFs, quenched solid density functional theory (QSDFT) should be used, including the allowance for reliable pore sizes between 0.35-40 nm.[11]

2.3 Thermogravimetric Analysis (TGA)

TGA allows for the compositional analysis of any materials with combustible components consequently the thermal stability of COFs can be investigated.[12] The sample is placed onto a thermo-balance in an electrically heated oven and TGA monitors the mass loss of the sample with increasing temperatures. The sample can be heated up to 900 °C (or higher) with a constant heating rate and desired atmosphere (synthetic air, nitrogen). A steady flow of the chosen gas passes the sample and leads to the removal of volatile guest molecules. The measured weight loss is attributed to the removal of volatile guest molecules, desorption of incorporated molecules as well as the decomposition of the materials.

Thermogravimetric measurements were performed in a stream of synthetic air (25 ml/min) on a Netzsch STA 440 C TG/DSC instrument. The measurements were carried out with a heating rate of 10 °C/min, and a temperature range from 30 °C to 900 °C was covered.

2.4 Infrared Spectroscopy (IR)

IR spectroscopy is a measurement technique which applies infrared light (of wavelength 700 nm to 1 mm) and is based on the excitation of energy levels in molecules. This method can be used to get more information about the presence of functional groups or to confirm the formation of chemical bonds. Modern IR instruments normally use Fourier transformed IR spectroscopy (FTIR) which applies polychromatic light to pass first through a Michaelson interferometer before exciting the sample.[13] This is followed by a background subtraction and Fourier transformation on the data resulting in a spectrum with a typically better signal-to-noise ratio and higher accuracy than with dispersive instruments. To be able to analyze any substance by FTIR, the dipole moment of the molecule has to change during the vibration. The diverse energies arising from vibration and/or vibration/rotation within the molecule are monitored. Due to the typical stimulation energies, it is possible to determine different functional groups in one molecule which are at the same time visible as characteristic absorption bands. The transitions between of the diverse vibrational states can be described by the quantum mechanical model *anharmonic oscillator*.[13]

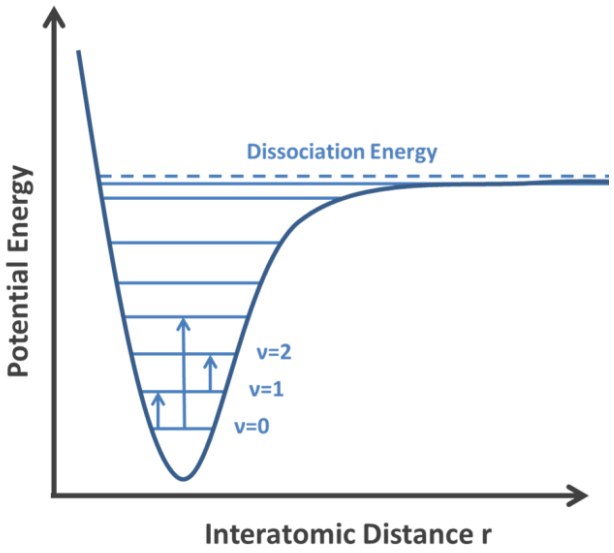

Figure 2-5: Potential of a generic anharmonic oscillator.[13]

One vibrational state is excited into a higher potential energy level and by absorbing electromagnetic waves, characteristic absorption bands can be observed. This absorption can happen, when the wavelength of the infrared light fits the energy difference between different vibrational states.[14]

IR investigations were performed on a Perkin Elmer Spectrum BX FT-IR instrument in combination with an attenuated total reflection (ATR) accessory comprising an ATR diamond crystal.

In addition, IR mapping of the sample was performed on a Thermo Scientific Nicolet iN 10 infrared microscope.

2.5 Ultraviolet-Visible Spectroscopy (UV-Vis)

For the optical characterization of the synthesized materials, UV-Vis spectroscopy can be performed. It is based on the absorption of electromagnetic waves in the ultraviolet and visible range. It enables insights into the electronic structure of materials by recording the optical transitions from the ground state to the excited state. The energy of the irradiation can be explained by the energy gap between the highest occupied molecular orbital (HOMO) and the lowest unoccupied molecular orbital (LUMO). In general it is possible to analyze any materials like bulk materials, solutions, as well as thin films and transparent substrates.[15]

UV-Vis data can give information about the electronic properties of the analyzed materials and in addition the Lambert-Beer law can be applied for quantifying the amount of the analyte in solution.

$$A = \log \frac{I}{I_0} = \varepsilon_\lambda dc \qquad \textbf{(2.7)}$$

Equation 2.7: Lambert-Beer law: A: Absorption; I: intensity of transmitted light; I_0: intensity of incident light; ε_λ: extinction coefficient; d: absorption path length of light; c: concentration of analyte.

Organic compounds, like COFs or their precursors providing π orbitals, are able to absorb in the UV-Vis region due to their available valence electrons and molecular or extended energy levels. They can be excited to higher energy levels where transitions typically occur between the nonbonding n or π bonding electrons to the π* excited state. Normally, COFs were not dissolved to measure the precursors in solution but as solids by performing diffuse reflectance measurements. Measurements of solids also require consideration of scattering effects at interfaces. Here, incident light is scattered in different directions which is called diffuse reflectance. Applying an integrating sphere in the system can provide reliable spectroscopic data. Therefore, the sample is placed in front of the incident light window and the reflected/scattered light is collected by using a sphere with barium sulfate inside and led to the detector. The obtained value becomes the reflectance with respect to the reflectance of the reference standard to be 100%. When the incident light is directed at the sample at an angle of 0 °, specularly reflected light exits the integrating sphere and cannot be detected. As a result only diffuse light is measured and therefore integrating spheres with different angles of incident are available.[16, 17]

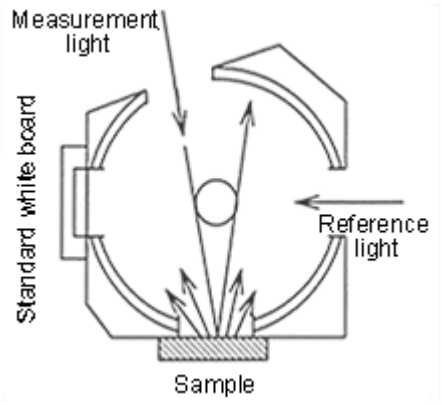

Figure 2-6: Measurement of diffuse reflectance including specular reflection (long arrows) in an integrating sphere.[17] Figure adapted from Ref. 17.

UV-Vis spectra were recorded using a Perkin-Elmer Lambda 1050 spectrometer equipped with a 150 mm integrating sphere. Diffuse reflectance spectra were collected with a Praying Mantis (Harrick) accessory and were referenced to barium sulfate powder as white standard. The powder sample was mixed with a small amount of the reference and measured in diffuse reflectance mode. The specular reflection of the sample surface was removed from the signal using apertures that allow only light scattered at angles > 20 ° to pass.

2.6 Fluorescence Spectroscopy

The specific amount of fluorophores within one material, e.g. fluorescent molecules attached at the walls of COF materials, can be determined by fluorescence spectroscopy. Fluorescence is one part of photoluminescence and differs in the internal excitation mechanism and resulting lifetimes of excited states from phosphorescence. In general, the absorption of light results in a vertical excitation of electrons. The electron further loses energy until the vibrational ground state of the excited electronic state is reached.[16] The different steps of fluorescence are shown in Figure 2-7.

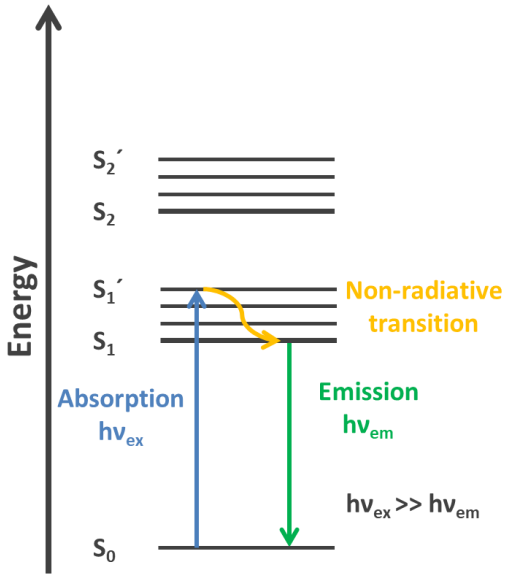

Figure 2-7: Jablonski diagram illustrating the absorption of light, the following non-radiative transition and the transition back to the ground state by emitting light at a lower wavelength (fluorescence light) compared to the absorbed wavelength.

In a first step, a photon of a certain energy $h\nu_{ex}$ level is absorbed by the fluorophore. This energy is generated by an external source, e.g. laser light or monochromatic light. While absorbing the energy the electron is rapidly excited from the ground state S_0 to the excited state $S_1´$. Non-radiative transitions occur within the excited state by vibrational relaxation of the fluorophore and the electron reaches a relaxed excited state S_1. In a last step, fluorescence emission takes place. Here, the excited electron falls back to the electronic ground state S_0 by emitting photons $h\nu_{em}$ with a lower wavelength. The difference in wavelength results in a red-shift of the emitted maximum wavelength, called Stokes-shift.[16, 18]

Fluorescence spectra in this work were recorded on a PTI spectrofluorometer with a xenon short arc lamp (UXL-75XE USHIO) and a photomultiplier detection system (model 810/814).

2.7 Fluorescence Microscopy

Fluorescence microscopy is a special variation of microscopy in general. It is based on the physical background of fluorescence explained in the chapter above. When materials are excited with a specific wavelength they emit light with a different wavelength (Stokes-Shift). Normally, fluorescence microscopy is used in biophysics to analyze interactions within cells.[19, 20] Furthermore, fluorescence microscopy can also detect

fluorescent molecules within organic or inorganic materials, such as the synthesized and functionalized COF materials. The magnified picture of the sample is only based on emitted light. The implementation of pinholes in the optical path of a microscope setup can increase the spatial resolution. Spinning-disk confocal microscopy is a specific type of a microscope setup improving the resolution of the sample detection even further. Here, pinholes are substituted with a spinning disc unit consisting of two fast rotating disks. In one disc, multiple lenses are concentrically arranged while the other disc contains pinholes that allow for multiple simultaneous scans. This results in the ability of screening the sample for many times leading to fast imaging.[16, 19, 20]

The postsynthetically modified fluorescent COFs were imaged using spinning disc microscopy (Zeiss Cell Observer SD utilizing a Yokogawa spinning disk unit CSU-X1). The objective was a 1.40 NA 63x Plan apochromat oil immersion objective (Zeiss). The dye FITC was imaged with 488 nm laser excitation. Images were acquired using an electron multiplier charge coupled device (EMCCD) camera (Photometrics Evolve^{TM}).

2.8 Electron Microscopy

Electron microscopy (EM) is an analytical method to image the interior, the surface or the chemical composition of a solid material by an electron beam. Electrons used in EM have a much smaller wavelength than visible light and the resolving power of a microscope is limited by the wavelength. An electron microscope can achieve a much higher resolution, currently about 0.1 nm, in comparison to a classical light microscope (about 200 nm). There are various types of electron microscopes which form images of the object in different ways based on the electron bombardment of the sample, whereby the electrons can be transmitted, absorbed, scattered, and emitted by the sample. In Figure 2-8 the different interacting processes are illustrated.[21]

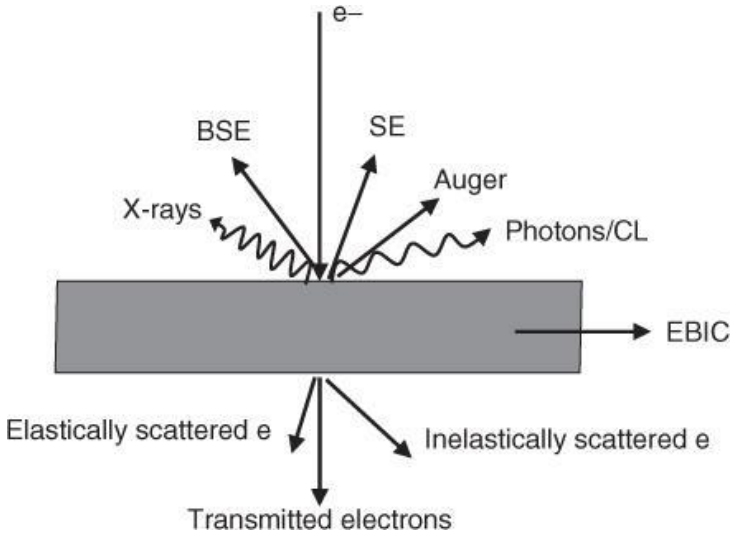

Figure 2-8: Interrelationship of incident electron beam, material and resulting secondary effects.[22] Figure adapted from Ref. 22.

2.8.1 Scanning Electron Microscopy (SEM)

An electron microscope is indicated as scanning electron microscope (SEM) when an electron beam is scanned over the surface of a material. Here, the electron beam is guided over the surface and the interactions of the electrons with the sample are used for the generation of the image. The electron beam can be accelerated by applying voltages from 0.1 to 30 kV. The images, which are typically generated by scanning electron microscopy, illustrate the surface of different objects and exhibit a high depth of field. The entire process usually takes place in a high vacuum in order to avoid interactions with other atoms or molecules.[21]

With the help of magnetic coils the electron beam is focused to a point on the object. If the electron beam encounters the object different interactions are possible. The impinging electrons interact with the sample and result in emission of electrons and photons from the specimen. The detection of these interactions, usually detected by an Everhart-Thornley detector, gives information about the consistence of the object by interpretation of the intensity of the signal. The primary electron beam coming from the anode will be scattered over the surface line by line, while the signal is converted to gray scale information and displayed on the screen synchronously. If all lines of the images are scanned, the scan starts again at the top of the screen and a new image will be generated. The magnification is the ratio between scanned sample surface and the monitor size. High resolution of the images involves small beam diameters in the range of 1 to 10 nm and focusing by an objective lens.

There are three different types of SEM detection and imaging. The secondary electron images, backscattered electron images and elemental X-ray maps. Secondary electrons (SE) are only emitted from the sample`s surface with an energy less than 50 eV. They are generated by inelastic scattering of high-energy electrons and are used for detailed images of the surface morphology. As opposed to secondary electrons, high-energy backscattered electrons (BSE) are elastically scattered by the atomic nucleus and retain the same energy as the incident primary electrons. Due to their higher energy they have a higher interaction volume. With increasing atomic number of the observed specimen, the probability of backscattering of electrons increases. As a result the detection reveals a high contrast difference between different elements of the sample. The last type of SEM detection is that beside electrons, X-rays are also generated in the interaction volume which can be used for quantitative chemical analysis. In the following picture the interactions between the incident beam and the resulting interactions are displayed (see Figure 2-9).[21]

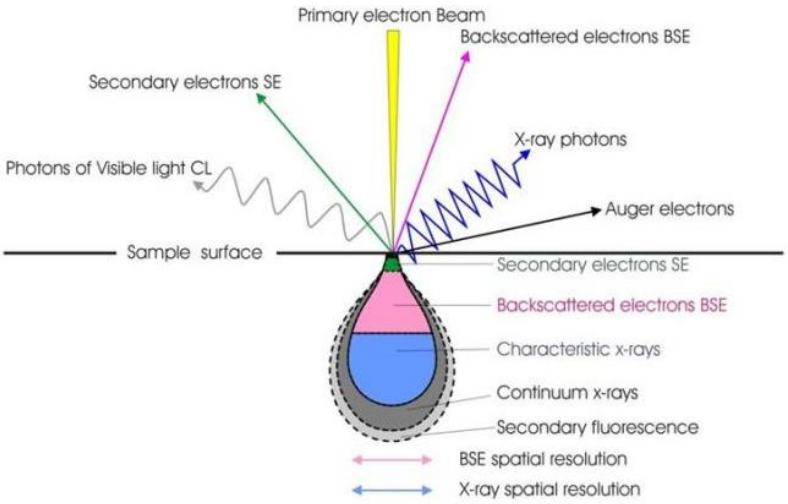

Figure 2-9: Electron-specimen interaction volume in a SEM and origin of the signals.[23] Figure adapted from Ref. 23.

If not stated otherwise, SEM measurements were performed on a Helios G3 UC instrument at 2 kV. For this purpose the samples were put on an adhesive graphite film and sputtered with carbon with a BALTEC MED 020 Coating System.

2.8.2 Transmission Electron Microscopy (TEM)

Another very important microscopy technique is transmission electron microscopy (TEM), which allows for a high magnification by a factor up to 10^6, and gives information about morphology and structure of the investigated sample.[24] In this method, the electrons radiate through the object, which has to be sufficiently thin. Depending on the atomic number of the different atoms which build up the sample, the acceleration voltage and the desired resolution, the sensible object thickness can range up from several micrometers to a few nanometers. The beam path runs in vacuum to avoid collision of the electrons with air molecules. Typical acceleration voltages of TEM are between 80 kV and 400 kV. The range below 200 kV is rather used for the study of biological and organic materials (here usually used 80 to 120 kV) while material science problems are solved rather with 200 kV or higher voltage. The high usable acceleration voltage is an essential feature of a TEM instrument. However, the maximum acceleration voltage is not always the most appropriate for a particular study. The higher the atomic number of the elements and the lower the acceleration voltage, the thinner the specimen must be (either films or very low concentration). Also for a high resolution image a thin specimen is required. The electrons supplied from the electron source are deflected by a condenser lens system in a way that they illuminate uniformly the object to be observed and that all electrons penetrate approximately parallel to the object. In the sample to be analyzed, the electrons change their direction of movement in the form of Rutherford scattering. Sometimes these electrons lose their kinetic energy, which arises as inelastic scattering. Elastically scattered electrons leaving the object at the same angle will be focused into the back focal plane of the objective lens at a special point. The non-scattered electrons can now be passed at this level by a contrast aperture. As atoms with a higher atomic number and thicker object regions scatter more, the resulting contrast is called mass thickness contrast. This allows, for amorphous solids, quite a simple interpretation of the obtained images.[25]

The contrast of crystalline materials follows special laws and is termed as diffraction contrast. The contrast is based on allowed and forbidden orientations of diffracted beams, and also affected by defects in different dimensions in the crystal structure. The projective lens system further magnifies the first image generated by the objective lens system and projects it to a detector. For this application, for example, a phosphor screen, which is usually coated with fluorescent zinc sulfide, is used. If the image should be recorded, a photographic film, imaging plate or a CCD camera is used. CCD

elements would be destroyed by direct bombardment with the high-energy beam electrons. That´s why the electron intensity is first transferred into light by a scintillator, which is then led to the CCD chip by a transfer optics. The use of imaging plates has the advantage that they are not damaged by the high-energy radiation and furthermore the image can be recorded directly. By changing the lens system the focal plane of the objective lens can be enlarged instead of the intermediate image. The result is an electron diffraction measurement which can be used to determine the crystal structure of the sample.[25] A schematic construction of a transmission electron microscopy and its most important components are shown in Figure 2-10.

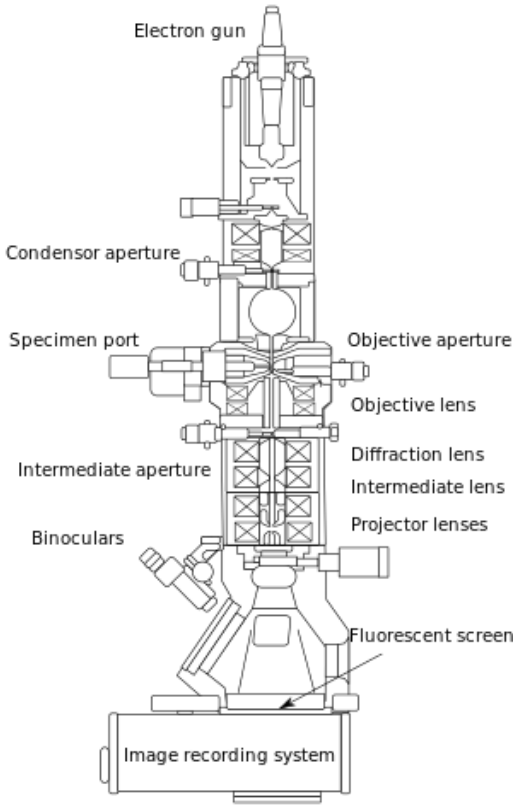

Figure 2-10: Schematic construction of a transmission electron microscope.[26] Figure adapted from Ref. 26.

If not stated otherwise, measurements were performed on a Tecnai G2 20 S Twin at an acceleration voltage of 200 kV.

2.9 Nuclear Magnetic Resonance (NMR)

NMR spectroscopy is a special method to study the chemical environment of certain nuclear isotopes by applying a static magnetic field. In addition, interactions with neighboring atoms and the composition of the compound can be determined. The analysis of NMR data provides information about structural properties and bonds of nuclear isotopes based on the change of the magnetic moment $\vec{\mu}$. In order to investigate elements, their nuclear spin has to be non-zero, which applies for ^{1}H, ^{13}C, ^{19}F, ^{29}Si and ^{31}P, amongst others.[27]

$$\vec{\mu} = \gamma \vec{s} \tag{2.8}$$

Equation 2.8: μ: Magnetic moment; γ: gyromagnetic constant; $\vec{s}$: nuclear spin.

Electromagnetic waves in the radio frequency are applied and lead to transitions between diverse energetic states when the resonance condition is met. The measured difference between the strength of the local magnetic field and the applied external field gives information about the electronic and chemical environment of the nuclei. The transition between these quantum states is induced by radio frequency energy ranging from a few kHz to several hundred MHz (Larmor frequency), when reaching resonance conditions. Consequently, NMR spectroscopy monitors the differences in the effective magnetic field which depends on the chemical environment.[28]

In general NMR spectroscopy can be performed in solution and using a solid material, respectively. NMR spectroscopy of liquids usually results in sharp spectra with high resolution. The mobility of the nuclei in deuterated solvents creates an averaging process which leads to the intrinsic elimination of dipole-dipole interactions causing broad peaks. For the characterization of solids special techniques have to be applied to get comparable structural information. The “magic angle spinning” (MAS) is a special method to eliminate anisotropic effects and sharpen broad peaks. The sample is rotated at high velocity at an angle of 54.7° to the applied magnetic field.[29]

^{1}H and ^{13}C NMR solution spectra were recorded on a Bruker Avance III-400 MHz and a Bruker Avance III-270 MHz spectrometer. Solid state MAS-NMR spectra for ^{11}B and ^{13}C were recorded on a Bruker DSX Avance 500 with a magnetic field of 11.2 Tesla. A 4 mm MAS rotor in a triple resonance sample head was used. The frequency of the rotors was 10 kHz.

2.10 Photoluminescence Spectroscopy (PL)

This spectroscopy method is a widely used technique to characterize the optical and electronic properties of semiconductors and molecules and can be referred to fluorescence spectroscopy (see Section 2.6). PL is based on the light emission after the absorption of photons (electromagnetic radiation).[30] The PL monitors the spontaneous emission of radiation, which is often in the visible light range, by relaxation from the electronic excited state back to the electronic ground state. The relaxation from the excited state usually happens in a vibrational mode resulting in a red-shift of the emitted light. The transition can be associated with two different phenomena, the so called fluorescence and phosphorescence. When the fluorophore relaxes quickly, while maintaining its spin multiplicity, fluorescence occurs. In contrast to that, phosphorescence arises with changing spin multiplicity and slow relaxation while the transition is quantum-mechanically forbidden. The time periods between absorption and emission can vary from femtoseconds up to milliseconds for phosphorescent molecular systems.[16]

Photoluminescence (PL) measurements were performed using a PicoQuant FluoTime300 time-correlated single photon counting (TCSPC) setup (see 2.11).

2.11 Time Correlated Single Photon Counting (TCSPC)

TCSPC is a technique to analyze the fast changing light intensity during PL measurements, normally in the picosecond and nanosecond range. One of the main applications is the analysis of the time-dependent behavior of pulsed or modulated light sources as well as the determination of fluorescence lifetimes. This is based on the same principle as for static PL (analysis of absolute energies and intensity of emitted photons) but analyses the time-resolved kinetics of the photoemission.[31]

Therefore, the sample´s fluorophores are excited with a pulsed light source (e.g., laser). The time-dependent measurement is started by the excitation pulse and the emitted photon is stopping the measurement when transiting from the excited state back to the ground state. The detector records the signal periods (start-stop times) in which a single photon can be detected (see Figure 2-11).[31]

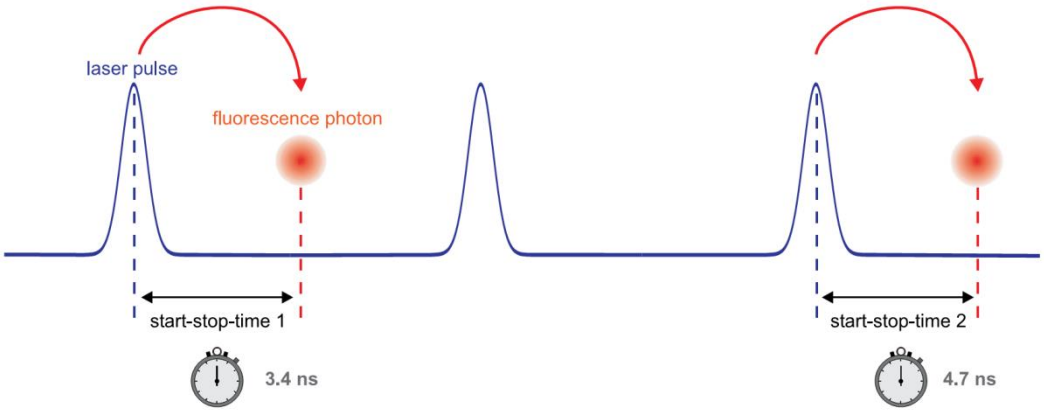

Figure 2-11: Measurement of start-stop times with TCSPC.[32] Figure adapted from Ref. 32.

To get statistically relevant data, TCSPC typically uses lasers with pulse frequencies between 100 kHz and 80 MHz, which allows for the collection of a multitude of single photon measurement to assemble an average lifetime. The important aspect is that the laser has to be weak enough to excite only one single photon per laser pulse cycle. Several measurement periods are repeated and plotted in a histogram which visualizes the exponential decrease of the fluorescent intensity after excitation (see Figure 2-12).[31]

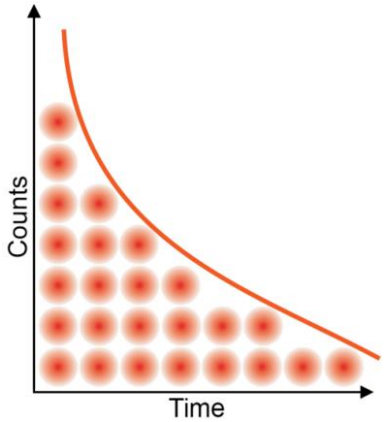

Figure 2-12: Histogram of start-stop times with TCSPC visualizing the exponential decay.[32] Figure adapted from Ref. 32.

For the highly sensitive single photon detection a Photomultiplier Tube (PMT), Hybrid PMT, Micro Channel Plate (MCP) or a Single Photon Avalanche Diode (SPAD) can be applied.[32] In this work, the steady-state spectrum was recorded using a 378 nm laser (PicoQuant LDH-P-C-375), while TCSPC histograms and the time-resolved emission spectra (TRES) were acquired with 508 nm laser pulses (PicoQuant LDH-P-C-510) of 0.10 ns pulse length and energy density of around 0.7 µJ/cm². In both cases, the emitted light is collected by a two-inch lens and focused onto a monochromator (Zolix Omni λ

300). Residual scattered light from the excitation laser is removed using a 400 nm dielectric longpass (Thorlabs FELH0400) or a 3 mm orange glass filter (Schott OG530) for the 378 nm or 508 nm laser, respectively. The monochromatic light is detected under magic angle (54.7°) using a highly-sensitive photomultiplier (PicoQuant PMA 192).

2.12 Electrical Conductivity – Hall Measurements

The Hall Effect, discovered by Edwin Hall in 1879, describes the formation of an electrical voltage in a live conductor, which is placed in a magnetic field. This external magnetic field is perpendicular to the current and compensates the Lorentz force, which affects the electrons in the material. When an electron moves along a direction perpendicular to an applied magnetic field, it experiences a force which acts normal to the direction of the magnetic field and the direction of the current, and moves in response to this force. Figure 2-13 illustrates the direction of the force on a charge carrier based on its direction of motion and the direction of the applied magnetic field.[33]

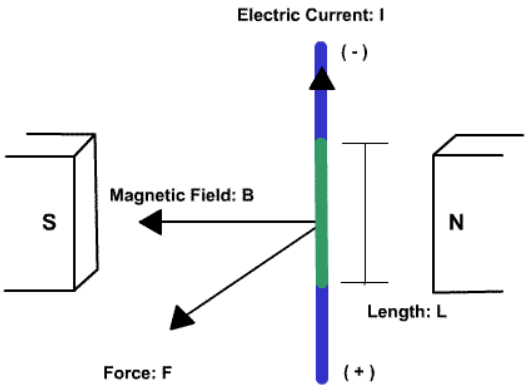

Figure 2-13: Illustration of Hall Effect; illustration of direction of force on charge carrier dependent on the applied magnetic field.[33] Figure adapted from Ref. 33.

In general, the Hall Effect measurements are used to determine several parameters which relate to the measurement and the Lorentz force. This includes: Hall voltage (V_H), carrier mobility (μ), carrier concentration (n), Hall coefficient (A_H), resistivity (R_H) and conductivity type (n/p).[34]

The most common method to measure the resistivity of materials is called van der Pauw method. This technique is based on a four point probe and includes the ability to measure the resistance of two-dimensional samples of a random shape. A very thin sample preparation leads to the reduction of errors in the calculation. The sample is then

placed into the sample holder and contacted with four gold probes (nodes) in a symmetric way. During the measurement the current is applied between contacts 1 and 2 (I_{12}) while the voltage is measured between contacts 3 and 4 (V_{34}). According to Ohm´s law, the resistance can be calculated from these two values:[16, 35]

$$R_{12,34} = \frac{V_{34}}{I_{12}} \tag{2.9}$$

Equation 2.9: Calculation of resistivity according to Ohm´s law.

The complete sheet resistance can be determined from the measurement of the resistance along the vertical ($R_{12,34}$) and horizontal ($R_{23,41}$) edge of the sample according to van der Pauw equation:

$$e^{\left(-\frac{\pi R_{12,34}}{R_S}\right)} + e^{\left(-\frac{\pi R_{23,41}}{R_S}\right)} = 1 \tag{2.10}$$

Equation 2.10: Calculation of sheet resistance R_s.

To obtain a better result of the measurement and to reduce parasitic error, the measurements are repeated while switching the polarities of current sources and voltage meter.[35]

$$R_{A=}\frac{R_{21,34}+R_{12,43}+R_{43,12}+R_{34,21}}{4} \tag{2.11}$$

$$R_{B=}\frac{R_{32,41}+R_{23,14}+R_{14,23}+R_{41,32}}{4} \tag{2.12}$$

$$e^{\left(-\frac{\pi R_A}{R_S}\right)} + e^{\left(-\frac{\pi R_B}{R_S}\right)} = 1 \tag{2.13}$$

Equation 2.11 – 2.13: Calculation of resistivity from the combination of switched polarities based on the van der Pauw equation.

Finally, the bulk electrical resistivity can be calculated from:

$$\rho = R_S\, d \tag{2.14}$$

Equation 2.14: Calculation of electrical resistivity ρ: R_s: sheet resistance, d: sample thickness.

Furthermore, the charge carrier concentration can be obtained from the Hall voltage V_H from the Hall Effect measurement. The as mentioned Hall voltage is determined by forcing a magnetic field being perpendicular to the sample and at the same time a current through the sample. Here, the current is forced on the opposite nodes of the sample and at the same time voltage is measured on the other opposite nodes. In addition, two measurement sets are performed depending on the magnetic field. In one set, the magnetic field is positive to the *z*-direction and the other set includes a magnetic field negative to the *z*-direction. The voltage is measured by switching the polarity of the current source between two contacts and altering this between all four contacts on the sample.[35]

$$V_H = \frac{V_{13} + V_{24} + V_{31} + V_{42}}{8} \tag{2.15}$$

Equation 2.15: Calculation of Hall voltage: V_{13}, V_{24}, V_{31} and V_{42} are the differences of the voltage for the positive and negative magnetic field between the respective contacts.

The Hall mobility of the charge carriers μ can be calculated from the charge carrier density n_s and the sheet resistance R_S obtained to the van der Pauw method.[35]

$$\mu = \frac{1}{q n_s R_S} \tag{2.16}$$

Equation 2.16: Calculation of Hall mobility μ: q: elementary charge, n_s: charge carrier density, R_S: sheet resistance.

Furthermore, electrical conductivity can be expressed as:

$$\sigma = \frac{1}{R}\frac{d}{A} \tag{2.17}$$

Equation 2.17: Calculation of electrical conductivity σ: R: resistance, d: thickness of the sample, A: area of the electrode.

Hall conductivity measurements were carried out on an ECOPIA HMS 3000 apparatus using a magnetic field of 0.55 T in the van der Pauw geometry connected by gold wires. The measurements were performed on pellets (10 mm diameter), which were prepared by pressing the finely ground material under different pressures, respectively. As-synthesized films were used without further preparation and connected directly.

2.13 References

1. G. Cao, *Nanostructures & nanomaterials: synthesis, properties & applications*, Imperial college press, **2004**.
2. M. Laue, *Annalen der Physik* **1912**, *343*, 370-384.
3. S. Lowell, J. E. Shields, M. A. Thomas, and M. Thommes, *Characterization of porous solids and powders: surface area, pore size, and density*, Springer Science & Business Media, **2012**.
4. K. S. Sing, *Pure and applied chemistry* **1985**, *57*, 603-619.
5. Z. A. ALOthman, *Materials* **2012**, *5*, 2874-2902.
6. Z. Ryu, J. Zheng, M. Wang, and B. Zhang, *Carbon* **1999**, *37*, 1257-1264.
7. B. Gawel, Characterization Techniques - Gas Asorption: Study of the porosity of materials, **2018**.
8. I. Langmuir, *J. Am. Chem. Soc.* **1916**, *38*, 2221-2295.
9. S. Brunauer, *J. Am. Chem. Soc.* **1938**, *60*, 309.
10. E. P. Barrett, L. G. Joyner, and P. P. Halenda, *J. Am. Chem. Soc.* **1951**, *73*, 373-380.
11. P. Ravikovitch, S. Ó. Domhnaill, A. Neimark, F. Schüth, and K. Unger, *Langmuir* **1995**, *11*, 4765-4772.
12. L. S. Pang, J. D. Saxby, and S. P. Chatfield, *J. Phys. Chem.* **1993**, *97*, 6941-6942.
13. M. Hesse, H. Meier, and B. Zeeh, *Spektroskopische Methoden in der organischen Chemie*, Georg Thieme Verlag, **2005**.
14. J. M. Hollas, *Modern spectroscopy*, John Wiley & Sons, **2004**.
15. P. W. Atkins, *Kurzlehrbuch Physikalische Chemie*, John Wiley & Sons, **2006**.
16. P. W. Atkins and J. De Paula, *Physikalische Chemie*, John Wiley & Sons, **2013**.
17. https://www.ssi.shimadzu.com/products/uv-vis-spectrophotometers/diffuse-reflectance-measurement.html, Accessed 13.08.2018.
18. J. R. Lakowicz, in *Fluorescence Studies on Biological Membranes*, Springer, **1988**, pp. 89-126.
19. F. Alexis, E. Pridgen, L. K. Molnar, and O. C. Farokhzad, *Mol. Pharmaceutics* **2008**, *5*, 505-515.
20. G. Cox, *Optical imaging techniques in cell biology*, CRC Press, **2012**.

21. G. Völksch, Anleitung zum Praktikum, Universität Jena, year unknown, http://www. chemie. uni-jena. de/institute/glaschemie/Anleitung_REM. pdf. URL link as of October, **2013**.
22. http://download.e-bookshelf.de/download/0000/7529/92/L-X-0000752992-0001829642.XHTML/images/c01f001.jpg, Accessed 13.08.2018.
23. http://www.gla.ac.uk/media/media_249720_en.jpg, Accessed 13.08.2018.
24. D. B. Williams and C. B. Carter, in *Transmission electron microscopy*, Springer, **1996**, pp. 3-17.
25. B. Fultz and J. M. Howe, *Transmission electron microscopy and diffractometry of materials*, Springer Science & Business Media, **2012**.
26. https://en.wikipedia.org/wiki/Transmission_electron_microscopy#/media/File:Scheme_TEM_en.svg, Accessed 13.08.2018.
27. R. S. Macomber, *A complete introduction to modern NMR spectroscopy*, Wiley New York, **1998**.
28. J. K. Sanders and B. K. Hunter, *Modern NMR spectroscopy: a guide for chemists*, **1988**.
29. L. Frydman and J. S. Harwood, *J. Am. Chem. Soc.* **1995**, *117*, 5367-5368.
30. G. R. Hayes and B. Deveaud, *phys. stat. sol. (a)* **2002**, *190*, 637-640.
31. K. Holldack, M. v. Hartrott, F. Hoeft, O. Neitzke, E. Bauch, and M. Wahl, Bunch fill pattern at BESSY monitored by time-correlated single photon counting, **2007**.
32. M. Wahl, *Technical Note: Time-Correlated Single Photon Counting (TCSPC)*, **2014**.
33. https://www.school-for-champions.com/science/magnetism_lorentz.htm#.W3LCo9IzaUk, Accessed 14.08.2018.
34. A. R. West, *Solid state chemistry and its applications*, John Wiley & Sons, **2014**.
35. O. Philips'Gloeilampenfabrieken, *Philips Res. Rep* **1958**, *13*, 1-9.

3 Microtubular Self-Assembly of Covalent Organic Frameworks

This chapter is based on the following publication:

Bappaditya Gole, Vladimir Stepanenko, Sabrina Rager, Matthias Grüne, Dana D. Medina, Thomas Bein, Frank Würthner, and Florian Beuerle, *Angew. Chem. Int. Ed.* **2018**, 57, 846-850, DOI 10.1002/anie.201708526.

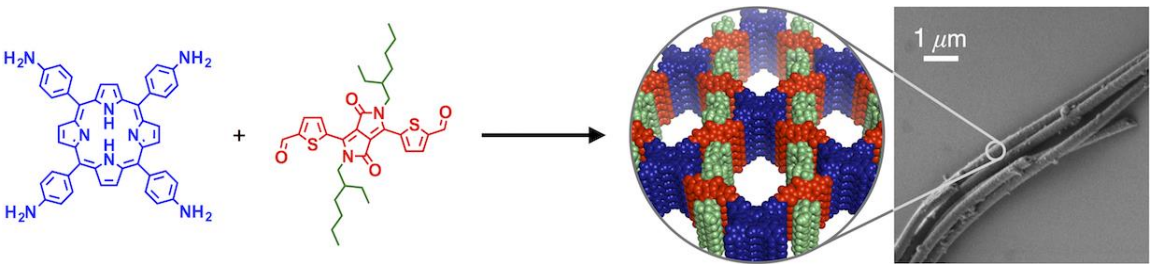

The joint project is a collaboration with a group of the University of Würzburg dealing with organic chemistry to investigate the synthesis, chemical and physical properties along with morphology of a diketopyrrolopyrrole- and porphyrin-based covalent organic framework. The following experiments were performed by S. Rager: 1) screening and development of the appropriate synthesis conditions for DPP-TAPP-COF; 2) theoretical structure simulation of a possible unit cell, calculation of the predicted PXRD and Pawley refinement; 3) characterization of the synthesized material by PXRD measurements; 4) preparation and evaluation of the COF material for nitrogen sorption measurements; 5) performance of stability measurements using TGA. Further synthesis optimizations, precursor synthesis, morphology studies *via* SEM, TEM and EDX as well as optical measurements were performed by Bappaditya Gole, Vladimir Stepanenko, Matthias Grüne, Frank Würthner, and Florian Beuerle.

Abstract

Despite significant progress in the synthesis of covalent organic frameworks (COFs), reports on a precise construction of template-free nano- and microstructures for such materials have been rare. In search of dye-containing porous materials, a novel conjugated framework named DPP-TAPP-COF with enhanced absorption capability up to 800 nm has been synthesized utilizing reversible imine condensations between 5,10,15,20-tetrakis(4-aminophenyl)-porphyrin (TAPP) and a diketopyrrolopyrrole (DPP) dialdehyde derivative. Surprisingly, the obtained COF exhibited spontaneous aggregation into hollow microtubular assemblies with outer and inner tube diameters of around 300 and 90 nm. A detailed mechanistic investigation revealed the time-dependent transformation of initial sheet-like agglomerates into the tubular microstructures.

3.1 Introduction

The formation of well-defined nanoscale superstructures has been a major achievement for supramolecular chemistry in recent years.[1-4] For a precise control over function and materials properties however, molecular organization often needs to be mastered on even larger spatial regimes, e.g. μm-scale.[5-7] In natural systems, function often emerges from defined microarchitectures that are assembled *via* protein-templated biomineralization.[8, 9] While the defined bottom-up fabrication of artificial microstructures is still quite challenging, it would be significantly improve the understanding of structure-property relationships for real applications.

Covalent organic frameworks (COFs), representing a class of porous and crystalline polymers [10-17] have recently been emerged as promising materials for potential applications in gas adsorption [18-20], energy storage [21-23], heterogeneous catalysis [24-27] or sensing.[28-30] In particular two-dimensional (2D) COFs comprising extended π-systems or well-defined donor-acceptor heterojunctions in nm-sized regimes render such materials promising candidates for optoelectronics applications.[31, 32] In most cases, however, 2D COFs are prepared and isolated as microcrystalline powders. Thereby, the limited long-range crystal growth and morphological definition is presumably due to internal defects [33] and kinetic trapping of smaller crystallites as a result of dispersive π-stacking of individual layers. Defined morphologies such as belts,[34] fibers [35] and spheres [36-38] have been observed for some COFs, but detailed mechanistic investigations have so far only been conducted in two examples for COF-based hollow spheres.[39, 40]

The template-assisted synthesis of COF nanotubes has also been reported recently.[41] However, in this case additional effort was required to initially prepare and finally remove the templates without causing irreversible modifications of the COF properties.

3.2 Results and Discussion

In this work, the successful synthesis of DPP-TAPP-COF containing diketopyrrolopyrrole (DPP) and tetraphenylporphyrin (TPP) moieties is reported. This imine-based COF adopts a unique hollow microtubular morphology with uniform diameters, rendering it, to the best of our knowledge, the first example for bottom-up microtubular self-assembly-based on COF materials.

During the quest for dye-containing COFs, the reaction of 5,10,15,20-tetrakis(4-aminophenyl)-porphyrin (TAPP) [42, 43] and the organic semiconductor DPP [44-46] dialdehyde derivative DPP-1 bearing solubilizing ethylhexyl side chains was studied (see Figure 3-1). Microcrystalline precipitates were obtained after an AcOH-catalyzed solvothermal reaction in *n*-BuOH/mesytilene (3:1) at 120 °C for five days. Washing with anhydrous THF and acetone followed by drying under high vacuum yielded DPP-TAPP-COF as a dark purple powder in 53% yield. Remarkably, even small deviations from these optimized conditions only resulted in amorphous products (see Experimental Section).

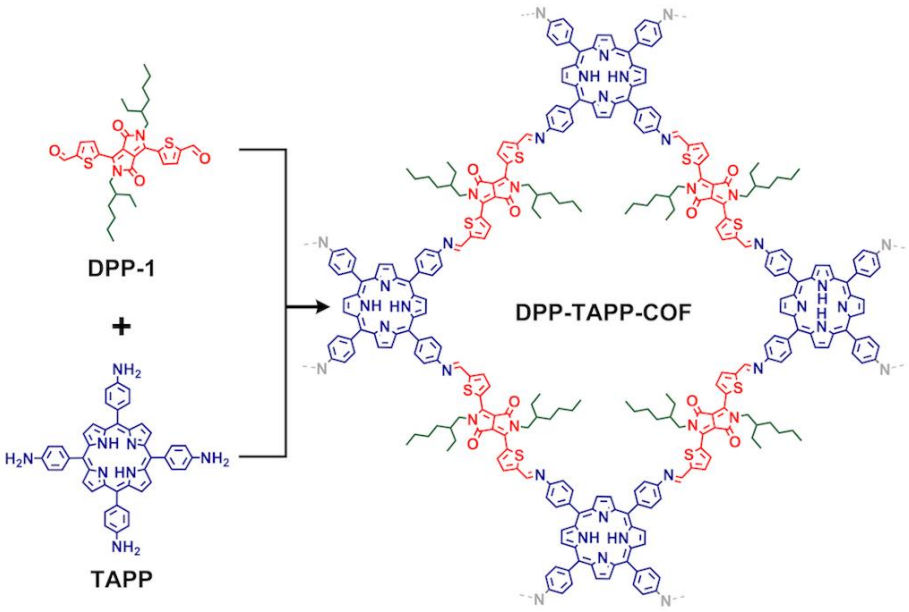

Figure 3-1: Synthesis route of DPP-TAPP-COF with precursor molecules DPP-1 and TAPP resulting in a tetragonal pore shaped network.

At first, powder X-ray diffraction (PXRD) revealed Bragg reflections centered at low 2θ angles of 2.68°, 3.51°, 4.26°, 5.49° and 7.17° corresponding to 110, 020, 120, 220 and 040 planes, respectively, thus implying the formation of small COF domains. A simulated diffraction pattern in the monoclinic *C*2/*m* space group (see Experimental section) with an eclipsed but slightly offset (~ 1 Å) AA stacking provides a good description of DPP-TAPP-COF. The final unit cell parameters were obtained by performing Pawley refinement and correspond to a = 45.3 Å, b = 48.1 Å, c = 3.9 Å; $\alpha = \gamma = 90°$, $\beta = 74.3°$ (R_{wp} = 3.82% and R_p = 2.86%) (see Figure 3-2).

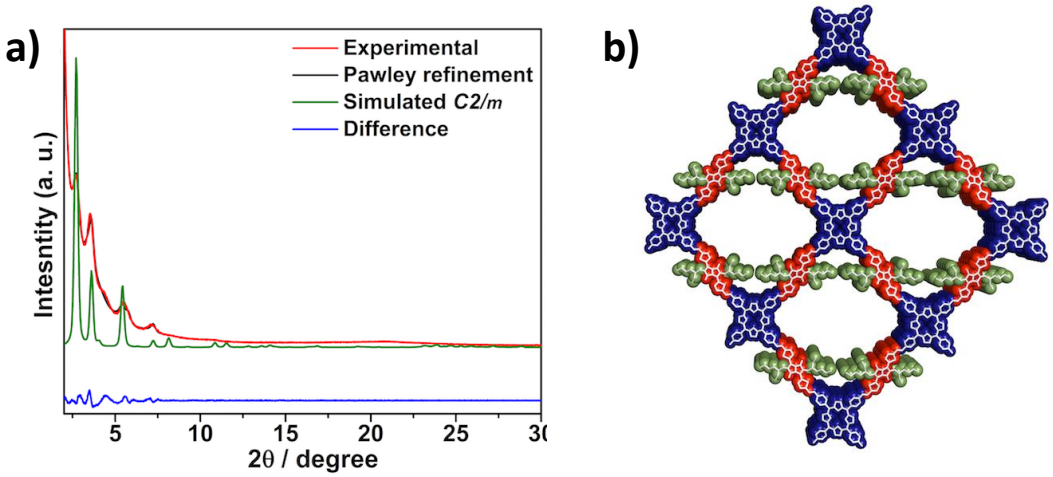

Figure 3-2: a) PXRD patterns of DPP-TAPP-COF: experimental data (red), Pawley refinement (black), simulated pattern (green), difference plot (blue), b) simulated unit cell for a monoclinic crystal system of space group *C2/m*.

Strikingly, scanning electron microscopy (SEM) and transmission electron microscopy (TEM) revealed that the DPP-TAPP-COF predominantly assembles into well-defined microtubular structures that are extended up to 20 µm (see Figure 3-3a,b,c). The majority of the microtubes were aggregated into bundles, in some cases, however, individual tubes were observed, which were possibly separated mechanically by sonication and sample preparation. Furthermore, SEM and scanning transmission electron microscopy (STEM) images clearly demonstrated the hollow nature and remarkably smooth surface of the tubes (see Figure 3-3b, e). Statistical analysis yielded mean values for outer and inner diameters of 303 ± 38 nm and 87 ± 21 nm, respectively, which corresponds to a mean wall thickness of 105 ± 9 nm. High resolution TEM revealed a periodic rhomboidal framework with domain sizes in the range of several tens of nm (see Figure 3-3d).

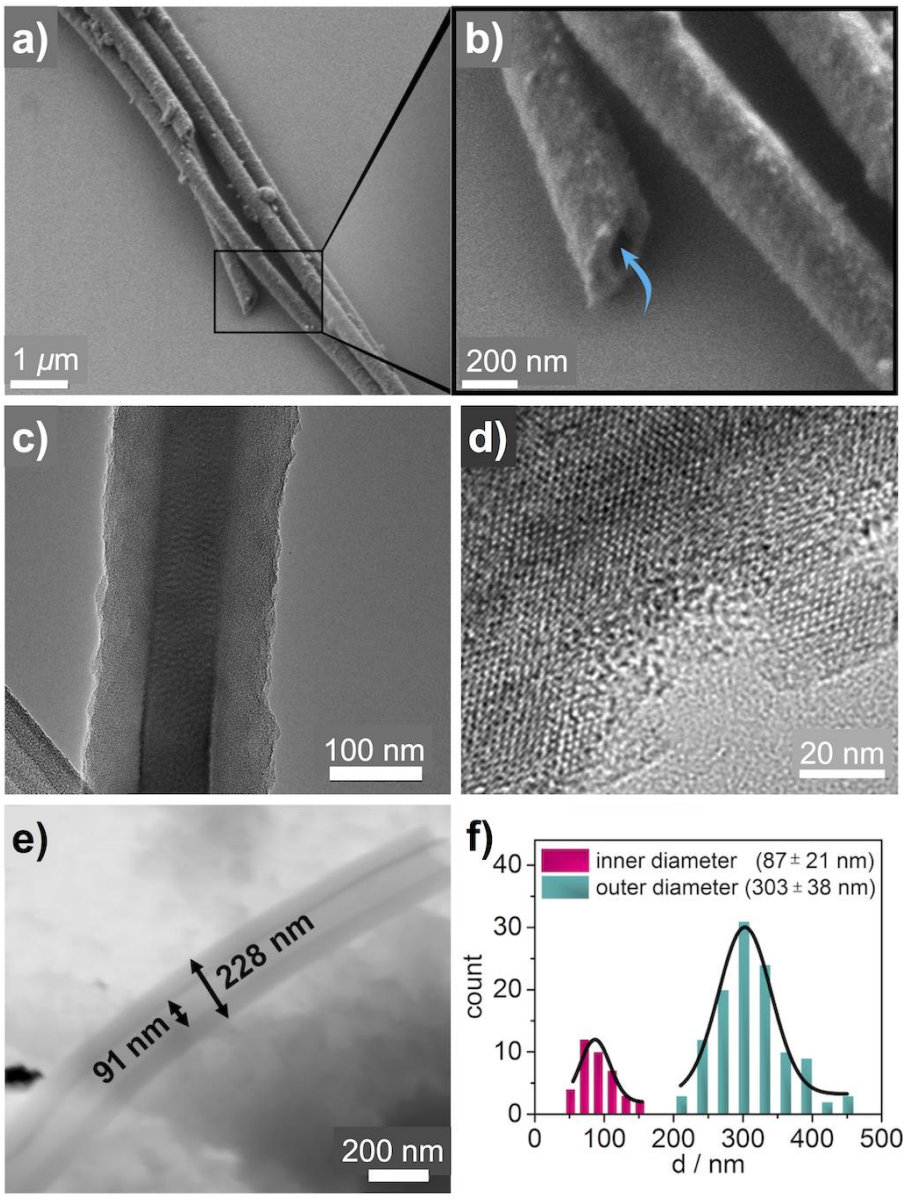

Figure 3-3: a), b) SEM and c) TEM micrographs of DPP-TAPP-COF nanotubes, d) high resolution TEM image of a microtube´s outer wall indicating crystalline domains, e) STEM image of a singular microtube indicating the hollow nature of the tube, f) statistical distribution of inner and outer tube diameters.

Indeed, framework formation was proven by several analytical techniques. The FT-IR spectrum (see Figure 3-4a) shows almost complete disappearance of the aldehyde band at 1649 cm^{-1} and the simultaneous rise of a new band at 1582 cm^{-1} corresponding to the C=N stretching mode. In addition, the N-H stretching band for the amino groups of TAPP at 3316 cm^{-1} is significantly weakened after polymerization. Similar spectral trends indicating identical functionalities and connectivity were observed for the model compound M-1 (see Figure 3-4b) as a representative “cutout” possessing two TPP units attached to one DPP-1 (see Experimental Section).

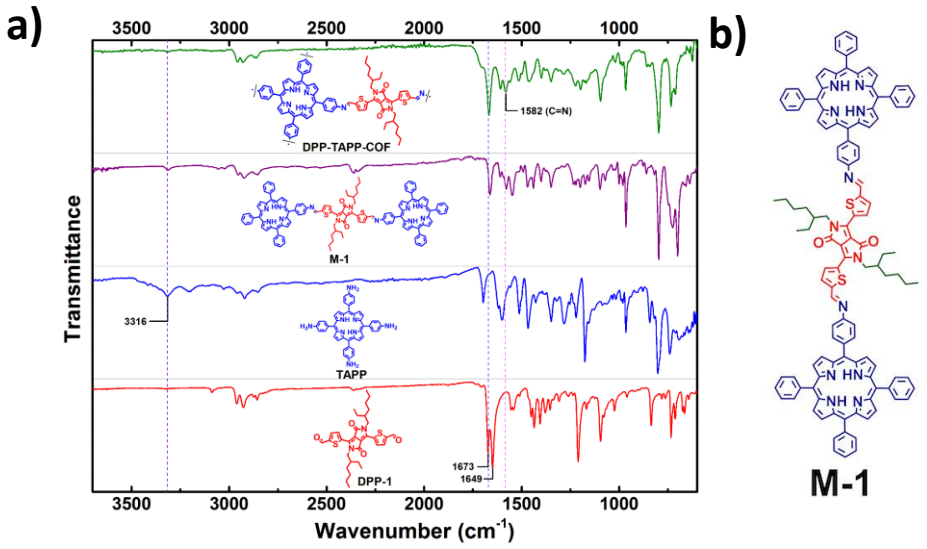

Figure 3-4: FTIR spectra for DPP-TAPP-COF (green) in comparison with model compound M-1 (purple) and corresponding monomers TAPP (blue) and DPP-1(red).

Thermogravimetric analysis (TGA) revealed a thermal stability up to 350 °C followed by a weight loss of around 20%, which is tentatively attributed to the loss of the alkyl side chains [47] and ultimate decomposition at 450 °C (see Figure 3-5a). Nitrogen sorption analysis was performed after activation at elevated temperatures under high vacuum for 12 hours. The obtained sorption isotherm and calculated BET surface area of 139 m^2g^{-1} indicate a fairly low N_2 uptake, which we attributed to the offset stacking and primarily to the sterically demanding side chains protruding into the pores (see Figure 3-5b).

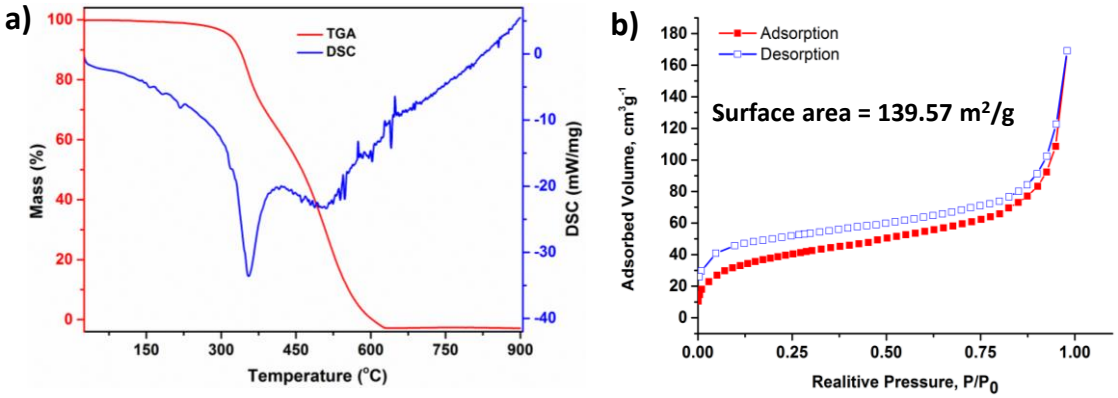

Figure 3-5: Thermogravimetric (TG) and DSC analyses for DPP-TAPP-COF under synthetic air, b) nitrogen sorption isotherm of DPP-TAPP-COF. Full red symbols: adsorption, empty blue symbols: desorption.

In addition, optical characterization including absorption was performed. Here, the absorption spectrum of M-1 nearly matches an overlay of NH_2-TPP and DPP-1, except for slightly increased *Q*-bands at 590 and 650 nm (see Figure 3-6a). Steric interactions of the phenyl rings with the porphyrin possibly induce a significant twist, thus resulting in limited π-conjugation. Diffuse reflectance spectra for DPP-TAPP-COF showed a significant shift of the maximum absorption to 670 nm (see Figure 3-6b), which can be rationalized by a planarization of the π-system and pronounced aggregation of the individual layers within the COF.[43] In addition the relative intensity ratio for the *Q* versus the Soret-bands increased from 0.4 and 0.41 for TAPP and M-1, respectively, to 1.47 for the COF. Due to this enhanced absorption, DPP-TAPP-COF more efficiently harvests photons in the visible and near IR region.

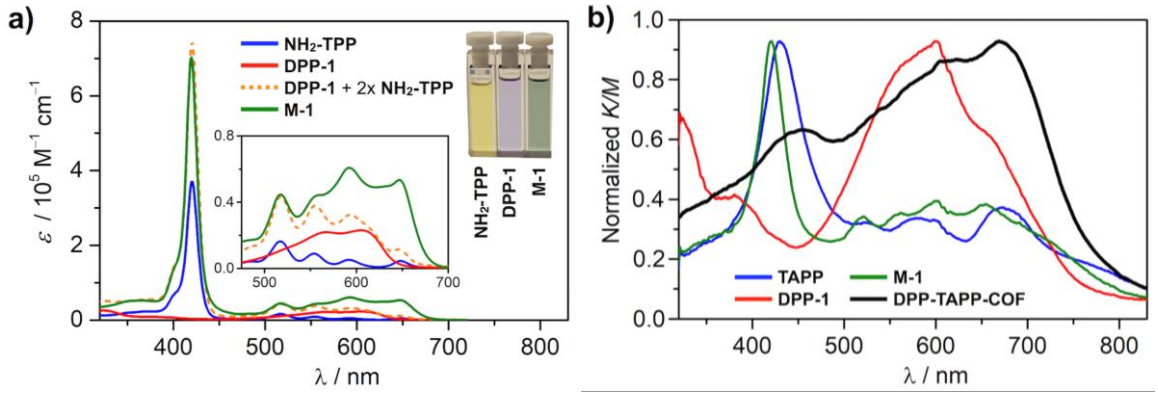

Figure 3-6: a) UV/Vis absorption spectra ($CHCl_3$, rt) of M-1, NH_2-TPP and DPP-1. Insets show enlarged region from 500 to 700 nm and the visual colors of the compounds in $CHCl_3$. b) Kubelka-Munk function for diffuse reflectance spectra of DPP-TAPP-COF, M-1 and molecular precursors TAPP and DPP-1. Spectra are normalized to global absorption maximum.

For time-dependent morphology studies, COF reactions were distributed to several pyrex tubes and quenched at different time interval followed by characterization and SEM measurements. The developed SEM images after one day indicated the formation of sheet-like agglomerates of small individual crystallites (see Figure 3-7a). After four days, significantly smoother plate surfaces were observed alongside initial signs for a scrolling of some of the thin sheets (see Figure 3-7b,c). After five days, hollow microtubes were isolated as the major product (see Figure 3-7d) in addition to some remaining plate-like aggregates.

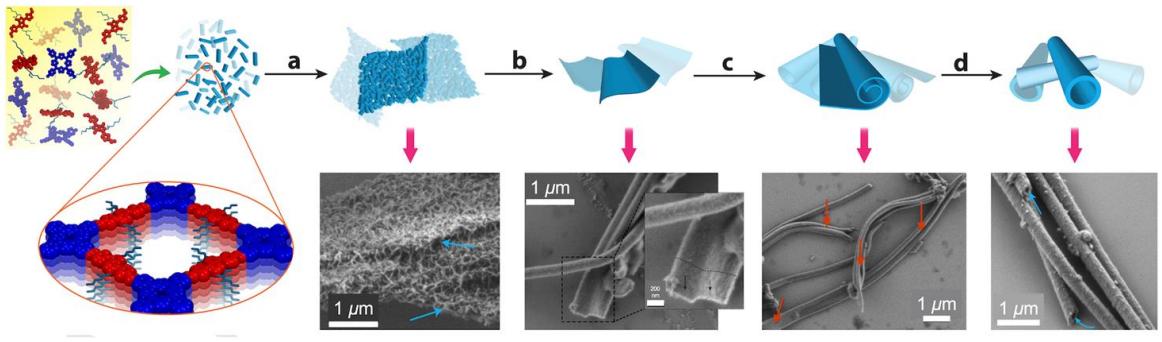

Figure 3-7: Proposed mechanism for microtube formation: a) agglomeration of small DPP-TAPP-COF crystallites into sheet-like aggregates, b) smoothing and densification of sheets by reversible imine condensations, c) rolling of the sheets due to solvent removal and d) tube formation and recombination by reversible imine condensations.

Further increase of the reaction time up to 15 days resulted in roughening and fracturing of the tube walls as evidenced by SEM and PXRD (see Characterization Details). However, the isolated COF microtubes are stable for several months and PXRD measurements showed no signs for structural collapse. Based on these data, there is no evidence for tube growth *via* Ostwald ripening, as it was recently invoked for the formation of spherical COF particles.[39] Instead, the following mechanism for microtube formation is proposed (see Figure 3-8).

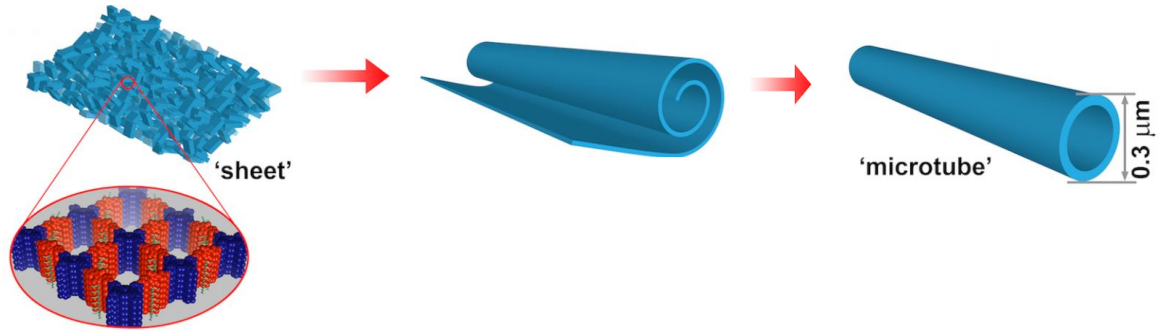

Figure 3-8: Proposed microtubular self-assembly of DPP-TAPP-COF.

Initially, small crystallites of imine-condensation products are formed that agglomerate into sheet-like aggregates, which is presumably induced by van der Waals interactions between the branched alkyl chains. Over time, initial crystallites grow further by condensation of unreacted precursors or grain boundary consumption *via* reactive aldehydes and amines at the interfaces (see Characterization Details).

This transformation is supported by a change in thickness for the initial and uniform sheets from around 500 to 100 nm, respectively. Hence, it is proposed that the spontaneous scrolling into tubular arrangements (red arrows in Figure 3-7c) minimizes

destabilizing interactions with solvent molecules, as it was previously shown for supramolecular nanotubes [48] and microporous polymers.[49] This assumption is also supported by similar wall thicknesses for the microtubes and the uniform sheets. Subsequently, well-defined uniform nanotubes are generated *via* dynamic imine formation of unreacted aldehyde and amino groups present at the edges.

3.3 Conclusion

In conclusion, we have demonstrated the successful implementation of DPP and TPP chromophores into one single conjugated COF *via* reversible imine condensations. UV-Vis studies revealed a significant redshift after framework formation that was attributed to enhanced conjugation and delocalization along and across the COF sheets. Remarkably, DPP-TAPP-COF crystallites self-assemble into microtubular aggregates with narrow size distribution as evidenced by SEM and STEM measurements. Time-dependent studies support the hypothesis that the microtubes originate from rolled-up crystallite sheets. These finding's pave the way for fascinating future experiments on single microtubes, as well as the inclusion of suitable guest molecules or even larger nanostructures thus allowing for an additional fine-tuning of materials properties.

3.4 Experimental Section

Solvents and reagents were purchased from commercial sources and used without further purification, unless otherwise mentioned.

2,5-Diethylhexyl-3,6-dithiophen-2-ylpyrrolo[3,4-c]pyrrole-1,4-dione (1),[50] tetraphenyl-porphyrin [51] and 5,10,15,20-tetrakis(4-aminophenyl)-porphyrin (TAPP) [51] were prepared according to previously reported procedures.

Spectroscopic measurements were conducted under ambient conditions using dry solvents. **Nuclear magnetic resonance (NMR)** spectra were recorded on a Bruker Avance III HD (400 MHz) spectrometer. Chemical shifts are reported in parts per million (ppm) with respect to residual $CHCl_3$ (0 ppm for ^1H and 77 ppm for ^{13}C) as the internal standard. Signal multiplicities are denoted as s (singlet), d (doublet), t (triplet), and m (multiplet). Processing of the raw data was performed by using the program Topspin 3.0.

Solid state **^{13}C cross-polarization magic-angle spinning (CP-MAS) NMR** spectra were measured on a Bruker Avance III HD 600 MHz NMR spectrometer with a

spinning rate of 17000 Hz and a contact time of 2 ms and on a Bruker DSX 400 MHz spectrometer with a spinning rate of 13500 Hz and a contact time of 2 ms.

Mass spectroscopic analyses (MALDI) were carried out on an Autoflex II BRUKER spectrometer using trans-2-(3-(4-t-butylphenyl)-2-methyl-2-propenylidene) malononitrile (DCTB) as matrix.

Elemental analyses (%) were carried out on an Elementar CHNS 932 analyzer.

Fourier transform infrared (FT-IR) spectroscopic analysis was performed on a Jasco FT/IR-430 Spectrometer.

Thermogravimetric analysis (TGA) measurements were performed on a Netzsch Jupiter ST 449 C instrument equipped with a Netzsch TASC 414/4 controller. The samples were heated from room temperature to 900 °C under synthetic air atmosphere at a heating rate of 1 °C/min.

Powder X-ray diffraction (PXRD) measurements were carried out in reflection mode on a Bruker D8 Discover diffractometer with Ni-filtered Kα-radiation (λ = 1.54060 Å) and a position-sensitive detector (LynxEye). The PXRD measurements of resulting COF materials were carried out on a silicon wafer and by applying low scan speed and small angle increments.

Scanning Electron Microscopy (SEM) images were recorded using a Zeiss Ultra Plus field emission scanning electron microscope equipped with GEMINI e-Beam column operated at 1 - 1.5 kV with an aperture size set to 30 μm to avoid excessive charging and radiation damage of the areas imaged.

Focused Ion Beam (FIB) experiments were carried out in a Dual-Beam System incorporating both FIB and SEM using FEI Helios Nanolab. The FIB milling was performed using a 30 kV Ga-ion beam with beam currents ranging from 90 to 170 pA. A protective platinum film (30 nm thick) was deposited on the sample prior to milling. SEM images were obtained using low acceleration voltages (5 kV) and low beam currents (0.17 nA) to limit beam damage.

Atomic Force Microscopy (AFM) measurements were performed at ambient conditions with a Bruker AXS MultiModeTM Nanoscope IV System in tapping mode. Silicon cantilevers (OMCL-AC160TS, Olympus) with a resonance frequency of ~ 300 kHz and spring constant of ~ 42 Nm^{-1} were used.

3.4.1 Syntheses

3.4.1.1 Synthesis of 5,5'-(2,5-bis(2-ethylhexyl)-3,6-dioxo-2,3,5,6-tetrahydro-pyrrolo[3,4-c]-pyrrole-1,4-diyl)dithio-phene-2-carbaldehyde (DPP-1)

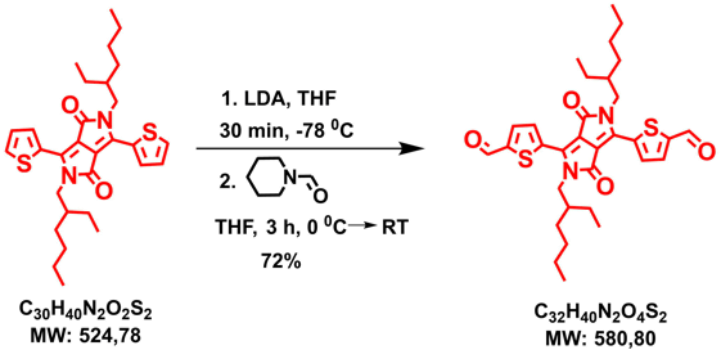

DPP-1 was prepared following a slightly modified literature procedure [52-54] resulting in increased isolated yields. In a three necked round bottom flask, the precursor molecule [50] (819 mg, 1.56 mmol, 1 eq) was dissolved in anhydrous THF (80 mL). At −78 °C, freshly prepared lithium diisopropylamide (LDA) (0.32 M, 12.5 mL, 2.5 eq) was added dropwise under N_2 and constant stirring. The mixture was stirred at the same temperature for another 30 minutes. Afterwards, the solution was slowly warmed up to 0 °C. Subsequently, 1-formylpiperidine (0.43 mL, 3.9 mmol, 2.5 eq) was added dropwise to the solution. The reaction was stirred at room temperature for another three hours. Finally, the reaction mixture was poured into 0.3 M aqueous HCl (150 mL) and stirred vigorously for ten minutes. The organic portion was extracted with $CHCl_3$ (5 × 50 mL). The combined phases were washed with a saturated aqueous solution of $NaHCO_3$ (3 × 30 mL) and brine solution, dried over Na_2SO_4 and finally concentrated under reduced pressure to get the crude product. The crude product was purified by silica gel column chromatography using $CHCl_3$/*n*-hexane (1:1) as eluent to obtain DPP-1 as a dark purple solid (650 mg, 1.12 mmol, 72%).

^{1}H NMR (400 MHz, $CDCl_3$, rt): δ = 10.03 (s, 2H), 9.05 (d, *J* = 4.16 Hz, 2H), 7.88 (d, *J* = 4.23 Hz, 2H), 4.07 (m, 4H), 1.85 (m, 2H), 1.38 (m, 16H), 0.91 (m, 12H) ppm.
MS (MALDI-TOF, DCTB): *m/z* = 580.262 $[M]^+$.

3.4.1.2 Synthesis of 5-(4-aminophenyl)-10,15,20-triphenylporphyrin (NH_2-TPP)

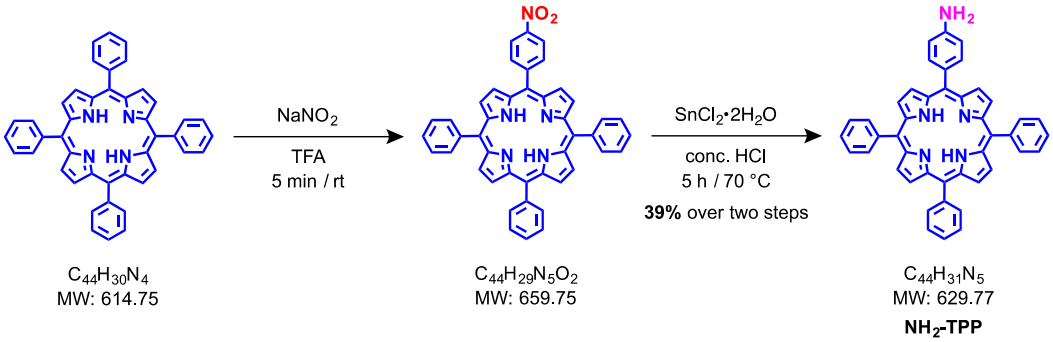

The title compound was prepared using a modified literature procedure.[55, 56] To a solution of tetraphenylporphyrin (1.5 g, 2.44 mmol, 1 eq) in trifluroacetic acid (70 mL), $NaNO_2$ (303.6 mg, 4.4 mmol, 1.8 eq) was added in one portion. After stirring the solution for five minutes at room temperature, the whole mixture was poured into water (300 mL). Finally, the organic layer was extracted with CH_2Cl_2 (5 × 50 mL). The combined organic phases were washed with a saturated aqueous solution of $NaHCO_3$ (3 × 30 mL), dried over Na_2SO_4 and finally concentrated under vacuum to get the crude nitration product. The crude product was used without further purification for the next step.

The crude product was dissolved in concentrated HCl (70 mL) under constant stirring and heated to 70 °C for one hour. After cooling down again to room temperature, $SnCl_2 \cdot 2H_2O$ (4.4 g, 19.5 mmol, 8 eq) was added in small portions under constant stirring. The reaction mixture was again heated to 70 °C with an overhead refluxing condenser for another five hours. Subsequently, the mixture was poured into an ice-water bath. The aqueous solution was neutralized by addition of aqueous ammonia until the pH reached 8. Afterwards, the aqueous solution was extracted with CH_2Cl_2 (5 × 50 mL). The combined organic phases were dried over anhydrous Na_2SO_4 and finally concentrated under vacuum. The obtained residue was purified by column chromatography using neutral alumina as stationary phase and CH_2Cl_2 as eluent to obtain NH_2-TPP (600 mg, 0.95 mmol, 39% over two steps) as a dark purple crystalline solid.

^{1}H NMR (400 MHz, DMSO-d_6, rt): δ = 8.98 (d, *J* = 4.5 Hz, 2H), 8.81 (m, 6H), 8.23 (m, 6H), 7.85 (m, 11H), 7.0 (d, *J* = 8.4 Hz, 2H), 5.62 (s, 2H), -2.86 (s, 2H) ppm.
MS (MALDI-TOF, DCTB): *m/z* = 629.236 $[M]^+$.

3.4.1.3 Synthesis of Model Compound M-1

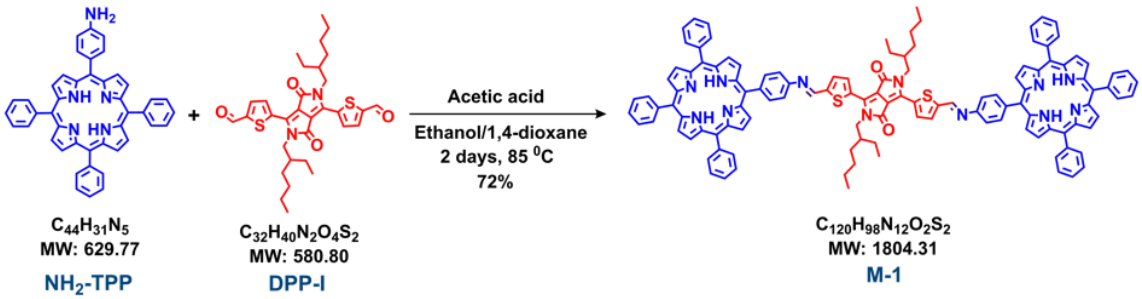

NH_2-TPP (55.42 mg, 0.088 mmol, 2.2 eq) and DPP-1 (23.23 mg, 0.04 mmol, 1 eq) were dissolved in a mixture of EtOH (10 ml), 1,4-dioxane (10 ml) and AcOH (0.05 mL). The reaction mixture was heated to 85 °C under constant stirring in the presence of molecular sieves 4Å for two days. After cooling down to room temperature, the solvents were completely removed under vacuum and the obtained residue was dissolved in $CHCl_3$ and filtrated in order to remove the molecular sieves. The filtrate was evaporated to dryness to yield a dark purple solid as the crude product. Final purification was performed by recycling gel permeation chromatography using $CHCl_3$ as the eluent to obtain pure model compound M-1 (52 mg, 28.8 µmol, 72%) as a dark purple solid.

^{1}H NMR (400 MHz, $CDCl_3$, rt): δ = 9.18 (d, *J* = 4.1 Hz, 2H), 9.02 (s, 2H), 8.92 (m, 16H), 8.29 (d, *J* = 8.5 Hz, 4H), 8.25 (m, 12H), 7.80 (m, 20H), 7.70 (d, *J* = 8.4 Hz, 4H), 4.26 (m, 4H), 2.05 (m, 2H), 1.48 (m, 16H), 1.02 (m, 12H), -2.75 (s, 2H) ppm.
^{13}C NMR (100 MHz, $CDCl_3$, rt): δ = 161.76, 152.26, 150.18, 147.45, 142.16, 140.90, 140.55, 136.56, 135.58, 134.58, 133.24, 132.81, 127.77, 126.73, 120.26, 119.67, 119.44, 110.02, 77.23, 46.26, 39.37, 30.29, 29.73, 28.51, 23.68, 23.18, 14.19, 10.60 ppm.
MS (MALDI-TOF, DCTB): *m/z* = 1803.295 $[M]^+$.
Elemental analysis (%) calculated for $C_{120}H_{98}N_{12}O_2S_2$: C 79.88, H 5.47, N 9.32, S 3.55; found: C 79.59, H 5.48, N 9.12, S 3.34.

3.4.1.4 Synthesis of DPP-TAPP-COF

A pyrex tube with a screw cap was charged with 5,10,15,20-tetrakis(4-aminophenyl)porphyrin (TAPP) [51] (6.75 mg, 0.01 mmol, 1 eq) and DPP-1 (11.61 mg, 0.02 mmol, 2 eq). To that mixture, *n*-butanol (3 mL), mesitylene (1 mL) and aqueous acetic (0.1 ml of 6.0 M aqueous solution) were added. The reaction mixture was sonicated for five minutes in order to homogeneously disperse all reactants. The reaction vessel was sealed with a screw cap and heated at 120 °C for five days. The obtained dark precipitate was collected by filtration through a sintered funnel and washed with dry THF and acetone for three times. The powder obtained was solvent exchanged with ethanol and acetone for three times each and subsequently dried under high vacuum for another four hours to obtain DPP-TAPP-COF as dark powder (9.35 mg, 53%).

FT-IR (transmittance/cm^{-1}): 1667, 1608, 1581, 1560, 1514, 1464, 1457, 1399, 1349, 1222, 1197, 1095, 1019, 966, 796, 733, 711, 624.
Elemental analysis (%): calculated for $C_{108}H_{106}N_{12}O_4S_4$: C 73.52, H 6.06, N 9.53, S 7.27; found: C 72.37, H 6.01, N 9.35, S 6.24.

3.4.1.5 Synthesis of DPP-TAPP-COF at Different Time Intervals

The reaction mixture was distributed to several pyrex tubes and individual samples were removed from the oven after specified time intervals. After cooling to room temperature, precipitates were collected and dried in a similar fashion as described before. The obtained materials were further characterized by PXRD, SEM, IR and solid-state NMR.

3.4.1.6 Synthesis of DPP-TAPP-COF Using Different Solvents

Different solvents and their combinations were investigated for COF synthesis as summarized in Table 3-1. All reactions were carried out using 0.02 mmol of DPP-1 and 0.01 mmol of TAPP. The obtained precipitates were analyzed by PXRD.

Table 3-1: Solvent and catalyst screening for DPP-TAPP-COF synthesis; blue row for best synthesis conditions.

Entry	Solvents				Temp.	Time	Remarks
	n-butanol	mesitylene	*o*-DCB	AcOH (6 M)			
1	**3 mL**	**1 mL**	**-**	**0.1 mL**	**120 °C**	**5 days**	**Crystalline**
2	2 mL	2 mL	-	0.1 mL	120 °C	5 days	Amorphous
3	2 mL	-	2 mL	0.1 mL	120 °C	5 days	Amorphous
4	3 mL	-	2 mL	0.1 mL	120 °C	5 days	Minor crystalline
5	4 mL	-	-	0.1 mL	120 °C	5 days	No reaction
6	3 mL	1 mL	-	0.2 mL	120 °C	5 days	Amorphous
7	1.5 mL	0.5 mL	-	0.1 mL	120 °C	5 days	Minor crystalline
8	4.5 mL	1.5 mL	-	0.1 mL	120 °C	5 days	Amorphous
9	3 mL	1 mL	-	-	120 °C	5 days	Amorphous
10	4.5 mL	1.5 mL	-	-	120 °C	5 days	Amorphous
11	9 mL	3 mL	-	0.1 mL 12 M	120 °C	5 days	Amorphous

3.4.2 Characterization Details

3.4.2.1 Simulation of DPP-TAPP-COF Crystal Structure

Based on the precursor geometries and linking groups the COF structure was constructed; the simulations were carried out with the visualization environment of *Materials Studio software 4.4*. Firstly, an optimized geometry of the two-dimensional COF layers was obtained by using the forcite module. Subsequently, the COF repeating unit was inserted into the unit cell of the appropriate size and symmetry. The geometry of the DPP-TAPP-COF layer was optimized in the unit cell using the Dreiding forcefield and the QEq correction for weak interactions. Moreover, DFTB+ calculations were carried out by using the mio Slater-Koster library. The X-ray diffraction pattern for the simulated structure was obtained by using the Reflex package in the *Materials Studio software*. Furthermore, Pawley refinement according to the experimental PXRD provided the final unit cell parameters. The refinement parameters R_p and R_{wp} are 2.86% and 3.82%, respectively.

Table 3-2: Refined crystal data.

Space group	*C2/m*
Crystal system	monoclinic
Chemical formula	$C_{216}H_{208}N_{24}O_8S_8$
Unit cell dimension	a = 45.29 Å b = 48.91 Å c = 3.9 Å α = γ = 90.00° β = 74.37°
Cell Volume	8358.91 $Å^3$

Table 3-3: Atomic parameters for DPP-TAPP-COF.

Atom	**x/a**	**y/b**	**z/c**
C1	444.701	-144.969	-0.54591
C2	448.515	-141.184	-0.51142
C3	447.624	-144.040	-0.52372
C4	443.798	-147.746	-0.56131
C5	440.929	-148.605	-0.63098
C6	442.330	-142.896	-0.54544
C7	442.895	-140.599	-0.77182
C8	440.620	-138.667	-0.76283
C9	437.681	-138.956	-0.52548
C10	437.108	-141.254	-0.29726
C11	439.384	-143.184	-0.30948
N12	435.518	-136.919	-0.52608
C13	430.646	-134.899	-0.34784
S14	431.978	-132.151	-0.62488
C15	428.526	-130.390	-0.47971
C16	426.409	-131.982	-0.22762
C17	427.589	-134.513	-0.15593
C18	427.756	-127.680	-0.57356
N19	429.538	-125.914	-0.82356
C20	427.936	-123.465	-0.85131
C21	424.982	-126.309	-0.41864
O22	428.949	-121.684	-107.609
C23	432.691	-137.142	-0.33762
C24	0.32384	0.73441	-0.08180
C25	0.35217	0.74910	-0.02123
C26	0.37928	0.72939	-0.12787
C27	0.40918	0.74120	-0.08992
C28	0.43427	0.71977	-0.15575
C29	0.46387	0.73150	-0.10998
C30	0.35841	0.77637	-0.22330

C31	0.36953	0.79953	-0.03393
H32	447.139	-139.369	-0.52539
H33	439.165	-147.292	-0.68969
H34	445.132	-140.392	-0.96755
H35	441.090	-136.907	-0.94432
H36	434.866	-141.522	-0.10464
H37	438.897	-144.916	-0.12352
H38	424.080	-131.242	-0.09684
H39	426.286	-136.027	0.03179
H40	431.751	-138.948	-0.16736
H41	0.32100	0.73987	-0.34617
H42	0.32713	0.71197	-0.08361
H43	0.34770	0.75329	0.26575
H44	0.38226	0.72259	-0.40502
H45	0.37380	0.71069	0.03740
H46	0.40585	0.74969	0.18014
H47	0.41652	0.75844	-0.27629
H48	0.43799	0.71113	-0.42614
H49	0.42674	0.70250	0.03057
H50	0.47465	0.74541	-0.33000
H51	0.48031	0.71504	-0.10042
H52	0.45984	0.74331	0.13897
H53	0.33713	0.78324	-0.28575
H54	0.37568	0.77273	-0.47787
H55	0.37623	0.81700	-0.21534
H56	0.38957	0.79380	0.05893
H57	0.35137	0.80670	0.19446
N58	0.50000	0.54318	0.50000
N59	0.45465	0.50000	0.47462

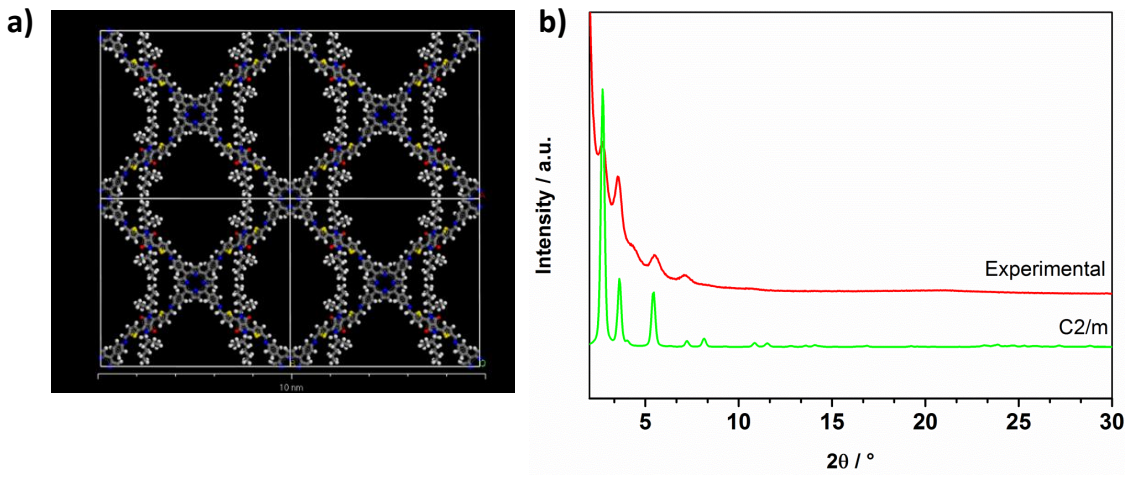

Figure 3-9: a) Simulation of DPP-TAPP-COF unit cell calculated in an eclipsed arrangement in the *C2/m* space group, b) powder XRD patterns of experimental data of DPP-TAPP-COF (red) simulated in the *C*2/*m* space group (green), respectively.

3.4.2.2 Scanning Electron Microscopy (SEM) and Scanning Transmission Electron Microscopy (STEM)

In order to get deeper insights into the mechanism of the tube formation, pH-dependent and time-dependent synthetic studies were performed and analyzed by SEM. Under optimized conditions, hollow nanotubes could be reproducibly obtained using AcOH as catalyst in 0.15 molar concentration. Interestingly, at lower catalyst concentrations (0.05 M), spherical particles were obtained instead. Reaction at slightly higher catalyst concentration (0.1 M) resulted in rod-like aggregates of similar spheres. STEM indicates that neither the spherical particles nor the rod-like aggregates are hollow structures but rather solid agglomerates. Therefore, it can be concluded that these particles are most likely not on-pathway intermediates towards the formation of the hollow microtubes but rather form *via* other pH-dependent pathways.

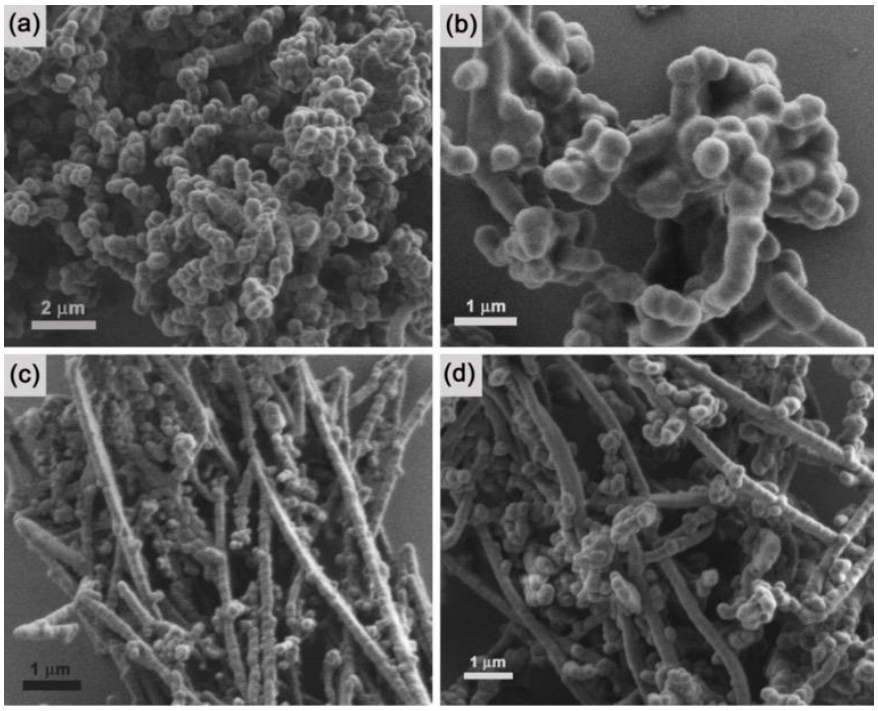

Figure 3-10: SEM micrographs of COF nanostructures obtained at different concentrations of AcOH as catalyst: (a) and (b) Spherical nanostructures obtained with 0.05 mol L^{-1} AcOH; (c) and (d) agglomeration of spherical nanostructures into rod-like aggregates with 0.1 mol L^{-1} AcOH.

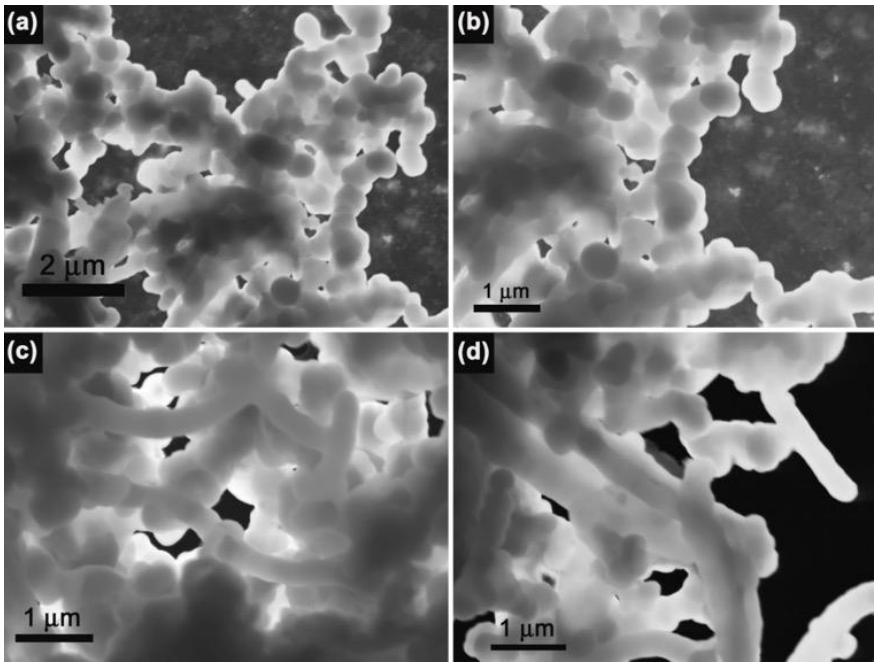

Figure 3-11: a) and b) STEM images of spherical particles obtained with 0.05 mol L^{-1} AcOH; c) and d) STEM images of rod-like aggregates obtained with 0.1 mol L^{-1} AcOH. All images indicate the solid nature of both nanostructures and exclude the formation of hollow structures.

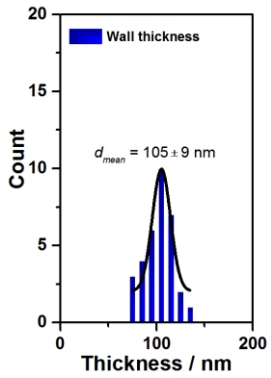

Figure 3-12: Statistical distribution of wall thickness for DPP-TAPP-COF nanotubes obtained from STEM micrographs.

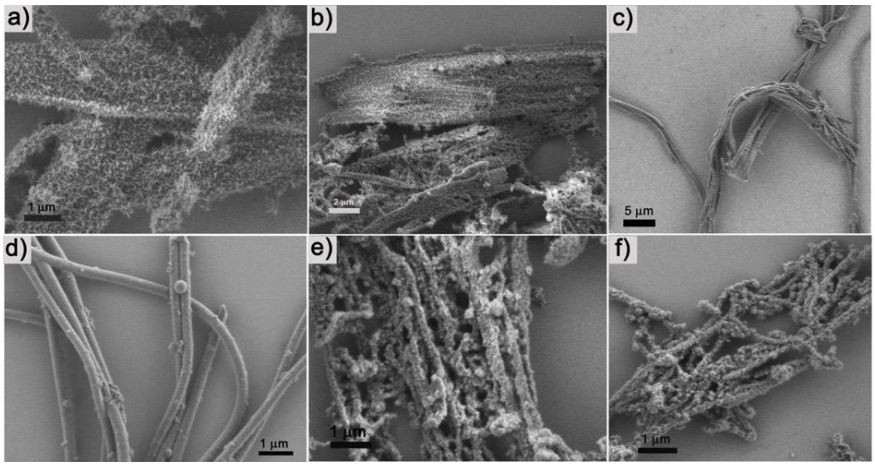

Figure 3-13: SEM micrographs of DPP-TAPP-COF synthesized in *n*-BuOH/mesitylene 3:1 at 120 °C; reaction was quenched after a) one day, b) three days, c) four days, d) five days, e) seven days and f) ten days.

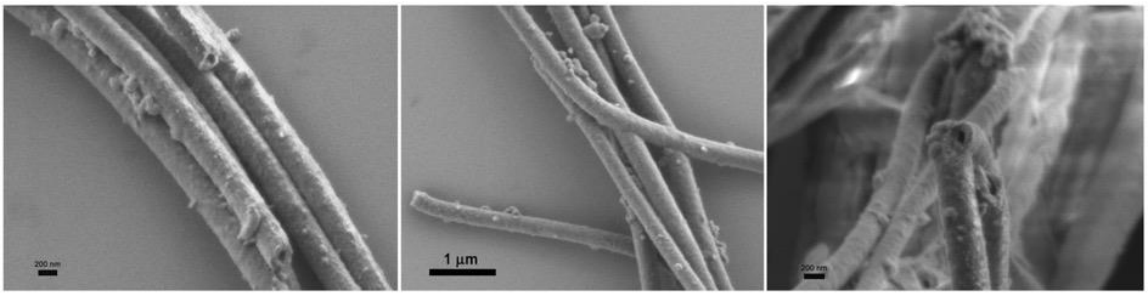

Figure 3-14: SEM micrographs of DPP-TAPP-COF nanotubes on different length scales.

3.4.2.3 Powder X-ray Diffraction

PXRD clearly revealed the predominantly amorphous character of the structures which are based on a different reaction procedure.

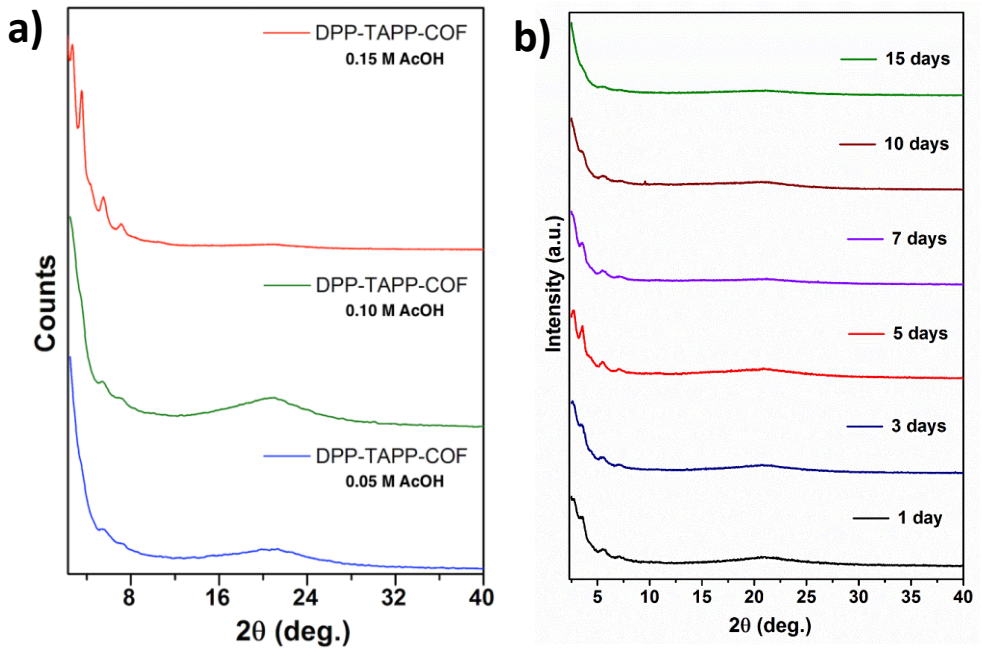

Figure 3-15: a) PXRD patterns for DPP-TAPP-COF synthesized in *n*-BuOH/mesitylene 3:1 at 120 °C with different concentrations of AcOH as catalyst, b) PXRD patterns for DPP-TAPP-COF synthesized in *n*-BuOH/mesitylene 3:1 at 120 °C; reaction was quenched after different time intervals as indicated.

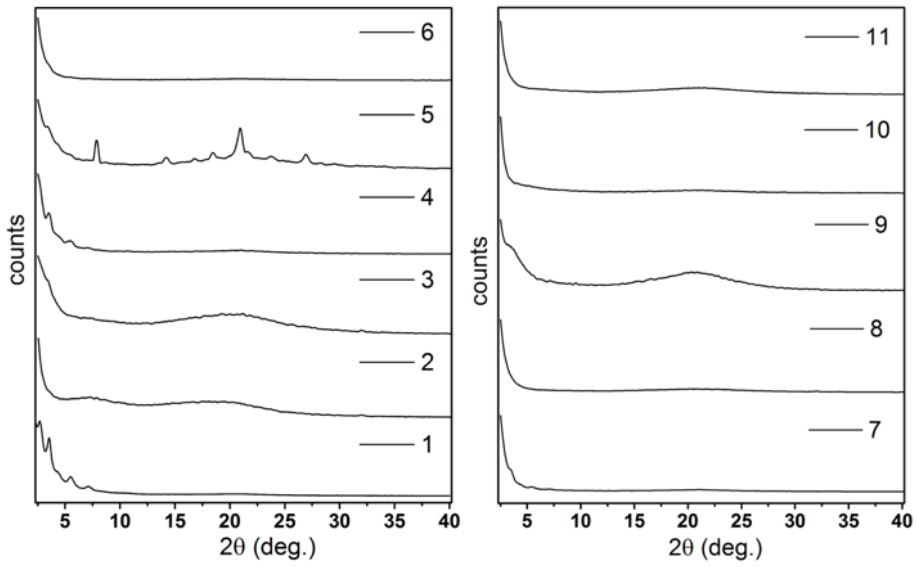

Figure 3-16: PXRD patterns for DPP-TAPP-COF synthesis in different solvents. Numbers indicate different entries of Table 3-1.

3.4.2.4 Focused Ion Beam (FIB) Microscopy

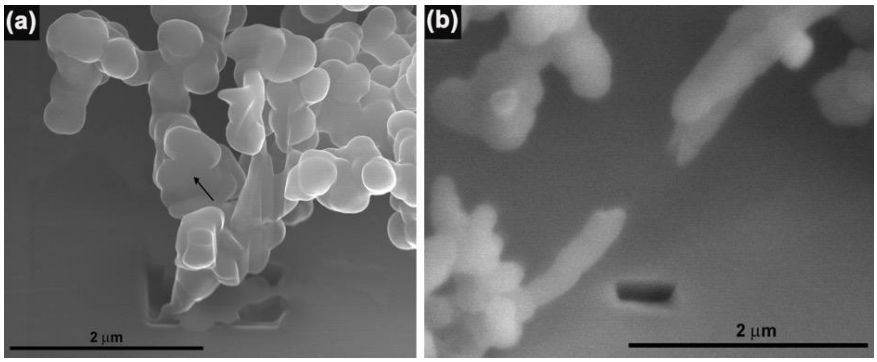

Figure 3-17: FIB experiments showing the solid nature and absence of hollow structures for a) spherical particles obtained with 0.05 mol L^{-1} AcOH, and b) rod-like aggregates obtained with 0.1 mol L^{-1} AcOH.

3.4.2.5 Energy-Dispersive X-ray Spectroscopy (EDX)

Energy-dispersive X-ray (EDX) spectroscopy on various spots of different tubes revealed a uniform atomic composition, thus indicating the homogeneous formation of a composite material.

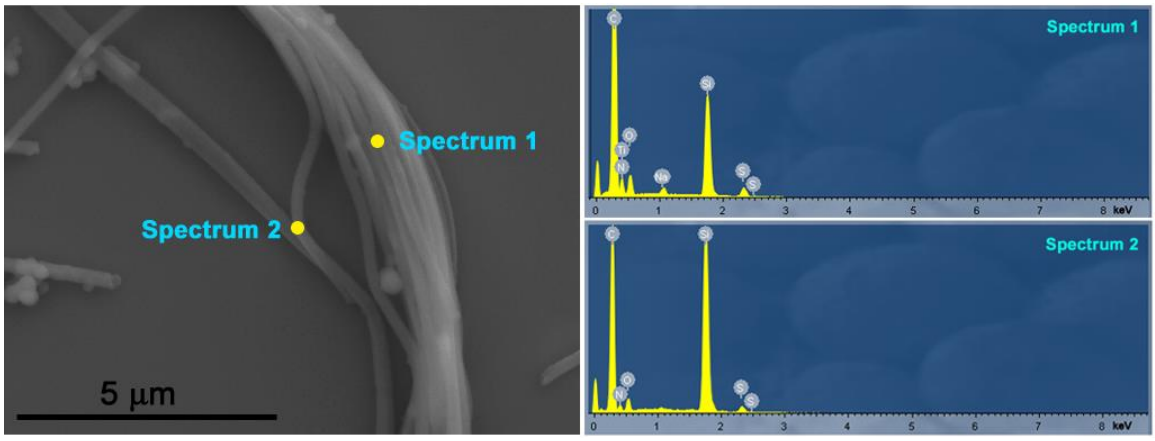

Figure 3-18: EDX mapping of the nanotubes at specific points indicating the elemental composition of C, N, O and S.

3.4.2.6 ^{13}C Cross-polarization Magic-Angle Spinning (CP-MAS)

NMR spectra for both DPP-TAPP-COF and M-1 are in excellent agreement with ^{13}C NMR solution data of M-1 obtained in $CDCl_3$. The absence of any aldehyde signal, expected to appear beyond 180 ppm, indicates virtually quantitative consumption of the DPP precursor. Furthermore, elemental analysis of the DPP-TAPP-COF showed the efficient formation of a polymeric material composed of moth monomers (see Figure 3-19).

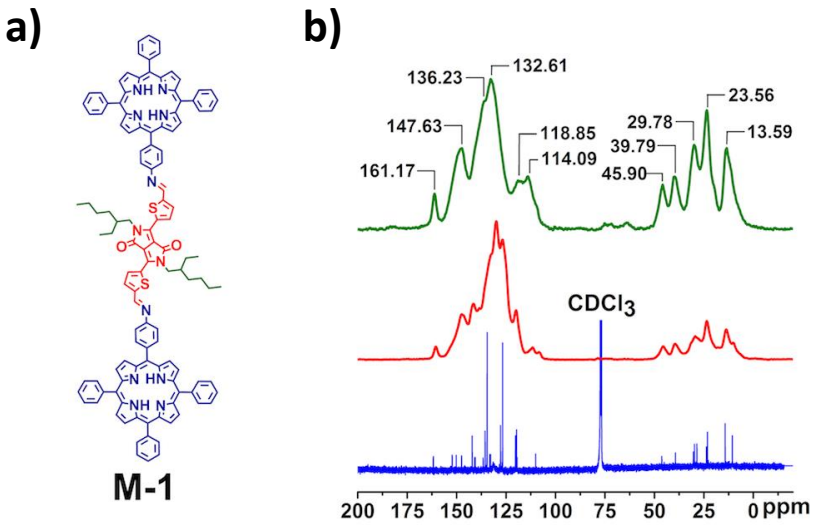

Figure 3-19: a) Model compound M-1, b) ^{13}C-CP-MAS-NMR spectra of DPP-TAPP-COF (green) and of solid M-1 (red), ^{13}C-NMR spectrum ($CDCl_3$, 400 MHz, rt) of M-1 (blue).

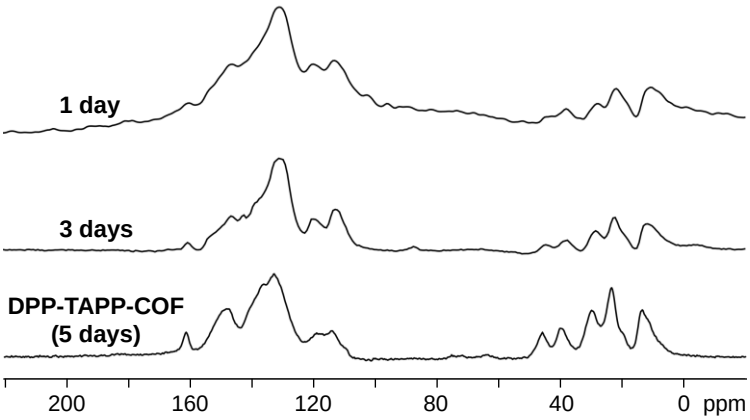

Figure 3-20: ^{13}C-CP-MAS-NMR spectra of DPP-TAPP-COF reactions quenched after one (100.6 MHz, 13.5 kHz spin rate, top), three (100.6 MHz, 13.5 kHz spin rate, middle) and five days (151.0 MHz, 17.0 kHz spin rate, bottom, optimized reaction conditions).

3.4.2.7 FT-IR Spectroscopy

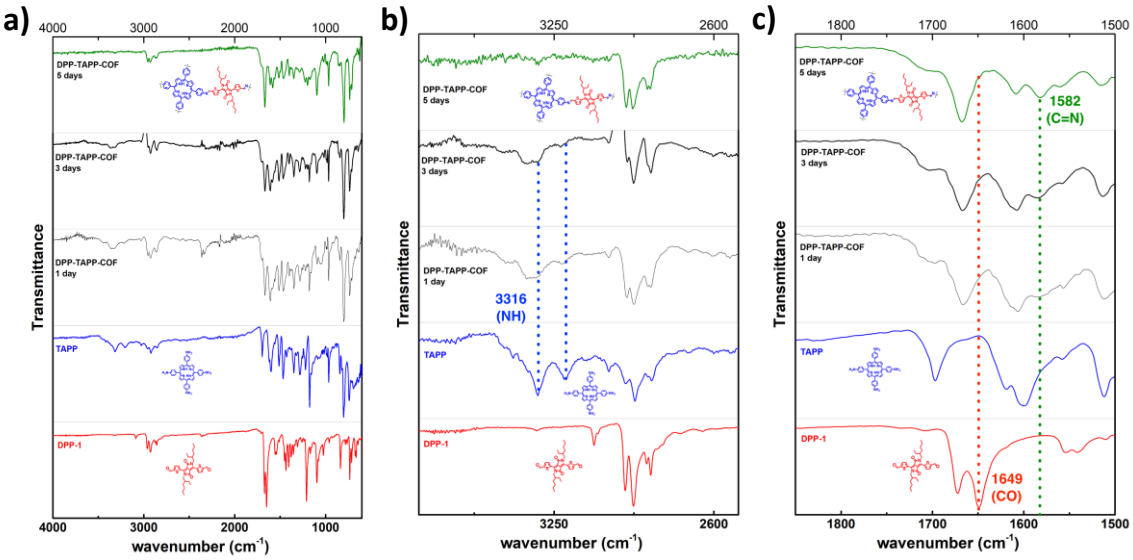

Figure 3-21: a) FT-IR spectra for DPP-TAPP-COF (green), COF reactions quenched after one and three days (black) in comparison with monomers TAPP (blue) and DPP-1 (red), highlighting characteristic regions for b) NH stretching bands and c) C=O and N=H stretching bands.

3.4.2.8 Atomic Force Microscopy (AFM)

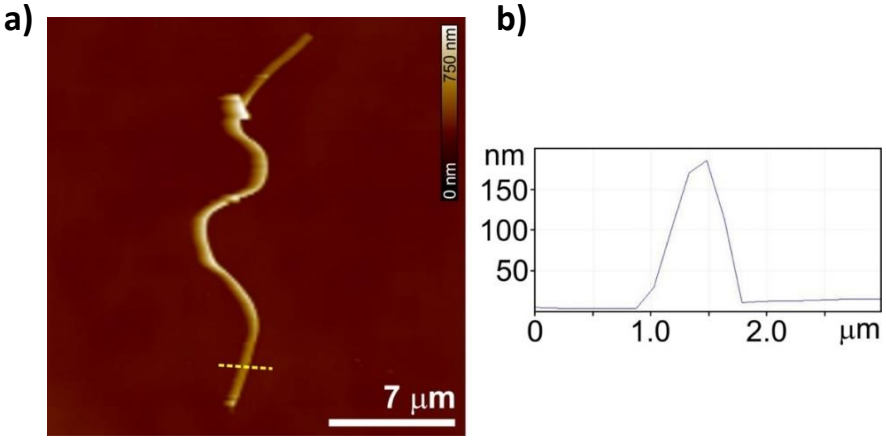

Figure 3-22: a) AFM image of one single nanotube, b) corresponding cross sectional height.

3.5 References

1. T. Aida, E. Meijer, and S. Stupp, *Science* **2012**, *335*, 813-817.
2. G. Zhang, O. Presly, F. White, I. M. Oppel, and M. Mastalerz, *Angew. Chem.* **2014**, *126*, 5226-5230.
3. S. Klotzbach and F. Beuerle, *Angew. Chem. Int. Ed.* **2015**, *54*, 10356-10360.
4. F. Würthner, C. R. Saha-Möller, B. Fimmel, S. Ogi, P. Leowanawat, and D. Schmidt, *Chem. Rev.* **2015**, *116*, 962-1052.
5. G. M. Whitesides and B. Grzybowski, *Science* **2002**, *295*, 2418-2421.
6. J.-F. Lutz, J.-M. Lehn, E. Meijer, and K. Matyjaszewski, *Nat. Rev. Mater.* **2016**, *1*, 16024.
7. X. Zhou, Q. Jin, L. Zhang, Z. Shen, L. Jiang, and M. Liu, *Small* **2016**, *12*, 4743-4752.
8. L. B. Gower, *Chem. Rev.* **2008**, *108*, 4551-4627.
9. H. Cölfen, *Nat. Mater.* **2010**, *9*, 960.
10. A. P. Côté, A. I. Benin, N. W. Ockwig, M. O'Keeffe, A. J. Matzger, and O. M. Yaghi, *Science* **2005**, *310*, 1166-1170.
11. E. L. Spitler and W. R. Dichtel, *Nat. Chem.* **2010**, *2*, 672.
12. L. Ascherl, T. Sick, J. T. Margraf, S. H. Lapidus, M. Calik, C. Hettstedt, K. Karaghiosoff, M. Döblinger, T. Clark, and K. W. Chapman, *Nat. Chem.* **2016**, *8*, 310.
13. D. Rodríguez-San-Miguel, A. Abrishamkar, J. A. Navarro, R. Rodriguez-Trujillo, D. B. Amabilino, R. Mas-Ballesté, F. Zamora, and J. Puigmartí-Luis, *Chem. Comm.* **2016**, *52*, 9212-9215.
14. P. J. Waller, F. Gándara, and O. M. Yaghi, *Acc. Chem. Res.* **2015**, *48*, 3053-3063.
15. X. Feng, X. Ding, and D. Jiang, *Chem. Soc. Rev.* **2012**, *41*, 6010-6022.
16. G. Lin, H. Ding, D. Yuan, B. Wang, and C. Wang, *J. Am. Chem. Soc.* **2016**, *138*, 3302-3305.
17. N. Huang, P. Wang, and D. Jiang, *Nat. Rev. Mater.* **2016**, *1*, 16068.
18. S. S. Han, H. Furukawa, O. M. Yaghi, and W. A. Goddard Iii, *J. Am. Chem. Soc.* **2008**, *130*, 11580-11581.
19. C. J. Doonan, D. J. Tranchemontagne, T. G. Glover, J. R. Hunt, and O. M. Yaghi, *Nat. Chem.* **2010**, *2*, 235.

20. Y. Zeng, R. Zou, Z. Luo, H. Zhang, X. Yao, X. Ma, R. Zou, and Y. Zhao, *J. Am. Chem. Soc.* **2015**, *137*, 1020-1023.
21. C. R. DeBlase, K. E. Silberstein, T.-T. Truong, H. D. Abruña, and W. R. Dichtel, *J. Am. Chem. Soc.* **2013**, *135*, 16821-16824.
22. C. R. Mulzer, L. Shen, R. P. Bisbey, J. R. McKone, N. Zhang, H. D. Abruña, and W. R. Dichtel, *ACS Cent. Sci.* **2016**, *2*, 667-673.
23. V. S. Vyas, V. W.-h. Lau, and B. V. Lotsch, *Chem. Mater.* **2016**, *28*, 5191-5204.
24. Q. Fang, S. Gu, J. Zheng, Z. Zhuang, S. Qiu, and Y. Yan, *Angew. Chem.* **2014**, *126*, 2922-2926.
25. H. Xu, J. Gao, and D. Jiang, *Nat. Chem.* **2015**, *7*, 905.
26. S. Lin, C. S. Diercks, Y.-B. Zhang, N. Kornienko, E. M. Nichols, Y. Zhao, A. R. Paris, D. Kim, P. Yang, and O. M. Yaghi, *Science* **2015**, *349*, 1208-1213.
27. H.-S. Xu, S.-Y. Ding, W.-K. An, H. Wu, and W. Wang, *J. Am. Chem. Soc.* **2016**, *138*, 11489-11492.
28. S. Dalapati, S. Jin, J. Gao, Y. Xu, A. Nagai, and D. Jiang, *J. Am. Chem. Soc.* **2013**, *135*, 17310-17313.
29. S.-Y. Ding, M. Dong, Y.-W. Wang, Y.-T. Chen, H.-Z. Wang, C.-Y. Su, and W. Wang, *J. Am. Chem. Soc.* **2016**, *138*, 3031-3037.
30. Z. Li, Y. Zhang, H. Xia, Y. Mu, and X. Liu, *Chem. Comm.* **2016**, *52*, 6613-6616.
31. X. Feng, L. Chen, Y. Honsho, O. Saengsawang, L. Liu, L. Wang, A. Saeki, S. Irle, S. Seki, and Y. Dong, *Adv. Mater.* **2012**, *24*, 3026-3031.
32. M. Dogru, M. Handloser, F. Auras, T. Kunz, D. Medina, A. Hartschuh, P. Knochel, and T. Bein, *Angew. Chem. Int. Ed.* **2013**, *52*, 2920-2924.
33. N. A. Zwaneveld, R. Pawlak, M. Abel, D. Catalin, D. Gigmes, D. Bertin, and L. Porte, *J. Am. Chem. Soc.* **2008**, *130*, 6678-6679.
34. S. Wan, J. Guo, J. Kim, H. Ihee, and D. Jiang, *Angew. Chem.* **2008**, *120*, 8958-8962.
35. W. Huang, Y. Jiang, X. Li, X. Li, J. Wang, Q. Wu, and X. Liu, *ACS Appl. Mater. Interfaces* **2013**, *5*, 8845-8849.
36. H. M. El-Kaderi, J. R. Hunt, J. L. Mendoza-Cortés, A. P. Côté, R. E. Taylor, M. O'Keeffe, and O. M. Yaghi, *Science* **2007**, *316*, 268-272.
37. S. B. Kalidindi, C. Wiktor, A. Ramakrishnan, J. Weßing, A. Schneemann, G. Van Tendeloo, and R. A. Fischer, *Chem. Comm.* **2013**, *49*, 463-465.

38. C. Qian, S. Q. Xu, G. F. Jiang, T. G. Zhan, and X. Zhao, *Chem. – Eur. J.* **2016**, *22*, 17784-17789.
39. S. Kandambeth, V. Venkatesh, D. B. Shinde, S. Kumari, A. Halder, S. Verma, and R. Banerjee, *Nat. Commun.* **2015**, *6*, 6786.
40. A. Halder, S. Kandambeth, B. P. Biswal, G. Kaur, N. C. Roy, M. Addicoat, J. K. Salunke, S. Banerjee, K. Vanka, and T. Heine, *Angew. Chem. Int. Ed.* **2016**, *55*, 7806-7810.
41. P. Pachfule, S. Kandmabeth, A. Mallick, and R. Banerjee, *Chem. Comm.* **2015**, *51*, 11717-11720.
42. S. Wan, F. Gándara, A. Asano, H. Furukawa, A. Saeki, S. K. Dey, L. Liao, M. W. Ambrogio, Y. Y. Botros, and X. Duan, *Chem. Mater.* **2011**, *23*, 4094-4097.
43. A. Nagai, X. Chen, X. Feng, X. Ding, Z. Guo, and D. Jiang, *Angew. Chem. Int. Ed.* **2013**, *52*, 3770-3774.
44. R. B. Zerdan, N. T. Shewmon, Y. Zhu, J. P. Mudrick, K. J. Chesney, J. Xue, and R. K. Castellano, *Adv. Funct. Mater.* **2014**, *24*, 5993-6004.
45. M. Grzybowski and D. T. Gryko, *Adv. Optical Mater.* **2015**, *3*, 280-320.
46. M. Stolte, S. L. Suraru, P. Diemer, T. He, C. Burschka, U. Zschieschang, H. Klauk, and F. Würthner, *Adv. Funct. Mater.* **2016**, *26*, 7415-7422.
47. Q. Ge, J. Ran, J. Miao, Z. Yang, and T. Xu, *ACS Appl. Mater. Interfaces* **2015**, *7*, 28545-28553.
48. N. Kameta, H. Minamikawa, and M. Masuda, *Soft Matter* **2011**, *7*, 4539-4561.
49. J. X. Jiang, F. Su, A. Trewin, C. D. Wood, N. L. Campbell, H. Niu, C. Dickinson, A. Y. Ganin, M. J. Rosseinsky, and Y. Z. Khimyak, *Angew. Chem. Int. Ed.* **2007**, *46*, 8574-8578.
50. L. Huo, J. Hou, H.-Y. Chen, S. Zhang, Y. Jiang, T. L. Chen, and Y. Yang, *Macromolecules* **2009**, *42*, 6564-6571.
51. S. Meng, Z. Xu, G. Hong, L. Zhao, Z. Zhao, J. Guo, H. Ji, and T. Liu, *Eur. J. Med. Chem.* **2015**, *92*, 35-48.
52. W. S. Yoon, S. K. Park, I. Cho, J. A. Oh, J. H. Kim, and S. Y. Park, *Adv. Funct. Mater.* **2013**, *23*, 3519-3524.
53. B. P. Karsten, R. K. Bouwer, J. C. Hummelen, R. M. Williams, and R. A. Janssen, *Photochem. Photobiol. Sci.* **2010**, *9*, 1055-1065.
54. B. P. Karsten, J. C. Bijleveld, and R. A. Janssen, *Macromol. Rapid. Commun.* **2010**, *31*, 1554-1559.

55. R. Luguya, L. Jaquinod, F. R. Fronczek, M. G. H. Vicente, and K. M. Smith, *Tetrahedron* **2004**, *60*, 2757-2763.

56. K. Ladomenou, T. Lazarides, M. K. Panda, G. Charalambidis, D. Daphnomili, and A. G. Coutsolelos, *Inorg. Chem.* **2012**, *51*, 10548-10556.

4 Scaffold-Induced Diketopyrrolopyrrole Molecular Stacks in a Covalent Organic Framework

This chapter is based on the following publication:

Sabrina Rager, Andreas Jakowetz, Bappaditya Gole, Florian Beuerle, Dana D. Medina, and Thomas Bein, *Chem. Mater*. **2019**, 31, 8, 2707-2712,
DOI: 10.1021/acs.chemmater.8b02882.

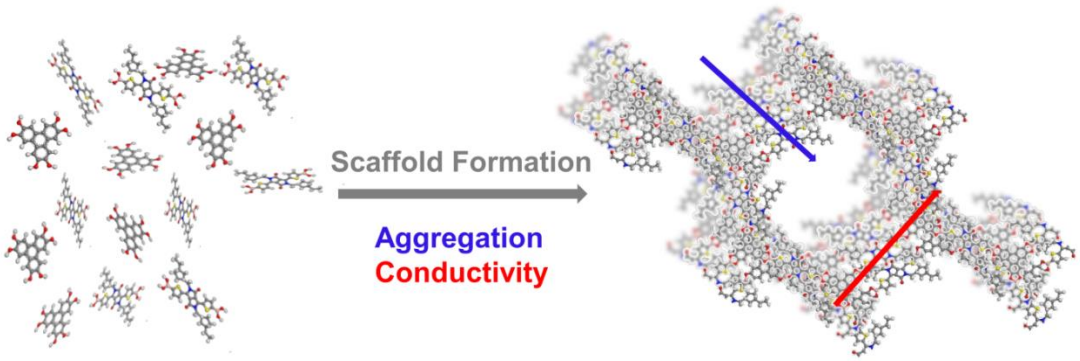

Abstract

In recent years, covalent organic frameworks (COFs) have attracted considerable attention due to their crystalline and porous nature, which positions them as intriguing candidates for diverse applications such as catalysis, sensing or optoelectronics. The incorporation of dyes or semiconducting moieties into a rigid two-dimensional COF can offer emergent features such as enhanced light harvesting or charge transport. However, this approach can be challenging when dealing with dye molecules that exhibit a large aromatic backbone, since the steric demand of solubilizing side chains also needs to be integrated into the framework. Here we report the successful synthesis of DPP2-HHTP-COF consisting of diketopyrrolopyrrole (DPP) diboronic acid and hexahydroxytriphenylene (HHTP) building blocks. The well-known boronate ester coupling motif guides the formation of a planar and rigid backbone and longe-range molecular DPP stacks, resulting in a highly crystalline and porous material. DPP2-HHTP-COF exhibits excellent optical properties including strong absorption over the visible spectral range, broad emission into the NIR and a singlet lifetime of over 5 ns attributed to the formation of molecular stacks with *J*-type interactions between the DPP subcomponents in the COF. Electrical conductivity measurements of crystalline DPP2-HHTP-COF pellets revealed conductivity values of up to 10^{-6} Scm^{-1}.

4.1 Introduction

The deterministic synthesis of crystalline porous materials has attracted much interest in recent years.[1, 2] Amongst these, covalent organic frameworks (COFs) offer highly versatile systems due to their tunable linkage chemistry and the diverse types of molecular building blocks incorporated into the backbone.[3, 4] By molecular design of the building blocks constituting the COFs, structural properties such as the pore geometry, dimensionality and accessibility can be predicted. In addition, by implementing functional building blocks such as photoactive molecules into the framework, physical properties such as a broad absorption range can be encoded, which is of particular importance for optoelectronic and photovoltaic applications.[5-7] Another important operative design tool is the binding motif connecting the building blocks, and fully conjugated or electronically separated systems can be realized depending on the type of cross-linking. In the particular case of assembling two-dimensional (2D) COFs, defined molecular stacks and thereby the decoupling of electronic properties in different

directions can be achieved.[8] One promising synthesis strategy is to harness this type of 2D COF assemblies to construct electroactive macromolecules with overlapping π-systems featuring desired properties such as long-range order and defined host cavities.

COFs featuring electrical conductivity were recently reported,[8] including COF-polymer hybrid systems based on a DAAQ-TFP COF film consisting of the electroactive diaminoanthraquinone building block, followed by electropolymerization of 3,4-ethylenedioxythiophene (EDOT) within the pores. The resulting poly(3,4-ethylenedioxythiophene) (PEDOT)-infiltrated COF showed enhanced electrical conductivity.[9] Zhang and coworkers reported the synthesis of a conducting tetrathiafulvalene imine-based COF that can act as an electron donor. Further doping with iodine improved the conductivity of the bulk material, to reach $1.8 \cdot 10^{-6}$ Scm^{-1} after two days of doping.[10]

To achieve strong and broadband light absorption, porphyrins and related dyes are prominent building blocks of choice for the construction of COFs. Through the functional design of these photoactive building blocks, 2D [11, 12] as well as 3D [13] COFs could be established. For example, metalloporphyrins allow for optical band gap tuning in the corresponding COFs.[11, 13, 14] Moreover, Dichtel *et al.*[15] and Jiang *et al.*[16] reported the synthesis of octahydroxyphthalocyanine-based COFs by reacting with boronic acid building blocks, and demonstrated the generation of photocurrent.[16-18] Another versatile family of dyes is based on the isoindigo motif, which has recently been used as a new acceptor in donor-acceptor conjugated polymers. This electron deficient dye can lead to intriguing properties such as broad absorption, high open circuit voltage as well as high mobilities, and can reach relatively high power conversion efficiencies when implemented into organic photovoltaic devices.[19-22] The isoindigo dye has also been successfully implemented into COFs.[19, 23] Furthermore, isoindigo building blocks can be used to obtain broad optical absorption from the visible into the near-infrared region.[23]

While highly symmetric dyes such as the porphyrins or phthalocyanines discussed above have been successfully implemented into COFs, the incorporation of dyes with sterically demanding side chains or ‘kinked’ (less symmetric) molecules into the backbone of 2D COFs is still a major challenge. Recently, we reported the template-free microtubular self-assembly of a COF based on imine condensation between (4-aminophenyl)porphyrin (TAPP) and a diketopyrrolopyrrole (DPP) dialdehyde derivative.[24] In this report, the formation of a network containing strongly absorbing dyes and sterically demanding building blocks was demonstrated. DPP-TAPP-COF

features remarkable optical absorption across the whole visible spectrum. Similar to the isoindigo building block, the DPP moiety is well-studied in organic semiconducting polymers and small molecule-based solar devices, showing high ambipolar carrier mobilities in organic field-effect transistors of around 0.3 $cm^2V^{-1}s^{-1}$ [25-28] and high power-conversion efficiencies.[29] To further extend the accessible family of DPP-based COFs, we chose the alternative flat and non-conjugated boronate ester coupling motif, allowing us to explore the photoactivity of the DPP building block within a well-defined aggregate in an ordered porous structure.

4.2 Results and Discussion

In this study, we report the synthesis of a novel COF based on DPP building blocks.[30, 31] The framework synthesis is based on the formation of boronate ester groups *via* co-condensation reaction of the new precursor ((2,5-bis(2-ethylhexyl)-3,6-dioxo-2,3,5,6-tetrahydropyrrolo[3,4-c]-pyrrole-1,4-diyl)bis(thiophene-5,2-diyl))diboronic acid (DPP2) and commercially available hexahydroxytriphenylene (HHTP) (see Figure 4-1a). The DPP2-HHTP-COF exhibits open pores with a high surface area, high crystallinity and promising optical properties through framework-induced stacking.

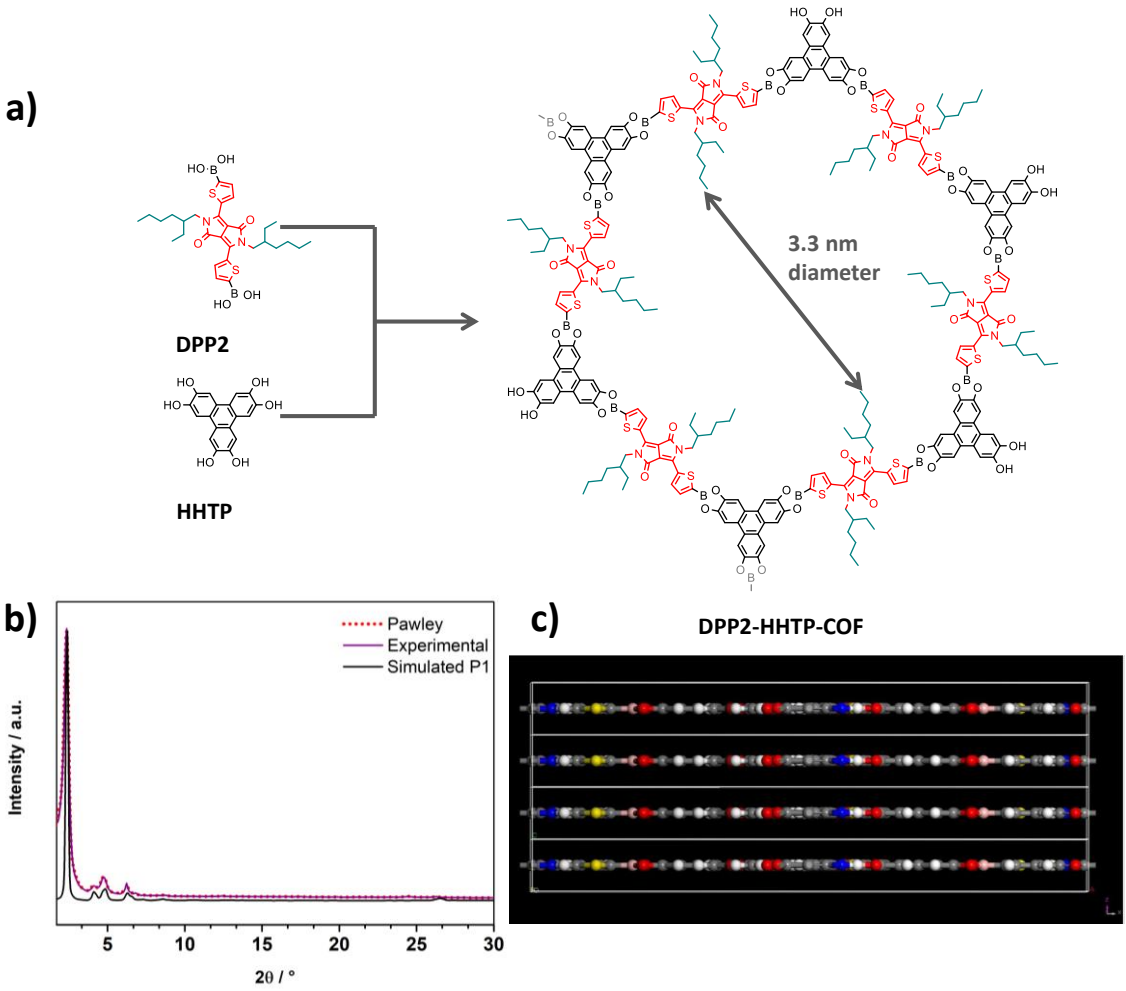

Figure 4-1: a) Schematic reaction pathway for the synthesis of DPP2-HHTP-COF. b) Experimentally obtained powder pattern of DPP2-HHTP-COF (purple) compared to the calculated diffraction pattern of the eclipsed 2D layer arrangement in the *P1* space group (black) and Pawley refinement (red). c) Simulated stacked unit cells for a triclinic crystal system of the space group *P1* (solubilizing ethylhexyl chains are omitted for clarity) to illustrate the flat and rigid boronate ester-based backbone.

The DPP2 linker was obtained in a 3-step synthesis described in the Experimental Section, whereas the HHTP counterpart is commercially available and was used without further purification. Subsequently, the synthesis conditions for DPP2-HHTP-COF were screened with regard to solvents, solvent ratio, concentration, and reagent ratio (for more details see Experimental Section). All COF syntheses were carried out under solvothermal conditions in a 10 mL Schott Duran glass vial covered with a teflon cap. In an optimized procedure, the organic precursors were dissolved in a solvent mixture of mesitylene and dioxane (1:1) and heated up to 100 °C for 24 hours. A high concentration of the reagents turned out to be crucial for the formation of a highly ordered crystalline framework. After work-up, including washing the crude product with dry acetone, DPP2-HHTP-COF was obtained as dark-purple powder.

The powder X-ray diffraction (PXRD) pattern of DPP2-HHTP-COF is shown Figure 4-1b. The XRD pattern indicates the formation of a highly crystalline framework with Bragg reflections centered at low 2θ values of 2.33°, 4.13°, 4.76° and 6.23°. These reflections are attributed to the 100, 110, 200 and 3-10 planes, respectively. Based on the symmetry of the applied building blocks including the sterically demanding alkyl groups pointing into the pores, the expected approximately hexagonal pore system with an eclipsed AA-stacked layer model with planar boronate ester-based backbone (Figure 4-1c) was simulated in the *P1* and *P6/mcc* space groups using the *Materials Studio software*. The simulated diffraction pattern in the *P1* space group provides a better description of our DPP2-HHTP-COF (see Figure 4-1b and Experimental Section). The final unit cell parameters in *P1* were obtained by performing Pawley refinement and correspond to a = 43.82 Å, b = 44.57 Å, c = 3.48 Å, α = 89.79°, β = 89.53°, γ = 122.76° (*Rwp* = 3.36% and *Rp* = 2.52%).

To assess the porosity of DPP2-HHTP-COF, nitrogen sorption measurements were carried out. Prior to the sorption experiments, the COF powder was degassed by keeping it at 150 °C in high vacuum overnight. The DPP2-HHTP-COF features a type VI isotherm with a steep nitrogen uptake at about p/p_0 = 0.25 indicating mesopore filling, and typical for a well-defined mesoporous framework structure. The Brunauer-Emmett-Teller (BET) surface area was calculated to be just above 1000 m^2g^{-1} (adsorption branch in the range of p/p_0 = 0.07-0.21). Calculation of the COF pore size distribution reveals a single pore size with a maximum at 3.3 nm, which is in good agreement with the expected open pore system of the framework.

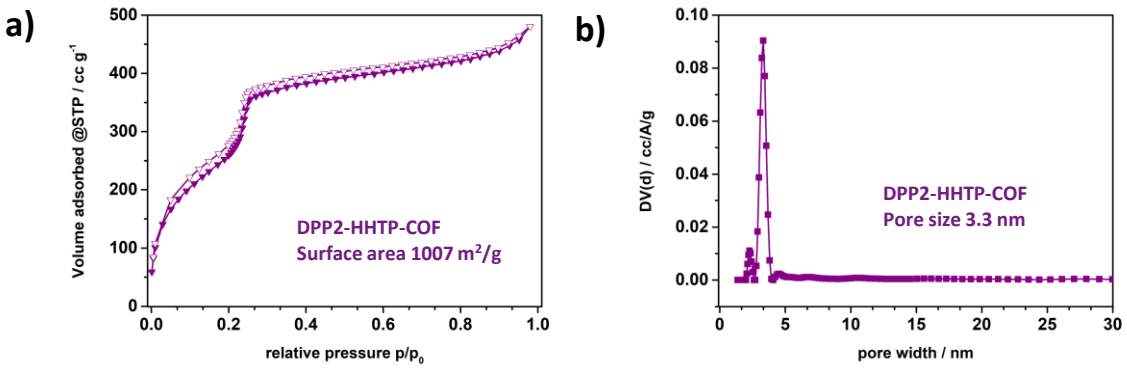

Figure 4-2: a) Sorption isotherm (full symbol: adsorption and empty symbol: desorption) of DPP2-HHTP-COF with calculated BET surface area, and b) pore size distribution of DPP2-HHTP-COF with a calculated pore size of 3.3 nm.

Thermogravimetric analysis (TGA) revealed a thermal stability under dynamic conditions of up to 350 °C. At higher temperatures, this is followed by a weight loss of around 20%, which can most likely be attributed to the loss of the solubilizing alkyl side chains, and final decomposition at 450 °C.

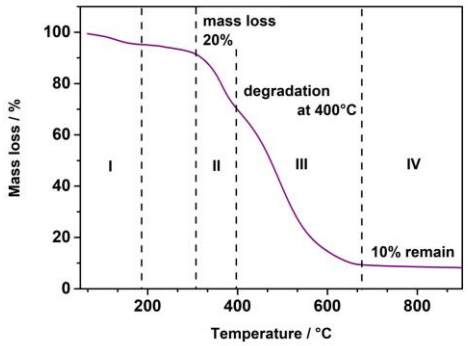

Figure 4-3: TGA data of DPP-HHTP-COF. The numbered areas illustrate the different steps of the decomposition of the material. (I) complete removal of volatile guest molecules at about 170 °C, (II) the subsequent mass loss of about 20% is proposed to relate to the loss of the solubilizing branched alkyl chains, (III) the further degradation of the framework starts at around 400 °C, (IV) the remaining amount of 10 wt% corresponds to approximately 3 mol B_2O_3, related to the sample weight.

Scanning electron microscopy (SEM) revealed that DPP2-HHTP-COF predominantly adopts a large needle-like morphology as shown in Figure 4-4a. In addition, a transmission electron microscopy (TEM) image of the framework illustrates crystalline COF domains that are highly intergrown, assembling in larger agglomerates (see Figure 4-4b).

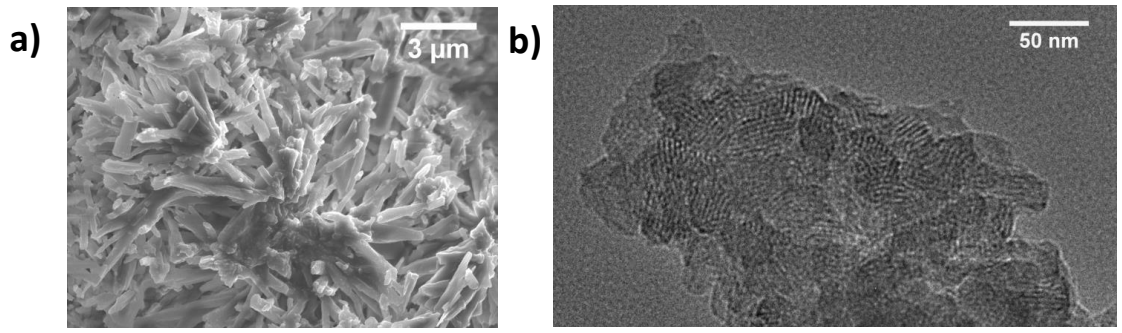

Figure 4-4: a) SEM image of DPP2-HHTP-COF showing needle-like agglomerate morphology and b) TEM image illustrating the intergrown COF crystallites exhibiting small domain sizes.

In contrast to the recently reported imine-based DPP-TAPP-COF that exhibits a relatively flexible backbone where the imine bonds can rotate out-of-plane to accommodate the sterically demanding side chains,[24] our simulations for the PXRD data

of DPP2-HHTP-COF suggest that the boronate ester linkages in DPP2-HHTP-COF enforce the formation of a planar backbone (see Figure 4-1c). This framework layout should be beneficial for promoting stacking interactions between the DPP molecules in the COF, thus leading to the enhanced crystallinity observed in the case of DPP2-HHTP-COF. Based on molecular interactions, it is likely that the planar layers are stacked in a slightly slipped fashion, as discussed in our previous report on the influence of sterically demanding side chains on the crystallite size and crystallinity of boronic acid-based benzoditiophene (BDT) COFs.[32] While Dichtel *et al.* implemented a thienoisoindigo derivative to form a kinked imine-based COF,[19] here we report the successful formation of a boronate-based crystalline framework with even larger, sterically demanding ethylhexyl groups, harnessing the favorable stacking of the DPP cores to form a well-defined kinked COF structure.

The optical characterization of bulk powder samples of DPP2-HHTP-COF is summarized in Figure 4-5. As mentioned above, this COF features a dark-purple color with a broad optical absorption ranging from the UV up to almost 700 nm (Figure 4-5a), as determined by diffuse reflectance measurements. The photoluminescence (PL) exhibits two distinct emission peaks, at around 620 nm and 680 nm, and covers a broad spectral range from the visible to near-infrared (Figure 4-5a). A time-correlated single photon counting (TCSPC) measurement of the peak emission at 620 nm is shown in Figure 4-5b, and the longest lifetime is fitted with around 5.6 ns.[33] We note, however, that the overall contribution of this decay component is small (3%) and the faster decay channels of 0.19 ns (61%) and 0.62 ns (36%) are predominant. The origin of the decay pathways cannot be determined through the TCSPC measurement and will not be further elucidated in this study. The decay at 680 nm shows very similar timescales, and a homogeneous decay across the whole spectrum can be observed in the time-resolved emission spectra (TRES) scan (see Experimental Section).

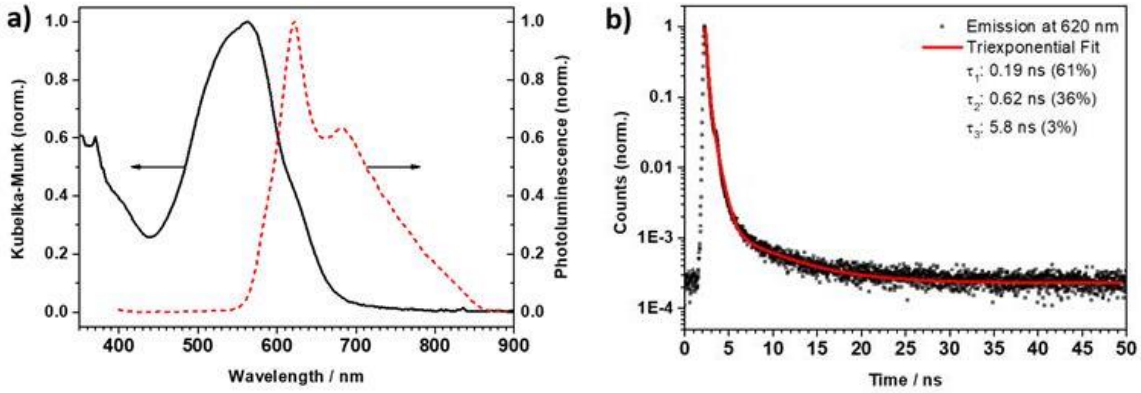

Figure 4-5: a) Absorption (black, solid) and photoluminescence (red, dashed) spectra of the DPP2-HHTP-COF. Absorption was measured through diffuse reflectance measurements and converted using the Kubelka-Munk equation. b) Time-correlated single photon counting (TCSPC) histogram (black squares), corresponding triexponential fit (solid line, red), and the respective fitted lifetimes. The percentages given with the different lifetimes correspond to the respective contribution to the overall decay intensity.

For completeness UV-vis, PL and TCSPC measurements were investigated on DPP2 and HHTP precursor (also see Experimental Section). Optical investigations including UV-Vis and PL studies on a DPP2 film revealed a red-shifted absorption as compared to monomers in solution. We attribute this red shift to the formation of well-defined stacks with *J*-type interaction along the COF molecular column.[34-36] This is further supported through the observed intensity sequence of the absorption peaks, with no oscillator strength gained by the second peak, which would be characteristic for classical *H*-aggregates.[37] We note that due to the slightly slipped stacking of the DPP2-HHTP sheets, the stack is not a *J*-aggregate in the classical Kasha picture but rather a molecular arrangement showing strong *J*-type character, which might be induced by CT interactions.[36]

To further better assign the spectral features in the emission spectra of DPP2-HHTP-COF, we first investigated the precursors both in solution and as a solid film, i.e. in its aggregated form. The measured transmission UV-Vis spectra are shown in Figure 4-6a and PL spectra can be found in Figure 4-6b. The absorption shows two distinct peaks with the largest feature at around 565 nm for DPP2 in solution (acetone, chloroform, and ethanol) and a peak at 572 nm in the solid thin film of DPP2. The overall red-shift of the film spectrum is attributed to a formation of *J*-type interactions within the molecular stacks. While the spectra of DPP2 in acetone, ethanol, and chloroform exhibit the main peak at around 580 nm, the solid film of DPP2 exhibits a main peak at 585 nm and the spectrum is red-shifted again. Furthermore, the overall

spectral shapes of the film, with the strongest peak being the first peak just above the absorption gap (in energy), supports the formation of *J*-aggregates rather than *H*-aggregates where the second peak gets promoted in classical Kasha-theory.

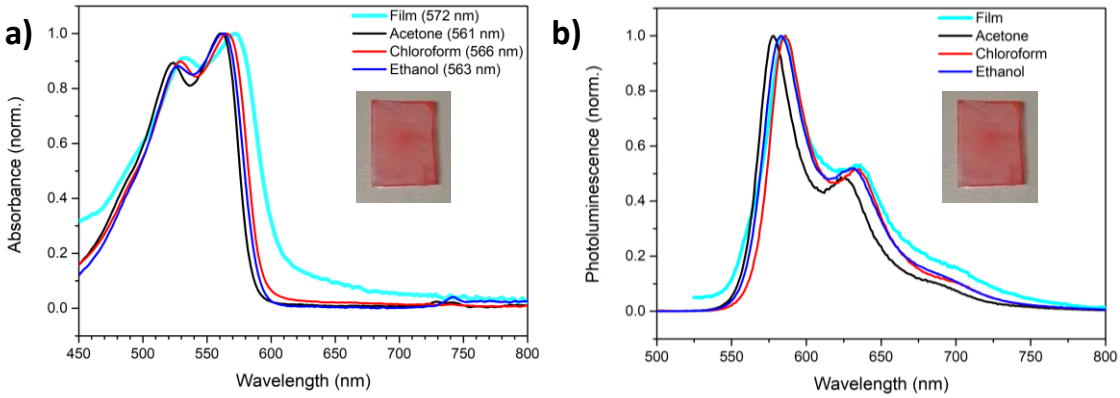

Figure 4-6: a) Transmission UV-Vis and b) photoluminescence spectra of DPP2 as precursor in solution (thin lines) and as a film (thick line). The values in the legend of a) indicate the position of the largest peak; the nature of the DPP2 precursor film is illustrated in the graphics.

Comparing crystalline and amorphous DPP2-HHTP-COF with the individual DPP2 and HHTP precursors indicates that the main emission at around 620 nm can be attributed to a DPP2 aggregate with *J*-type interaction, as in the case for neat solid DPP2, while the broad peak up to over 850 nm seems to originate from transitions generated through the COF formation.

The absorption and PL emissions of crystalline and amorphous DPP2-HHTP-COF powders are shown in Figure 4-7a and b, together with the spectra of solid DPP2 as powder. The comparison between crystalline solid precursor and COF (crystalline and amorphous) in Figure 4-7a clearly shows a strong extension of the absorption into the red for the crystalline COF. We note that in the PL Figure 4-7b the spectral difference between the DPP2 powder and the film is caused by the very different sampling volume. In the film, the emission is collected from a thin film (order of 100 nm) while in the powder, the light is fully absorbed by the DPP2 crystallites (>10 µm scale). Hence, the emission from regions inside the crystallites is self-absorbed by the outer layers and hence the first peak around the HOMO-LUMO difference is truncated. The DPP2 spectrum can be recalculated qualitatively through the UV-Vis of the DPP2 film (Figure 4-7c), however absolute values are difficult to determine due to the too large thickness of the crystallites. Since the DPP2-HHTP-COF can only be measured as a powder, we use the powder DPP2 data for the following comparison in order to have

the same sampling volume. While the amorphous DPP2-HHTP-COF exhibits one broad peak, the crystalline DPP2-HHTP-COF shows an additional peak at around 620 nm, which is also observed in the DPP2 solid, which from the film measurements show molecular stacks with *J*-type interaction. Since crystalline and amorphous COFs are synthesized in similar steps and conditions, this additional peak might be attributed to a similarly arranged stack of DPP as part of the COF framework, i.e. the 2D sheets arrange in such a way that the DPP2 linker forms *J*-type interactions across the stacked sheets. Notably, if the peak had originated from molecular DPP2 aggregates within the pore system, a much smaller framework surface area and pore size distribution should have been observed.

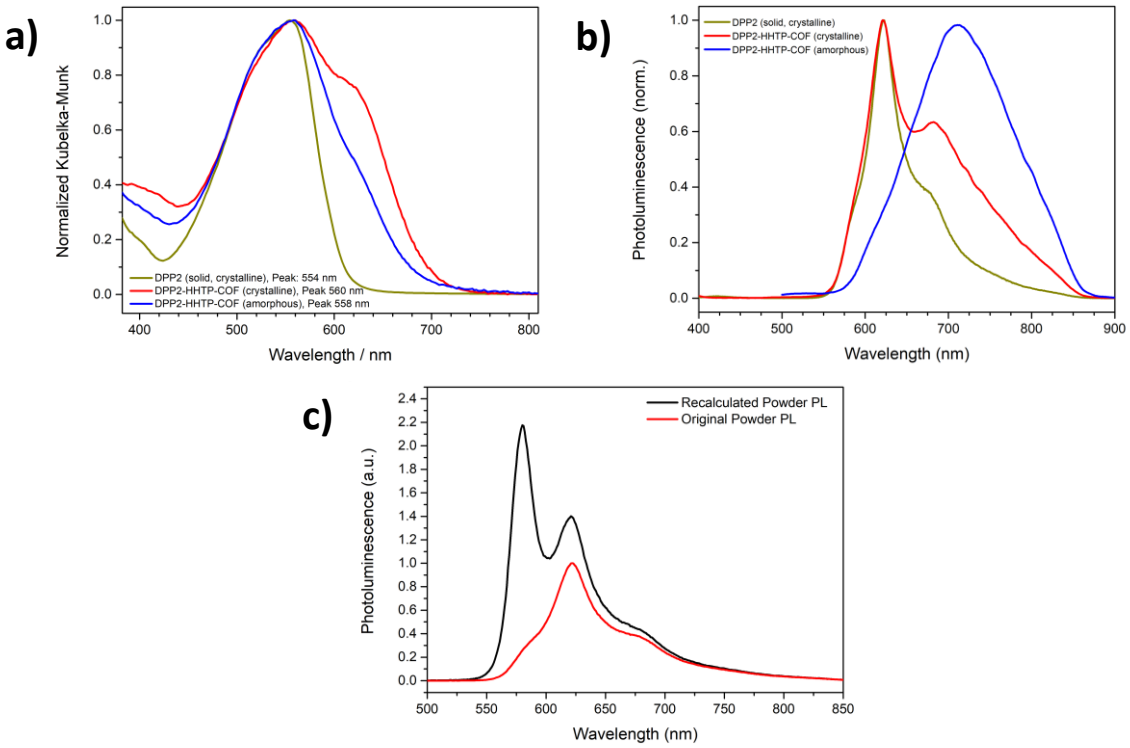

Figure 4-7: a) Diffusive reflectance absorption and b) photoluminescence spectra of solid DPP2 and DPP2-HHTP-COF (crystalline and amorphous). The values in the legend of a) indicate the position of the largest peak. c) Photoluminescence spectrum of solid DPP2 precursor as a powder (red line) and a qualitative recalculation of the emission spectrum without self-absorption (black line).

XRD measurements also show that there are no detectable amounts of residual precursor DPP2 in the sample – especially not in an amount that would generate this well-pronounced peak in the emission spectrum. For better illustration, we performed different XRD measurements on our as-synthesized materials and its precursor. For this purpose, the crystalline COF, the amorphous COF and the DPP2 precursor were placed

on a silicon wafer and measured on a Bruker D8 diffractometer in reflection mode, respectively (start: 1.6°2θ; end: 30° 2θ; step: 0.05 °; scan speed: 3 sec/step). The direct comparison between all three components is shown in Figure 4-8 with logarithmic scale to visualize reflections even in high 2θ regions. Compared to the DPP2 precursor data, the crystalline DPP2-HHTP-COF material is free of even small traces of (crystalline) impurities of the precursor. In addition, the amorphous material also does not correspond to the reflections of the DPP2 precursor.

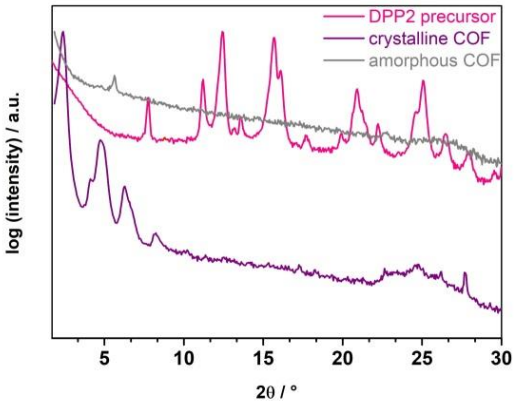

Figure 4-8: PXRD measurements of crystalline DPP2-HHTP-COF (purple), amorphous DPP2-HHTP-COF (grey) and aggregated DPP2 solid precursor (pink); the amorphous phase shows no significant agreement with the crystalline material and the precursor, respectively. Please note the logarithmic scale of the intensity axis.

Concerning aggregation behavior, we also figured out that the slightly slipped stacking arrangement of the COF will most likely not result in *J*-aggregates as in Kasha's picture but rather in molecular stacks with *J*-type interaction when taking charge transfer into account as by Hestand and Spano.[36]

We note that in a slip stack assembly, two displacements are possible; along the short and the long axis of the dye as sketched in Figure 4-9. According to Hestand & Spano, small shifts of about 1.4 Å along either short or long axis of the building block can result in a *J*-type interaction in perylene aggregates (as compared to around 5.5 Å shift along the long axis required for a Kasha *J*-aggregate).

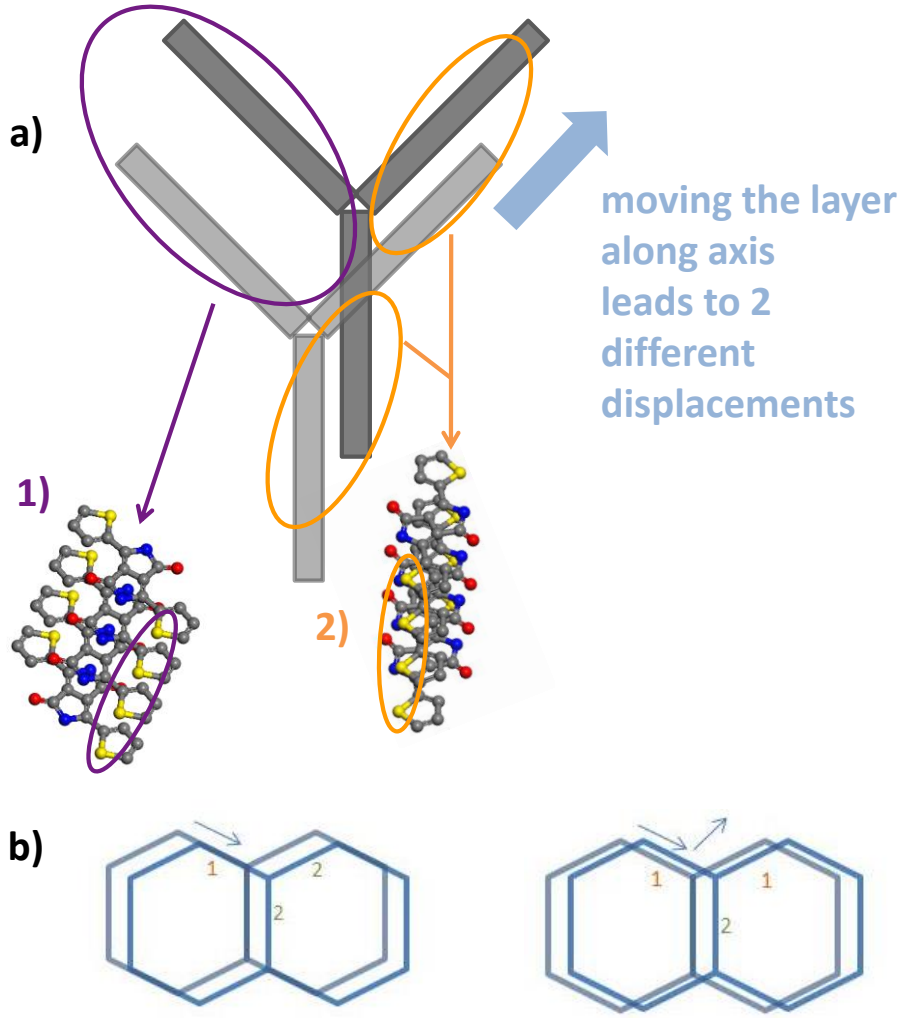

Figure 4-9: a) Fragment of the hexagonal framework to illustrate possible displacement in a hexagonal pore. Linker molecules are represented and simplified by grey rectangles while dark and bright shading illustrates to neighboring layers. This results in two different DPP aggregation types regarding the position of the sulfur atoms: 1) sulfur placed in front of the previous atom, i.e. displacement along short axis of linker molecule (purple); 2) sulfur located next to the atom of the adjacent layer, i.e. displacement along long axis of linker molecule (orange). b) Two possible layer-to-layer offsets of the overall hexagonal pattern, showing that, in any case, there are always two different displacements yielding two well-defined aggregation types 1 and 2.

Assuming the requirement of similar displacements in our COF system, i.e. of around 1.4 Å, we simulated a corresponding slip-stack model with $\alpha = 68°$. The simulated X-ray diffraction pattern refined for line broadening due to small COF domains could, within the limits, successfully reproduce the experimental XRD pattern (see Figure 4-10) and therefore leads to a consistent interpretation concerning the correlation between structural features and spectroscopic signatures in the COF. Notably, PXRD was refined for line broadening assuming spherical COF crystallites of 30 nm in size according to the TEM analysis.

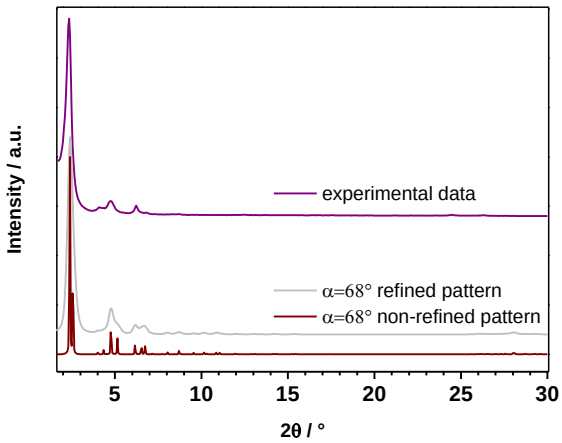

Figure 4-10: Experimental powder XRD data of the DPP2-HHTP-COF (purple). Simulated XRD pattern for the *P1* unit cell with parameters as those given in the Experimental Section, except of alpha which is set to 68° (deep red), with the patterns refined to a crystal diameter of 30 nm (grey).

The conductivity of the DPP2-HHTP-COF was determined on a compressed powder pellet, using the architecture of a four-point probe, also called the van der Pauw measurement technique. In these measurements, based on the Hall effect several material parameters can be determined ultimately yielding the electric conductivity, which is an intriguing parameter to evaluate with regards to the well-aligned photoactive dyes. The as-synthesized bulk material was finely grounded manually and pressed into a pellet shape with 10 mm diameter by applying different pressures (for more details see Experimental Section).

During this procedure, the fundamental characteristics of the DPP2-HHTP-COF structure, mainly crystallinity could be preserved and structural changes could not be detected by PXRD (see Figure 4-11). The slightly lower crystallinity compared to the as-synthesized powder is attributed to the effect of the applied pressure. To evaluate the impact of crystallinity on the electrical conductivity, van der Pauw measurements were performed and the electrical conductivity was determined for amorphous DPP2-HHTP-COF powder. For this purpose, DPP2 and HHTP were allowed to react under reaction conditions yielding an amorphous polymer by changing solvents and reaction time (synthesis conditions see Experimental Section). Also, the amorphous COFs were treated with diverse pressures and no higher crystallinity could be observed.

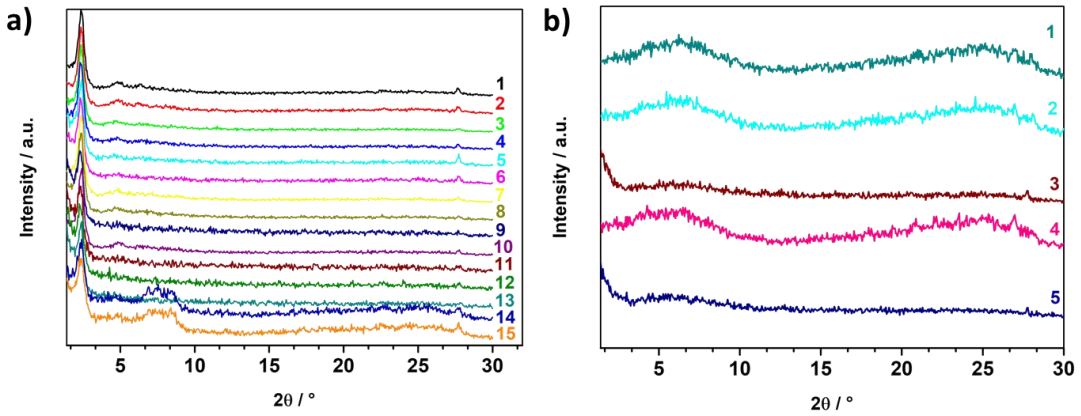

Figure 4-11: XRD measurements for a) crystalline pellets of DPP2-HHTP-COF and b) amorphous pellets of DPP2-HHTP-COF (see Table 4-1).

Table 4-1: Overview of the different materials prepared for subsequent Hall measurements.

Sample name	Sample number	Applied pressure / GPa	Pellet thickness / µm
Crystalline DPP2-HHTP-COF pellet	1	0.75	240
	2	0.75	260
	3	0.70	190
	4	0.80	250
	5	0.80	70
	6	0.75	140
	7	0.90	190
	8	0.90	120
	9	1.20	120
	10	1.20	320
	11	1.20	150
	12	1.15	180
	13	1.15	160
	14	0.90	130
	15	1.15	220
Amorphous DPP2-HHTP-COF pellet	1	1.20	130
	2	1.20	130
	3	1.20	410
	4	1.25	320
	5	1.20	180

Moreover, several batches of the DPP2-HHTP-COF pressed pellets were measured in order to get a representative averaged electrical conductivity value. For the crystalline DPP2-HHTP-COF we measured conductivities up to 2.2×10^{-6} Scm^{-1} (for more details see Experimental Section). This is one order of magnitude higher than reports for other

boronate ester-based COFs in the literature.[38] The amorphous samples exhibited conductivities of around 2×10^{-7} Scm^{-1}, one order of magnitude smaller than the peak value for the crystalline pellets, but showing less variation across different samples.

Comparing the values obtained for the crystalline and amorphous pellets indicates that the conductivity of the material is limited by several parameters. Grain boundaries between different domains in the crystalline COF would be expected to represent barriers for conductivity. Hence, the bulk conductivity will depend on the orientation and number of grain boundaries in the current path. In the van der Pauw geometry conductivity is measured within the pellet plane. In the DPP2-HHTP-COF, charge transport most likely occurs along the molecular stacks and the largest conductivity is measured at 2.2×10^{-6} Scm^{-1}. Here, the overall measurement strongly depends on the spontaneous organization of the single crystallites between the contacts, which leads to the strong difference in conductivity values, which are shown in the Experimental Section. Here, in the case of the crystallites being oriented with their COF-stacking axis along the electrical conduction channel, conductivity is much larger than in the case where their stacking direction is perpendicular to the direct line between the contacts, leading to reduced transport and values of around 10^{-8} Scm^{-1}. In contrast, in the amorphous powder there is no preferential direction of charge transport. Therefore the overall measurement path across different domains in the crystalline COF can be compared to one large amorphous conduction channel in the amorphous material. This results in very similar values around 10^{-7} Scm^{-1} across different samples of the latter, which are generally smaller than the peak value achieved in crystalline samples (also illustrated in the Experimental Section). The conductivity of the neat precursor molecular building blocks, which were also prepared as pellets and measured as described above, reaching values around 1×10^{-8} Scm^{-1}, was significantly below the peak value of the condensed network of the corresponding DPP2-HHTP-COF. This finding underscores the importance of assembling the building blocks in a π-stacked framework and its orientation in order to achieve substantial conductivity.

4.3 Conclusion

In this study, we have demonstrated the successful implementation of DPP chromophores and HHTP into a boronate ester-linked COF exhibiting a highly porous and crystalline structure. We attribute this to the rather rigid and flat boronate ester bond

inducing favorable stacking interactions between the adjacent COF layers. Even rather short reaction times result in a very crystalline framework with strong absorption across the visible spectrum. The longest singlet lifetime component of 5.6 ns is attributed to the high crystallinity and efficient electronic coupling of the 2D COF layers, resulting in efficient stabilisation of the excitons across the DPP stacks.

Furthermore, this is the first report on macroscopic conductivity values in boronate ester-based framework powders, obtained with four-point probe van der Pauw measurements. While maintaining the structural characteristics of the material, we were able to produce pellets of the bulk material that showed conductivities of up to 2.2×10^{-6} Scm^{-1}. This is the highest value for boronate ester-based COF bulk materials reported to date.

The spectroscopic data together with the relatively high conductivity values hold promise for DPP2-HHTP-COF and related COFs concerning future applications in solar cells or as conductive layers, e.g. in transistor devices. Further investigations regarding the detailed pathways of charge conduction in these intriguing frameworks are underway in our laboratories.

4.4 Experimental Section

All applied materials (if not otherwise noted) were purchased from Aldrich or TCI in the common purities purum and puriss. All materials were used without further purification if not further noticed.

Powder X-ray diffraction (PXRD) measurements were performed on a Bruker D8 Discover diffractometer with Ni filtered Kα radiation (λ = 1.54060 Å) and a position-sensitive detector (LynxEye) in reflection mode. For high resolution measurements, the as-synthesized COF material was placed on a silicon wafer and the measurement was carried out by applying a low scan speed.

Scanning electron microscopy (SEM) was performed on a FEI Helios G3 UC instrument at 2 kV. For this purpose, the samples were put on an adhesive graphite film and sputtered with carbon with a BALTEC MED 020 Coating System.

Transmission electron microscopy (TEM) data were obtained with a Tecnai G2 20 S-Twin instrument at an acceleration voltage of 200 kV.

Nitrogen sorption was measured using a Quantachrome AUTOSORB 1 station at 77.3 K after degassing the sample for at least 12 h under vacuum at 150 °C. The Brunauer–

Emmett–Teller (BET) surface area was calculated from the adsorption branch in the range of p/p_0 = 0.07–0.21. Pore sizes were calculated with a QSDFT adsorption model of N_2 on carbon (cylindrical, adsorption branch).

Thermogravimetric (TG) measurements were performed in a stream of synthetic air (25 ml/min) on a Netzsch STA 440 C TG/DSC instrument. The measurements were carried out with a heating rate of 10 °C/min, and a temperature range from 30 °C to 900 °C was covered.

^{1}H/^{13}C NMR solution spectra were recorded on a Bruker Avance III-400 MHz and a Bruker Avance III-270 MHz spectrometer. For this purpose, 4 mg of material were dissolved in characteristic deuterated solvents, respectively. Chemical shifts are reported in parts per million (ppm) with respect to residual $CHCl_3$ (0 ppm for ^{1}H and 77 ppm for ^{13}C) as the internal standard. Signal multiplicities are denoted as s (singlet), d (doublet), t (triplet), and m (multiplet).

UV-Vis spectra were recorded using a Perkin-Elmer Lambda 1050 spectrometer equipped with a 150 mm integrating sphere. The spectra were collected with a Praying Mantis (Harrick) accessory and were referenced to barium sulfate powder as white standard. The powder sample was mixed with a small amount of the reference and measured in diffuse reflectance mode.

The **IR-Spectra** were recorded on a Perkin Elmer Spectrum BX FT-IR instrument in combination with an attenuated total reflection (ATR) accessory comprising an ATR diamond crystal. All samples were measured at room temperature without further preparation.

Photoluminescence (PL) measurements were performed using a PicoQuant FluoTime300 time-correlated single photon counting (TCSPC) setup.

Hall conductivity measurements were carried out on an ECOPIA HMS 3000 apparatus using a magnetic field of 0.55 T in the van der Pauw geometry.

4.4.1 Syntheses

4.4.1.1 Synthesis of Precursor DPP2

Compounds $(Ethex)_2$-DPP[39] and $(Bpin)_2$-DPP[40] were synthesized according to literature procedures and structural identity was proven by comparing ^{1}H-NMR data to literature reports.

Synthesis of racemic 2,5-bis(2-ethylhexyl)-3,6-di(thiophen-2-yl)-2,5-dihydropyrrolo[3,4-c]pyrrole-1,4-dione (Ethex)$_2$-DPP)[39]

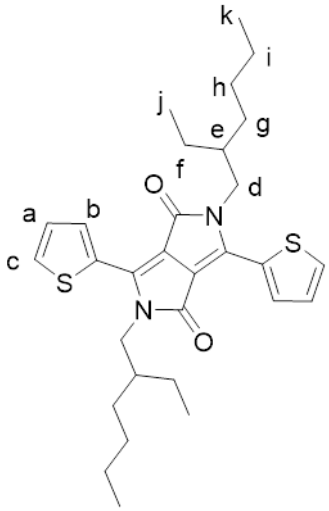

Molecular Weight: 524,78

In a three-necked flask, 3,6-di(thiophen-2-yl)-2,5-dihydropyrrolo[3,4-c]pyrrole-1,4-dione (**DPP**) (2.52 g, 8.4 mmol, 1 eq.) and potassium carbonate (6.6 g, 48 mmol, 3 eq.) were dissolved in DMF (120 mL). The mixture was heated to 120 °C for one hour and racemic 2-ethylhexyl bromide (8.5 mL, 48 mmol, 3 eq.) was added dropwise. The reaction mixture was then stirred for 48 hours at 120 °C. The temperature was increased to 150 °C for the last four hours. After cooling down, the solvent was reduced *in vacuo*. The dark purple residue was then dissolved in CH_2Cl_2 (300 mL) and washed with water (3 × 150 mL) and saturated brine (2 × 150 mL). The combined aqueous phases were extracted with CH_2Cl_2 (2 × 100 mL). The organic phases were dried over Na_2SO_4 and the solvent was removed under reduced pressure. The crude product was subsequently purified by column chromatography on silica gel (CH_2Cl_2 / pentane 50:50, later increased to 80:20) to afford the product as a dark red powder (1.26 g, 2.40 mmol, 30 %).

^{1}H NMR (400 MHz, $CDCl_3$, rt): δ = 8.89 (dd, ^3J = 3.9, ^4J = 1.2 Hz, 2H, H_c), 7.63 (dd, ^3J = 5.0, ^4J = 1.2 Hz, 2H, H_b), 7.27 (dd, ^3J = 5.0, 3.9 Hz, 2H, H_a), 4.08-3.97 (m, 4H, H_d), 1.90-1.79 (m, 2H, H_e), 1.40-1.18 (m, 16H, $H_{f\text{-}i}$), 0.90-0.82 (m, 12H, $H_{j\text{-}k}$) ppm.

Synthesis of 2,5-bis(2-ethylhexyl)-3,6-bis(5-(4,4,5,5-tetramethyl-1,3,2-dioxaborolan-2-yl)thiophen-2-yl)-2,5-dihydropyrrolo[3,4-c]pyrrole-1,4-dione $(Bpin)_2$-DPP)[40]

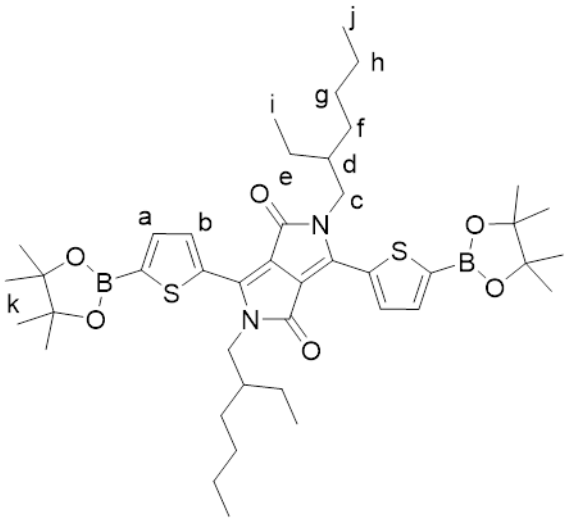

Molecular Weight: 776,71

$(EtHex)_2$-DPP (286 mg, 0.545 mmol, 1 eq.) was dissolved in THF (40 mL) in a Schlenk flask under inert gas. The mixture was cooled down to −78 °C and LDA solution (0.375 M in THF, 2.18 mL, 0.818 mmol, 1.5 eq.) was added dropwise. After stirring for two hours at the low temperature, isopropoxyboronic acid pinacol ester (0.165 mL, 0.818 mmol, 1.5 eq.) was added. Afterwards, the solution was allowed to warm up to room temperature and stirred for another two hours. The mixture was then poured into ice water (100 mL) followed by extraction with CH_2Cl_2 (2 × 100 mL) and $CHCl_3$ (2 × 100 mL). The combined organic phases were washed with saturated $NaHCO_3$ solution (2 × 100 mL) and brine (2 × 100 mL) and dried over Na_2SO_4. The solvents were removed under reduced pressure and the crude product was washed with hexane (5 mL) to yield the desired product as a red solid in sufficient purity (220 mg, 0.28 mmol, 52 %).

^{1}H NMR (400 MHz, $CDCl_3$, rt): δ = 8.92 (d, ^{3}J = 3.9 Hz, 2 H, H_a), 7.71 (d, ^{3}J = 3.9 Hz, 2H, H_b), 4.13-4.00 (m, 4H, H_c),1.88-1.80 (m, 2H, H_d), 1.40-1.18 (m, 16 H, H_{e-h}), 1.37 (s, 24 H, H_k) 0.90-0.82 (m, 12H, H_{i-j}) ppm.

Synthesis of ((2,5-bis(2-ethylhexyl)-3,6-dioxo-2,3,5,6-tetrahydropyrrolo[3,4-c]-pyrrole-1,4-diyl)bis(thiophene-5,2-diyl))diboronic acid (DPP2)

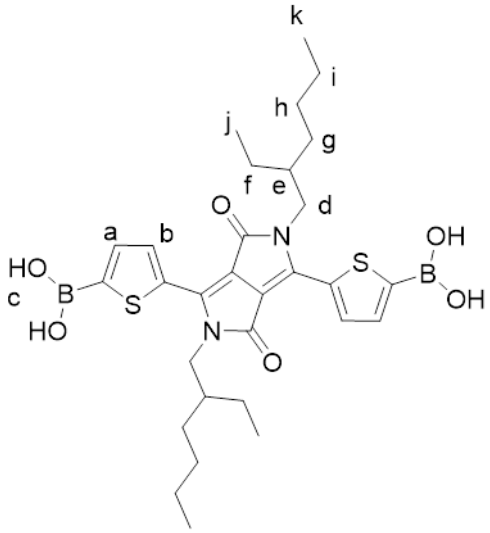

Molecular Weight: 612,41

$(Bpin)_2$-DPP (57.3 mg, 73.4 μmol, 1 eq.) was dissolved in a small amount of THF (0.5 mL). Water (2.5 mL) was added and the solution was stirred for two hours. Then, 6-molar hydrochloric acid (2.5 mL) was added and the mixture was stirred overnight at room temperature. Water (25 mL) was added and stirring was continued for two hours whereupon a dark red precipitate emerged while the solution became clear. The precipitate was filtered and washed with CH_2Cl_2 (2 × 5 mL) to afford the title compound as a shining red solid which was dried for eight hours under high vacuum (34.4 mg, 56.2 μmol, 77 %).

IR: 3358 (s), 2955 (w), 2930 (w), 2194 (vw), 2096 (vw), 2054 (vw), 1601 (vs), 1581 (vs), 1512 (m), 1443 (m), 1408 (s), 1368 (m), 1324 (vs), 1288 (m), 1254 (w), 1222 (w), 1125 (s), 1083 (s), 1032 (m), 919 (vw), 817 (m), 742 (m), 711 (m), 683 (w), 657 (w).

^{1}H NMR (400 MHz, THF-d_6, rt): δ = 9.11 (d, ^{3}J = 3.8 Hz, 2H, H_a), 7.67 (d, ^{3}J = 3.8 Hz, 2H, H_b), 7.67 (s, 4H, H_c), 4.16-4.05 (m, 4H, H_d), 1.97-1.89 (m, 2H, H_e), 1.42-1.22 (m, 16H, $H_{f\text{-}i}$), 0.92-0.84 (m, 12H, $H_{j\text{-}k}$) ppm.

^{13}C NMR (100 MHz, DMSO-d_6, rt): δ = 160.82, 139.83, 136.37, 135.30, 133.74, 107.26, 67.04, 30.44, 29.59, 27.76, 25.15, 23.22, 22.37, 13.78, 10.29 ppm.

4.4.1.2 Synthesis of DPP2-HHTP-COF

Extensive screening of the reaction conditions led to the following optimized synthesis procedure for DPP2-HHTP-COF. We note that the high concentration in the reaction mixture is crucial for obtaining high yield and high crystallinity. Furthermore, the framework also forms by allowing for increased reaction time (160 hours) with the adverse effect of reduced crystallinity (DPP2-HHTP-COF amorphous).

A 10 mL Schott Duran glass was charged with DPP2 (25.02 mg, 0.153 mmol, 4 eq.) and 2,3,6,7,10,11-hexahydroxytriphenylene (HHTP) (11.8 mg, 0.039 mmol, 1 eq.). The solvent mixture consisting of mesitylene and dioxane at the ratio 1:1 was added to the powder (1 mL). This reaction mixture was sonicated for one minute to achieve a homogenous dispersion and further heated at 100 °C for 24 hours. The reddish purple solid was isolated by filtration and washed with dry acetone (2 × 5 mL). Finally, DPP2-HHTP-COF was obtained as dark purple powder (73%).

Furthermore, the amorphous DPP2-HHTP-COF was synthesized in a procedure similar to that for the crystalline material but with another solvent ratio and using an increased reaction time. To the same weights of the precursors, a solvent mixture of mesitylene and ethanol in the ratio of 1.5:1 was added (1 mL) and the reaction mixture was placed at 120 °C for 160 hours.

4.4.2 Characterization Details

4.4.2.1 Simulation of DPP2-HHTP-COF Crystal Structure

Based on the symmetry of the applied building blocks, the final 2D COF structure can be approximately predicted and then confirmed with experimental powder X-ray diffraction (PXRD) data. The simulation was carried out with the visualization environment of *Materials Studio software 4.4*, and the geometry of the two-dimensional layers was optimized with calculations using forcite methods. Based on the geometry of the precursor molecules, the repeating unit was constructed in a unit cell of the *P1* space group. The repeating fragments were placed in the triclinic unit cell and connected to each other, resulting in the complete unit cell. The geometry of the DPP2-HHTP-COF layer was optimized in the unit cell using the Dreiding forcefield and the QEq correction for weak interactions. Pawley refinements resulted in good values fitting our experimental PXRD data.

Table 4-2: Refined crystal data.

	DPP2-HHTP-COF
Chemical formula	$C_{11}H_{126}O_{18}B_6N_6S_6$
Formula weight	2269.64 g/mol
Crystal system	triclinic
Space group	*P*1 (1)
Unit cell dimension	a = 43.82 Å b = 44.57 Å c = 3.48 Å α = 89.79° β = 89.53° γ = 122.76°
Cell volume	5711.01 $Å^3$

Table 4-3: Atomic parameters for DPP2-HHTP-COF.

Atom	**Atom label**	**x/a**	**y/b**	**z/c**
N1	N	0.47822	0.44153	0.50000
C2	C	0.51432	0.46933	0.50000
C3	C	0.54376	0.46256	0.50000
S4	S	0.53744	0.42101	0.50000
C5	C	0.51747	0.50174	0.50000
C6	C	0.45834	0.45970	0.50000
O7	O	0.42581	0.44320	0.50000
C8	C	0.57845	0.48875	0.50000
C9	C	0.60049	0.47518	0.50000
C10	C	0.58188	0.43912	0.50000
B11	B	0.59987	0.41656	0.50000
O12	O	0.63787	0.43160	0.50000
O13	O	0.58032	0.37827	0.50000
C14	C	0.63990	0.40125	0.50000
C15	C	0.60763	0.37121	0.50000
C16	C	0.60280	0.33675	0.50000
C17	C	0.67072	0.40023	0.50000
C18	C	0.66893	0.36701	0.50000
C19	C	0.63494	0.33539	0.50000
H20	H	0.42478	0.68696	0.50000
H21	H	0.49348	0.86341	0.50000
H22	H	0.06807	0.58547	0.50000
H23	H	0.27132	0.69699	0.50000
N24	N	0.55847	0.03669	0.50000
C25	C	0.53067	0.04499	0.50000
C26	C	0.53744	0.08121	0.50000
S27	S	0.57899	0.11643	0.50000

C28	C	0.49826	0.01573	0.50000
C29	C	0.54030	0.99864	0.50000
O30	O	0.55680	0.98261	0.50000
C31	C	0.51125	0.08970	0.50000
C32	C	0.52482	0.12531	0.50000
C33	C	0.56088	0.14275	0.50000
B34	B	0.58344	0.18331	0.50000
O35	O	0.56840	0.20627	0.50000
O36	O	0.62173	0.20205	0.50000
C37	C	0.59875	0.23865	0.50000
C38	C	0.62879	0.23642	0.50000
C39	C	0.66325	0.26604	0.50000
C40	C	0.59977	0.27048	0.50000
C41	C	0.63299	0.30192	0.50000
C42	C	0.66461	0.29954	0.50000
H43	H	0.31304	0.73783	0.50000
H44	H	0.13659	0.63008	0.50000
H45	H	0.41453	0.48260	0.50000
H46	H	0.30301	0.57433	0.50000
C47	C	0.40260	0.93780	0.50000
C48	C	0.37678	0.89805	0.50000
C49	C	0.33809	0.88858	0.50000
C50	C	0.31303	0.84866	0.50000
C51	C	0.27423	0.83882	0.50000
C52	C	0.24305	0.80106	0.50000
C53	C	0.37013	0.86026	0.50000
C54	C	0.33149	0.83090	0.50000
H55	H	0.39250	0.94778	0.26106
H56	H	0.39032	0.94214	0.76346
H57	H	0.37678	0.89805	0.82268
H58	H	0.33282	0.90033	0.23793
H59	H	0.33252	0.89993	0.76346
H60	H	0.31839	0.83695	0.76175
H61	H	0.31789	0.83676	0.23654
H62	H	0.27046	0.85261	0.24657
H63	H	0.26850	0.85004	0.76346
H64	H	0.24666	0.78547	0.73554
H65	H	0.24168	0.78823	0.21549
H66	H	0.21772	0.80152	0.54897
H67	H	0.38344	0.85675	0.75950
H68	H	0.38237	0.85587	0.23654
H69	H	0.31958	0.82931	0.20914
H70	H	0.31644	0.83681	0.72266
H71	H	0.32984	0.80483	0.56820
N72	N	0.96331	0.52178	0.50000

C73	C	0.95501	0.48568	0.50000
C74	C	0.91879	0.45624	0.50000
S75	S	0.88357	0.46256	0.50000
C76	C	0.98427	0.48253	0.50000
C77	C	0.00136	0.54166	0.50000
O78	O	0.01739	0.57419	0.50000
C79	C	0.91030	0.42155	0.50000
C80	C	0.87469	0.39951	0.50000
C81	C	0.85725	0.41812	0.50000
B82	B	0.81669	0.40013	0.50000
O83	O	0.79373	0.36213	0.50000
O84	O	0.79795	0.41968	0.50000
C85	C	0.76135	0.36010	0.50000
C86	C	0.76358	0.39237	0.50000
C87	C	0.73396	0.39720	0.50000
C88	C	0.72952	0.32928	0.50000
C89	C	0.69808	0.33107	0.50000
C90	C	0.70046	0.36506	0.50000
H91	H	0.26217	0.57522	0.50000
H92	H	0.36992	0.50652	0.50000
H93	H	0.51740	0.93193	0.50000
H94	H	0.42567	0.72868	0.50000
C95	C	0.06220	0.46479	0.50000
C96	C	0.10195	0.47874	0.50000
C97	C	0.11142	0.44951	0.50000
C98	C	0.15134	0.46437	0.50000
C99	C	0.16118	0.43541	0.50000
C100	C	0.19894	0.44199	0.50000
C101	C	0.13974	0.50987	0.50000
C102	C	0.16910	0.50059	0.50000
H103	H	0.05222	0.44472	0.26106
H104	H	0.05786	0.44817	0.76346
H105	H	0.10195	0.47874	0.82268
H106	H	0.09967	0.43249	0.23793
H107	H	0.10007	0.43259	0.76346
H108	H	0.16305	0.48144	0.76175
H109	H	0.16324	0.48112	0.23654
H110	H	0.14739	0.41785	0.24657
H111	H	0.14996	0.41846	0.76346
H112	H	0.21453	0.46119	0.73554
H113	H	0.21177	0.45345	0.21549
H114	H	0.19848	0.41619	0.54897
H115	H	0.14325	0.52669	0.75950
H116	H	0.14413	0.52651	0.23654
H117	H	0.17069	0.49027	0.20914

H118	H	0.16319	0.47963	0.72266
H119	H	0.19517	0.52500	0.56820
N120	N	0.52178	0.55847	0.50000
C121	C	0.48568	0.53067	0.50000
C122	C	0.45624	0.53744	0.50000
S123	S	0.46256	0.57899	0.50000
C124	C	0.48253	0.49826	0.50000
C125	C	0.54166	0.54030	0.50000
O126	O	0.57419	0.55680	0.50000
C127	C	0.42155	0.51125	0.50000
C128	C	0.39951	0.52482	0.50000
C129	C	0.41812	0.56088	0.50000
B130	B	0.40013	0.58344	0.50000
O131	O	0.36213	0.56840	0.50000
O132	O	0.41968	0.62173	0.50000
C133	C	0.36010	0.59875	0.50000
C134	C	0.39237	0.62879	0.50000
C135	C	0.39720	0.66325	0.50000
C136	C	0.32928	0.59977	0.50000
C137	C	0.33107	0.63299	0.50000
C138	C	0.36506	0.66461	0.50000
H139	H	0.57522	0.31304	0.50000
H140	H	0.50652	0.13659	0.50000
H141	H	0.93193	0.41453	0.50000
H142	H	0.72868	0.30301	0.50000
C143	C	0.46479	0.40260	0.50000
C144	C	0.47874	0.37678	0.50000
C145	C	0.44951	0.33809	0.50000
C146	C	0.46437	0.31303	0.50000
C147	C	0.43541	0.27423	0.50000
C148	C	0.44199	0.24305	0.50000
C149	C	0.50987	0.37013	0.50000
C150	C	0.50059	0.33149	0.50000
H151	H	0.44472	0.39250	0.26106
H152	H	0.44817	0.39032	0.76346
H153	H	0.47874	0.37678	0.82268
H154	H	0.43249	0.33282	0.23793
H155	H	0.43259	0.33252	0.76346
H156	H	0.48144	0.31839	0.76175
H157	H	0.48112	0.31789	0.23654
H158	H	0.41785	0.27046	0.24657
H159	H	0.41846	0.26850	0.76346
H160	H	0.46119	0.24666	0.73554
H161	H	0.45345	0.24168	0.21549
H162	H	0.41619	0.21772	0.54897

H163	H	0.52669	0.38344	0.75950
H164	H	0.52651	0.38237	0.23654
H165	H	0.49027	0.31958	0.20914
H166	H	0.47963	0.31644	0.72266
H167	H	0.52500	0.32984	0.56820
N168	N	0.44153	0.96331	0.50000
C169	C	0.46933	0.95501	0.50000
C170	C	0.46256	0.91879	0.50000
S171	S	0.42101	0.88357	0.50000
C172	C	0.50174	0.98427	0.50000
C173	C	0.45970	0.00136	0.50000
O174	O	0.44320	0.01739	0.50000
C175	C	0.48875	0.91030	0.50000
C176	C	0.47518	0.87469	0.50000
C177	C	0.43912	0.85725	0.50000
B178	B	0.41656	0.81669	0.50000
O179	O	0.43160	0.79373	0.50000
O180	O	0.37827	0.79795	0.50000
C181	C	0.40125	0.76135	0.50000
C182	C	0.37121	0.76358	0.50000
C183	C	0.33675	0.73396	0.50000
C184	C	0.40023	0.72952	0.50000
C185	C	0.36701	0.69808	0.50000
C186	C	0.33539	0.70046	0.50000
H187	H	0.68696	0.26217	0.50000
H188	H	0.86341	0.36992	0.50000
H189	H	0.58547	0.51740	0.50000
H190	H	0.69699	0.42567	0.50000
C191	C	0.59740	0.06220	0.50000
C192	C	0.62322	0.10195	0.50000
C193	C	0.66191	0.11142	0.50000
C194	C	0.68697	0.15134	0.50000
C195	C	0.72577	0.16118	0.50000
C196	C	0.75695	0.19894	0.50000
C197	C	0.62987	0.13974	0.50000
C198	C	0.66851	0.16910	0.50000
H199	H	0.60750	0.05222	0.26106
H200	H	0.60968	0.05786	0.76346
H201	H	0.62322	0.10195	0.82268
H202	H	0.66718	0.09967	0.23793
H203	H	0.66748	0.10007	0.76346
H204	H	0.68161	0.16305	0.76175
H205	H	0.68211	0.16324	0.23654
H206	H	0.72954	0.14739	0.24657
H207	H	0.73150	0.14996	0.76346

H208	H	0.75334	0.21453	0.73554
H209	H	0.75832	0.21177	0.21549
H210	H	0.78228	0.19848	0.54897
H211	H	0.61656	0.14325	0.75950
H212	H	0.61763	0.14413	0.23654
H213	H	0.68042	0.17069	0.20914
H214	H	0.68356	0.16319	0.72266
H215	H	0.67016	0.19517	0.56820
N216	N	0.03669	0.47822	0.50000
C217	C	0.04499	0.51432	0.50000
C218	C	0.08121	0.54376	0.50000
S219	S	0.11643	0.53744	0.50000
C220	C	0.01573	0.51747	0.50000
C221	C	0.99864	0.45834	0.50000
O222	O	0.98261	0.42581	0.50000
C223	C	0.08970	0.57845	0.50000
C224	C	0.12531	0.60049	0.50000
C225	C	0.14275	0.58188	0.50000
B226	B	0.18331	0.59987	0.50000
O227	O	0.20627	0.63787	0.50000
O228	O	0.20205	0.58032	0.50000
C229	C	0.23865	0.63990	0.50000
C230	C	0.23642	0.60763	0.50000
C231	C	0.26604	0.60280	0.50000
C232	C	0.27048	0.67072	0.50000
C233	C	0.30192	0.66893	0.50000
C234	C	0.29954	0.63494	0.50000
H235	H	0.73783	0.42478	0.50000
H236	H	0.63008	0.49348	0.50000
H237	H	0.48260	0.06807	0.50000
H238	H	0.57433	0.27132	0.50000
C239	C	0.93780	0.53521	0.50000
C240	C	0.89805	0.52126	0.50000
C241	C	0.88858	0.55049	0.50000
C242	C	0.84866	0.53563	0.50000
C243	C	0.83882	0.56459	0.50000
C244	C	0.80106	0.55801	0.50000
C245	C	0.86026	0.49013	0.50000
C246	C	0.83090	0.49941	0.50000
H247	H	0.94778	0.55528	0.26106
H248	H	0.94214	0.55183	0.76346
H249	H	0.89805	0.52126	0.82268
H250	H	0.90033	0.56751	0.23793
H251	H	0.89993	0.56741	0.76346
H252	H	0.83695	0.51856	0.76175

H253	H	0.83676	0.51888	0.23654
H254	H	0.85261	0.58215	0.24657
H255	H	0.85004	0.58154	0.76346
H256	H	0.78547	0.53881	0.73554
H257	H	0.78823	0.54655	0.21549
H258	H	0.80152	0.58381	0.54897
H259	H	0.85675	0.47331	0.75950
H260	H	0.85587	0.47349	0.23654
H261	H	0.82931	0.50973	0.20914
H262	H	0.83681	0.52037	0.72266
H263	H	0.80483	0.47500	0.56820
C264	C	0.54923	0.59823	0.49535
H265	H	0.56677	0.60630	0.22361
H266	H	0.56697	0.60592	0.76082
C267	C	0.52703	0.61569	0.49683
H268	H	0.52703	0.61569	0.16902
C269	C	0.55525	0.65619	0.49206
H270	H	0.57402	0.66130	0.23690
H271	H	0.57297	0.66376	0.75755
C272	C	0.54976	0.68752	0.49119
H273	H	0.53164	0.68322	0.75000
H274	H	0.53394	0.68597	0.22524
C275	C	0.58024	0.72738	0.48622
H276	H	0.59864	0.73042	0.23525
H277	H	0.59774	0.73373	0.75178
C278	C	0.58099	0.76233	0.48454
H279	H	0.59530	0.77826	0.21196
H280	H	0.59620	0.77873	0.74706
H281	H	0.55201	0.75586	0.49336
C282	C	0.50239	0.63049	0.49869
H283	H	0.48275	0.61613	0.74971
H284	H	0.48453	0.62076	0.23332
C285	C	0.50898	0.66811	0.49628
H286	H	0.52095	0.68154	0.20597
H287	H	0.52872	0.68465	0.73380
H288	H	0.48215	0.66602	0.54729

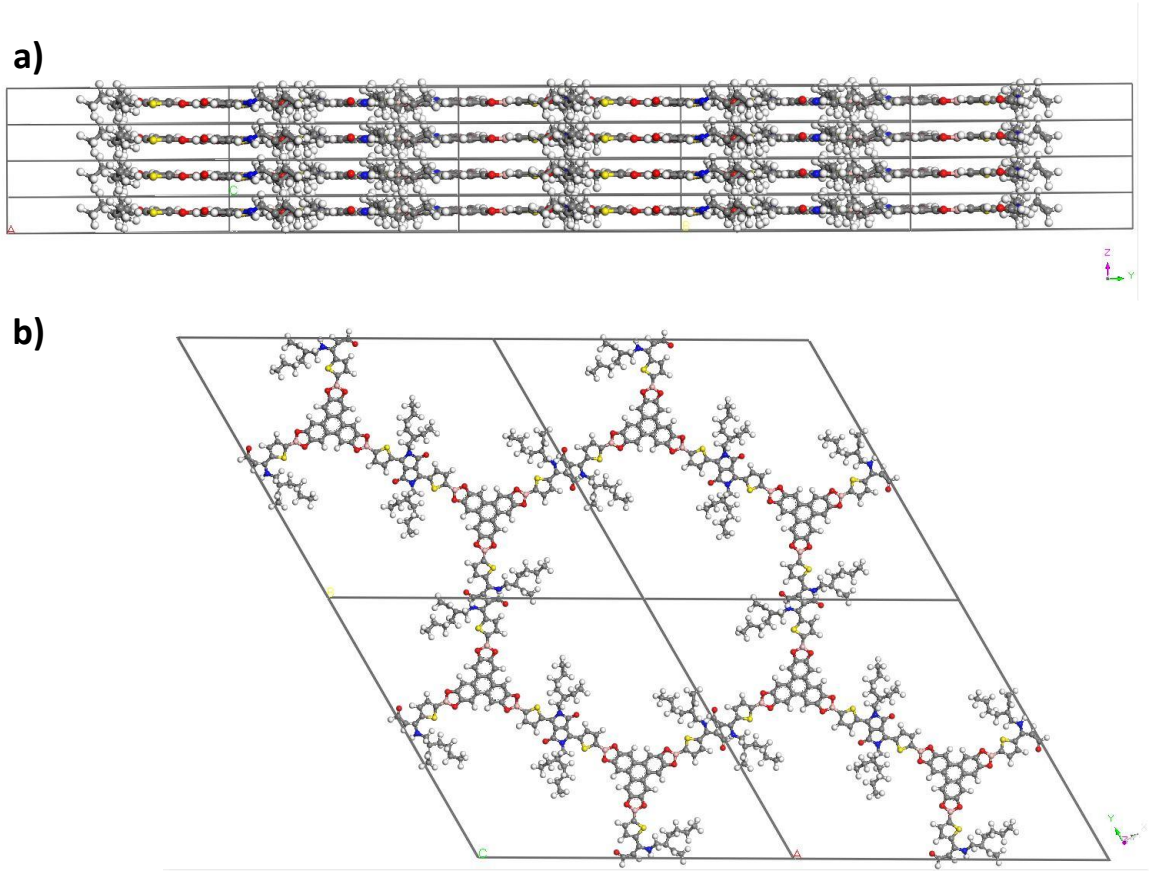

Figure 4-12: a) Side view of *P1* simulated crystal along the *y*-axis of 4 unit cells stacked on top of each other demonstrating the flat and rigid backbone consisting of HHTP and DPP including the distribution of the alkyl chains, b) simulation of the crystal lattice of 4 unit cells in an eclipsed arrangement for DPP2-HHTP-COF illustrating the resulting pore shape, viewed along *z*.

Another possible space group for this system is space group *P*6/*mcc*, which includes the flipping of the eclipsed layers in one crystal unit cell. This possible arrangement was also calculated and illustrated in the figure below. In addition, the calculated PXRD patterns of the different space groups are compared to the experimental data. The simulated pattern for *P*1 fits the experimental data well, whereas the pattern for *P*6/*mcc* is slightly shifted to smaller 2θ values. This is visualized by the vertical lines for the detected reflections in the experimental data.

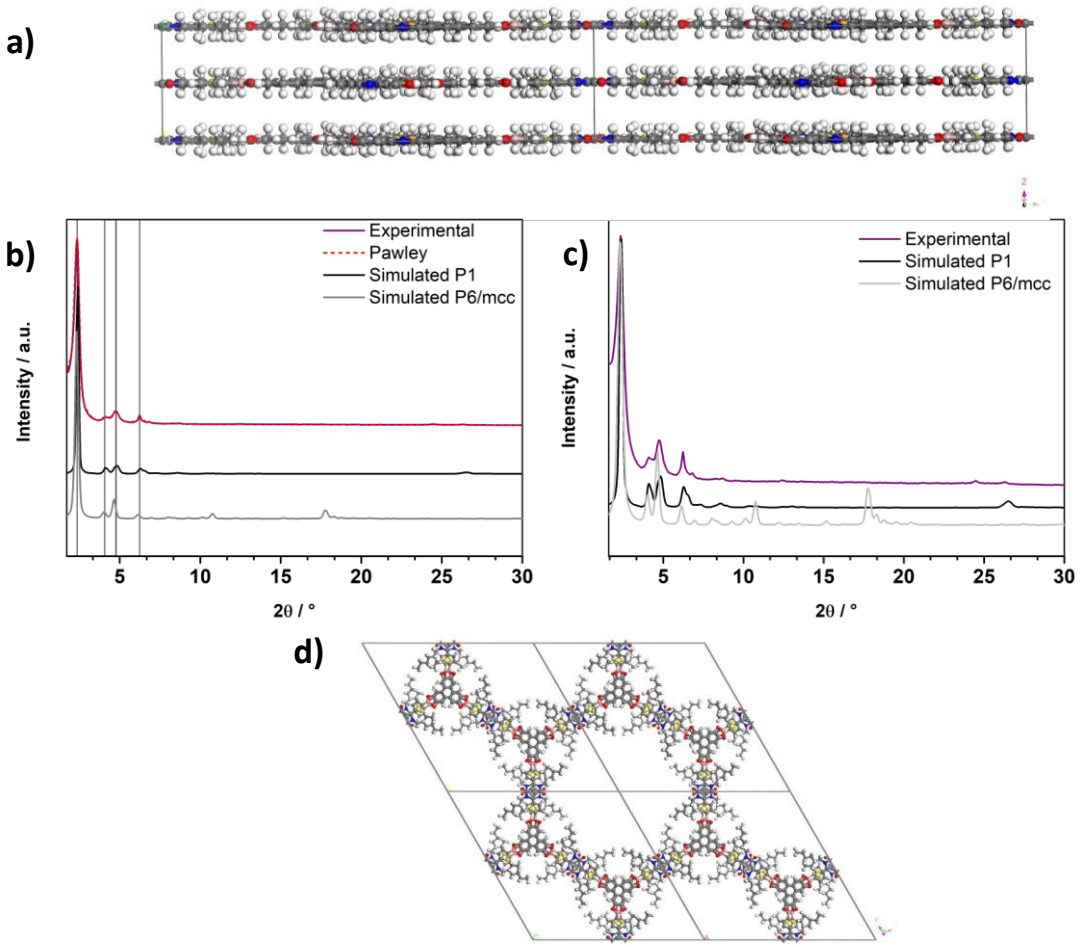

Figure 4-13: a) Simulation of the crystal unit cell in an eclipsed arrangement in the *P6/mcc* space group illustrating two flipped layers stacked on top of each other, b) differences between the calculated patterns for space groups *P1* (black) and *P6/mcc* (grey) in comparison to the experimental data (purple) and the corresponding Pawley refinement (red dashed), c) PXRD pattern of experimental data (purple), and simulated in *P1* (black) and *P6/mcc* (grey) in logarithmic scale, d) top view on AB plane for the *P6/mcc* space group.

4.4.2.2 IR Measurement of DPP2-HHTP-COF

The successful formation of the boronate ester-linked DPP2-HHTP-COF was confirmed by IR-spectroscopy (see Figure 4-14). The characteristic B-O stretching modes at 1347 cm^{-1} and the C-O stretching mode at 1240 cm^{-1} indicate the coupling of the precursors. Moreover, the characteristic O-H vibration is still visible around 3300 cm^{-1} due to the existence of hydroxyl groups at the outer surface of the COF material arising from the HHTP precursor.

IR: 3960 (vw), 3633 (vw), 3327 (m), 2957 (m), 2927 (w), 2181 (vw), 1639 (vs), 1564 (m), 1509 (m), 1441 (s), 1394 (s), 1347 (vs), 1290 (vs), 1285 (vs), 1240 (s), 1159 (m), 1102 (s), 1067 (s), 1028 (s), 966 (m), 868 (w), 828 (w), 736 (m), 722 (w), 722 (m), 678 (vw), 657 (vw).

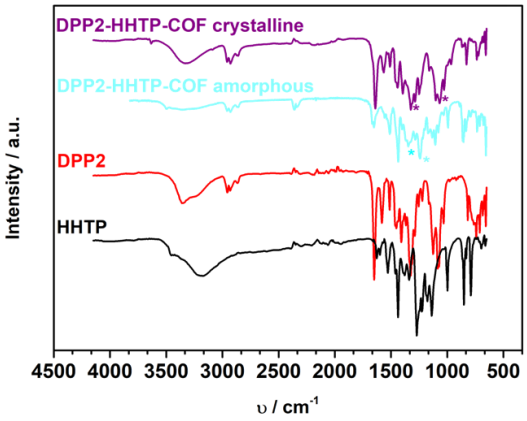

Figure 4-14: IR spectra of DPP2-HHTP-COF illustrating the formation of the framework by marking the typical boronate ester vibrations with a star; DPP2-HHTP-COF crystalline (purple), DPP2-HHTP-COF amorphous (light blue), DPP2 precursor (red) and HHTP precursor (black); the vibration at around 3400 cm^{-1} is attributed to the remaining hydroxyl groups of the HHTP counterpart.

4.4.2.3 Steady-State and Time-Resolved Optical Characterization

Photoluminescence (PL) measurements were performed using a PicoQuant FluoTime300 time-correlated single photon counting (TCSPC) setup. The steady-state spectrum was recorded using a 378 nm laser (PicoQuant LDH-P-C-375), while TCSPC histograms and the time-resolved emission spectra (TRES) were acquired with 508 nm laser pulses (PicoQuant LDH-P-C-510) of 0.10 ns length and energy density of around 0.7 µJ/cm². In both cases, the emitted light was collected by a two-inch lens and focused onto a monochromator (Zolix Omni-λ 300). Residual scattered light from the excitation laser was removed using a 400 nm dielectric longpass (Thorlabs FELH0400) or a 3 mm orange glass filter (Schott OG530) for the 378 nm or 508 nm laser, respectively. The monochromatic light was detected under magic angle (54.7°) using a highly-sensitive photomultiplier (PicoQuant PMA 192).

We note that the steady-state PL spectra excited with 378 nm and 508 nm looked identical, but due to a larger spectral range, we chose the 378 nm spectrum in this study.

4.4.2.4 TCSPC Measurements on Crystalline DPP2-HHTP-COF

The comparison between time-correlated single photon counting (TCSPC) decays at 620 nm and 680 nm measured on the crystalline DPP2-HHTP-COF sample can be found in Figure 4-15. The corresponding results of triexponential fits can be found in Table 4-4 with short, medium, and long timescales τ_1, τ_2, and τ_3, respectively. We note that the given uncertainties are fitting errors and are for most of the results much smaller than the actual instrument response time. The latter is mainly determined through the laser pulse length and is around 0.10 ns. To illustrate the much faster instrument response, it is shown together with the DPP2-HHTP-COF data in Figure 4-15b. From the direct comparison of the decays at 620 nm and 680 nm, we see that all three timescales of the triexponential fits are very similar. The emission at 680 nm shows slightly larger values for τ_1 and τ_2 and a higher contribution of τ_2 to the overall intensity. While the 620 nm emission exhibits the largest value of τ_3 of 5.6 ns, it has to be noted that the values for 620 nm and 680 nm both have a relatively large error and match within their combined error margin.

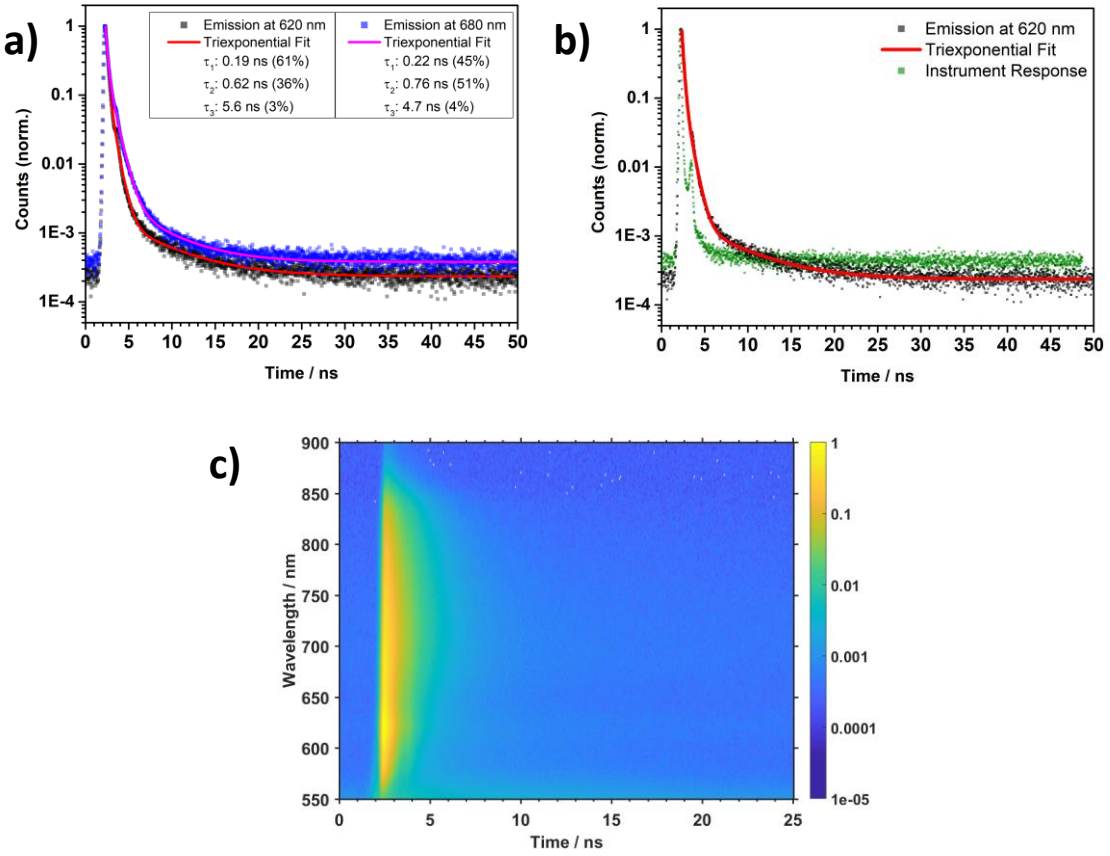

Figure 4-15: a) TCSPC decays of crystalline DPP2-HHTP-COF at both distinct peaks of the PL spectrum, i.e. at 620 nm (black squares) and 680 nm (blue squares). The corresponding triexponential fits are given as solid lines in red and magenta for the 620 nm and 680 nm data, respectively, b) TCSPC decay of crystalline DPP2-HHTP-COF at 620 nm (black squares) and the instrument response of the 508 nm laser (green squares), c) time-resolved emission spectra (TRES) of crystalline DPP2-HHTP-COF. The data are normalized to the main peak and the color scale is logarithmic.

Table 4-4: Fitting results of the triexponential fits to the respective TCSPC datasets of the crystalline DPP2-HHTP-COF. We note that uncertainties are fitting errors and, partly, much smaller than the instrument response of around 0.10 ns.

	620 nm	**Fractional intensity**	**680 nm**	**Fractional intensity**
τ_1	(0.190 ± 0.004) ns	61%	(0.223 ± 0.004) ns	45%
τ_2	(0.619 ± 0.011) ns	36%	(0.760 ± 0.008) ns	51%
τ_3	(5.6 ± 0.5) ns	3%	(4.7 ± 0.3) ns	4%

4.4.2.5 Comparison of TCSPC Measurements of Crystalline and Amorphous DPP2-HHTP-COF

Figure 4-16 contains a direct comparison between crystalline and amorphous DPP2-HHTP-COF samples regarding their time-resolved PL decays. Here, for both samples, the decay was probed within the broad emission feature, which both samples have in common. For the crystalline material, it was monitored at 680 nm while for the amorphous sample, the peak at 705 nm was used. As in the previous section, the datasets were fitted with triexponential functions with short, medium, and long timescales τ_1, τ_2, and τ_3, respectively. The fitting results are summarized in Table 4-5. We see that both decays exhibit the same timescales, i.e. the same within their error margins. Furthermore, the contributions to the overall decay intensities of the three timescales are also very similar. From this observation and the similarity in their broad PL feature, we relate this emission to a state generated through the COF formation, while the specific origin would require further investigation and is not part of this study.

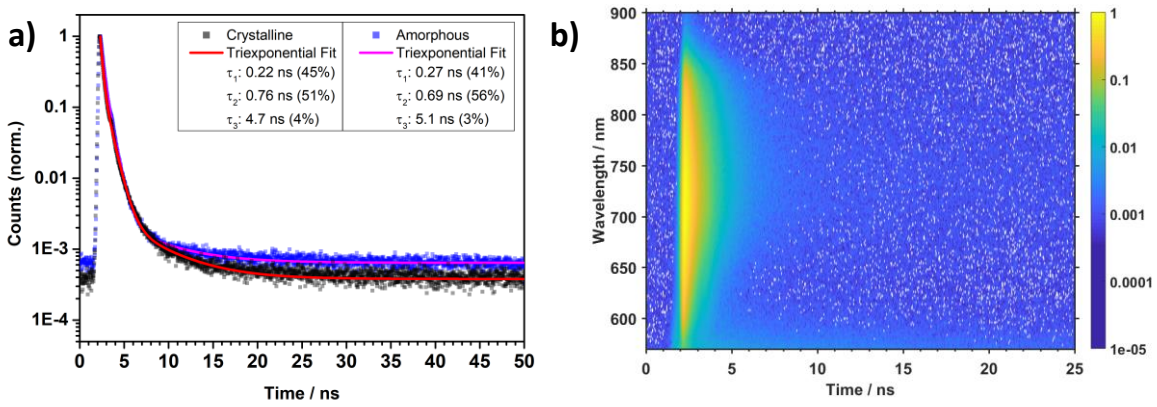

Figure 4-16: a) TCSPC decays of crystalline and amorphous DPP2-HHTP-COF at 680 nm (black squares) and at 705 nm (blue squares), respectively. The corresponding triexponential fits are given as solid lines in red and magenta for the crystalline and amorphous samples, respectively, b) time-resolved emission spectra (TRES) of amorphous DPP2-HHTP-COF. The data is normalized to the main peak and the color scale is logarithmic.

Table 4-5: Fitting results of the triexponential fits to the respective TCSPC datasets of the crystalline and amorphous DPP2-HHTP-COF. We note that uncertainties are fitting errors and, partly, much smaller than the instrument response of around 0.10 ns.

	Crystalline DPP2-HHTP-COF	**Fractional intensity**	**Amorphous DPP2-HHTP-COF**	**Fractional intensity**
τ_1	(0.223 ± 0.004) ns	45%	(0.267 ± 0.005) ns	41%
τ_2	(0.760 ± 0.008) ns	51%	(0.694 ± 0.006) ns	56%
τ_3	(4.7 ± 0.3) ns	4%	(5.1 ± 0.4) ns	3%

4.4.2.6 PL and TCSPC Measurements on Precursors DPP2 and HHTP

Figure 4-17a shows the PL spectra of solid powder DPP2 and solid HHTP precursors. While the former spectra have already been discussed, the latter is shown here for the sake of completeness. The main PL peak of HHTP is further to the blue spectral region than the observed PL of the COF materials. Therefore, we conclude that HHTP aggregates do not play a role in the COF emission, unlike the DPP2, and that no residual HHTP can be observed either. This is supported by the long lifetimes observed in the COF, which are much larger than the 1.0 ns decay component of the solid HHTP (see Figure 4-17b and Table 4-6). It has to be noted, however, that the HHTP emission is very weak, which is the reason for the large background in the TCSPC measurement.
The TCSPC histogram and fit of solid powder DPP2 are shown in Figure 4-17 and the corresponding short, medium, and long timescales τ_1, τ_2, and τ_3, respectively, can be found in Table 4-6. All three timescales are very similar to those of the crystalline DPP2-HHTP-COF emission at 620 nm, which we attribute to DPP stacks as part of the COF matrix. The only difference is in the fractional contributions, where τ_1 shows a smaller and τ_2 a larger contribution in the solid DPP2 compared to the COF. For the solid DPP2 precursor, τ_3 is larger than in the COF, but we note that they both lie within their combined error margins. These very similar characteristics support our assumption that the crystalline DPP2-HHTP-COF exhibits well-ordered DPP2 stacks, showing a *J*-type interaction. Despite their similarity with respect to their error margins, a slightly reduced value for the DPP2-HHTP-COF singlet lifetime could originate from the interaction of the DPP2 and HHTP molecules within the COF framework as next neighbors. While a reduced singlet lifetime has been observed upon COF formation, our study shows a relatively small change in singlet lifetime from aggregated DPP2 to the DPP2-HHTP-COF.[5]

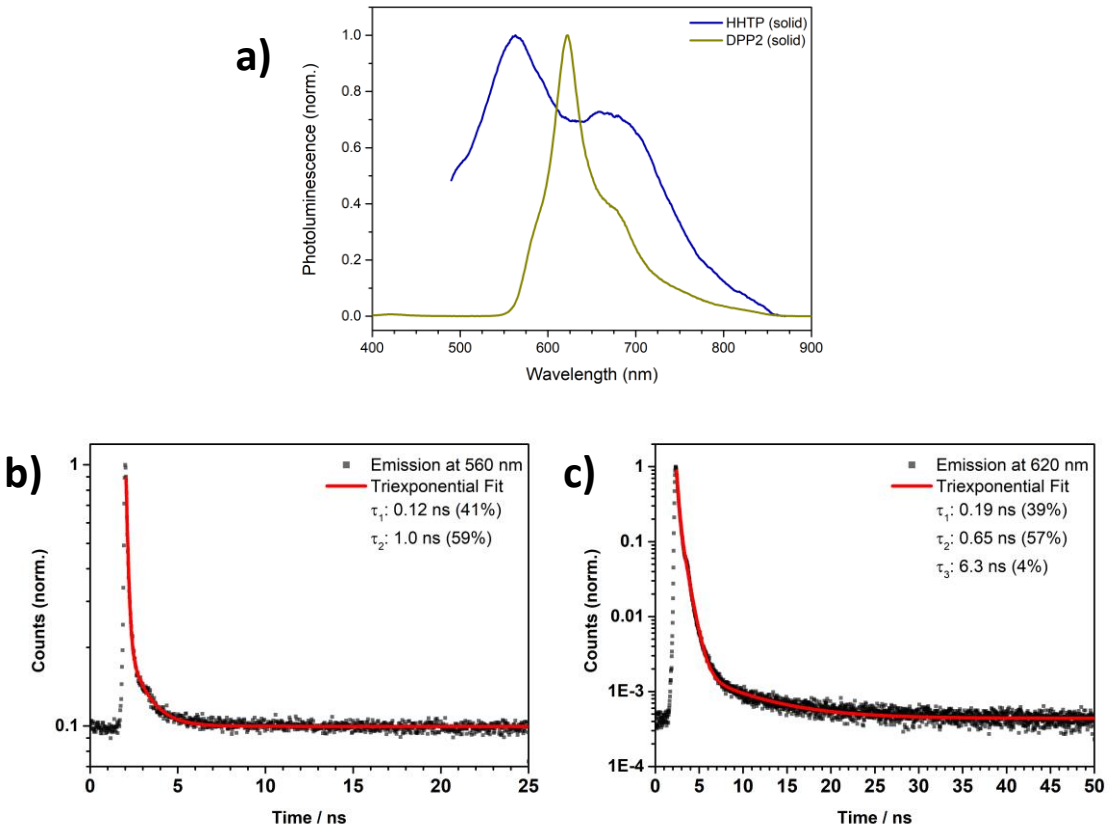

Figure 4-17: a) Photoluminescence spectra of solid DPP2 (green) and solid HHTP precursors (blue), b) TCSPC decay of neat HHTP in solid (powder) form at 560 nm (black squares) and a biexponential fit to the data (red line) c) TCSPC decay of neat DPP2 in solid (powder) form at 620 nm (black squares) and a triexponential fit to the data (red line).

Table 4-6: Fitting results of the multiexponential fits to the respective TCSPC datasets of HHTP and solid DPP2. We note that uncertainties are fitting errors and, partly, much smaller than the instrument response of around 0.10 ns.

	DPP2 - solid	**Fractional intensity**	**HHTP - solid**	**Fractional intensity**
τ_1	(0.189 ± 0.004) ns	39%	(0.117 ± 0.005) ns	41%
τ_2	(0.647 ± 0.007) ns	57%	(1.04 ± 0.06) ns	59%
τ_3	(6.3 ± 0.5) ns	4%	-	-

4.4.2.7 Conductivity Measurements

Hall conductivity measurements were carried out on an ECOPIA HMS 3000 apparatus using a magnetic field of 0.55 T in the van der Pauw geometry connected by gold wires. The measurements were performed on pellets (10 mm diameter), which were prepared by pressing the finely ground materials (precursors and COF material) under a pressure of 0.75 to 1.2 GPa, respectively.

Figure 4-18: a) Illustration of the 10 nm diameter DPP2-HHTP-COF pellet and b) construction of the Hall measurement setup in the van der Pauw geometry.

Table 4-7: Overview of different precursor materials prepared for subsequent Hall measurements.

Sample name	**Sample number**	**Applied pressure / GPa**	**Pellet thickness / µm**
DPP	1-5	0.85	190
DPP2	1-4	0.80	170

Table 4-8: Results for Hall measurements on precursor pellets.

Precursor pellet	**Average conductivity / Scm^{-1}**
DPP	6.81×10^{-08}
DPP2	1.33×10^{-08}

Table 4-9: Results for Hall measurements on crystalline DPP2-HHTP-COF pellets.

Crystalline DPP2-HHTP-COF pellet	**Conductivity / Scm^{-1}**
1	4.99×10^{-08}
2	1.72×10^{-08}
3	1.08×10^{-07}
4	7.32×10^{-08}
5	1.11×10^{-07}
6	4.99×10^{-08}
7	2.20×10^{-06}
8	7.21×10^{-07}
9	5.66×10^{-08}
10	7.12×10^{-08}
11	3.52×10^{-08}
12	7.02×10^{-08}
13	2.15×10^{-08}
14	4.29×10^{-08}
15	8.52×10^{-08}

Table 4-10: Results for Hall measurements on amorphous DPP2-HHTP-COF pellets.

Amorphous DPP2-HHTP-COF pellet	**Conductivity / Scm^{-1}**
1	1.96×10^{-07}
2	2.47×10^{-07}
3	1.26×10^{-07}
4	1.89×10^{-07}
5	2.07×10^{-07}

4.5 References

1. A. P. Côté, A. I. Benin, N. W. Ockwig, M. O'Keeffe, A. J. Matzger, and O. M. Yaghi, *Science* **2005**, *310*, 1166-1170.
2. F. J. Uribe-Romo, J. R. Hunt, H. Furukawa, C. Klöck, M. O'Keeffe, and O. M. Yaghi, *J. Am. Chem. Soc.* **2009**, *131*, 4570-4571.
3. F. Beuerle and B. Gole, *Angew. Chem. Int. Ed.* **2018**, *57*, 4850-4878.
4. M. S. Lohse and T. Bein, *Adv. Funct. Mater.* **2018**, *28*, 1705553.
5. N. Keller, D. Bessinger, S. Reuter, M. Calik, L. Ascherl, F. C. Hanusch, F. Auras, and T. Bein, *J. Am. Chem. Soc.* **2017**, *139*, 8194-8199.
6. M. Calik, F. Auras, L. M. Salonen, K. Bader, I. Grill, M. Handloser, D. D. Medina, M. Dogru, F. Löbermann, D. Trauner, A. Hartschuh, and T. Bein, *J. Am. Chem. Soc.* **2014**, *136*, 17802-17807.
7. D. D. Medina, T. Sick, and T. Bein, *Adv. Energy Mater.* **2017**, *7*, 1700387.
8. D. D. Medina, M. L. Petrus, A. N. Jumabekov, J. T. Margraf, S. Weinberger, J. M. Rotter, T. Clark, and T. Bein, *ACS Nano* **2017**, *11*, 2706-2713.
9. C. R. Mulzer, L. Shen, R. P. Bisbey, J. R. McKone, N. Zhang, H. D. Abruña, and W. R. Dichtel, *ACS Cent. Sci.* **2016**, *2*, 667-673.
10. H. Ding, Y. Li, H. Hu, Y. Sun, J. Wang, C. Wang, C. Wang, G. Zhang, B. Wang, W. Xu, and D. Zhang, *Chem. Eur. J.* **2014**, *20*, 14614-14618.
11. H. Liao, H. Wang, H. Ding, X. Meng, H. Xu, B. Wang, X. Ai, and C. Wang, *J. Mater. Chem. A* **2016**, *4*, 7416-7421.
12. S. Jin, M. Supur, M. Addicoat, K. Furukawa, L. Chen, T. Nakamura, S. Fukuzumi, S. Irle, and D. Jiang, *J. Am. Chem. Soc.* **2015**, *137*, 7817-7827.
13. G. Lin, H. Ding, R. Chen, Z. Peng, B. Wang, and C. Wang, *J. Am. Chem. Soc.* **2017**, *139*, 8705-8709.
14. Y. Hou, X. Zhang, C. Wang, D. Qi, Y. Gu, Z. Wang, and J. Jiang, *New J. Chem.* **2017**, *41*, 6145-6151.
15. E. L. Spitler and W. R. Dichtel, *Nat. Chem.* **2010**, *2*, 672.
16. X. Ding, J. Guo, X. Feng, Y. Honsho, J. Guo, S. Seki, P. Maitarad, A. Saeki, S. Nagase, and D. Jiang, *Angew. Chem. Int. Ed.* **2011**, *50*, 1289-1293.
17. E. L. Spitler, J. W. Colson, F. J. Uribe-Romo, A. R. Woll, M. R. Giovino, A. Saldivar, and W. R. Dichtel, *Angew. Chem. Int. Ed.* **2012**, *51*, 2623-2627.

18. V. S. P. K. Neti, X. Wu, M. Hosseini, R. A. Bernal, S. Deng, and L. Echegoyen, *CrystEngComm* **2013**, *15*, 7157-7160.
19. M. Matsumoto, R. R. Dasari, W. Ji, C. H. Feriante, T. C. Parker, S. R. Marder, and W. R. Dichtel, *J. Am. Chem. Soc.* **2017**, *139*, 4999-5002.
20. T. Lei, J.-Y. Wang, and J. Pei, *Acc. Chem. Res.* **2014**, *47*, 1117-1126.
21. E. Wang, W. Mammo, and M. R. Andersson, *Adv. Mat.* **2014**, *26*, 1801-1826.
22. Y. Deng, J. Liu, J. Wang, L. Liu, W. Li, H. Tian, X. Zhang, Z. Xie, Y. Geng, and F. Wang, *Adv. Mat.* **2014**, *26*, 471-476.
23. D. Bessinger, L. Ascherl, F. Auras, and T. Bein, *J. Am. Chem. Soc.* **2017**, *139*, 12035-12042.
24. B. Gole, V. Stepanenko, S. Rager, M. Grüne, D. D. Medina, T. Bein, F. Würthner, and F. Beuerle, *Angew. Chem. Int. Ed.* **2018**, *57*, 846-850.
25. B. Zhao, K. Sun, F. Xue, and J. Ouyang, *Org Electron* **2012**, *13*, 2516-2524.
26. W. Li, K. H. Hendriks, M. M. Wienk, and R. A. J. Janssen, *Acc. Chem. Res.* **2016**, *49*, 78-85.
27. R. Di Pietro, T. Erdmann, J. H. Carpenter, N. Wang, R. R. Shivhare, P. Formanek, C. Heintze, B. Voit, D. Neher, H. Ade, and A. Kiriy, *Chem. Mat.* **2017**, *29*, 10220-10232.
28. E. D. Głowacki, H. Coskun, M. A. Blood-Forsythe, U. Monkowius, L. Leonat, M. Grzybowski, D. Gryko, M. S. White, A. Aspuru-Guzik, and N. S. Sariciftci, *Org Electron* **2014**, *15*, 3521-3528.
29. Y. Li, P. Sonar, L. Murphy, and W. Hong, *Energy Environ. Sci.* **2013**, *6*, 1684-1710.
30. M. Grzybowski and D. T. Gryko, *Adv. Optical Mater.* **2015**, *3*, 280-320.
31. M. Kaur and D. H. Choi, *Chem. Soc. Rev.* **2015**, *44*, 58-77.
32. M. S. Lohse, J. M. Rotter, J. T. Margraf, V. Werner, M. Becker, S. Herbert, P. Knochel, T. Clark, T. Bein, and D. D. Medina, *CrystEngComm* **2016**, *18*, 4295-4302.
33. S. Jin, K. Furukawa, M. Addicoat, L. Chen, S. Takahashi, S. Irle, T. Nakamura, and D. Jiang, *Chem. Sci.* **2013**, *4*, 4505-4511.
34. T. E. Kaiser, H. Wang, V. Stepanenko, and F. Würthner, *Angew. Chem. Int. Ed.* **2007**, *46*, 5541-5544.
35. F. Würthner, T. E. Kaiser, and C. R. Saha-Möller, *Angew. Chem. Int. Ed.* **2011**, *50*, 3376-3410.

36. N. J. Hestand and F. C. Spano, *Acc. Chem. Res.* **2017**, *50*, 341-350.

37. F. C. Spano, *Acc. Chem. Res.* **2010**, *43*, 429-439.

38. S. Duhović and M. Dincă, *Chem. Mater.* **2015**, *27*, 5487-5490.

39. L. Huo, J. Hou, H.-Y. Chen, S. Zhang, Y. Jiang, T. L. Chen, and Y. Yang, *Macromolecules* **2009**, *42*, 6564-6571.

40. H. Bürckstümmer, A. Weissenstein, D. Bialas, and F. Würthner, *J. Org. Chem.* **2011**, *76*, 2426-2432.

5 Mobility Studies on Acene-Based Covalent Organic Frameworks

This chapter is based on the following publication:

Sabrina Rager, Stephan Reuter, Andreas C. Jakowetz, and Thomas Bein, **2019**, in preparation.

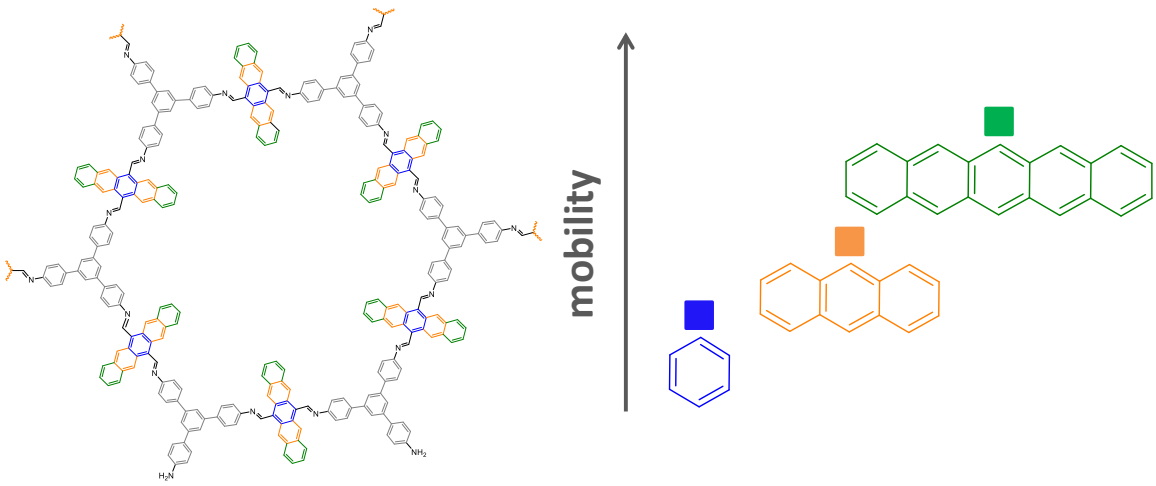

Abstract

Covalent organic frameworks (COFs) are a class of porous and crystalline materials with well-defined structures and extensive potential applications. These applications can be tailored by implementing desired building blocks with promising optoelectronic properties. During the search of suitable building blocks for electroactive COFs, a series of acene-based COFs including functionalized benzene, anthracene and pentacene moieties was investigated. These COFs feature high mobility values measured for pressed powder as pellets as well as in films and devices. Mobility measurements were performed revealing a dependence of the obtained mobility values on the type of mobility setup. Remarkably, the mobility values can be tailored by elongation of the acene backbone in the COF. Hole-only devices (HOD) revealed mobility values reaching up to 0.0027 $cm^2V^{-1}s^{-1}$ which are to date the highest experimentally obtained values.

5.1 Introduction

Covalent organic frameworks (COFs) are known to be an exciting and newly studied type of porous organic materials. They are constructed from differently functionalized organic building blocks *via* strong covalent bonds. COFs feature high crystallinity, extraordinary porosity and large surface areas. These characteristics as well as their functionalities can be tailored by implementing different molecular building blocks resulting in diverse potential applications in gas storage, optoelectronics and conducting devices.[1-3] Moreover, the symmetry and spatial extension of the molecular building units define the symmetry, topology and metrics of the COF pore system, which allows for realizing 2D (layered) and 3D porous materials.[4-6]

The broad selection of proven and potential building blocks, combined with the different binding motifs available, can lead to COFs with intriguing optoelectronic properties. This is particularly important with respect to charge conductivity for which the binding motif and hence the option of a conjugated bond can lead to differently favorable directions of transport. Considering 2D (layered) COFs, in-plane conductivity can be controlled by conjugated bonds such as imine groups, while out-of-plane transport is possible along the molecular stacks, directed through π-π-interactions. Here, the π-π stacking can also be strongly influenced through the right combination of building blocks. In general, intrinsic charge-carrier mobilities in COFs have been found to reach high values using time-resolved microwave conductivity, which is a technique

usually limited to a probing volume at the order of a few nanometers.[7] On the other hand, both the overall charge carrier mobility and the conductivity of COFs in full devices are still comparably low with respect to state-of-the-art semiconducting polymers, thus still impeding the applications of COFs in (opto)electronics and requiring further insight into the factors limiting transport in order to improve performance, for instance by doping.[8]

The latter has a great influence on the electronic behavior and has successfully been used to improve the performance of conjugated polymers.[9-12] This approach was also transferred to COFs and allowed to improve a tetrathiafulvalene-imine-based COF, using iodine and tetracyanaoquinodimethane, through formation of radicals. Conductivity measurements on thin film devices revealed values of up to 1.2×10^{-4} Sm^{-1}. Exposure of the film to iodine vapor in a closed chamber resulted in even higher values of a maximum of 0.28 Sm^{-1}.[9] Another study also showed improved charge-carrier mobility upon doping, which was calculated directly from the accessed conductivity.[13, 14]

The history of conductive polymers goes back for several decades where the first conductive polymers were reported to possibly substitute metallic conductors and semiconductors. These conductive polymers were especially based on polyenes and polyaromatics, including also doping with other substances and reaching high conductivity values.[15, 16] To date, there are several conductive polymer systems combining attractive features of metals and conventional polymers: great electrical and optical properties, high flexibility, scalable synthesis and processing, such as in PEDOT:PSS polymer which is widely used in organic solar cells.[17-20]

Strikingly, small molecules such as oligoacenes are also able to offer high electrical conductivity and mobility.[21, 22] For example, pentacene was synthesized as a thin film yielding mobility values as high as 3 $cm^2V^{-1}s^{-1}$.[23] Pure and non-functionalized pentacene shows its peak mobility values as single crystal.[24] Its hole mobility can be estimated to be 35 $cm^2V^{-1}s^{-1}$ at room temperature and shown to increase to 58 $cm^2V^{-1}s^{-1}$ at elevated temperatures indicating band transport.[25] Notably, these high values result from a careful purification process and imply the importance of reducing defects and impurities in general.[25] To avoid this highly demanding purification step, solution-processable derivatives of pentacene have been developed. The most studied and well-known candidate is 6,13-bis-triisopropyl-silylethynyl pentacene (TIPS-pentacene).[26] It can be used to prepare a solution-processed organic film yielding carrier mobilities of

over 1 $cm^2V^{-1}s^{-1}$, which is opening the door to possible applications as semiconductor in organic thin film transistors.[26]

As already mentioned above, the purity and the number of defects in a system have a great influence on the electronic properties of the resulting material. This usually requires the formation of single crystals or at least highly crystalline domains. While the monomers themselves arrange depending on the processing conditions, a desired highly crystalline arrangement can also be enforced by embedding appropriately functionalized monomers in a COF lattice, as we have shown in recent studies.[27, 28] Here, a highly ordered, porous and crystalline framework is used as a scaffold to produce highly crystalline stacks and domains of the implemented building blocks, ideally mimicking single-crystal characteristics. In addition, due to the reversible co-condensation reaction, defects are reduced in situ. Moreover, if so desired, the accessible porosity of the framework can be filled with other molecules interacting with the backbone thus resulting in potentially new ways to exploit collective aggregate properties such as ordered heterojunctions.

Here, we integrate a series of acene-based molecules in COFs and examine the impact of the COF scaffold on the electrical characteristics of the resulting 2D materials. For this purpose, we implement the acene monomers in a symmetric fashion into the COF, with the acene backbone perpendicular to the linking direction and hence reaching into the free pore system unlike related systems reported in the literature.[29] Following this approach, we were able to keep the unit cell of the systems similar and increase the hole mobility by orders of magnitude when elongating the acenes due to the larger π-overlap between the sheets.

5.2 Results and Discussion

5.2.1 Structural Characterization

We report a series of acene-based that are constructed from 1,3,5-tri(4-aminophenyl)benzene (TAPB) and dialdehyde-functionalized acenes. To minimize structural variation between these different COFs and hence to be able to isolate the impact of the acene, we performed experiments with symmetric acenes with dialdehyde functionalization of the central ring, i.e. terephthaldialdehyde and anthracenedialdehyde. Through this, we aimed to obtain crystalline and porous frameworks with expanded electronic and optical properties through the backbone elongation. The framework

formation was performed under solvothermal reaction conditions. The connection between the desired building blocks through imine bond formation *via* co-condensation can be catalyzed by addition of acetic acid. The reversible bond formation allows for elimination of defects resulting in an improved crystallinity (for more information see Experimental Section). Depending on the applied building blocks, the pore shape, volume and surface area as well as the stacking behavior can be controlled. The schematic synthesis route and the resulting frameworks are illustrated in Figure 5-1 below. The extension of the acene backbone towards pentacene is visualized through colors.

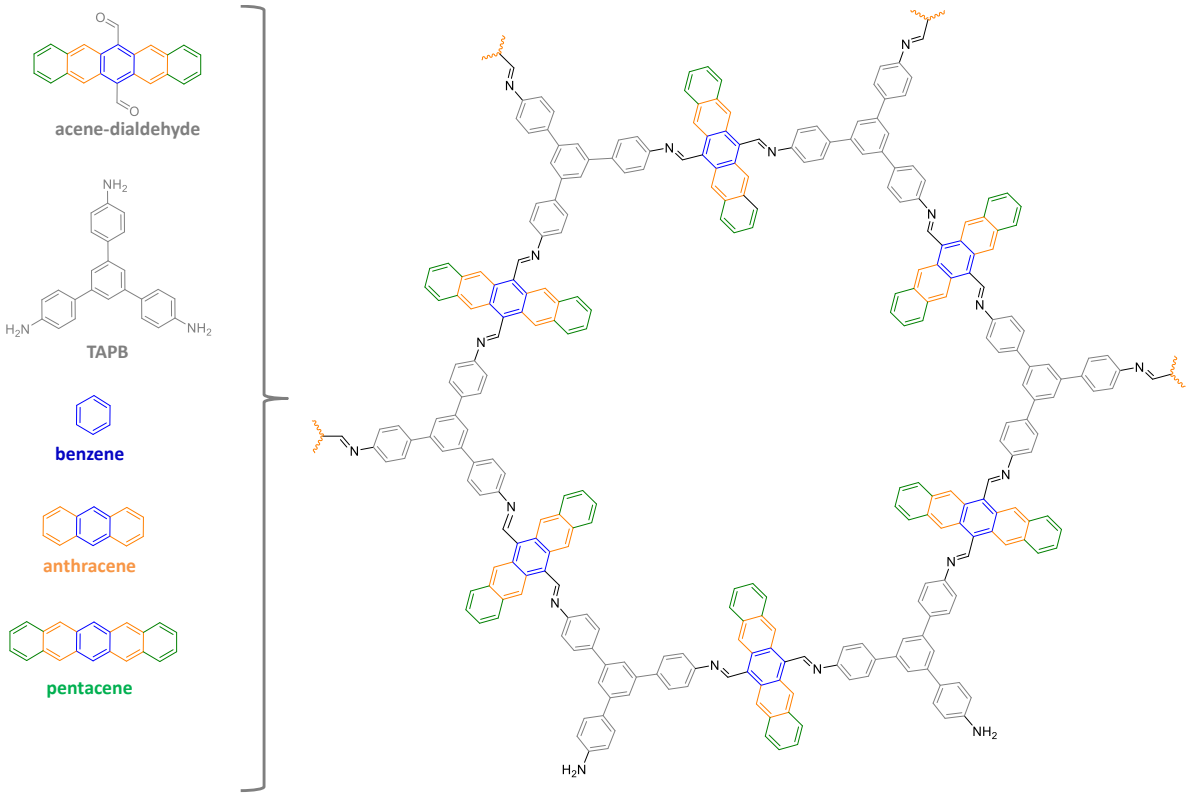

Figure 5-1: Illustration of the schematic synthesis route for the hexagonal pore-shaped COF based on the building blocks TAPB in combination with benzene (blue), anthracene (orange) and pentacene (green) linkers resulting in imine-based frameworks.

The resulting materials were treated with supercritical CO_2 (sc-CO_2) extraction after synthesis before further analysis was performed. Comparing the series of COFs *via* powder X-ray diffraction (PXRD) revealed sharp Bragg reflections centered at low 2θ angles in the same range for all materials. For TA-TAPB-COF (see Figure 5-2a) we attribute the evident Bragg reflections at 2θ values of 2.79°, 4.84°, 5.58°, 7.40° and 9.66° to the 100, 110, 200, 210 and 220 planes, respectively. The 2θ values for

Anthra-TAPB-COF (see Figure 5-2b) appear at almost the same positions and are only slighted shifted. In this case, we ascribe the 2θ values of 2.80°, 4.89°, 5.58°, 7.43° and 9.42° to the same 100, 110, 200, 210 and 220 planes, whereas the relative intensities of the individual reflections are distinct from TA-TAPB-COF due to a different electron density distribution in the channels. For both COFs this also implies the formation of small COF domains due to the relatively broad peak width. Consequently, the simulated diffraction patterns in the hexagonal *P6* space group with AA-stacking provide a good description of the synthesized COFs. The well-defined X-ray diffractograms with sharp reflections demonstrate the excellent crystallinity of these acene-based COFs. The detailed simulation data for all materials are given in the Experimental Section.

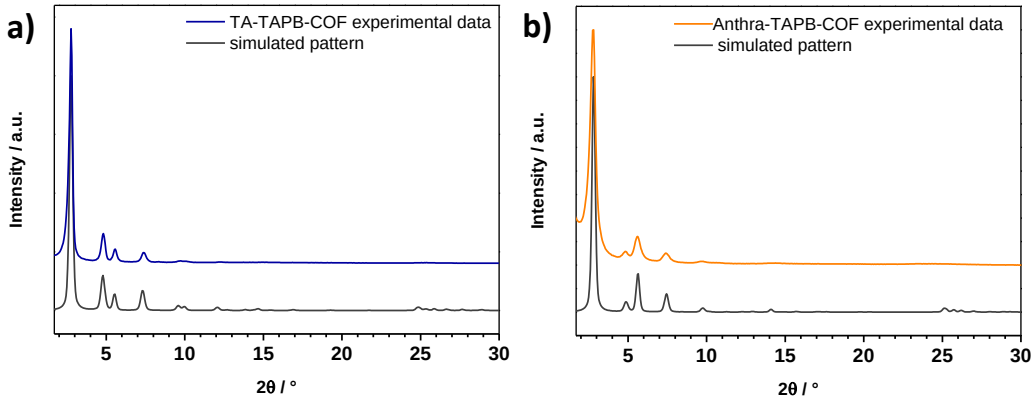

Figure 5-2: PXRD of synthesized COF powders compared to the simulated diffraction patterns of the 2D layer arrangements with refined particle domain sizes. a) TA-TAPB-COF (25 nm domain size) experimental (blue) and simulated pattern (grey), b) Anthra-TAPB-COF (40 nm domain size) experimental (orange) and simulated pattern (grey).

The series of COFs studied here combines acene-based linear building blocks with trigonal TAPB subunits to form hexagonal structures. The simplest structure is TA-TAPB-COF (expected pore size: 3.3 nm; calculated stacking distance in *z*-direction: 3.65 Å) which is built up from TAPB and terephthaldialdehyde (TA). The elongation of the backbone in the framework includes the implementation of 9,10-anthracenedicarboxaldehyde (Anthra). Here, the additional carbon atoms protrude into the pores and can interact with the atoms of the next layers by an extended π-π overlap (Anthra-TAPB-COF; expected pore size: 2.7 nm; calculated stacking distance in *z*-direction: 3.59 Å).

The porosity of the synthesized materials was evaluated by nitrogen sorption measurements at 77 K. Here, the materials were outgassed for at least 12 hours in vacuum at 120 °C. The obtained isotherms and their corresponding pore size

distributions as well as the calculated BET surface areas are illustrated in Figure 5-3. The TA-TAPB-COF structure (Figure 5-3a) shows a typical type IV isotherm with a relatively steep N_2 uptake indicating a mesoporous structure with a calculated BET surface area of more than 1000 m^2g^{-1}. In the case of Anthra-TAPB-COF, we measured a slightly smaller BET surface area of less than 900 m^2g^{-1}. In addition and as expected the pore size also shrinks by almost 1 nm which we attribute to the elongated acene backbones pointing into the pores. Moreover, the latter material also shows a type IV isotherm but with a lower N_2 uptake and smaller pore volume. Both calculated pore size distributions are consistent with theoretical values and fit the simulated pore shapes and sizes.

Table 5-1: Predicted and measured parameters for TA-TAPB-COF and Anthra-TAPB-COF, respectively.

	TA-TAPB-COF	**Anthra-TAPB-COF**
Surface area	1011 m^2g^{-1}	885 m^2g^{-1}
Predicted pore size	3.3 nm	2.7 nm
Measured pore size	3.4 nm	2.6 nm
Predicted stacking distance	3.65 Å	3.59 Å

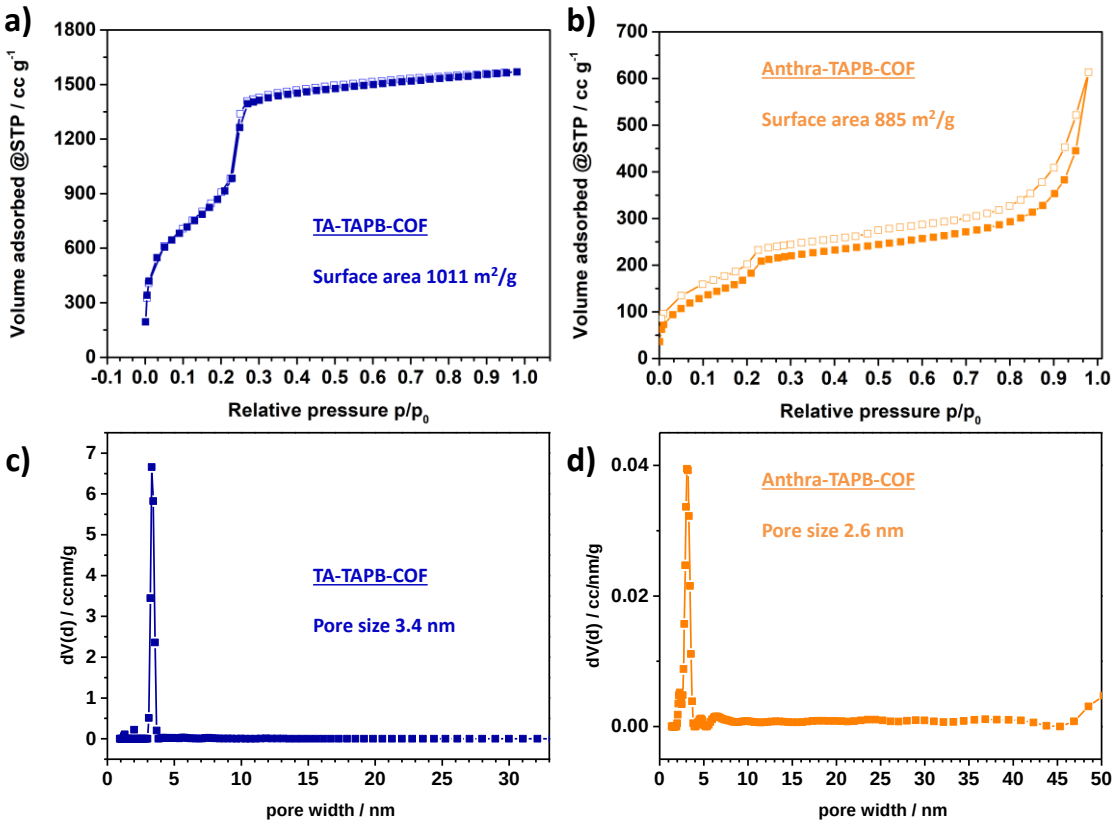

Figure 5-3: Nitrogen sorption isotherm and corresponding pore size distributions of a), c) TA-TAPB-COF (blue) and b), d) Anthra-TAPB-COF (orange). Full symbols: adsorption, empty symbols: desorption.

Electron microscopy was used to further analyze the morphology and crystallinity, and also to evaluate the distribution of COF domains within the materials. For TA-TAPB-COF, scanning electron microscopy (SEM) reveals small spherical particles in the range of 1 µm that have grown into larger aggregates. These spherical particles possess a rough surface and the size is equally distributed throughout the whole powder Figure 5-4a). Moreover, the TEM image of TA-TAPB-COF shows crystalline COF domains of several tens of nanometers with well-aligned hexagonal sheets which perfectly illustrate the channel orientation and crystal structure (see Figure 5-4b).

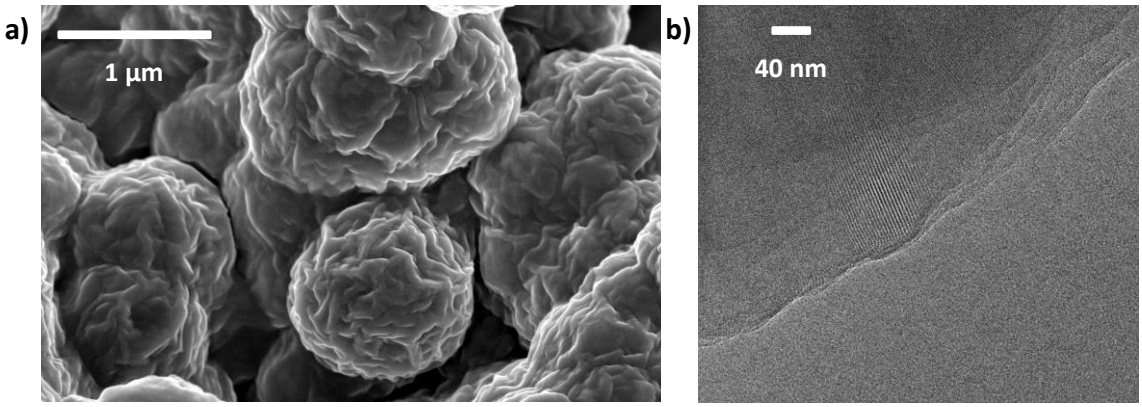

Figure 5-4: a) SEM image of TA-TAPB-COF powder, b) TEM micrograph of TA-TAPB-COF powder showing a crystalline domain with the projection showing a side view of the hexagonal channel system.

Compared to TA-TAPB-COF, the Anthra-TAPB-COF structure with elongated acene in the linear linker features a completely different morphology. As shown in Figure 5-5a, the implementation of anthracene into the framework leads to smaller roundish particles which grow into coral-like aggregates. TEM measurements reveal abundant crystalline COF domains Figure 5-5b) on a length scale of around 40 nm, showing projections with views along the hexagonal COF channels as well as side views of the channel systems.

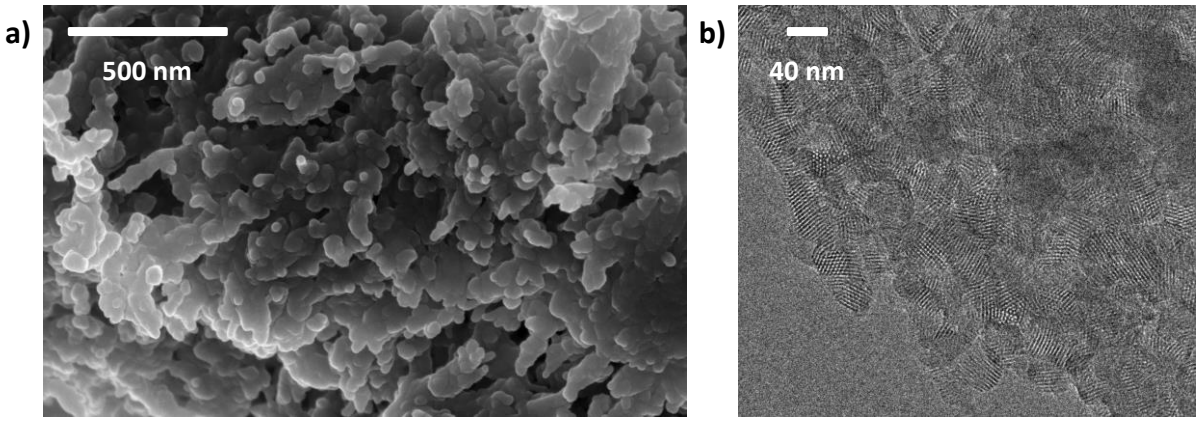

Figure 5-5: a) SEM image of Anthra-TAPB-COF powder, b) TEM micrograph of Anthra-TAPB-COF powder showing the crystalline sample with the projection along the *c*-axis illustrating the hexagonal structure.

5.2.2 Electrical Characterization of Bulk Material

Oligoacenes are small molecules that show very high charge carrier mobilities in single crystals. With our implementation of these buildings blocks into the highly crystalline COF systems, we see them as excellent candidates for conductive and electroactive materials. Therefore, we performed several types of experiments on our synthesized

materials regarding electrical conductivity and charge carrier mobility. We used methods to further compare the materials transferred on films and on bulk materials pressed into pellets while keeping the overall morphology and high crystallinity. The combination of different methods made it possible to resolve conductivity and mobility limitations imposed by intrinsic properties of the materials and by the morphology of the samples.

First, conductivity measurements were performed with the bulk materials. Here, the as-synthesized and sc-CO_2 extracted COFs were pressed into pellets of different thickness. Their crystallinity was checked again after the measurements to ascertain the integrity of the structures. The pellets were analyzed in the van der Pauw geometry, measuring four-point probe conductivity and the Hall mobility of the samples. To get deeper insight into the materials, we also compared crystalline and amorphous COF materials (see Experimental Section for synthetic details) as well as the precursors. This allows us to draw conclusions about the impact of structure on the electronic properties. The PXRD patterns for the respective crystalline materials are shown in Figure 5-6a and Figure 5-6b. The crystallinity was maintained for different thicknesses and pressure conditions during preparation. In general, applying high pressures on crystalline materials leads to a slight loss in crystallinity due to the deformation of the single grains (see change in PXRD patterns and the declined signal-to-noise-ratio). Overall, TA-TAPB-COF retains a higher crystallinity at high pressures as compared to Anthra-TAPB-COF.

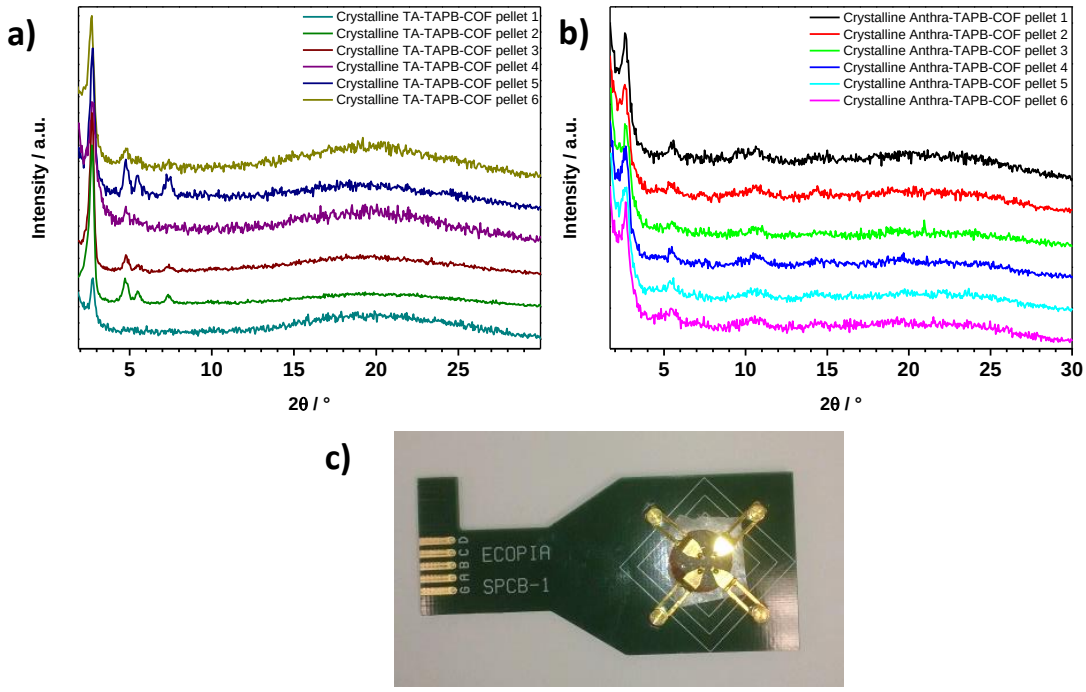

Figure 5-6: PXRD pattern of a) crystalline TA-TAPB-COF and b) crystalline Anthra-TAPB-COF pressed into pellets for van der Pauw measurements (TA-TAPB-COF: pellet 1: 190 µm, 0.85 GPa; pellet 2: 90 µm, 1.35 GPa; pellet 3: 130 µm, 0.98 GPa; pellet 4: 200 µm, 0.9 GPa; pellet 5: 230 µm, 0.45 GPa; pellet 6: 160 µm, 1.00 GPa); (Anthra-TAPB-COF: pellet 1: 140 µm, 1.00 GPa; pellet 2: 110 µm, 1.10 GPa; pellet 3: 90 µm, 1.3 GPa; pellet 4: 100 µm, 1.20 GPa; pellet 5: 120 µm, 1.05 GPa; pellet 6: 100 µm, 1.20 GPa); c) van der Pauw setup with a 10 mm pressed pellet to illustrate the general geometry.

To exclude preferred orientation effects in individual samples, several measurements were investigated on each pellet to achieve good. The obtained values for each system are listed in the Experimental Section and the averaged values for conductivity and Hall mobility are given in Table 5-2. We note that the value for conductivity rises by around one order of magnitude with the larger acene (Anthra) backbone in the COF. We attribute this result to the larger π-overlap of the single 2D sheets resulting in a more conductive material.

Table 5-2: Averaged conductivity and Hall mobility values for crystalline TA-TAPB-COF and Anthra-TAPB-COF, respectively, obtained with the van der Pauw measurement method on pressed pellets with standard deviation.

	Averaged conductivity [Scm^{-1}]	**Averaged Hall mobility [$cm^2V^{-1}s^{-1}$]**
TA-TAPB-COF	$9.61 \times 10^{-08} \pm 7{,}83\times 10^{-08}$	$2.64 \times 10^{02} \pm 53.7$
Anthra-TAPB-COF	$3.03 \times 10^{-07} \pm 2.74\times 10^{-07}$	$4.40 \times 10^{02} \pm 205$

5.2.3 Electrical Characterization of COF Films

In addition to measurements on pellets, we performed conductivity measurements with the van der Pauw method on grown films of the COF materials. To this end, we synthesized several films *via* solvothermal reaction on glass substrates. A detailed description of the reactions is given in the Experimental Section. The thickness of the films was determined by SEM cross section measurements to be around 250-300 nm. On the smooth and consistent TA-TAPB-COF film, some particles sized several micrometers can be detected on the surface. These particles reveal the same morphology as the TA-TAPB-COF bulk material and also expose a near spherical shape, with larger aggregates also present (see Figure 5-7b).

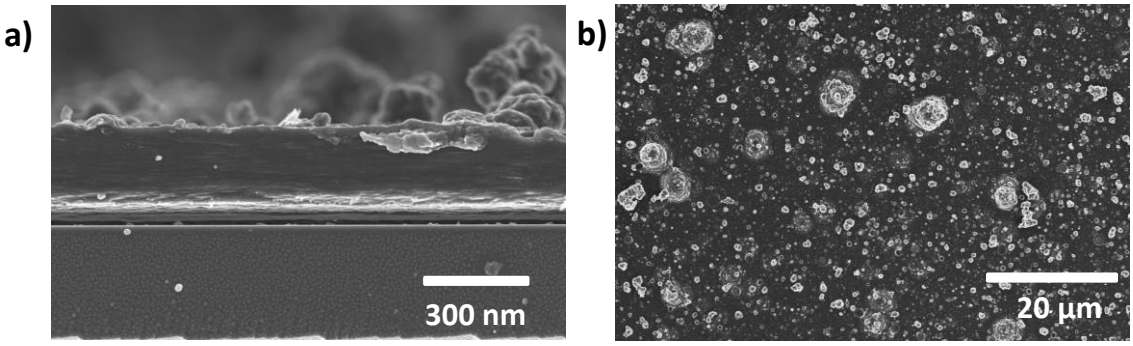

Figure 5-7: SEM micrographs of TA-TAPB-COF film grown on glass substrate a) cross section, b) top view.

After intensive screening of the reaction conditions, smooth films of Anthra-TAPB-COF were successfully synthesized with a thickness of around 250-300 nm. Compared to TA-TAPB-COF, a few additional smaller aggregated particles could be observed on the surface of the film (see Figure 5-8).

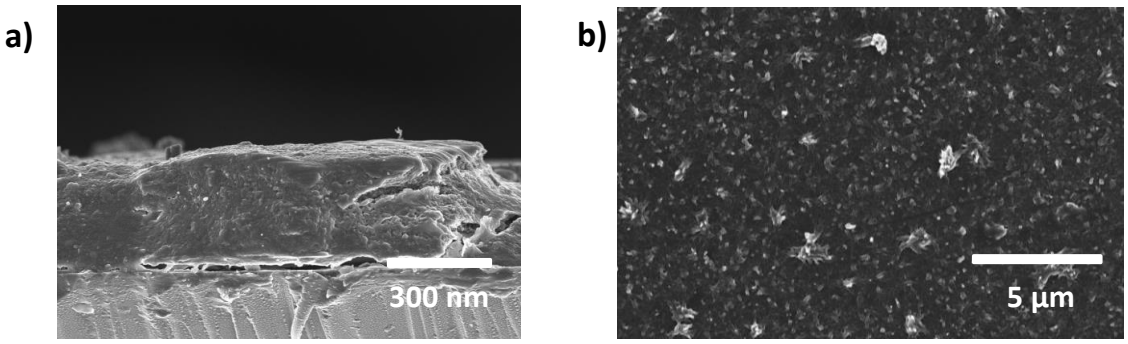

Figure 5-8: SEM micrographs of Anthra-TAPB-COF film grown on glass substrate a) cross section, b) top view.

The PXRD pattern of the synthesized films as well as the setup for the van der Pauw film measurements are illustrated in Figure 5-9. High resolution detector scan measurements reveal no characteristic reflections of the COFs, which can be attributed to non-crystallinity or vertical alignment, in the small *2θ* region for either of the films. Consequently, the randomly distributed particles attached to the surface of the films also do not contribute crystalline material to the film. The bump between 20° and 30° *2θ* can be attributed to the glass substrate on which the films grew. The as-synthesized films exhibit a smooth surface and yellow color for TA-TAPB-COF and orange for Anthra-TAPB-COF (see Figure 5-9c). For further conductivity experiments, the films were connected *via* four gold wires similar to the measurements on pellets and the setup is depicted in Figure 5-9b.

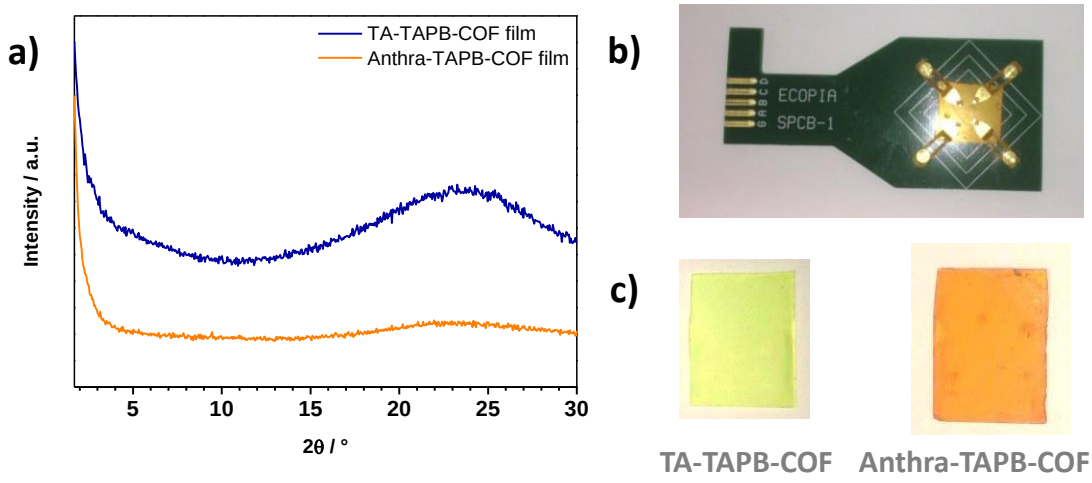

Figure 5-9: a) PXRD pattern of TA-TAPB-COF film (blue) and Anthra-TAPB.-COF film (orange) synthesized on glass substrates measured in detector scan mode (tube fixed at 0.01 °*2θ*), b) Anthra-TAPB-COF film in holder for van der Pauw measurements, c) photos of TA-TAPB-COF film (yellow) and Anthra-TAPB-COF film (orange) to illustrate the overall appearance of the materials, respectively.

The measured and averaged values for different film batches are given in Table 5-3 below. Values for TA-TAPB-COF reveal almost the same conductivity compared to Anthra-TAPB-COF in the range of 10^{-8} Scm^{-1}. Strikingly, the elongation of the acene backbone in the linear linker has a great influence on the Hall mobility values. Whereas the averaged Hall mobility value for the terephthalaldehyde-based framework is around 10^{1} $cm^2V^{-1}s^{-1}$, the one for the Anthra-based network reaches values of up to two orders of magnitude higher. In addition, outstanding mobility values can be accomplished with maximum results of 10^{4} $cm^2V^{-1}s^{-1}$. In this measurement method, the grain boundaries and the constitution of the material have a great influence on the conductivity values whereas Hall mobility depends on the applied magnetic field. Here, only the difference

of the voltage is determined followed by a calculation leading to the actual mobility. Consequently, the Hall mobility values as well as the conductivity strongly depend on the material, geometry of the measurement method and the domain size of the crystallites. In addition, both are affected by grain boundaries.

Table 5-3: Averaged conductivity and Hall mobility values for TA-TAPB-COF films and Anthra-TAPB-COF films, respectively, obtained with the van der Pauw measurement method on glass substrates.

TA-TAPB-COF films	**Conductivity [Scm^{-1}]**	**Hall mobility [$cm^2V^{-1}s^{-1}$]**
	7.22×10^{-09}	9.03×10^{00}
	5.33×10^{-08}	1.27×10^{02}
	4.01×10^{-07}	3.06×10^{02}
	3.76×10^{-08}	1.72×10^{01}
	5.33×10^{-08}	9.22×10^{01}
	1.21×10^{-09}	8.31×10^{-01}
	1.36×10^{-08}	2.82×10^{00}
	4.74×10^{-08}	2.49×10^{01}
	3.03×10^{-08}	1.46×10^{01}
	4.64×10^{-08}	1.59×10^{01}
Average	**6.91×10^{-08}**	**6.10×10^{01}**

Anthra-TAPB-COF films	**Conductivity [Scm^{-1}]**	**Hall mobility [$cm^2V^{-1}s^{-1}$]**
	2.73×10^{-08}	1.51×10^{02}
	3.37×10^{-08}	3.96×10^{02}
	2.92×10^{-08}	1.40×10^{02}
	2.78×10^{-08}	2.48×10^{04}
	4.45×10^{-08}	1.33×10^{02}
	4.38×10^{-08}	2.67×10^{02}
	5.91×10^{-08}	3.39×10^{02}
	2.57×10^{-08}	1.96×10^{02}
	3.75×10^{-08}	1.70×10^{02}
	2.77×10^{-08}	1.36×10^{02}
Average	**3.56×10^{-08}**	**2.67×10^{03}**

5.2.4 Electrical Characterization of Hole-Only Devices (HOD)

Since charge carrier mobility values can strongly depend on the method used, we also were interested in values for operational devices by measuring their voltage-current characteristics. Here, the reaction conditions for film synthesis were transferred to ITO-coated glass substrates. Molybdenum oxide (MoO_x) is known to have a high work function, leading to the selective collection of holes from the device.[30] For this purpose, a thin layer of MoO_x (10 nm) was evaporated onto the ITO covered glass before synthesizing the COF film. Furthermore, a second evaporated layer of MoO_x (10 nm) followed by the evaporation of Au (40 nm) completed the hole-only device (HOD)

architecture. The charge-carrier mobility of the material can be extracted from the measured current-voltage measurements using the Mott-Gurney equation:

$$J = \frac{9}{8}\varepsilon_0\varepsilon_r\mu\frac{V^2}{L^3} \quad \textbf{(5.1)}$$

Equation 5.1: Mott-Gurney equation; J: current density, ε_0: permittivity of free space, ε_r: dielectric constant of the COF, μ: charge carrier mobility, L: thickness of the COF layer, V: voltage drop across the device.

The architecture of the HODs as well as a picture of the fabricated devices with TA-TAPB-COF and Anthra-TAPB-COF films are shown in Figure 5-10 (crystallinity can be compared to films, see above). Every single device has an active and accessible pixel area of 16 mm^2, providing access to four individual pixels and hence four mobility values per sample.

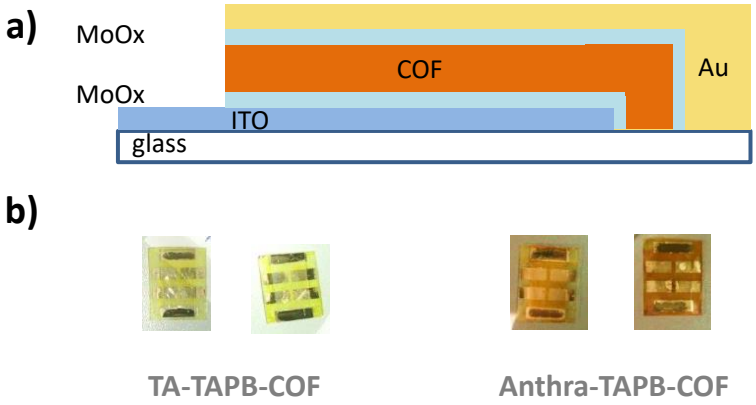

Figure 5-10: a) Architecture of the HODs for mobility measurements illustrating the different layers. b) Fabricated devices of TA-TAPB-COF (left) and Anthra-TAPB-COF (right) showing the applied geometry and setup of the resulted devices.

To determine the thickness of the fabricated COF devices we performed SEM cross section measurements on cracked samples and on material cuts using a focused ion beam (FIB; see Experimental Section). The distribution of the different layers can be seen in Figure 5-11. The COF layers were analyzed to be 250 nm thick covered with the 40 nm Au electrode layer, respectively. The obtained thicknesses were then used for the mobility calculations with the Mott-Gurney equation. We note that the MoO_x cannot be visualized due to the relatively thin layer of 10 nm and the missing image contrast compared to gold or ITO.

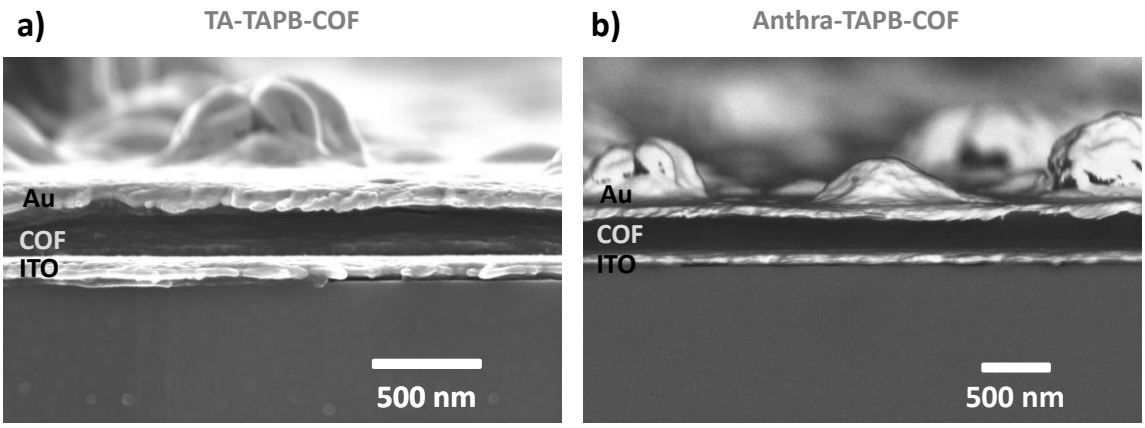

Figure 5-11: SEM cross section micrograph of a) 250 nm TA-TAPB-COF HOD and b) 250 nm Anthra-TAPB-COF HOD.

Next to SEM cross-section measurements, the surface morphology and consequently the thickness of the deposited films were examined using a FIB method. We found the rather smooth films to contain intergrown domains with several agglomerates on the film surface for both materials, respectively.

Figure 5-12 illustrates a FIB-cut TA-TAPB-COF device which was examined by SEM to determine the thickness. The investigation revealed a thickness of 250 nm and confirms the results obtained above for cross section measurements on the cracked devices. It can be observed that the relatively smooth COF film covered with bigger agglomerates is embedded between the two electrodes ITO/MoO_x and MoO_x/Au. The thickness determined with this method was used for further mobility calculations using the Mott-Gurney equation.

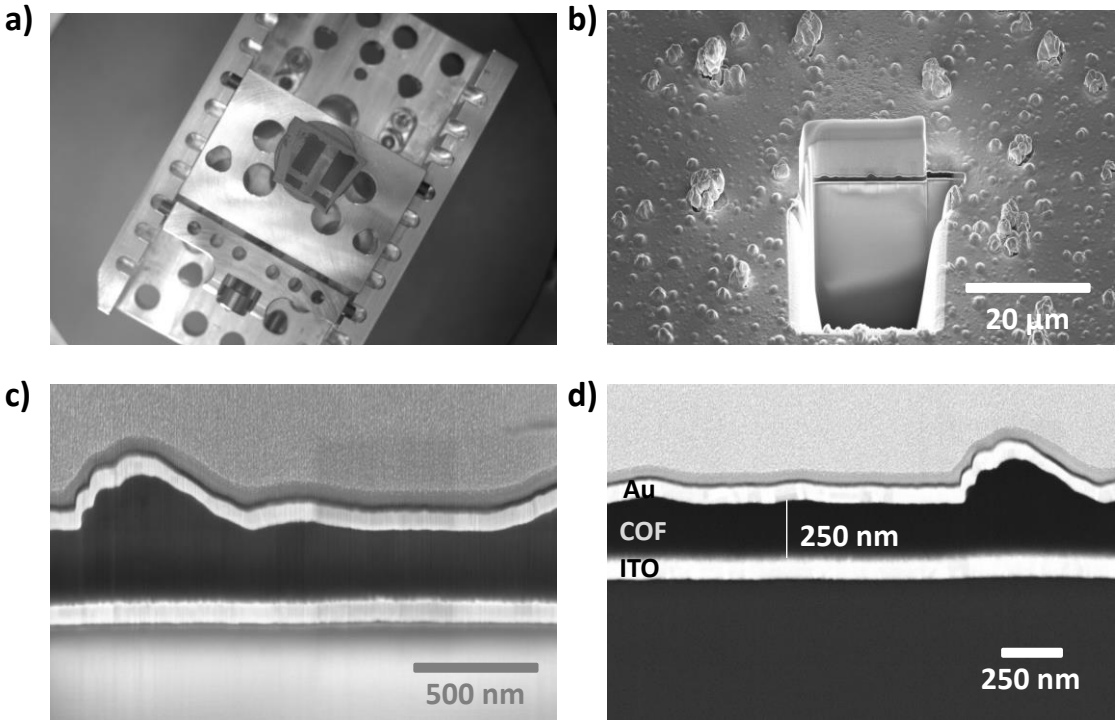

Figure 5-12: Pictures of FIB method applied on a HOD with a 250 nm thick TA-TAPB-COF. Here, a cross-sectional area was fabricated using a Ga acceleration voltage of 30 kV. Afterwards, the cross section was analyzed by SEM, probing secondary electrons and backscattered electrons at different acceleration voltages. a) Top view of the prepared device with two pixels, b) top view of the prepared cross sectional area by FIB, c) overview of different film layers with high magnification to better illustrate the distribution of the transferred materials (ITO/COF/Au/sputtered carbon/Pt protection by electron beam/ ion beam), d) cross sectional area of HOD showing the thickness of the films compared to the electrode materials.

As mentioned above, the charge carrier mobility was calculated using the Mott-Gurney equation with the parameters noted in Figure 5-13 and the data below. For the relative dielectric constant of the COF material we used the recently reported value for COFs of 1.7 derived from impedance measurements.[31] To study the effect of the length of the backbone on the charge-carrier mobility we performed the experiments on TA-TAPB-COF and Anthra-TAPB-COF devices, respectively. Both materials showed thicknesses of around 250 nm, as mentioned above. The measurements were performed in the dark and mobility values were obtained ranging from 4.5×10^{-6} $cm^2V^{-1}s^{-1}$ to 2.7×10^{-3} $cm^2V^{-1}s^{-1}$, where the highest value was obtained for the anthracene-containing COF film. The corresponding data and quadratic fits as well as the parameters chosen for calculations are shown in Figure 5-13.

To obtain high mobility values, directed pathways for transport are needed with as few as possible defects along the way. Within the *ab*-plane of 2D COFs, electronic barriers

are expected to be minimized due to the fully conjugated imine bonds. In *c*-direction, the COF layers need to stack perfectly into a single COF domain resulting in a flawless stack between the electrodes to achieve significant conductivity. Following this argument, when extending the linear linker from TA to anthracene we can expect to achieve a better stacking induced by π-π interactions resulting in a better orientation of the COF sheets. In this case we can minimize electronic defects within the stacks due to disorder and charges can travel more efficiently along the paths in the *ab*-plane. The increased π-π interactions also lead to a better delocalization of charges across the stack, facilitating transport and hence leading to increased mobilities.

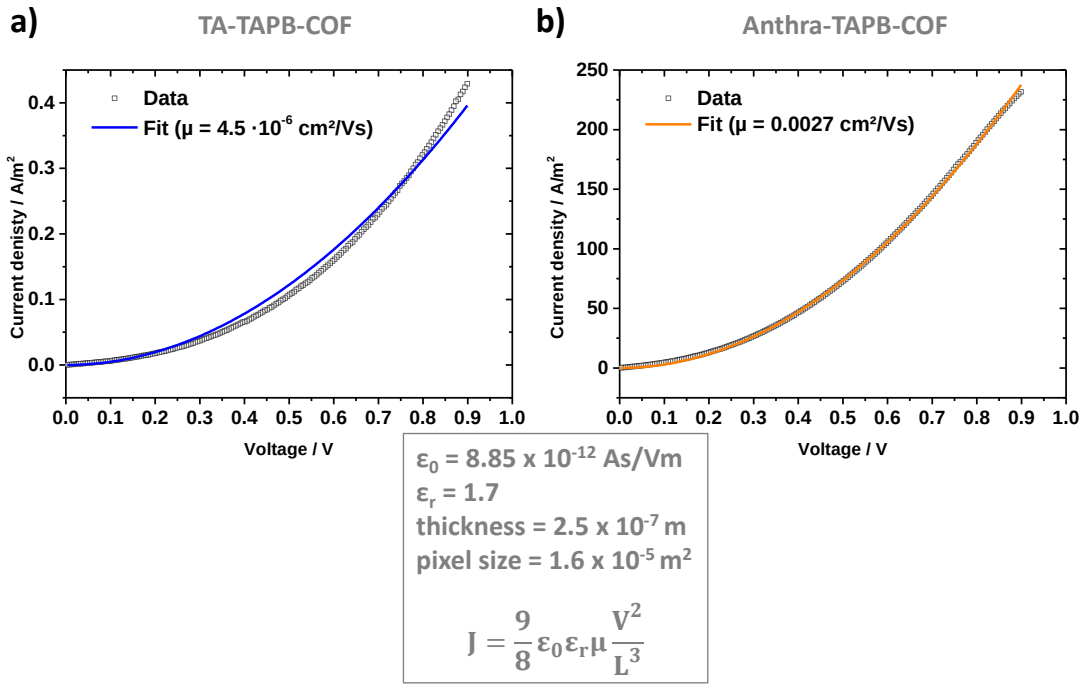

Figure 5-13: Current density as a function of voltage (*J*-*V*) of hole-only devices containing a) TA-TAPB-COF layers of 250 nm and b) Anthra-TAPB-COF layers of 250 nm thickness. The calculated values are given with the quadratic fit in the top left corner of the plots, respectively. The Mott-Gurney equation with the applied parameters for calculating the mobility is given in the grey box.

5.3 Conclusion

In this study, we have demonstrated the successful integration of acene-based building blocks in combination with trigonal TAPB into imine-linked 2D COFs featuring hexagonal porous frameworks. Our systems varied in the length of the acene building block influencing the stacking behavior and π-overlap between the COF sheets. Both materials exhibit a porous and crystalline structure with promising electrical characteristics. To learn more about electronic transport in these materials, we performed mobility measurements on bulk powders, thin films and film-based devices. We compared diverse geometries and setups for a better understanding and a more representative evaluation.

In a first experiment, we performed investigations on crystalline and amorphous materials pressed into pellets. We saw a distinct limitation through grain boundaries and defects in the structure, whereas the Hall mobility strongly depends on the single crystallite size and can therefore reach higher values than on a macroscopic scale.

For further investigations, we synthesized thin COF films and constructed hole-only devices (HODs). While van der Pauw measurements already showed an increase in values for the longer anthracene unit, similar results were obtained from current-voltage measurements on HODs. The Mott-Guerney equation revealed a mobility improvement with the longer anthracene backbone by about three orders of magnitude. The macroscopic measurements on HODs showed values for TA-TAPB-COF in the range of 10^{-6} $cm^2V^{-1}s^{-1}$and Anthra-TAPB-COF even reaching 10^{-3} $cm^2V^{-1}s^{-1}$. Further film devices have to be constructed to get a better statistical validation of the values. Nevertheless, our results give a strong indication on the mobility behavior of these materials and the importance of π-overlap within these materials. Across the different methods used, we demonstrated the dependency of mobility values obtained for different COF systems with an increase towards the longer backbone acene.

Our applied COF systems varied regarding the length of the implemented building block influencing the stacking behavior. We performed mobility measurements on different shapes of the materials, i.e., bulk, thin films and film-based devices. For every system, the values strongly depended on the applied measurement technique and the according symmetry of the setup and the nature of the material, i.e. crystallinity and crystallite domain size.

In the case of bulk material, we pressed the crystalline and amorphous powders into pellets to apply the van der Pauw technique with a four-point probe geometry. Here, the

values for conductivity strongly depend on the grain boundaries, their density, defects in the crystal structure and quality of the pellet, whereas the mobility values are determined by changing the magnetic field. This means that the difference of the voltage is just measured within one single crystallite and is not influenced by boundaries or appearance of the pellet itself. Based on these results, a further elongation of this backbone towards a pentacene building block seems to be a promising pathway due to the even larger π-systems and therefore overlaps. As a first step, we synthesized a suitable pentacenedialdehyde linker for implementation in a TAPB-based framework. So far, intensive screening of the reaction conditions has only led to amorphous material resulting from the reaction, in spite of demanding work-up schemes and treatments with sc-CO_2 extraction (see Figure 5-14).

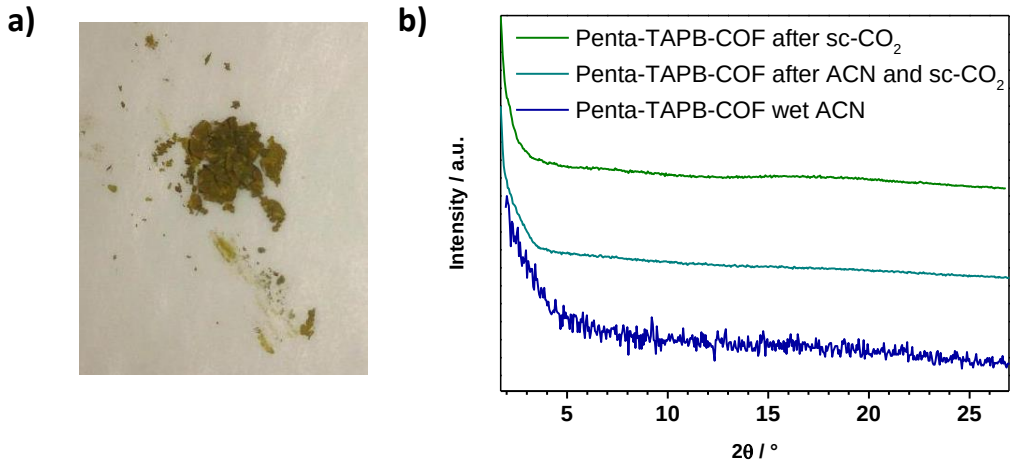

Figure 5-14: a) Picture of amorphous Penta-TAPB-COF as-synthesized to demonstrate the color of the powder, b) PXRD pattern showing the amorphous structure after diverse work-up conditions (ACN: washing with acetonitrile, sc-CO_2: supercritical CO_2 extraction).

Considering that numerous COFs have already been created with the TAPB node, it is expected that crystalline framework formation can still be realized with further intensive screening of all reaction and work-up parameters. In addition, pentacene-based molecules are often known to deteriorate and oxidize in air. While the condensation reaction was taking place under argon, PXRD and work-up were carried out in air which might lead to framework decomposition.

The pentacene-based COF will be subject of future experiments and will hopefully complement this mobility study to prove our hypothesis that elongation of the backbone improves the stacking interactions and consequently enhances charge carrier mobility. At the same time, these findings can potentially also be transferred to even longer or broader conjugated molecules enabling us to tailor mobility and electrical characteristics

of the resulting COF materials. Exploring the mechanism of synthesis and combining it with diverse measurement techniques will help identifying attractive candidates for future applications. COFs with high intrinsic charge carrier mobility and conductivity, without the need of doping, could open up new possibilities in current-based sensors and could lead to improved operation of electroactive and optoelectronic COF devices in general

5.4 Experimental Section

All applied materials (if not otherwise mentioned) were purchased from Aldrich or TCI in the common purities purum and puriss. All materials were used without further purification unless noted otherwise. Solvents were distilled in the vacuum for further use if not purchased from the supplier.

Powder X ray diffraction (PXRD) measurements were performed on a Bruker D8 Discover diffractometer with Ni filtered Kα radiation (λ = 1.54060 Å) and a position-sensitive detector (LynxEye) in reflection mode. For high resolution measurements, the as-synthesized COF material was placed on a silicon wafer and the measurement was carried out by applying a low scan speed (scanspeed: 7-10 sec/step; increment: 0.05 °2θ). For film measurements, the samples were measured by applying a detector scan. For this purpose, the tube was fixed at 0.01 °2θ and a low scan speed was applied speed (scanspeed: 5-8 sec/step; increment: 0.05 °2θ).

Based on the symmetry of the applied building blocks, the final eclipsed 2D COF structure can be approximately predicted and then be confirmed with experimental powder X-ray diffraction (PXRD) data. The **simulation** was carried out with the visualization environment of *Materials Studio software 4.4*, and the geometry of the two-dimensional layers was optimized with calculations using forcite and the DFTB+ method, respectively. Based on the geometry of the precursor molecules anthracene-linker and TAPB, the repeating unit was constructed into a unit of the *P6* space group. The repeating fragments were placed in the bare hexagonal unit cell and connected to each other, resulting in the complete unit cell. The geometry of the diverse reported COF layers was optimized in the unit cell using the Dreiding forcefield and the QEq correction for weak interactions.

Scanning electron microscopy (SEM) was performed on an FEI Helios G3 UC instrument at 2 kV. For this purpose the samples were put on an adhesive graphite film and sputtered with carbon with a BALTEC MED 020 Coating Sytem.

The **Focused Ion Beam (FIB)** method was also performed on an FEI Helios G3 UC instrument with a Ga energy of 30 kV. The resulting cross section was further analyzed by SEM using secondary electrons as well as backscattered electrons at different acceleration voltages.

Transmission electron microscopy (TEM) data were obtained with a Tecnai G2 20 S Twin at an acceleration voltage of 200 kV.

Nitrogen sorption was measured using a Quantachrome AUTOSORB 1 station at 77.3 K after degassing the samples for at least 12 h under vacuum at 100 °C (Anthra-TAPB-COF) and 120 °C (TA-TAPB-COF), respectively. The Brunauer–Emmett–Teller (BET) surface areas were calculated from the adsorption branch in the range of p/p_0 = 0.05–0.36 for each system. Pore sizes were calculated with a QSDFT adsorption model of N_2 on carbon (cylindrical/spherical, adsorption branch).

Super critical CO_2 extraction (sc-CO_2) was used as work-up for the diverse COFs to achieve a crystalline material with well-defined porosity. Therefore, the material (13 mg) was placed in a holder in a steel autoclave and sealed. The autoclave was filled with CO_2 and cooled down to 5-8 °C by putting the container into an ice bath. The material was further extracted at supercritical conditions for CO_2 (40 °C, 85 bar) for at least three hours.

Hall conductivity measurements were carried out on an ECOPIA HMS 3000 apparatus using a magnetic field of 0.55 T in the van der Pauw geometry connected by gold wires. The measurements were performed on films of different thicknesses (see Characterization Details) and on pellets (10 mm diameter), which were prepared by pressing the finely ground materials (precursors and COF material) under a pressure of 0.75 to 1.2 GPa, respectively.

Hole-only mobility measurements were recorded under vacuum using a Metrohm potentiostat (PGSTAT302N) at a scan rate of 0.1 Vs^{-1}.

5.4.1 Syntheses

Extensive screening of the reaction conditions led to the following synthesis procedures for the different COF materials (see next section). The crystalline materials were stored after CO_2 extraction work-up. The amorphous COF materials were stored without further CO_2 extraction for supplementary measurements.

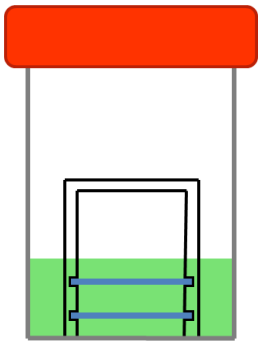

For mobility measurements on thin films a solvothermal reaction procedure was chosen. Here, the desired substrate was put upside-down into the reaction vessel. The substrate stabilized by a Teflon holder was immersed into the reaction mixture (see on the left side). For each film synthesis the appropriate reaction conditions, including the complete dissolution of the bulk reaction mixture, had to be identified.

5.4.1.1 Synthesis of TA-TAPB-COF Bulk Material

A 10 mL Schott Duran glass was charged with terephthalaldehyde (TA) (12.7 mg, 0.095 mmol, 1.5 eq) and 1,3,5-tri(4-aminophenyl)benzene (TAPB) (22.1 mg, 0.063 mmol, 1 eq.). A solvent mixture consisting of mesitylene and dioxane in the ratio 1:8 was given to the powder mixture (1.00 mL). In addition, acetic acid (6 M, 100 μL) was added acting as catalyst for forming the imine bonds. This reaction mixture was sonicated and further heated up to 70 °C for 72 hours. The resulting yellow solid was isolated by filtration and washed with dioxane (7 mL). This amorphous TA-TAPB-COF material was finally treated with sc-CO_2 extraction to achieve a crystalline product. Finally, TA-TAPB-COF was obtained as yellow powder (80%).

For amorphous COF material, the work-up using sc-CO_2 extraction was omitted while keeping all other reaction parameters constant.

5.4.1.2 Synthesis of TA-TAPB-COF Film Material

A 100 mL Schott Duran glass vial was charged with a smaller 10 mL glass vessel to reduce the reaction volume in the aperture and the reaction surface as well as for stabilizing the Teflon holder in the system. The smaller glass vessel was filled with the precursor molecules terephthalaldehyde (TA) (12.7 mg, 0.095 mmol, 1.5 eq) and 1,3,5-tri(4-aminophenyl)benzene (TAPB) (22.1 mg, 0.063 mmol, 1 eq.) followed by the solvent mixture consisting of dioxane and mesitylene at the ratio 8:1 (1.5 mL) including

the whole substrate to be covered. In addition, acetic acid (6 M, 150 µL) was added acting as catalyst for forming the imine bonds. This reaction mixture was mixed and further heated up to 70 °C for 24 hours. After the required reaction time, the substrate was removed from the reaction mixture and carefully cleaned from COF bulk material formed at the top of the substrate. The isolated film was further used for device construction.

To examine also thicker films and for FIB methods, the reaction time was extended to three days instead of 24 hours. All other reaction parameters remained unchanged.

5.4.1.3 Synthesis of Anthra-TAPB-COF Bulk Material

A 10 mL Schott Duran glass was charged with 9,10-anthracenedicarboxaldehyde (Anthra) (7.08 mg, 0.031 mmol, 1.5 eq) and 1,3,5-tri(4-aminophenyl)benzene (TAPB) (7.06 mg, 0.020 mmol, 1 eq.). A solvent mixture consisting mesitylene and chloroform at the ratio 1:2 was given to the powder mixture (0.50 mL). In addition, acetic acid (6 M, 50 µL) was added acting as catalyst for forming the imine bonds. This reaction mixture was sonicated and further heated up to 120 °C for 72 hours. The reddish orange solid was isolated by filtration and washed with freshly distilled chloroform (50 mL). This amorphous Anthra-TAPB-COF material was then treated with sc-CO_2 extraction to achieve a crystalline product. Finally, Anthra-TAPB-COF was obtained as redish orange powder (79%).

For amorphous COF material, the work-up using sc-CO_2 extraction was omitted while keeping all other reaction parameters constant.

5.4.1.4 Synthesis of Anthra-TAPB-COF Film Material

A 100 mL Schott Duran glass vial was charged with a smaller 10 mL glass vessel to reduce the reaction volume in the aperture. The smaller glass vessel was filled with the precursor molecules 9,10-anthracenedicarboxaldehyde (Anthra) (1.00 mg, 0.004 mmol, 1.4 eq) and 1,3,5-tri(4-aminophenyl)benzene (TAPB) (1,00 mg, 0.003 mmol, 1 eq.) followed by the solvent mixture consisting of chloroform and mesitylene in the ratio 2.4:1 (1.5 mL) including the whole substrate to be covered. In addition, acetic acid (6 M, 150 µL) was added acting as catalyst for forming the imine bonds. This reaction mixture was mixed and further heated up to 120 °C for 24 hours. After the needed reaction time, the substrate was removed from the reaction mixture and carefully

cleaned from COF bulk material formed at the top of the substrate. The isolated film was further used for device construction

5.4.1.5 Synthesis of 5a,6,13,13a-tetrahydro-6,13-[4,5]epidioxolo-pentacen-17-one (1)

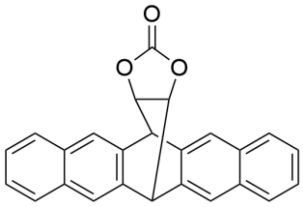

Pentacene (200 mg, 0.71 mmol, 1 eq.), 1,3-dioxol-2-one (0.07 mL, 1.3 mmol, 1.8 eq.) and 3 mL of toluene were added into an autoclave and heated to 180 °C for 72 hours. After cooling, the crystalline product was transferred into a flask, the solvent removed under reduced pressure and the solid purified *via* column chromatography (CH_2Cl_2:hexane 2:1) to obtain a colorless solid (187 mg, 0.51 mmol, 72%).

^{1}H-NMR (400 MHz, $CDCl_3$): 7.87 (m, 4H), 7.80 (m, 4H), 7.47 (m, 4H), 5.05 (s, 2H), 4.93 (s, 2H).

5.4.1.6 Synthesis of 5a,6,13,13a-tetrahydro-6,13-ethanopentacene-15,16-diol (2)

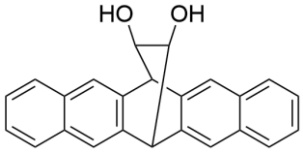

Compound **1** (187 mg, 0.51 mmol, 1 eq.) was suspended in 1,4-dioxane (8.4 mL) and aqueous, degassed 4M NaOH (2.8 mL) and refluxed for 2 hours under an argon atmosphere. Afterwards, the product was extracted with CH_2Cl_2 (3 × 15 mL), the combined organic phases dried over $MgSO_4$ and the solvent removed under reduced pressure to yield compound **2** as a light yellow solid (156 mg, 0.46 mmol, 90%).

^{1}H-NMR (400 MHz, $CDCl_3$): 7.86 (m, 2H), 7.80 (m, 6H), 7.45 (m, 4H), 4.66 (s, 2H), 4.23 (s, 2H), 2.22 (s, 2H).

5.4.1.7 Synthesis of Pentacene-6,13-dicarbaldehyde (Penta)

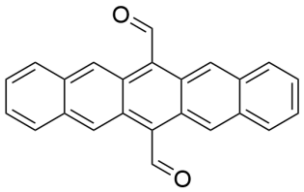

Compund **2** (117 mg, 0.35 mmol, 1 eq.) was dissolved in dry DMSO (5.90 mL) under an argon atmosphere and heated to 160 °C before adding IBX (2-Iodoxybenzoic acid) (stabilized, 45 wt%, , 258 mg, 0.42 mmol, 1.2 eq.). The solution was stirred for 20 minutes, afterwards letting it cool down to room temperature. The solution turns green.

To the green solution CH_2Cl_2 (degassed) (15 mL) and water (degassed) (10 mL) were added and the aqueous phase was extracted with CH_2Cl_2 (3 × 15 mL), under an argon atmosphere, dried over $MgSO_4$ and the solvent quickly removed under reduced pressure before the product was put under an argon atmosphere once more. Due to the instability of the molecule, it was thoroughly washed with methanol under an argon atmosphere, dried and directly used without further purification (69 mg, estimated 0.21 mmol, 59%). NMR analysis shows side products due to the insufficient purification method.

^{1}H-NMR (400 MHz, $CDCl_3$): 11.80 (s, 2H), 8.01 (m, 4H), 7.50 (m, 4H), 7.43 (m, 4H).

5.4.1.8 Synthesis of Penta-TAPB-COF Amorphous Bulk Material

A 10 mL Schott Duran glass was charged with 6,13-pentacenedicarboxaldehyde (Penta) (3.35 mg, 0.010 mmol, 1.5 eq) and 1,3,5-tri(4-aminophenyl)benzene (TAPB) (2.35 mg, 6.70 μmol, 1 eq.).

Based on successful results for the anthracene-based COF, the following solvent and acid combinations/ratios were used:

Table 5-4: Investigated solvent and acid combinations for Penta-TAPB-COF.

$CHCl_3$	Mesitylene	acetic acid 6M
400 µL	100 µL	50 µL (10%)
333 µL	167 µL	50 µL (10%)
250 µL	250 µL	50 µL (10%)
167 µL	333 µL	50 µL (10%)
333 µL	167 µL	25 µL (5%)
333 µL	167 µL	/

The reaction mixtures were further heated up to 120 °C for 72 hours. The brownish solid was isolated by filtration. Finally, amorphous Penta-TAPB-COF was obtained as brownish powder (69%).

5.4.2 Characterization Details

5.4.2.1 Simulation of Crystal Structures

Simulation of TA-TAPB-COF

Table 5-5: Refined crystal data for TA-TAPB-COF.

	TA-TAPB-COF
Chemical formula	$C_{72}H_{48}N_6$
Formula weight	997.10 g/mol
Crystal system	hexagonal
Space group	P 6 (168)
Unit cell dimension	a = b = 36.89 Å c = 3.65 Å α = β = 90.0° γ = 120.0°
Cell volume	4234.56 $Å^3$

Table 5-6: Atomic parameters for TA-TAPB-COF.

Atom	Atom label	x/a	y/b	z/c
C1	C	0.71006	0.35719	0.46962
C2	C	0.68591	0.37607	0.46950
C3	C	0.75594	0.38239	0.47057
C4	C	0.77637	0.42195	0.31515
C5	C	0.81918	0.44556	0.32104
C6	C	0.84272	0.43000	0.47011
C7	C	0.82279	0.39066	0.62604
C8	C	0.77995	0.36731	0.62885

N9	N	0.88655	0.45557	0.46841
C10	C	0.91285	0.44293	0.49917
C11	C	0.95737	0.47235	0.49850
H12	H	0.70076	0.40906	0.46968
H13	H	0.75960	0.43439	0.17767
H14	H	0.83441	0.47574	0.19846
H15	H	0.84005	0.37860	0.76036
H16	H	0.76584	0.33813	0.76859
H17	H	0.90268	0.41054	0.51507
C18	C	0.45771	0.47262	0.49937
C19	C	0.48512	0.45774	0.49845

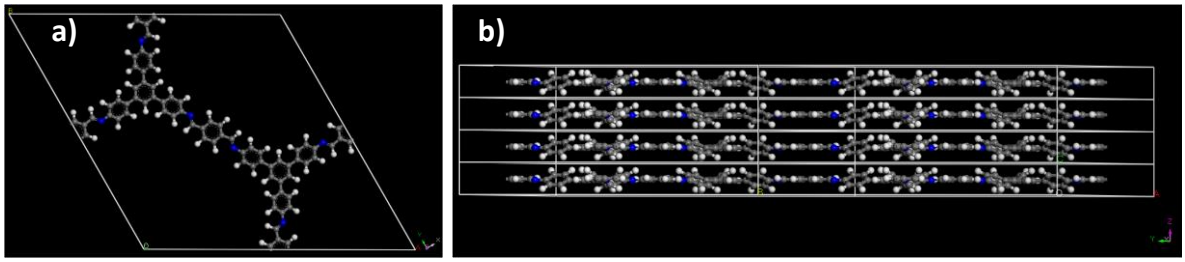

Figure 5-15: a) Simulation of the crystal lattice of the unit cell in an eclipsed arrangement for TA-TAPB-COF and b) side view along the *c*-axis of 4 unit cells stacked on top of each other demonstrating the twisted structure of the TAPB and the planarity of the TA building block.

Simulation of Anthra-TAPB-COF

Table 5-7: Refined crystal data for Anthra-TAPB-COF.

	Anthra-TAPB-COF
Chemical formula	$C_{69}H_{76}N_6$
Formula weight	1312.61 g/mol
Crystal system	hexagonal
Space group	P 6 (168)
Unit cell dimension	a = b = 36.26 Å c = 3.59 Å α = β = 90.0° γ = 120.0°
Cell volume	4041.10 $Å^3$

Table 5-8: Atomic parameters for Anthra-TAPB-COF.

Atom	**Atom label**	**x/a**	**y/b**	**z/c**
C1	C	0.71006	0.35719	0.46962
C2	C	0.68591	0.37607	0.46950
C3	C	0.75594	0.38239	0.47057
C4	C	0.77637	0.42195	0.31515
C5	C	0.81918	0.44556	0.32104

C6	C	0.84272	0.43000	0.47011
C7	C	0.82279	0.39066	0.62604
C8	C	0.77995	0.36731	0.62885
N9	N	0.88655	0.45557	0.46841
C10	C	0.91285	0.44293	0.49917
C11	C	0.95737	0.47235	0.49850
H12	H	0.70172	0.41210	0.46929
H13	H	0.75737	0.43548	0.17826
H14	H	0.83576	0.47574	0.19923
H15	H	0.84215	0.37713	0.75554
H16	H	0.76397	0.33463	0.76590
H17	H	0.90125	0.40764	0.52801
C18	C	0.45771	0.47262	0.49937
C19	C	0.48512	0.45774	0.49845
C20	C	0.58458	0.55479	0.50117
C21	C	0.59946	0.59708	0.50205
C22	C	0.57205	0.61196	0.50113
C23	C	0.52976	0.58455	0.49933
H24	H	0.60765	0.54226	0.50194
H25	H	0.63506	0.62015	0.50356
H26	H	0.58457	0.64756	0.50187
H27	H	0.50669	0.59708	0.49855

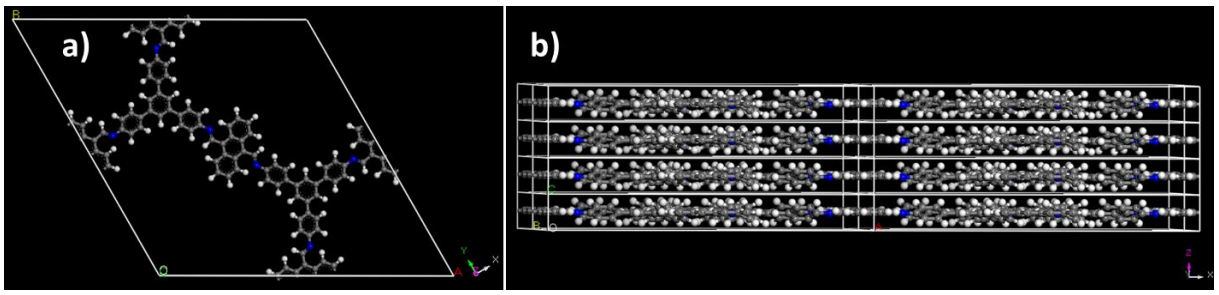

Figure 5-16: a) Simulation of the crystal lattice of the unit cell in an eclipsed arrangement for Anthra-TAPB-COF and b) side view along the *c*-axis of 4 unit cells stacked on top of each other demonstrating the twisted structure of the TAPB and the planarity of the anthracene building block.

Simulation of Penta-TAPB-COF

To predict the structure of Penta-TAPB-COF, simulations of the crystal structure were performed.

Table 5-9: Refined crystal data for Penta-TAPB-COF.

	Penta-TAPB-COF
Chemical formula	$C_{120}H_{72}N_6$
Formula weight	1597.90 g/mol
Crystal system	hexagonal
Space group	P 6 (168)
Unit cell dimension	a = b = 37.48 Å c = 3.69 Å α = β = 90.0° γ = 120.0°
Cell volume	4401.46 $Å^3$

Table 5-10: Atomic parameters for Penta-TAPB-COF.

Atom	**Atom label**	**x/a**	**y/b**	**z/c**
C1	C	0.71035	0.35567	0.26421
C2	C	0.68768	0.37632	0.26273
C3	C	0.75653	0.37933	0.27773
C4	C	0.77900	0.41976	0.13637
C5	C	0.82189	0.44239	0.16526
C6	C	0.84363	0.42521	0.32827
C7	C	0.82176	0.38437	0.45689
C8	C	0.77881	0.36203	0.43712
N9	N	0.88760	0.45037	0.35856
C10	C	0.91151	0.44342	0.56952
C11	C	0.95670	0.47252	0.57785
H12	H	0.70389	0.40950	0.26405
H13	H	0.76385	0.43400	-0.00379
H14	H	0.83837	0.47353	0.05818
H15	H	0.83734	0.36954	0.57798
H16	H	0.76335	0.33168	0.55960
H17	H	0.89899	0.41662	0.74602
C18	C	0.45683	0.47265	0.57785
C19	C	0.48426	0.45691	0.57785
C20	C	0.41396	0.44454	0.57785
C21	C	0.39816	0.40215	0.57785
C22	C	0.42518	0.38689	0.57785
C23	C	0.46763	0.41411	0.57785
C24	C	0.40926	0.34441	0.57785

C25	C	0.36678	0.31736	0.57785
C26	C	0.33997	0.33245	0.57785
C27	C	0.35551	0.37469	0.57785
H28	H	0.39223	0.45511	0.57785
H29	H	0.48725	0.40134	0.57785
H30	H	0.42962	0.33214	0.57785
H31	H	0.35463	0.28464	0.57785
H32	H	0.30708	0.31140	0.57785
H33	H	0.33423	0.38587	0.57785

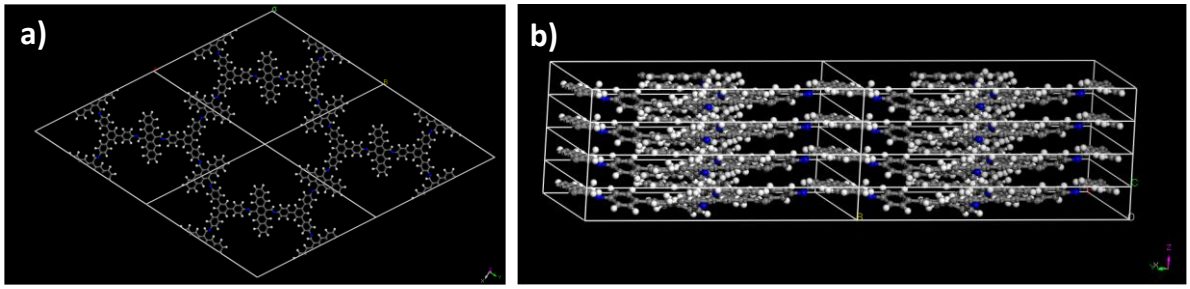

Figure 5-17: a) Simulation of the crystal lattice of four unit cells in an eclipsed arrangement for Penta-TAPB-COF resulting in a hexagonal pore and b) side view along the *c*-axis of 4 unit cells stacked on top of each other demonstrating the twisted structure of the TAPB and the planarity of the pentacene building block

5.4.2.2 Electrical Characterization of Bulk Material

The following pellets were pressed out of the synthesized COF materials (10 mm diameter pellets, 15-40 mg of COF material for one pellet). Due to the different applied pressures also varying thicknesses of the pellets can be achieved. The values of the measured thickness and the conductivity and Hall mobility are given in the tables below. Per pellet, several measurements were performed to achieve a good averaged value. These values were further averaged to get an overview of the material´s electrical behavior.

Table 5-11: Measured conductivity and Hall mobility values for crystalline TA-TAPB-COF pressed into pellets of different thicknesses; values are averaged at the end of each table per pellet.

Pellet 1	Conductivity [Scm^{-1}]	Hall mobility [$cm^2V^{-1}s^{-1}$]
(190 µm)	6.47×10^{-08}	1.19×10^{02}
	4.52×10^{-07}	4.84×10^{02}
	1.54×10^{-07}	6.12×10^{00}
	8.60×10^{-08}	5.62×10^{00}
	4.36×10^{-07}	2.56×10^{02}
	6.13×10^{-07}	3.02×10^{02}
	1.06×10^{-08}	1.74×10^{01}
	1.56×10^{-07}	1.35×10^{02}
	3.30×10^{-07}	8.50×10^{02}
	1.00×10^{-06}	9.72×10^{01}
Average	**3.30×10^{-07}**	**2.27×10^{02}**

Pellet 2	Conductivity [Scm^{-1}]	Hall mobility [$cm^2V^{-1}s^{-1}$]
(90 µm)	6.65×10^{-07}	2.37×10^{02}
	4.60×10^{-07}	3.82×10^{02}
	2.22×10^{-07}	1.45×10^{02}
	4.15×10^{-07}	3.16×10^{01}
	5.25×10^{-07}	1.74×10^{02}
	3.60×10^{-07}	3.01×10^{02}
	6.67×10^{-07}	2.50×10^{02}
	4.25×10^{-07}	4.34×10^{01}
	2.69×10^{-07}	2.44×10^{02}
	4.49×10^{-07}	5.63×10^{02}
Average	**4.46×10^{-07}**	**2.37×10^{02}**

Pellet 3	Conductivity [Scm^{-1}]	Hall mobility [$cm^2V^{-1}s^{-1}$]
(130 µm)	5.04×10^{-07}	6.05×10^{01}
	3.54×10^{-07}	9.04×10^{02}
	3.13×10^{-07}	3.12×10^{02}
	3.57×10^{-07}	2.22×10^{02}
	3.16×10^{-07}	1.19×10^{01}
	2.95×10^{-07}	6.48×10^{02}
	2.23×10^{-07}	1.63×10^{00}
	2.90×10^{-07}	1.67×10^{01}
	3.93×10^{-07}	3.76×10^{02}
	4.12×10^{-07}	1.26×10^{02}
Average	**3.46×10^{-07}**	**2.68×10^{02}**

Pellet 4	Conductivity [Scm^{-1}]	Hall mobility [$cm^2V^{-1}s^{-1}$]
(200 µm)	1.99×10^{-07}	2.01×10^{02}
	2.13×10^{-07}	9.20×10^{00}
	1.96×10^{-07}	4.07×10^{01}
	4.77×10^{-07}	4.31×10^{02}
	2.78×10^{-07}	7.51×10^{02}
	1.19×10^{-08}	1.32×10^{01}
	2.18×10^{-07}	2.05×10^{01}
	2.13×10^{-07}	6.08×10^{01}
	2.80×10^{-07}	1.10×10^{02}
	5.76×10^{-07}	7.29×10^{02}
Average	**2.66×10^{-07}**	**2.37×10^{02}**

Pellet 5	Conductivity [Scm^{-1}]	Hall mobility [$cm^2V^{-1}s^{-1}$]
(230 µm)	1.21×10^{-08}	1.20×10^{02}
	2.71×10^{-08}	1.72×10^{01}
	1.31×10^{-08}	1.46×10^{02}
	1.43×10^{-08}	1.45×10^{02}
	2.43×10^{-08}	3.10×10^{01}
	2.70×10^{-08}	1.33×10^{02}
	2.30×10^{-08}	1.24×10^{01}
	2.03×10^{-08}	1.32×10^{02}
	2.01×10^{-08}	2.22×10^{01}
	1.56×10^{-08}	3.25×10^{01}
Average	**1.97×10^{-08}**	**7.91×10^{01}**

Pellet 6	Conductivity [Scm^{-1}]	Hall mobility [$cm^2V^{-1}s^{-1}$]
(160 µm)	2.13×10^{-08}	1.36×10^{01}
	3.06×10^{-08}	2.14×10^{02}
	3.20×10^{-08}	6.33×10^{00}
	2.68×10^{-08}	7.44×10^{01}
	2.99×10^{-08}	1.00×10^{02}
	2.80×10^{-08}	9.39×10^{01}
	1.79×10^{-08}	7.45×10^{01}
	2.04×10^{-08}	7.33×10^{01}
	2.99×10^{-08}	1.76×10^{02}
	3.32×10^{-08}	2.70×10^{02}
Average	**2.70×10^{-08}**	**1.09×10^{02}**

Table 5-12: Measured conductivity and Hall mobility values for crystalline Anthra-TAPB-COF pressed into pellets of different thickness; values are averaged at the end of each table per pellet.

Pellet 1	Conductivity [Scm^{-1}]	Hall mobility [$cm^2V^{-1}s^{-1}$]
(140 µm)	3.42×10^{-08}	2.02×10^{01}
	5.62×10^{-08}	6.55×10^{01}
	3.43×10^{-08}	1.69×10^{02}
	4.79×10^{-08}	2.35×10^{02}
	6.42×10^{-08}	2.93×10^{02}
	4.97×10^{-08}	5.37×10^{01}
	4.89×10^{-08}	1.68×10^{02}
	4.79×10^{-08}	1.52×10^{01}
	4.31×10^{-08}	1.96×10^{01}
	2.75×10^{-08}	1.12×10^{01}
Average	**4.54×10^{-08}**	**1.05×10^{02}**

Pellet 2	Conductivity [Scm^{-1}]	Hall mobility [$cm^2V^{-1}s^{-1}$]
(110 µm)	1.30×10^{-06}	3.56×10^{02}
	8.42×10^{-07}	1.75×10^{03}
	8.49×10^{-07}	2.08×10^{02}
	1.36×10^{-06}	1.35×10^{03}
	1.60×10^{-06}	4.94×10^{02}
	1.43×10^{-06}	9.92×10^{01}
	5.48×10^{-07}	7.78×10^{02}
	7.61×10^{-07}	2.64×10^{02}
	4.52×10^{-07}	2.60×10^{02}
	3.92×10^{-07}	7.84×10^{01}
Average	**9.54×10^{-07}**	**5.64×10^{02}**

Pellet 3	Conductivity [Scm^{-1}]	Hall mobility [$cm^2V^{-1}s^{-1}$]
(90 µm)	3.96×10^{-08}	1.21×10^{02}
	1.30×10^{-07}	4.44×10^{01}
	1.63×10^{-07}	6.82×10^{02}
	1.15×10^{-07}	5.38×10^{02}
	1.28×10^{-07}	6.04×10^{02}
	2.30×10^{-07}	8.65×10^{02}
	1.40×10^{-07}	6.04×10^{02}
	8.33×10^{-08}	3.83×10^{02}
	6.65×10^{-08}	2.72×10^{02}
	7.61×10^{-08}	2.87×10^{02}
Average	**1.17×10^{-07}**	**4.40×10^{02}**

Pellet 4	Conductivity [Scm^{-1}]	Hall mobility [$cm^2V^{-1}s^{-1}$]
(100 µm)	7.59×10^{-08}	2.34×10^{02}
	3.72×10^{-07}	1.82×10^{03}
	1.98×10^{-06}	1.34×10^{03}
	1.20×10^{-07}	3.32×10^{02}
	6.08×10^{-08}	1.98×10^{02}
	6.92×10^{-08}	1.93×10^{02}
	8.71×10^{-08}	2.20×10^{01}
	6.70×10^{-08}	8.99×10^{01}
	7.94×10^{-07}	2.25×10^{03}
	7.42×10^{-08}	2.38×10^{02}
Average	**3.70×10^{-07}**	**6.70×10^{02}**

Pellet 5	Conductivity [Scm^{-1}]	Hall mobility [$cm^2V^{-1}s^{-1}$]
(120 µm)	1.95×10^{-07}	5.13×10^{02}
	1.59×10^{-07}	6.93×10^{00}
	1.24×10^{-07}	1.80×10^{02}
	5.05×10^{-07}	3.32×10^{03}
	1.55×10^{-07}	2.55×10^{01}
	1.71×10^{-07}	2.03×10^{02}
	1.88×10^{-07}	4.03×10^{01}
	2.81×10^{-07}	1.39×10^{03}
	2.75×10^{-07}	1.54×10^{02}
	4.01×10^{-07}	4.02×10^{02}
Average	**2.45×10^{-07}**	**6.23×10^{02}**

Pellet 6	Conductivity [Scm^{-1}]	Hall mobility [$cm^2V^{-1}s^{-1}$]
(100 µm)	3.59×10^{-08}	1.43×10^{02}
	1.44×10^{-07}	1.30×10^{02}
	2.31×10^{-07}	6.06×10^{02}
	2.35×10^{-07}	1.34×10^{02}
	6.67×10^{-07}	5.74×10^{02}
	2.05×10^{-07}	3.99×10^{02}
	5.20×10^{-07}	1.19×10^{03}
	2.62×10^{-07}	8.62×10^{01}
	3.81×10^{-07}	5.31×10^{01}
	7.36×10^{-07}	2.36×10^{03}
Average	**3.42×10^{-07}**	**5.67×10^{02}**

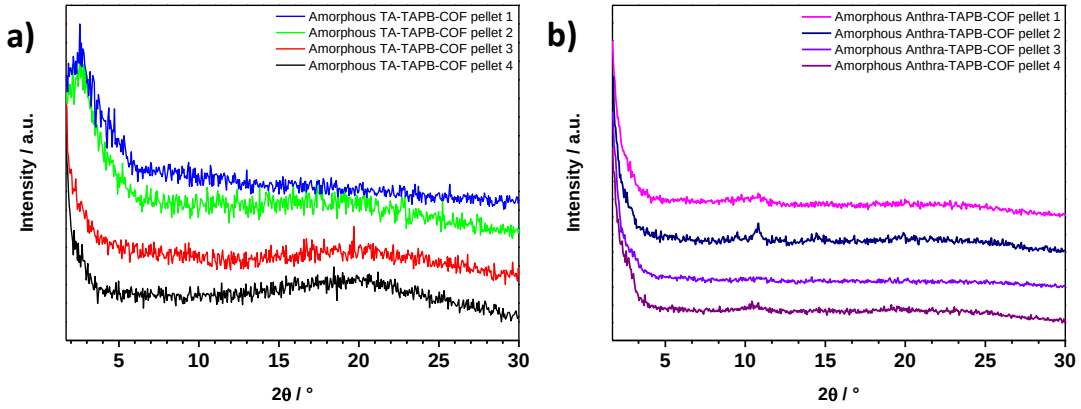

Figure 5-18: a) PXRD pattern of amorphous TA-TAPB-COF pressed into pellets for van der Pauw measurements, b) PXRD pattern of amorphous Anthra-TAPB-COF pressed into pellets for van der Pauw measurements.

Table 5-13: Averaged measured conductivity and Hall mobility values for amorphous TA-TAPB-COF, Anthra-TAPB-COF and the precursors (TA, Anthra, TAPB), respectively.

	Averaged conductivity [Scm^{-1}]	**Averaged Hall mobility [$cm^2V^{-1}s^{-1}$]**
Amorphous		
TA-TAPB-COF	2.31×10^{-07}	5.97×10^{02}
Amorphous		
Anthra-TAPB-COF	3.97×10^{-07}	7.86×10^{02}
Precursors		
TA	4.30×10^{-07}	9.01×10^{02}
TAPB	3.60×10^{-07}	3.00×10^{02}
Anthra	5.26×10^{-07}	1.84×10^{03}

5.4.2.3 Electrical Characterization of Film Material

The thickness of the synthesized films was determined by SEM cross section measurements as well as using a focused ion beam method (FIB). The films were placed in the van der Pauw holder and measured with the same parameters as installed for the bulk pellet measurements.

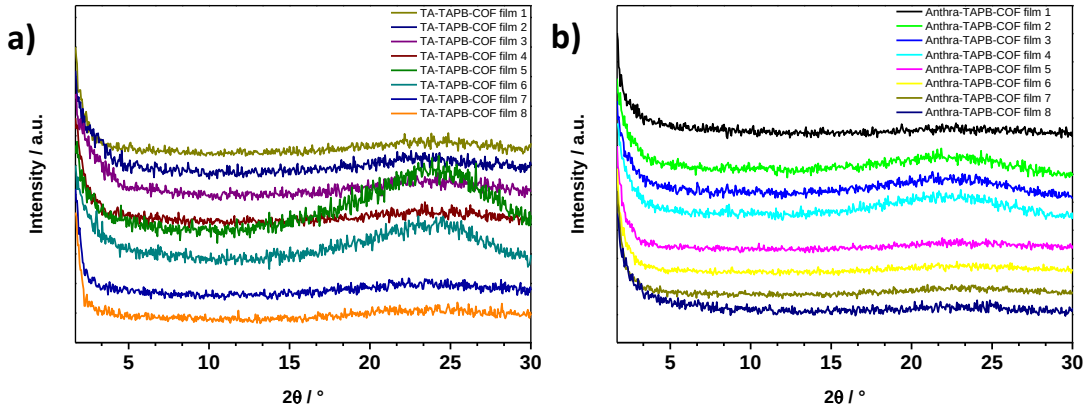

Figure 5-19: PXRD pattern measured in reflection mode on glass substrates of a) TA-TAPB-COF (250-300 nm) and b) Anthra-TAPB-COF (250-300 nm).

The focused ion beam method (FIB) was applied for a thick TA-TAPB-COF film which was synthesized under the given conditions with a longer reaction time, namely three days instead of one to achieve a thicker film of the same material. As visible in the figure below, a cross-sectional area was prepared using a Ga energy of 30 kV on the surface of the film. The film thickness was analyzed by SEM resulting in average values of 1.6 µm. The cross section shows the TA-TAPB-COF film appearing in black color on the grey glass surface. For conductivity reasons, the film was coated before with Pt depositing on the surface resulting in a very thin Pt film (80 – 100 nm in Figure 5-20d) followed by a thicker layer on top. The film appears to be quite smooth with a well-distributed thickness accompanied by few agglomerated particles (attributed to secondary nucleation) on top of the film (see Figure 5-20).

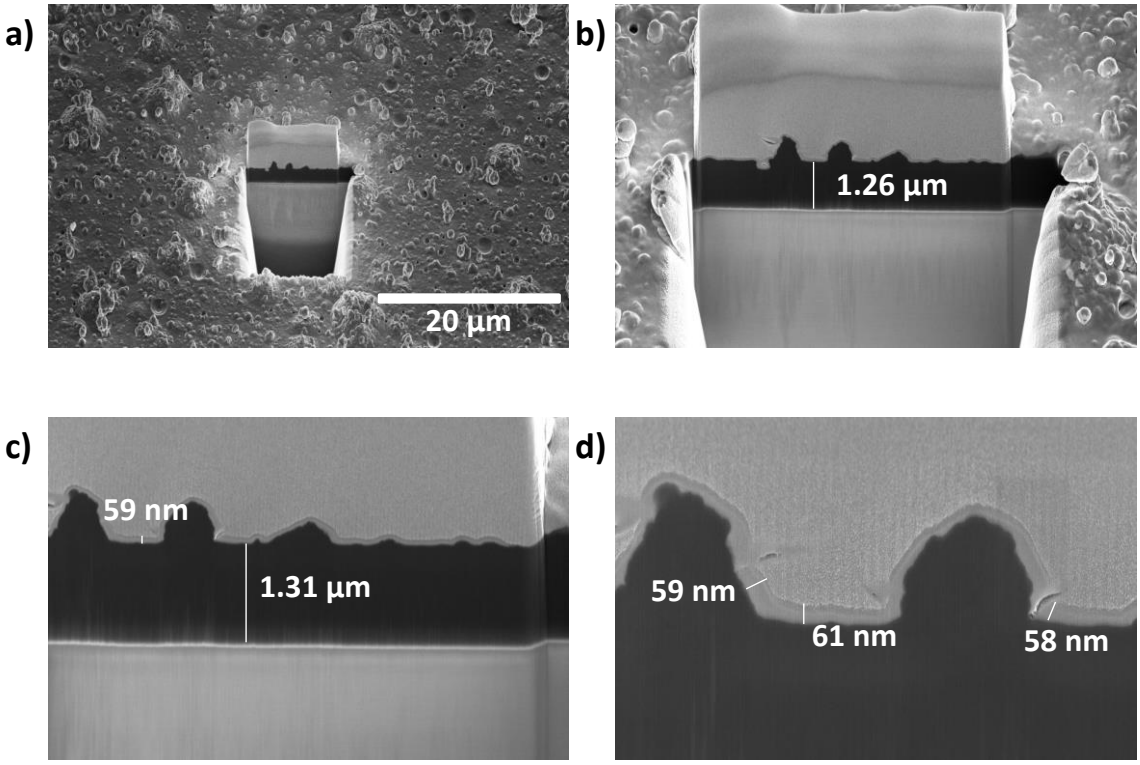

Figure 5-20: Pictures obtained with the FIB method applied on a 1.3 µm thick TA-TAPB-COF film. Here, a cross-sectional area was fabricated using a Ga energy of 30 kV. Afterwards, the cross section was analyzed by SEM applying secondary electrons and backscattered electrons at different acceleration voltages. a) Top view of prepared cross-sectional area, b) - d) different scales of measured film thickness with specified values. The COF film was protected by a thin Pt film (around 60 nm) induced by an electron beam followed by a thick Pt coverage produced by an ion beam.

5.4.2.4 Electrical Characterization of Hole-Only Devices (HOD)

Hole-only devices were prepared under the following conditions: ITO substrates (1.5 × 2.0 cm, VisionTek, 12−15 Ωsq^{-1}) were etched (to achieve the shape illustrated in Figure 5-10a) applying Zn powder in combination with a 2 M HCL solution and cleaned with HELLMANEX soap and ethanol. After cleaning, MoO_x was deposited on the substrate by thermal evaporation in the vacuum (1×10^{-6} mbar). The COF films were grown on the material as mentioned above. A top electrode of MoO_x (10 nm) followed by a gold layer (40 nm) was again deposited in the vacuum (1×10^{-6} mbar). The thickness of the films was determined by SEM cross section measurements as well as a focused ion beam method (FIB) for each device, respectively.

To obtain deeper insights into the material, thin film devices were also fabricated with different thickness (see Experimental Section). The following FIB method determined the exact thickness and resulted in around 20 nm sample thickness. The cross-sectional area was fabricated using a Ga energy of 30 kV. Afterwards, the cross section was

analyzed by SEM applying secondary electrons and backscattered electrons at different acceleration voltages. The thickness of the investigated thin films showed a limitation concerning mobility, i.e. short circuits.

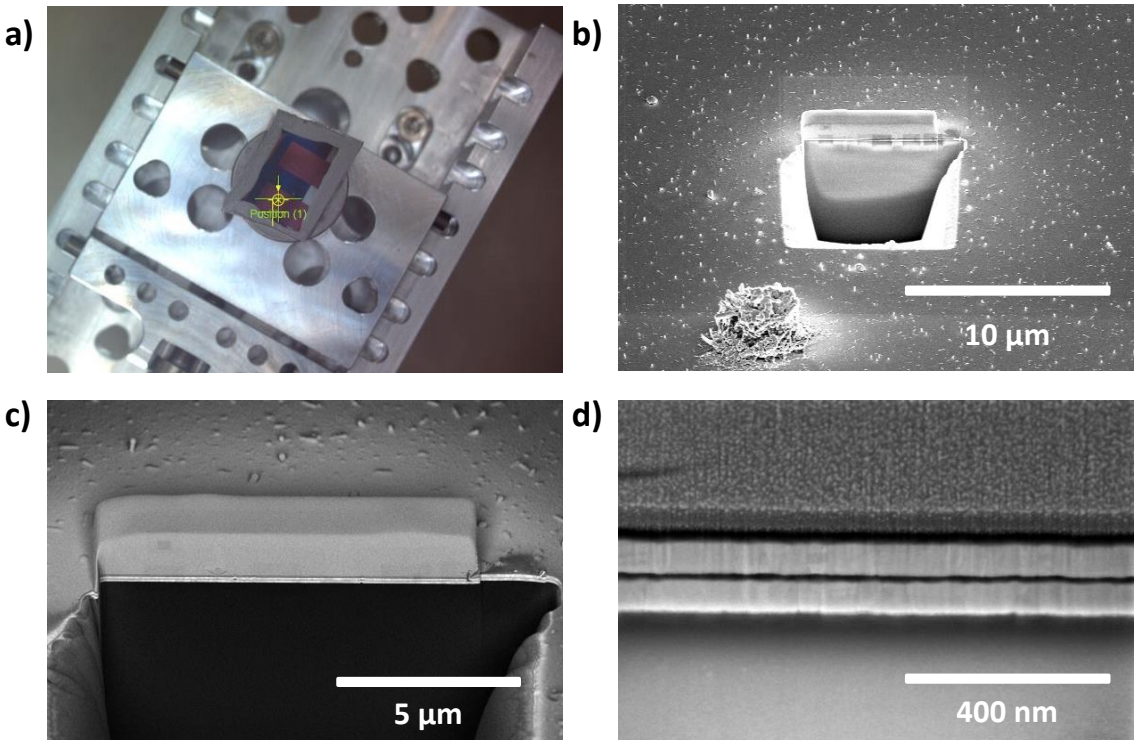

Figure 5-21: Pictures of FIB method applied on a 16 nm thin film of Anthra-TAPB-COF. a) top view of Anthra-TAPB-COF thin film device illustrating the position of the further FIB Ga beam positioned on a pixel, b) top view of the prepared cross-sectional area, also visualizing the roughness of the synthesized film, c) higher magnification to show the size of the cross-sectional area, d) measured film thickness resulting in a film of around 20 nm.

5.5 References

1. S.-Y. Ding and W. Wang, *Chem. Soc. Rev.* **2013**, *42*, 548-568.
2. A. P. Côté, A. I. Benin, N. W. Ockwig, M. O'Keeffe, A. J. Matzger, and O. M. Yaghi, *Science* **2005**, *310*, 1166-1170.
3. M. S. Lohse and T. Bein, *Adv. Funct. Mater.* **2018**, *28*, 1705553.
4. F. J. Uribe-Romo, J. R. Hunt, H. Furukawa, C. Klöck, M. O'Keeffe, and O. M. Yaghi, *J. Am. Chem. Soc.* **2009**, *131*, 4570-4571.
5. H. M. El-Kaderi, J. R. Hunt, J. L. Mendoza-Cortés, A. P. Côté, R. E. Taylor, M. O'Keeffe, and O. M. Yaghi, *Science* **2007**, *316*, 268-272.
6. X. Feng, X. Ding, and D. Jiang, *Chem. Soc. Rev.* **2012**, *41*, 6010-6022.
7. S. Wan, F. Gándara, A. Asano, H. Furukawa, A. Saeki, S. K. Dey, L. Liao, M. W. Ambrogio, Y. Y. Botros, X. Duan, S. Seki, J. F. Stoddart, and O. M. Yaghi, *Chem. Mater.* **2011**, *23*, 4094-4097.
8. N. Huang, P. Wang, and D. Jiang, *Nat. Rev. Mater.* **2016**, *1*, 16068.
9. S.-L. Cai, Y.-B. Zhang, A. B. Pun, B. He, J. Yang, F. M. Toma, I. D. Sharp, O. M. Yaghi, J. Fan, S.-R. Zheng, W.-G. Zhang, and Y. Liu, *Chem. Sci.* **2014**, *5*, 4693-4700.
10. S. Jin, T. Sakurai, T. Kowalczyk, S. Dalapati, F. Xu, H. Wei, X. Chen, J. Gao, S. Seki, and S. Irle, *Chem. – Eur. J.* **2014**, *20*, 14608-14613.
11. H. Ding, Y. Li, H. Hu, Y. Sun, J. Wang, C. Wang, C. Wang, G. Zhang, B. Wang, and W. Xu, *Chem. – Eur. J.* **2014**, *20*, 14614-14618.
12. F. Deschler, E. Da Como, T. Limmer, R. Tautz, T. Godde, M. Bayer, E. von Hauff, S. Yilmaz, S. Allard, U. Scherf, and J. Feldmann, *Phys. Rev. Lett.* **2011**, *107*, 127402.
13. L. Wang, B. Dong, R. Ge, F. Jiang, and J. Xu, *ACS Appl. Mater. Interfaces* **2017**, *9*, 7108-7114.
14. A. J. Mozer, N. S. Sariciftci, A. Pivrikas, R. Österbacka, G. Juška, L. Brassat, and H. Bässler, *Phys. Rev. B* **2005**, *71*, 035214.
15. D. Kumar and R. C. Sharma, *Eur. Polym. J.* **1998**, *34*, 1053-1060.
16. C. K. Chiang, C. R. Fincher, Y. W. Park, A. J. Heeger, H. Shirakawa, E. J. Louis, S. C. Gau, and A. G. MacDiarmid, *Phys. Rev. Lett.* **1977**, *39*, 1098-1101.
17. D. Ateh, H. Navsaria, and P. Vadgama, *J. Royal Soc. Interface* **2006**, *3*, 741-752.

18. R. Balint, N. J. Cassidy, and S. H. Cartmell, *Acta Biomater.* **2014**, *10*, 2341-2353.
19. S. I. Na, S. S. Kim, J. Jo, and D. Y. Kim, *Adv. Mater.* **2008**, *20*, 4061-4067.
20. Y. H. Kim, C. Sachse, M. L. Machala, C. May, L. Müller-Meskamp, and K. Leo, *Adv. Funct. Mater.* **2011**, *21*, 1076-1081.
21. H. Klauk, *Organic electronics: materials, manufacturing, and applications*, John Wiley & Sons, **2006**.
22. M. Pope and C. E. Swenberg, *Ann. Rev. Phys. Chem.* **1984**, *35*, 613-655.
23. H. Klauk, M. Halik, U. Zschieschang, G. Schmid, W. Radlik, and W. Weber, *J. App. Phys.* **2002**, *92*, 5259-5263.
24. M. Pope and C. E. Swenberg, *Electronic processes in organic crystals and polymers*, Oxford University Press New York, **1999**.
25. O. D. Jurchescu, J. Baas, and T. T. Palstra, *Appl. Phys. Lett.* **2004**, *84*, 3061-3063.
26. S. K. Park, T. N. Jackson, J. E. Anthony, and D. A. Mourey, *Appl. Phys. Lett.* **2007**, *91*, 063514.
27. S. Rager, A. C. Jakowetz, B. Gole, F. Beuerle, D. D. Medina, and T. Bein, *Chem. Mater.* **2019**, *31*, 2707-2712.
28. N. Keller, D. Bessinger, S. Reuter, M. Calik, L. Ascherl, F. C. Hanusch, F. Auras, and T. Bein, *J. Am. Chem. Soc.* **2017**, *139*, 8194-8199.
29. N. Huang, X. Ding, J. Kim, H. Ihee, and D. Jiang, *Angew. Chem. Int. Ed.* **2015**, *54*, 8704-8707.
30. D. D. Medina, V. Werner, F. Auras, R. Tautz, M. Dogru, J. Schuster, S. Linke, M. Döblinger, J. Feldmann, P. Knochel, and T. Bein, *ACS Nano* **2014**, *8*, 4042-4052.
31. D. D. Medina, M. L. Petrus, A. N. Jumabekov, J. T. Margraf, S. Weinberger, J. M. Rotter, T. Clark, and T. Bein, *ACS nano* **2017**, *11*, 2706-2713.

6 A new Postsynthetic Modification Approach for Covalent Organic Frameworks

This chapter is based on the following publication:

Sabrina Rager, Constantin v. Schirnding, Torben Sick, Dana D. Medina, Andreas C. Jakowetz, and Thomas Bein, **2019**, to be submitted.

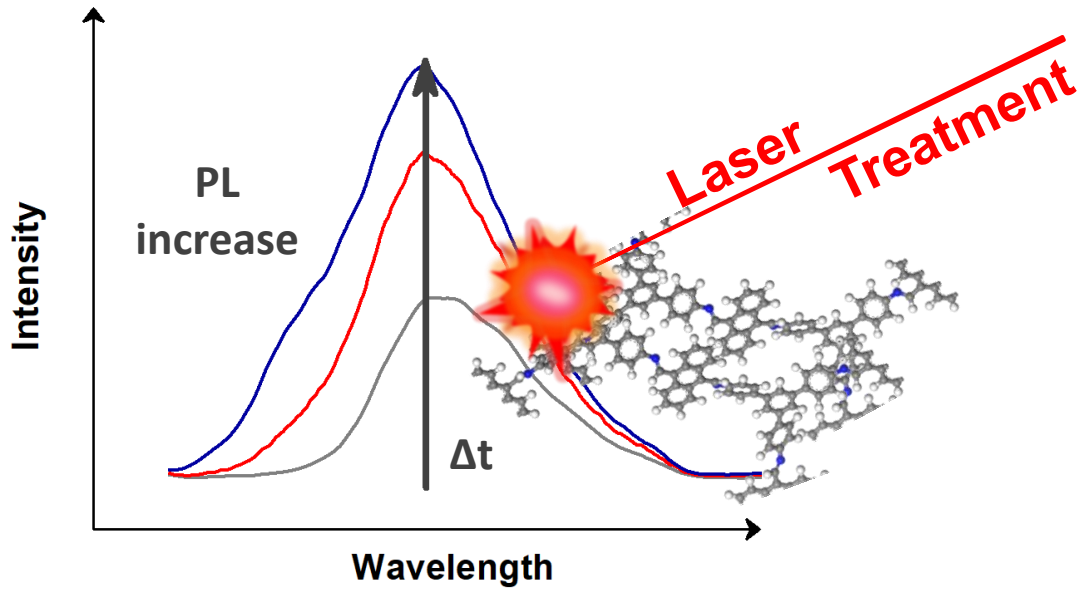

Abstract

Covalent organic frameworks (COFs), crystalline porous materials made of organic building blocks, have attracted much interest during the last years in view of their great tunability and associated range of potential applications. The implementation of building blocks offering important features such as charge transport or light harvesting into two-dimensional frameworks is an intriguing goal in materials science. However, combining promising optical properties of the chosen building blocks with high electrical conductivity can be challenging when dealing with defects within the structure arising from synthesis. Here, we report a new postsynthetic treatment based on light-induced defect reduction. This is demonstrated on a novel imine-based Anthra-TAPB-COF consisting of anthracene-9,10-dicarboxaldehyde (Anthra) and 1,3,5-tris(4-aminophenyl)benzene (TAPB) building blocks. The applied laser light leads to opening and reformation of imine bonds resulting in a significant decrease of defect sites and an increase of photoluminescence. Due to the absorption profile, this technique is particularly interesting for thin film treatments, which could improve the performance of optoelectronic devices.

6.1 Introduction

In recent years, scientists have developed a new class of porous crystalline materials called covalent organic frameworks (COFs).[1] COFs can be seen as multi-dimensional polymers and a large variety of structures can be realised due to the vast number of applicable building blocks and diverse binding motifs.[2] Their structure can be extended from stacked two-dimensional sheets to three-dimensional networks.[3, 4] Their main characteristics, apart from porosity and high crystallinity, include high structural and chemical diversity based on a vast range of molecular building blocks, and in some cases even high chemical stability.[5] Moreover, recent investigations even showed the ability to synthesize woven structures which incorporate flexibility and dynamics within the framework.[6, 7]

A special task when exploring COFs is to find a suitable precursor combination for the framework formation. Often, the choice of building blocks is based on their intrinsic properties which are desired to be embedded into a solid framework targeting a specific functionality.[8] For optoelectronic applications, molecules with optical properties such as strong absorption of visible light and photoluminescence as well as high electrical conductivity and charge carrier mobility are of particular interest.

Many synthetic procedures do not directly provide an ideal crystalline COF structure with the expected porosity. This may be due to the presence of unreacted precursors, oligomers obstructing the channel system, packing defects, grain boundaries and other deviations from the ideal structure. One way to enhance porosity post-synthesis *via* removal of guest molecules is by extraction, for example soxhlet-extraction.[9] Next to the conventional methods, such as ultrasound-assisted or shaking extraction, other improvements have been developed during the last years. This includes microwave-assisted processes and microwave-assisted solvent-extraction converting conventional soxhlet-extraction into a more efficient tool.[10]

Other postsynthetic treatments are solvent rinsing or supercritical CO_2-extraction, which was used to obtain porous coordination polymers and was demonstrated to be suitable for the recovery of crystalline frameworks.[11, 12] Recently, our group reported the reorganization of randomly displaced 1,3,5-tris(4-aminophenyl)benzene (TAPB) COF layers into crystalline networks using supercritical CO_2 extraction. While applying this postsynthetic process, the displacement and reorganisation can be cycled and allows for tuning the COF crystallinity and porosity.[12]

However, postsynthetic processing methods for COFs concerning solvent-free and clean technologies have not been widely explored. Therefore, enhancing structural properties by postsynthetic treatments (PST) is still an open challenge. Here, we are aiming at developing a fast and straightforward way to improve the COF structural and associated optical features, which ideally would be widely applicable to other polymer and COF systems. As recently reported by Kim *et al.*, imine bonds and subsequently a COF film were formed at a water-air interface *via* a photon-assisted imine condensation reaction upon irradiation with a solar simulator.[13] That synthesis was successfully performed for a 1,3,5-tris(4-aminophenyl)-benzene (TAPB) and terephthalaldehyde (TA) based COF. In our study, we transfer the above-mentioned photon-assisted imine condensation reaction to a PST. For higher photoactivity at longer wavelengths, we chose an anthracene derivative as linear linking molecule rather than TA in combination with TAPB.

Anthracene is a widely-studied molecule and has already been implemented into different COF systems.[14-16] One of the first examples was reported by our group, dealing with the incorporation of a anthracene catechol derivative, modified with methyl chains at the backbone to increase solubility in combination with a boronic acid counterpart resulting in an open pore structure of around 4 nm.[16] Anthracene-based

COFs were also explored by Jiang's group with both boronate ester and imine binding motifs.[14, 15] In the case of 2,3,6,7-tetrahydroxy anthracene reacted with 1,3,5-benzenetriboronic acid, the COF showed a photo-activated and thermally reversible cycloaddition reaction between anthracene units of successive COF layers.[14] Another linear implementation of the anthracene backbone with imine coupling, was used in COFs serving as heterogeneous catalysts for Diels-Alder reactions.[15]

Using the anthracene building block, we explore a new PST approach under illumination in the solid state. Here, we use a UV laser to illuminate the COF material under argon. Upon this treatment, we detect and improve photophysical features related to structural rearrangement and bond formation in the solid matrix over several minutes. This PST effect is established as an increase of the COF´s photoluminescence signal upon longer illumination times. Furthermore, we were able to confirm photo-induced imine bond formation through infrared microscopy, pointing towards a reduced concentration of defects and traps after the irradiation treatment.

6.2 Results and Discussion

First, we report the synthesis of a novel COF based on an anthracene building block and TAPB. The framework synthesis is based on the formation of fully conjugated imine bonds *via* co-condensation of anthracene-9,10-dicarboxaldehyde (Anthra) and 1,3,5-tris(4-aminophenyl)benzene (TAPB) (see Figure 6-1a). Briefly, the COF was synthesized under solvothermal reaction conditions yielding Anthra-TAPB-COF with excellent crystallinity, porosity, as well as the capability to heal defects within the framework in a postsynthetic laser-induced healing treatment.

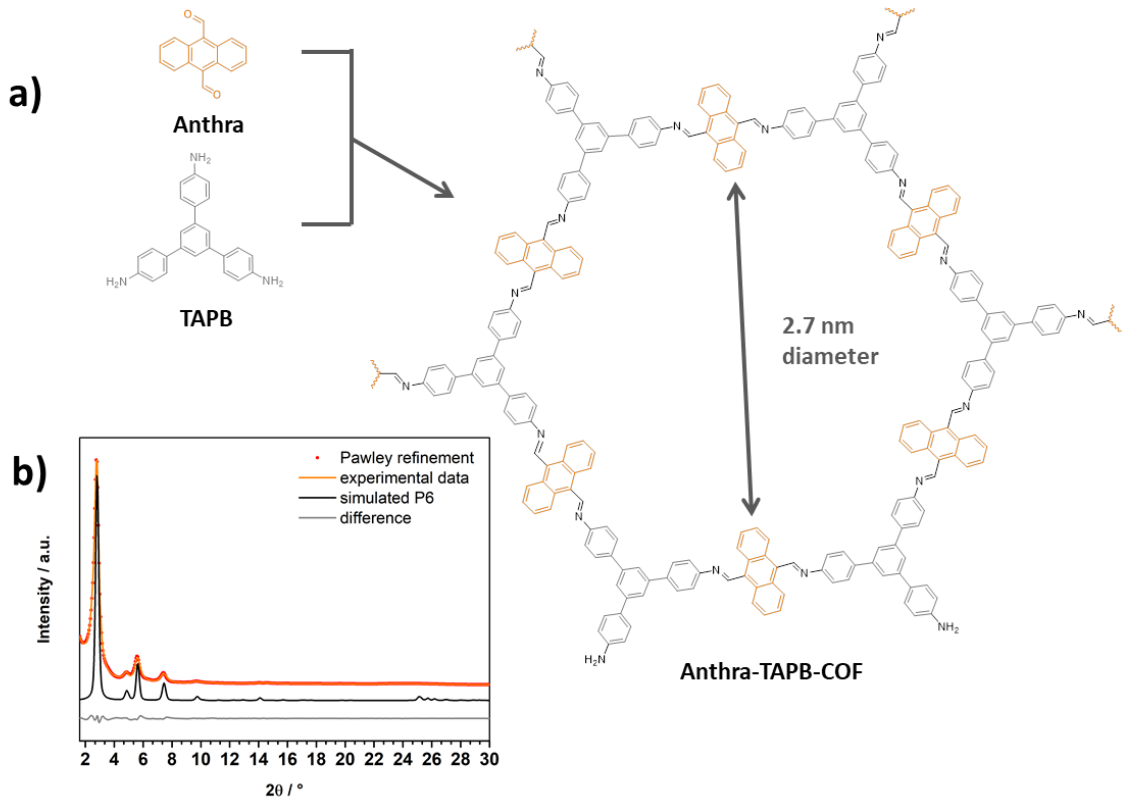

Figure 6-1: a) Synthesis scheme for Anthra-TAPB-COF and the resulting COF pore with displayed pore size of 2.7 nm, b) PXRD pattern of experimental Anthra-TAPB-COF (orange), Pawley refined data (red), simulated pattern in *P6* space group (black) and resulting difference (grey).

Powder X-ray diffraction (PXRD) measurements were conducted to get insight in the crystallinity of the material (see Figure 6-1b). The as-synthesized COF material is of low crystallinity (see Experimental Section). After sc-CO_2 extraction work-up, the material shows a significant enhancement of the reflections in the small *2θ* region. The final Pawley refined experimental data are shown in Figure 6-1b, including the simulation for the *P6* space group. The data clearly show the formation of a crystalline framework after successful work-up (for more details see Experimental Section). The PXRD measurement revealed Bragg reflections centered at relative small *2θ* angles of 2.81°, 4.87°, 5.62°, 7.47° and 9.75°. These reflections are attributed to the 100, 110, 200, 210 and 220 crystal planes, respectively. Based on the symmetry of the applied building blocks, the simulation was carried out for an expected hexagonal *P6* space group including an AA-stacking mode of the different layers in an eclipsed mode. Using the *Materials Studio software* the calculations resulted in a good fit between the simulated pattern and the experimental data and provide a good structural description of our Anthra-TAPB-COF (see Figure 6-1b). The final unit cell parameters were obtained

by Pawley refinement and correspond to a = b = 36.26 Å, c = 3.55 Å, α = β = 90.00°, γ = 120.00° (Rwp = 4.26% and Rp = 2.89%).

To assess the porosity of our newly synthesized Anthra-TAPB-COF, nitrogen sorption measurements were carried out. Prior to the sorption experiments the COF powder was degassed by keeping it at 100 °C in high vacuum overnight. Considering the amorphous material obtained in the synthesis, it is necessary to work up the TAPB-based material with sc-CO_2 to improve porosity and surface area. In addition, the material has to be washed with a large amount of freshly distilled chloroform to remove most of the residues in the pores. The Anthra-TAPB-COF features a type IV isotherm with a relatively small uptake (pore volume), which we attribute to the anthracene building block reaching into the pores. Pore filling starts at about p/p_0 = 0.21 which indicates a well-defined mesoporous framework. The Brunauer-Emmett-Teller (BET) surface area was calculated to be around 700 m^2g^{-1} (adsorption branch in the range of p/p_0 = 0.05-0.21). Calculation of the COF pore size distribution reveals a well-defined pore size value with a maximum at 3.0 nm, which is in good accordance with the simulated pore size measurement of the expected framework in *Materials Studio* (see Figure 6-1b). Furthermore, thermogravimetric analysis (TGA) revealed a thermal stability under dynamic conditions of up to 350 °C followed by final decomposition at 600 °C (see Experimental Section).

To get an insight in the morphology and the distribution of the pores within the framework, scanning and transmission electron microscopy (SEM) and (TEM) investigations were performed, respectively. SEM images revealed that the Anthra-TAPB-COF emerges as large agglomerates consisting of individual particles. These individual particles fuse to create larger spherical shapes. This is confirmed in a TEM image of the framework, illustrating crystalline COF domains that are intergrown and assembled into larger agglomerates. The high crystallinity is apparent in many ordered domains, and the expected honeycomb pore structure is visible in projections along the *c*-axis. The TEM image shows numerous projections of the pore channels arising from the 2D stacking of the COF layers.

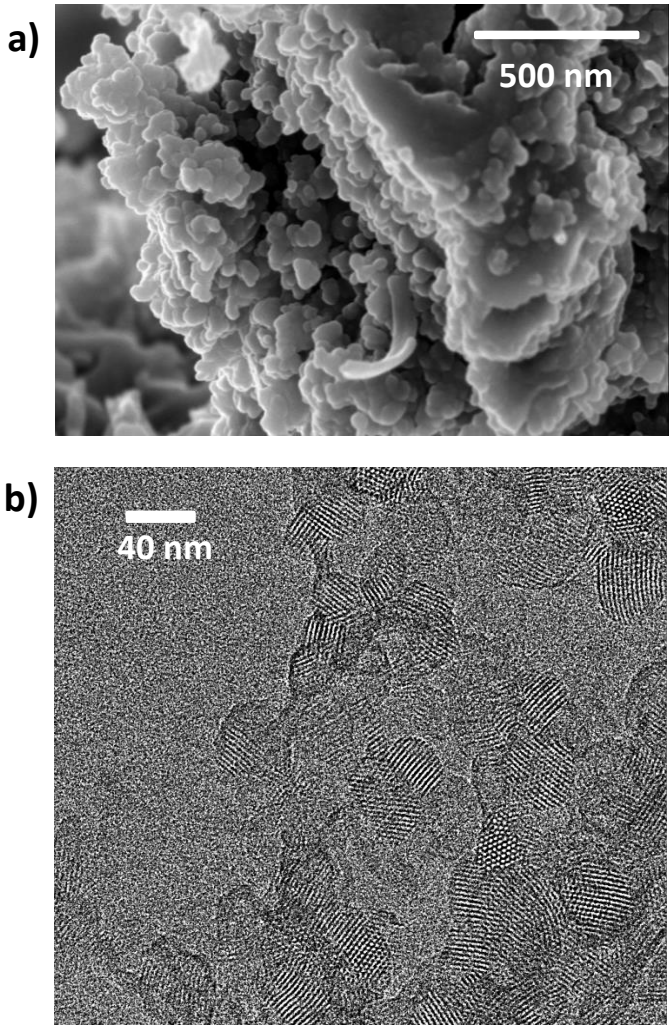

Figure 6-2: a) SEM image of Anthra-TAPB-COF showing the spherically shaped individual particles agglomerated and fused into larger morphologies, b) TEM image of crystalline Anthra-TAPB-COF.

The optical absorption, recorded through diffuse reflectance measurements, and photoluminescence (PL) spectra of Anthra-TAPB-COF bulk powder are summarized in Figure 6-3. To prevent any degradation of the COF through photo oxidation in the presence of oxygen, we performed all PL measurements in a sealed argon atmosphere. The impact of our postsynthetic treatment (PST) was measured through PL, after different times of laser illumination of the sample. Here, the PST was performed with the same laser used for PL excitation. All details concerning the experimental methods are discussed in the Experimental Section.

The crystalline Anthra-TAPB-COF was illuminated with tightly focused, pulsed 375 nm and 510 nm lasers, respectively (50 pJ pulses; 100 μm diamater). Upon illumination with either of the two lasers, we were able to detect a striking increase of the PL. In the following, we focus on results obtained with the UV laser, while results for the

illumination at 510 nm can be found in the Experimental Section. Using the 375 nm laser, the PL peak value is increased from around 1300 to almost 1700 counts, i.e. by around 30%, over the course of the experiment lasting about 40 min. Normalization of the measured data reveals the same values for the peak wavelength (see Experimental Section), which indicates that the material is not degraded. Since the pores are empty after the CO_2 extraction, it can be excluded that new material is formed within the pores.

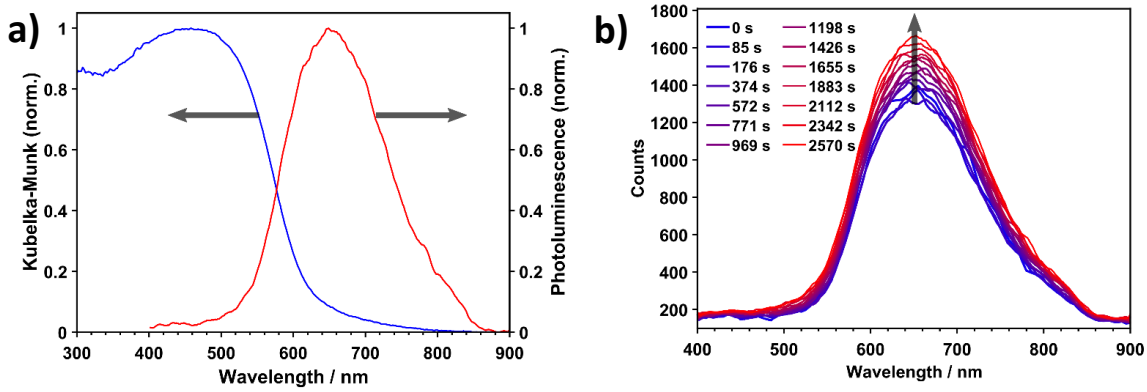

Figure 6-3: a) Absorption (blue) and photoluminescence (red) spectra of Anthra-TAPB-COF bulk material. The absorption was measured through diffuse reflectance and converted *via* the Kubelka-Munk equation, b) photoluminescence spectra of bulk Anthra-TAPB-COF measured after different illumination times (under argon), using a 375 nm pulsed laser. For more information see Experimental Section.

The same illumination experiment was repeated for a COF made from TAPB and terephthalaldehyde (TA), and the same trend was observed over time, i.e. a distinct increase in PL (see Experimental Section). While anthracene has been reported to be UV-sensitive with the possibility to dimerize,[14] the TA-TAPB COF shows that this property is not related to the anthracene block. However, a COF from anthracene dialdehyde and tetrakis-(aminophenyl)pyrene does not exhibit the PL increase behavior upon illumination (see Experimental Section), which points towards the important role of TAPB for this PST.

To further explore the origin of the effect, we annealed the Anthra-TAPB-COF at 250 °C on a hotplate in an argon glovebox for 40 min, in order to evaluate possible heating effects of the focused laser beam on the sample. For this purpose, the material was held between two glass slides fixed with Kapton tape and placed on the hotplate. Here, the measurement was performed with an LED of lower light intensity to minimize any effects of the UV light. The results (see Figure 6-4) show that while the PL is only slightly reduced after 20 min, it continues to get weaker up to 40 min, accompanied by a

slight change in the spectrum. Therefore, the laser-induced PL increase cannot be explained through local heating. The increase of the PL is consequently attributed to a structural improvement of the framework, i.e., removing defects in the crystal structure. This leads to the hypothesis that under high-intensity illumination, the COF is able to form and possibly even to break and reform imine bonds, thus reorganizing and improving the whole framework by PST. This mechanism would be in accordance with the recent report by Kim *et al.* on imine bond formation in sunlight.[13]

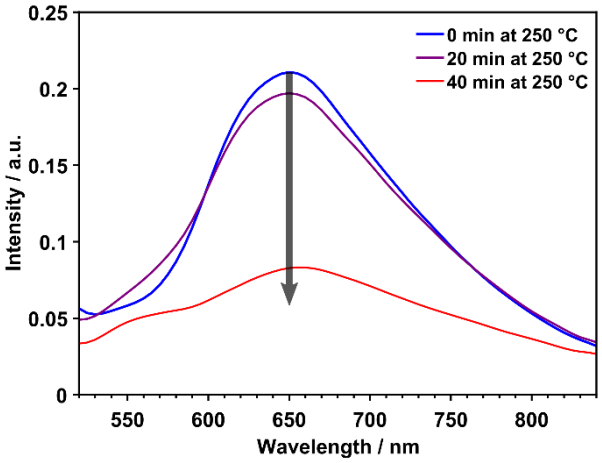

Figure 6-4: Photoluminescence spectra of Anthra-TAPB-COF bulk before and after thermal treatment on a hotplate at 250 °C in argon.

To further support the influence of light on our system and the possible light-induced bond formation, we performed the same experiment on the neat precursors Anthra and TAPB, respectively, and on a stoichiometric mixture of both precursor powders. The absorption and PL of both neat powders can be found in Figure 6-5a. For the neat materials, in contrast to the crystalline framework, we observed a considerable decrease in PL which we attribute to a decomposition of the materials themselves (see Experimental Section). The precursor mixture of Anthra and TAPB, which was prepared at the same molar ratio as the one used for the COF synthesis, was prepared as a homogeneous powder. As shown in Figure 6-5b, there is a striking change in the time-dependent PL measurement. While the peak of Anthra is getting smaller (similar to the neat Anthra measurement), the TAPB peaks are getting stronger. However, the peak positions are shifting, indicating not only a simple degradation of the Anthra molecules and hence stronger absorption and emission by the TAPB blocks. Furthermore, the peak ratio of the TAPB PL changes and the final spectrum is not only a pure superposition of the individual PL spectra. We attribute this change to the formation of a different

electronic system between TAPB and Anthra precursors, i.e. imine bond formation through the intense UV light over time, which again is in accordance with the report by Kim *et al.*.[13] This is further supported by a missing change in PL spectra when mixing TAPB with non-functionalized anthracene (see Experimental Section), since there are no aldehyde groups to form the imine bond.

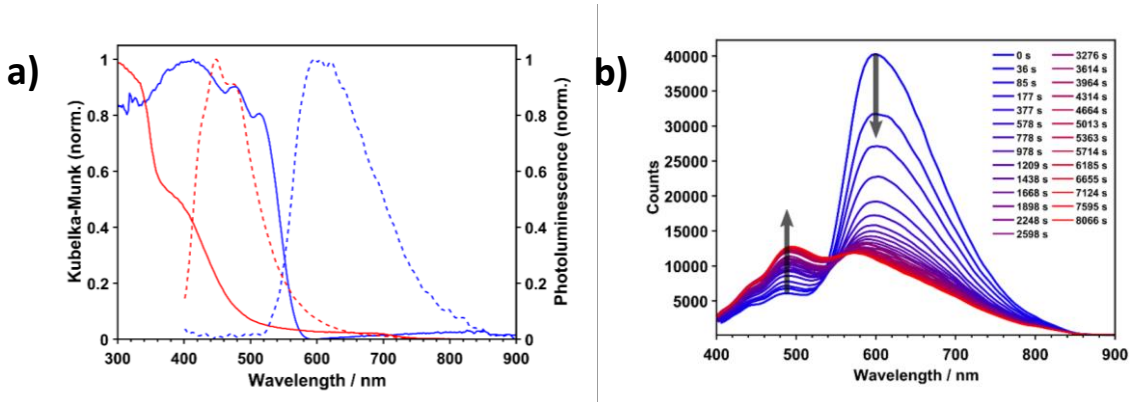

Figure 6-5: a) Absorption (solid) and photoluminescence (dashed) spectra of the anthracene-dialdehyde (blue) and TAPB (red) bulk materials. The absorption was measured through diffuse reflectance and converted *via* the Kubelka-Munk equation. b) Photoluminescence spectra of a powder blend of Anthracene-dialdehyde and TAPB precursors, measured after different illumination times (under argon), using a 375 nm pulsed laser. For more information see Experimental Section.

The emerging imine bonds can also be observed through IR microscope investigations. As above, we used a solid precursor mixture containing Anthra and TAPB at the stoichiometric ratio used in synthesis. Due to the different penetration depths of IR and UV light, we performed the investigation on a thin layer of material obtained by dropcasting onto a silicon wafer. We used high throughput IR microscopy, scanning the precursor mixture and recording an IR spectrum every 150 µm across the whole sample of a total size of 4 mm. This way we generated a map of IR spectra over the complete area of the dropcast precursor mixture spot. Then, the sample underwent the postsynthetic laser treatment for 30 seconds with a 355 nm laser with around 200 mJ pulses and a diameter of 6 mm, covering the whole mixture sample with the laser. Afterwards, we analyzed the sample again *via* the IR mapping method as above and were able to visualize the changes in the IR spectrum at exactly the same location as before the laser treatment (more details are given in the Experimental Section).

In Figure 6-6, the different intensity maps of the active vibrations contributing to the COF formation are depicted as a color code. Here, the IR maps are illustrated for each vibration, before (Figure 6-6a, b, c) and after laser treatment (Figure 6-6d, e, f),

respectively. At the same time, the color code is specified for each vibration below the graphic and represents the vibration activity.

The IR maps demonstrate that after the laser treatment the vibrations of the precursors significantly reduce their intensity. The aldehyde (1682 cm^{-1}, Figure 6-6a, d) as well as the amine vibration (1623 cm^{-1}, Figure 6-6b, e) are reduced in activity. This can be attributed to the loss of the free functional groups and consequently the formation of imine bonds. Comparing the changes in the IR map of the imine vibration (1596 cm^{-1}, Figure 6-6c, f) the opposite transformation can be detected. Whereas before laser treatment almost no imine vibration is active, the IR map after laser treatment clearly shows the formation of imine bonds, consistent with the intensity reduction of aldehyde and amine vibrations (more measurement details in the Experimental Section).

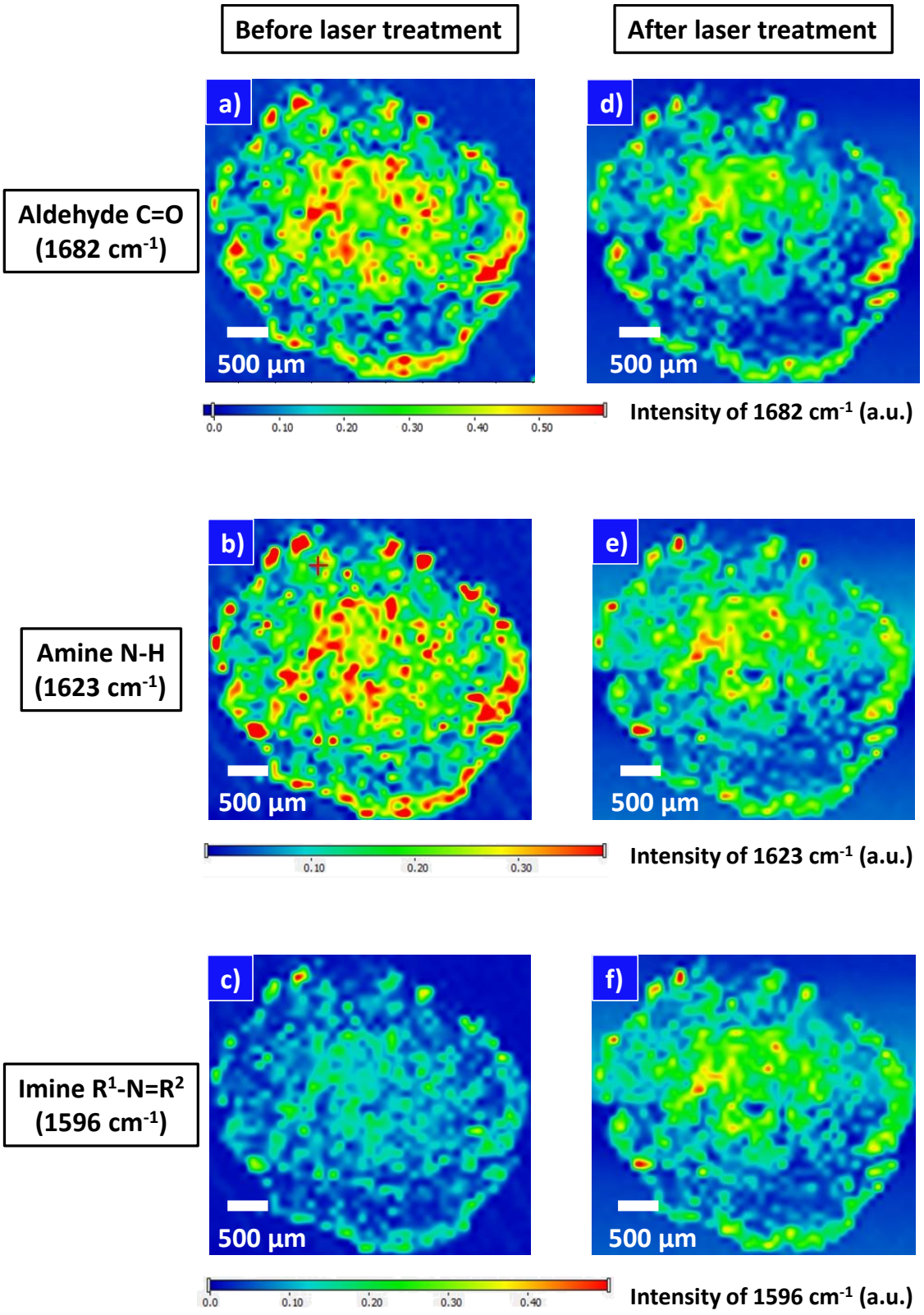

Figure 6-6: Infrared microscopy images of anthracene dialdehyde and TAPB precursors mixed as solid powders on a flat Si substrate. Images of aldehyde (a, d), amine (b, e), and imine (c, f) IR vibration activities, respectively. The given color bars for each vibration are attached below the respective graphics and are given in arbitrary units. The range is displayed from blue (zero activity) to red (higher activity). The measurements were performed before (a, b, c) and after laser treatment (d, e, f), respectively.

6.3 Conclusion

In this work, we have demonstrated a new technique for postsynthetically treating COFs without changing the structural composition but healing the structure from defects. For this purpose, we successfully implemented TAPB, in combination with an anthracene-based building block perpendicular to the linking direction, into an imine-based COF resulting in a porous and highly crystalline framework. When illuminating our as-synthesized material with a high intensity laser, we observed an auspicious increase in PL without shifting the position of the maximum, indicating a non-structural change. We also observe this effect for another TAPB-based COF without anthracene moieties and hypothesize that it is related to the formation of imine bonds.

We investigated the impact of laser illumination on a stoichiometric mixture of the precursors for the Anthra-TAPB-COF. Strikingly, the laser light induces the formation of imine bonds between the precursors. The PL increases for TAPB and decreases for the anthracene part while the spectrum is shifting, generating new spectral features over time. IR experiments reveal a decrease of the aldehyde and amine vibration activities, respectively, and an increase in the number of imine bonds.

This newly developed postsynthetic treatment and healing approach offers a broad field to further improve and develop COFs. It allows for a treatment without the need of a particular chemical environment such as solvents or substrates and can be performed within seconds to minutes at room temperature. While this technique has been demonstrated for TAPB-based imine-conjugated COFs, it may be transferable to other imine-conjugated COFs. Our PST approach is of particular interest for thin films, which can be fully penetrated by light, and which are also the most relevant systems when developing COFs into functional optoelectronic devices. Therefore, our PST could improve future devices by removing materials defects and loss mechanisms with little effort and within a short time.

6.4 Experimental Section

All materials (if not otherwise mentioned) were purchased from Aldrich or TCI in the common purities purum and puriss. All materials were used without further purification if not noted otherwise. Solvents were distilled in the vacuum for further use, if not purchased from the supplier in suitably dried form.

Powder X ray diffraction (PXRD) measurements were performed on a Bruker D8 Discover diffractometer with Ni filtered Kα radiation (λ = 1.54060 Å) and a position-

sensitive detector (LynxEye) in reflection mode. For high resolution measurements, the as-synthesized COF material was placed on a silicon wafer and the measurement was carried out by applying a low scan speed (scanspeed: 5-10 sec/step; increment: 0.05°*2θ*).

The **simulation** was carried out with the visualization environment of *Materials Studio software 4.4*, and the geometry of the two-dimensional layers was optimized with calculations using forcite and DFTB+ methods, respectively.

Nitrogen sorption was measured using a Quantachrome AUTOSORB 1 station at 77.3 K after degassing the sample for at least 12 h under vacuum at 100 °C. The Brunauer–Emmett–Teller (BET) surface areas were calculated from the adsorption branch in the range of $p/p_0 = 0.05–0.32$. Pore sizes were calculated with a QSDFT adsorption model of N_2 on carbon (cylindrical/spherical, adsorption branch).

Scanning electron microscopy (SEM) was performed on an FEI Helios G3 UC instrument at 2 kV. For this purpose the samples were put on an adhesive graphite film and sputtered with carbon with a BALTEC MED 020 Coating Sytem.

Transmission electron microscopy (TEM) data were obtained with a Tecnai G2 20 S Twin instrument at an acceleration voltage of 200 kV.

Thermogravimetric (TG) measurements were performed in a stream of synthetic air (25 ml/min) on a Netzsch STA 440 C TG/DSC instrument. The measurements were carried out with a heating rate of 10 °C/min, and a temperature range from 30 °C to 900 °C was covered.

IR microscope infrared spectra were measured with a Thermo Scientific Nicolet iN 10 infrared microscope. The operation mode was in reflection setting and the recording time for each spectrum was 12 seconds. The IR spectra are depicted in absorbance scale. After measurement no further modification of the IR spectra was performed and they were analyzed as RAW data. The obtained IR spectral maps were analyzed with ImageJ.

Photoluminescence (PL) measurements were performed using a PicoQuant FluoTime300 time-correlated single photon counting (TCSPC) setup with samples in an argon filled container. Steady-state spectra were recorded using a 375 nm (PicoQuant LDH-P-C-375) or 510 nm (PicoQuant LDH-P-C-510) laser of 50 pJ pulses and around 100 µm focal diameter. The emitted photoluminescence was collected by a two-inch lens and focused onto a monochromator (Zolix Omni-λ 300). Residual scattered light from the excitation laser was removed using a 400 nm dielectric longpass (Thorlabs

FELH0400) or a 3 mm orange glass filter (Schott OG530) for the 375 nm or 510 nm laser, respectively. The monochromatic light was detected under magic angle (54.7°) using a highly-sensitive photomultiplier (PicoQuant PMA 192).

Super critical CO_2 extraction (sc-CO_2) was used as work-up for the diverse COFs to achieve a crystalline material. To this end, the material (15 mg) was placed in a holder in a steel autoclave and locked accurately. Then the autoclave was filled with CO_2 and cooled down. The material was further extracted at super critical conditions for CO_2 (40°C, 85 bar) for at least three hours.

Annealing experiments were performed to exclude the influence of heat on the PL increase. Due to the use of 375 nm UV laser which exhibits a high energy, the COF material is exposed to higher temperatures, which can also have an influence on the framework. As shown above, TGA measurements reveal a thermal stability up to 350 °C and in combination with the PL data we claim that the structure is still intact. Therefore, we decided to check the influence of heat in general by using a hotplate. The COF material was placed between two glass slides and fixed with Kapton tape. Under inert gas, the substrate was placed on the hotplate at 250 °C for about 40 minutes. After the heating treatment, the material was illuminated with a 375 nm LED with offers the same wavelength but lower energy compared to our used laser. It can be observed that these time-dependent PL measurements show a constant or lower PL which we attribute to decomposition or non-transformation of our COF.

Postsynthetic Treatment (PST) The powder samples were sandwiched between two quartz slides and placed in an argon-filled container to prevent photo-oxidation. The PST was performed using intense laser light. In the case of the photoluminescence (PL) studies, the laser used for PL excitation was also used for the PST. Due to the small diameter of the TSCPC laser beams on the order of 100 µm, we used a high-power 355 nm laser (Innolas Spitlight600, 3rd harmonic) output for the IR measurement samples. The UV beam was reflected off a glass slide, resulting in around 20 mJ pulses and a beam diameter of 6 mm. This allowed us to cover the whole sample at once and therefore detect a change over the whole area.

6.4.1 Syntheses

To get a deeper insight into the behavior of TAPB and anthracene, respectively, three combinations of the precursors were synthesized, characterized and treated with postsynthetic laser healing conditions.

For the experiments dealing with the laser-induced imine formation using the pure solid precursor mixtures, the same ratios and weights of the precursors applied in the COF reactions were used, respectively.

6.4.1.1 Anthra-TAPB-COF Material

Extensive screening of the reaction conditions led to the following synthesis procedure for Anthra-TAPB-COF. The crystalline material could be retained after CO_2 extraction work-up. Moreover, the amorphous COF material resulting directly from the synthesis was preserved without further CO_2 extraction for supplementary measurements on the system.

A 10 mL Schott Duran glass was charged with 9,10-anthracenedicarboxaldehyde (Anthra) (7.08 mg, 0.031 mmol, 1.5 eq) and 1,3,5-tris(4-aminophenyl)benzene (TAPB) (7.06 mg, 0.020 mmol, 1 eq.). A solvent mixture consisting of mesitylene and chloroform at the ratio 1:2 was given to the powder mixture (0.50 mL). In addition, acetic acid (6 M, 50 µL) was added acting as catalyst for forming the imine bonds. This reaction mixture was sonicated and further heated up to 120 °C for 72 hours. The reddish orange solid was isolated by filtration and washed with freshly distilled chloroform (50 mL). This amorphous Anthra-TAPB-COF material was finally treated with sc-CO_2 extraction in combination with soxhlet extraction in chloroform to achieve a crystalline product. Finally, Anthra-TAPB-COF was obtained as reddish orange powder (76 % yield).

6.4.1.2 TA-TAPB-COF Material

A 10 mL Schott Duran glass was charged with terephthalaldehyde (TA) (12.7 mg, 0.095 mmol, 1.5 eq) and 1,3,5-tri(4-aminophenyl)benzene (TAPB) (22.1 mg, 0.063 mmol, 1 eq.). A solvent mixture consisting of mesitylene and dioxane at the ratio 1:8 was given to the powder mixture (1.00 mL). In addition, acetic acid (6 M, 100 µL) was added acting as catalyst for forming the imine bonds. This reaction mixture was sonicated and further heated up to 70 °C for 72 hours. The yellow solid was isolated by filtration and washed with dioxane (7 mL). This amorphous TA-TAPB-COF material

was treated with sc-CO_2 extraction to achieve a crystalline product. Finally, TA-TAPB-COF was obtained as yellow powder (82% yield).

6.4.1.3 Anthra-Pyr-COF Material

A 10 mL Schott Duran glass was charged with 9,10-anthracenedicarboxaldehyde (Anthra) (4.69 mg, 0.01 mmol, 1 eq) and 1,3,6,8-tetrakis(4-aminophenyl)pyrene (Pyrene) (6.99 mg, 0.01 mmol, 1 eq.). A solvent mixture consisting of mesitylene and chloroform in the ratio 2:1 was given to the powder mixture (0.3 mL). In addition, acetic acid (6 M, 50 µL) was added acting as catalyst for forming the imine bonds. This reaction mixture was sonicated and further heated up to 100 °C for 72 hours. The redish solid was isolated by filtration and washed with mesitylene (5 mL). This already crystalline Anthra-Pyrene-COF was finally treated with sc-CO_2 extraction to achieve a purified crystalline product. Finally, Anthra-Pyr-COF was obtained as red powder (77% yield).

6.4.2 Characterization Details

6.4.2.1 Simulation of Anthra-TAPB-COF Crystal Structure

Based on the symmetry of the applied building blocks, the expected eclipsed 2D COF structure can be approximately predicted and then confirmed with experimental powder X-ray diffraction (PXRD) data. The simulation was carried out with the visualization environment of *Materials Studio software 4.4*, and the geometry of the two dimensional layers was optimized with calculations using forcite and DFTB+ methods, respectively. Based on the geometry of the precursor molecules anthracene and TAPB, the repeating unit was constructed with symmetry in the *P6* space group. The repeating fragments were placed in the bare hexagonal unit cell and connected to each other, resulting in the complete unit cell. The geometry of the Anthra-TAPB-COF layer was optimized in the unit cell using the Dreiding forcefield and the QEq correction for weak interactions. Pawley refinements resulted in a good fit of our experimental PXRD data.

Table 6-1: Refined crystal data for Anthra-TAPB-COF.

	Anthra-TAPB-COF
Chemical formula	$C_{69}H_{76}N_6$
Formula weight	1312.61 g/mol
Crystal system	hexagonal
Space group	P 6 (168)
Unit cell dimension	a = b = 36.26 Å c = 3.55 Å α = β = 90.0° γ = 120.0°
Cell volume	4041.10 $Å^3$

Table 6-2: Atomic parameters for Anthra-TAPB-COF.

Atom	**Atom label**	**x/a**	**y/b**	**z/c**
C1	C	0.71006	0.35719	0.46962
C2	C	0.68591	0.37607	0.46950
C3	C	0.75594	0.38239	0.47057
C4	C	0.77637	0.42195	0.31515
C5	C	0.81918	0.44556	0.32104
C6	C	0.84272	0.43000	0.47011
C7	C	0.82279	0.39066	0.62604
C8	C	0.77995	0.36731	0.62885
N9	N	0.88655	0.45557	0.46841
C10	C	0.91285	0.44293	0.49917
C11	C	0.95737	0.47235	0.49850
H12	H	0.70172	0.41210	0.46929
H13	H	0.75737	0.43548	0.17826
H14	H	0.83576	0.38563	0.19923
H15	H	0.84215	0.37713	0.75554
H16	H	0.76397	0.33463	0.76590
H17	H	0.90125	0.40764	0.52801
C18	C	0.45771	0.47262	0.49937
C19	C	0.48512	0.45774	0.49845
C20	C	0.58458	0.55479	0.50117
C21	C	0.59946	0.59708	0.50205
C22	C	0.57205	0.61196	0.50113
C23	C	0.52976	0.58455	0.49933
H24	H	0.60765	0.54226	0.50194
H25	H	0.63506	0.62015	0.50356
H26	H	0.58457	0.64756	0.50187
H27	H	0.50669	0.59708	0.49855

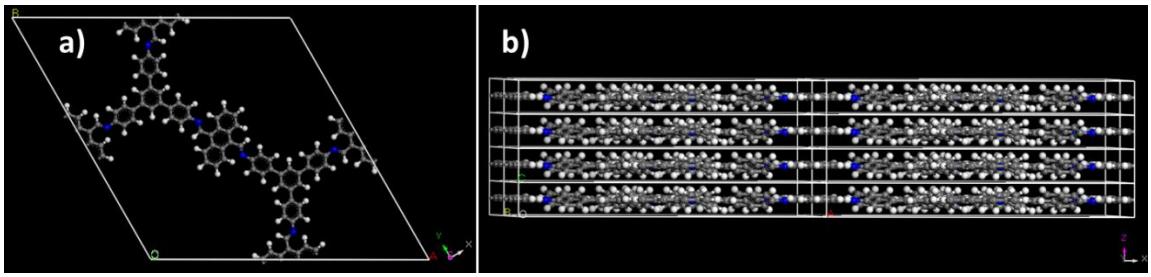

Figure 6-7: a) Simulation of the crystal lattice of the unit cell in an eclipsed arrangement for Anthra-TAPB-COF and b) side view along the *c*-axis of 4 unit cells stacked on top of each other, demonstrating the twisted structure of the TAPB and the planarity of the anthracene building block.

6.4.2.2 Structural Characterization of COF Materials

Anthra-TAPB-COF

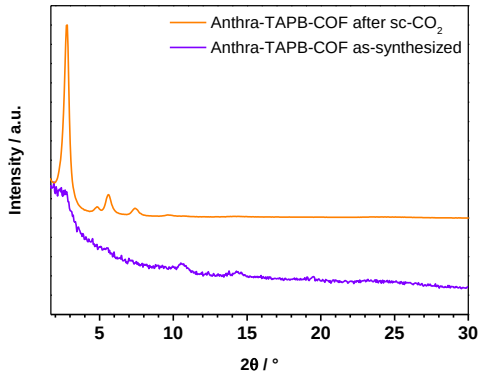

Figure 6-8: PXRD pattern of experimental as-synthesized Anthra-TAPB-COF (violet) and Anthra-TAPB-COF after sc-CO_2 extraction.

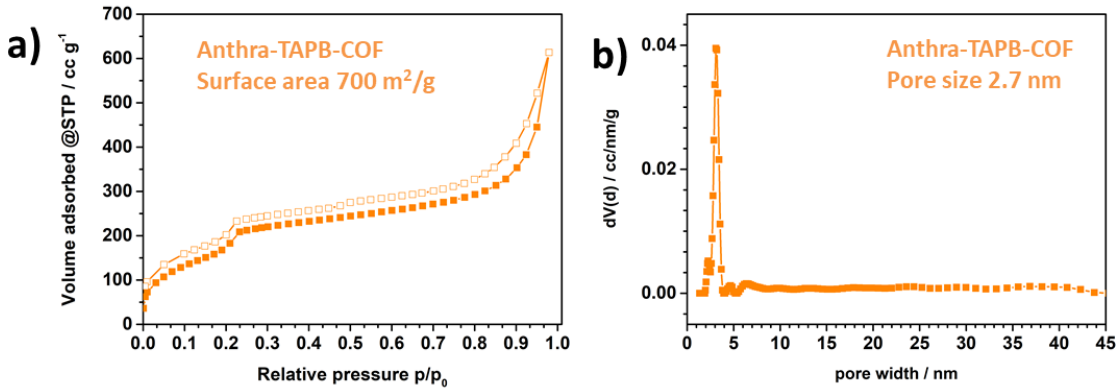

Figure 6-9: a) Sorption isotherm (full symbols: adsorption and empty symbols: desorption) of Anthra-TAPB-COF with calculated BET surface area, b) pore size distribution of Anthra-TAPB-COF with a calculated pore size of 2.7 nm, which agrees well with the expected pore size.

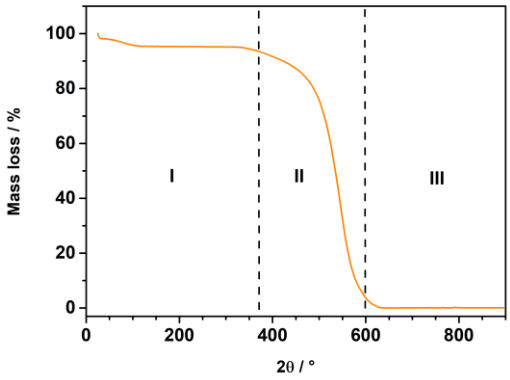

Figure 6-10: TGA data of Anthra-TAPB-COF; the analysis indicates a complete removal of volatile guest molecules (I); degradation of the material starts at around 350 °C (II), followed by complete decomposition between 500 and 600 °C (III).

TA-TAPB-COF

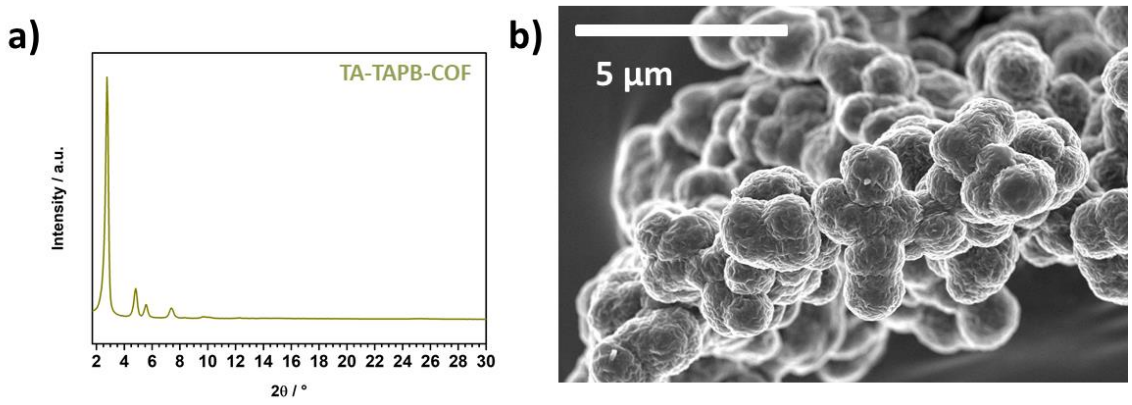

Figure 6-11: a) PXRD pattern of crystalline TA-TAPB-COF after sc-CO_2, b) SEM image of TA-TAPB-COF illustrating a spherical morphology of individual particles agglomerating into larger aggregates.

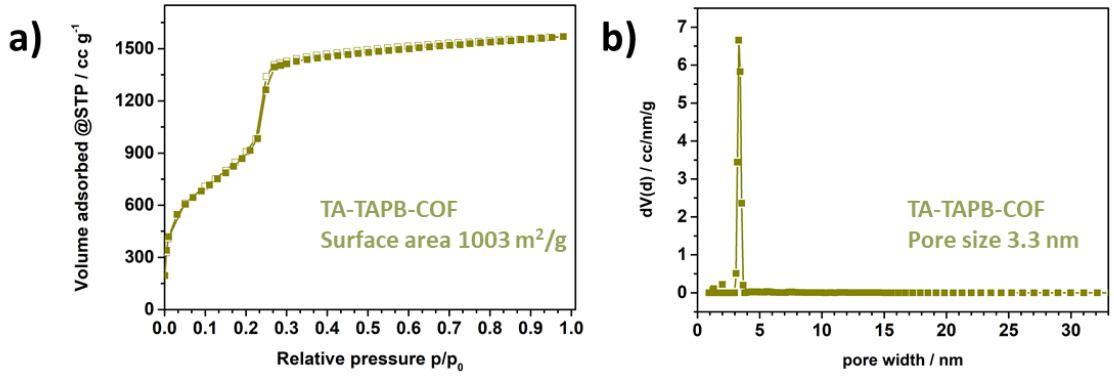

Figure 6-12: a) Sorption isotherm (full symbols: adsorption and empty symbols: desorption) of TA-TAPB-COF with calculated BET surface area, b) pore size distribution of TA-TAPB-COF with a calculated pore size of 3.3 nm.

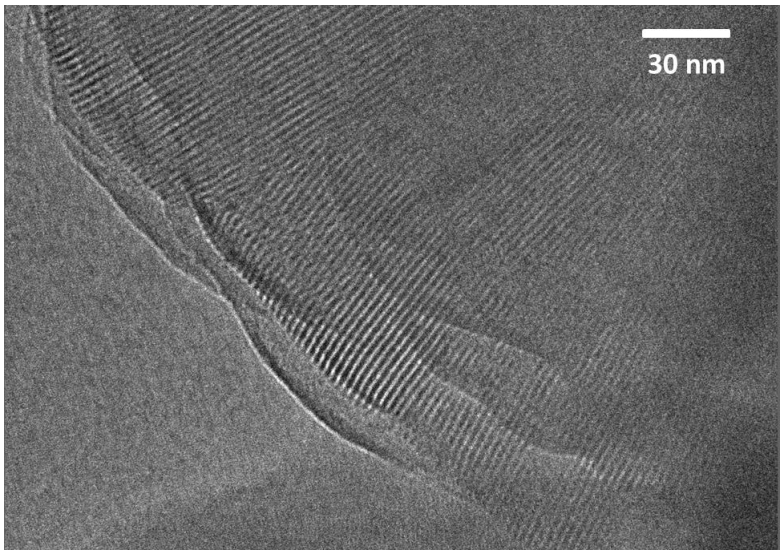

Figure 6-13: TEM image of TA-TAPB-COF illustrating the straight pores within the framework pointing into the middle of the crystallite.

Anthra-Pyr-COF

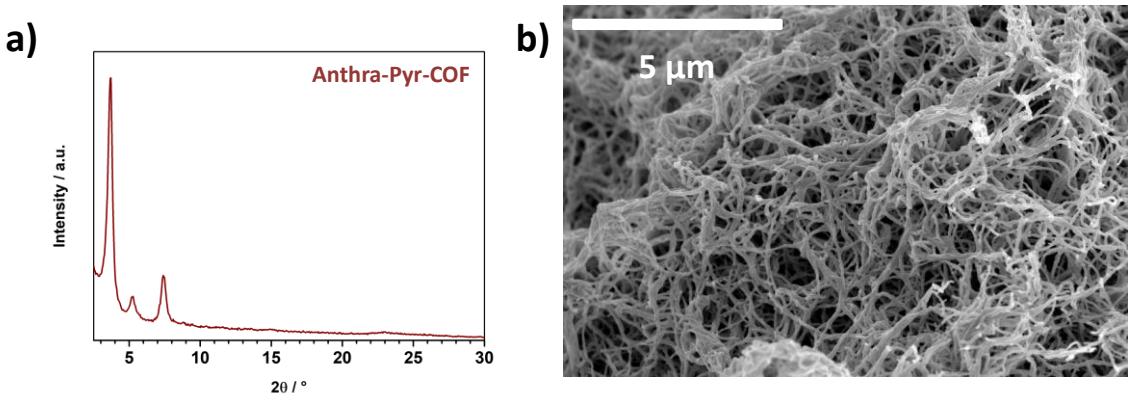

Figure 6-14: a) PXRD pattern of crystalline Anthra-Pyr-COF after sc-CO_2, b) SEM image of Anthra-Pyr-COF illustrating a filament-like morphology.

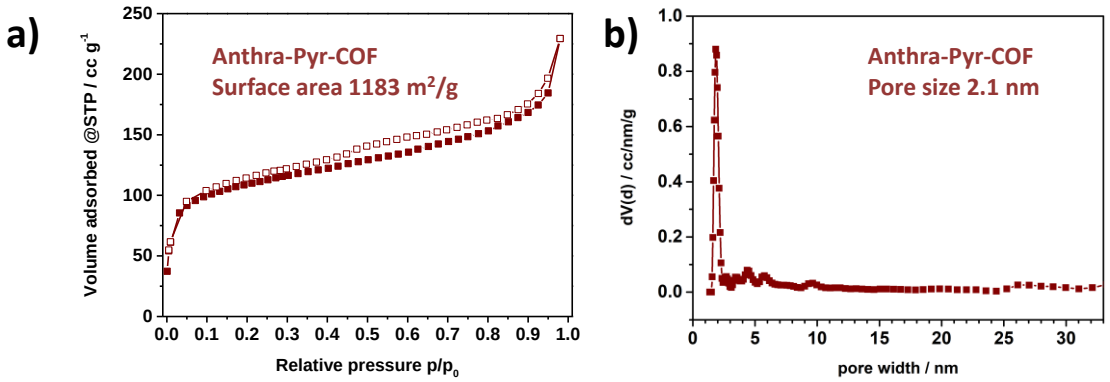

Figure 6-15: a) Sorption isotherm (full symbols: adsorption and empty symbols: desorption) of Anthra-Pyr-COF with calculated BET surface area, b) pore size distribution of Anthra-Pyr-COF with a calculated pore size of 2.1 nm.

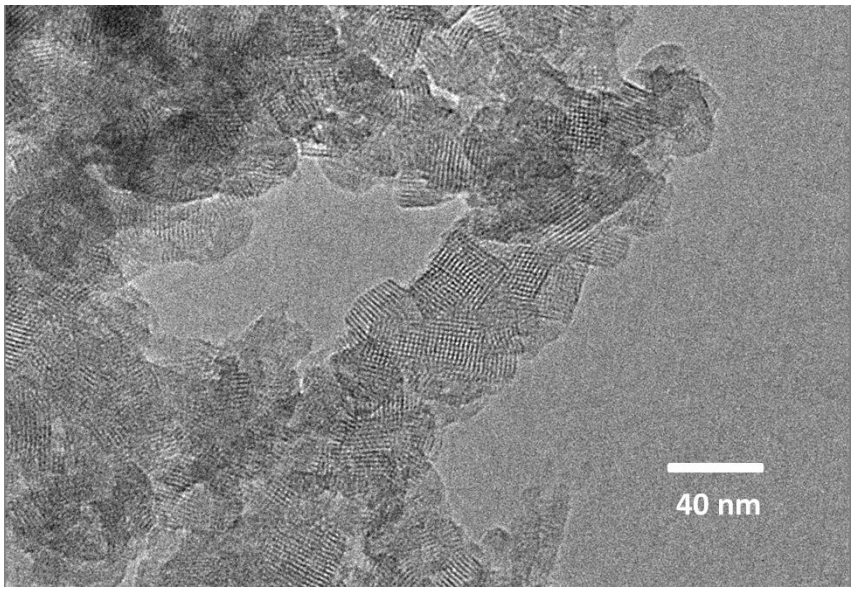

Figure 6-16: TEM image of Anthra-Pyr-COF illustrating small defined crystallites intergrown into bigger agglomerates.

6.4.2.3 Time-Dependent Optical Characterization of COF Materials

For static time-dependent PL measurements we performed all experiments under argon to avoid oxidation and degradation of our materials and to achieve the same conditions.

COFs were measured to get insights in their behavior during illumination and compared to each other.

Precursors were measured to evaluate their degradation and the diverse PL behavior under the same conditions.

Different mixtures of the precursors for every COF at the molar ratios used for COF synthesis were measured to examine the ability to cleave and form imine bonds under illumination

Anthra-TAPB-COF and Precursors

a) Anthra-TAPB-COF

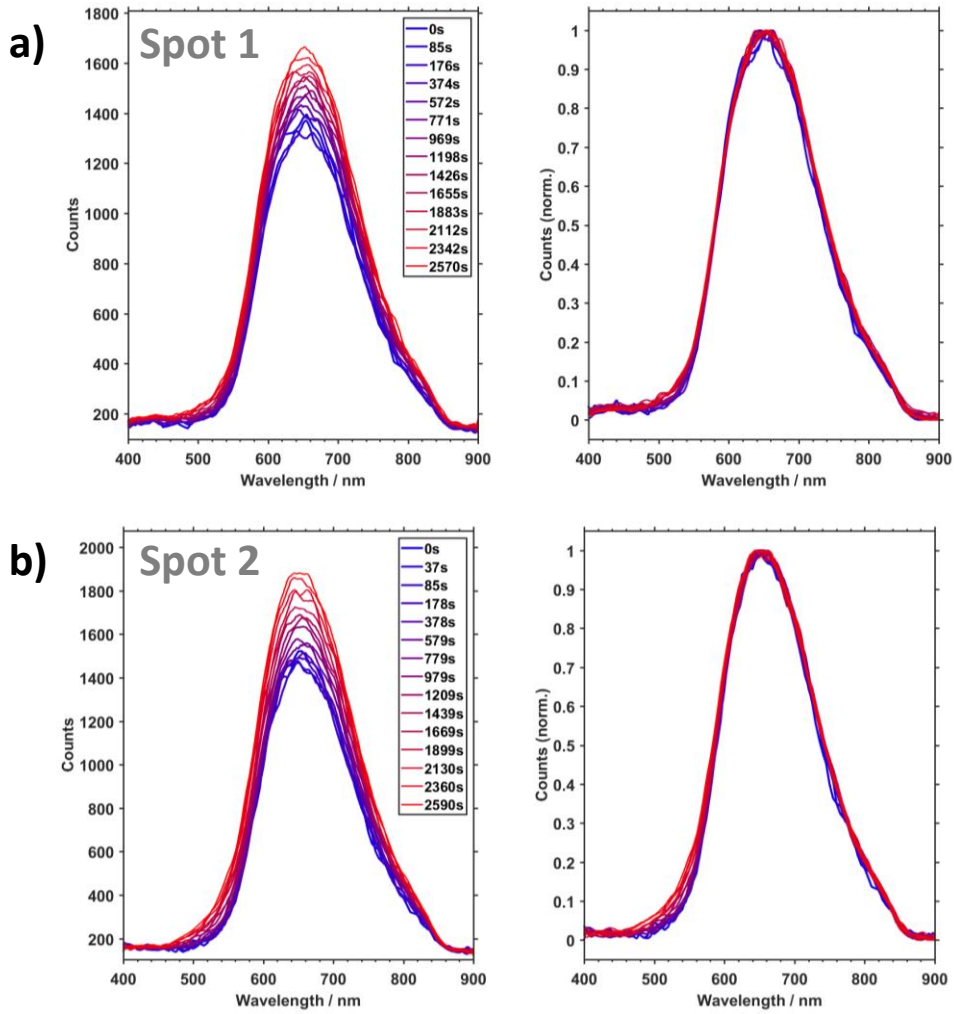

Figure 6-17: Time dependent photoluminescence spectra of solid Anthra-TAPB-COF with time scale (left) and normalized photoluminescence values (right) illuminated with 375 nm laser measured on two different spots a) and b).

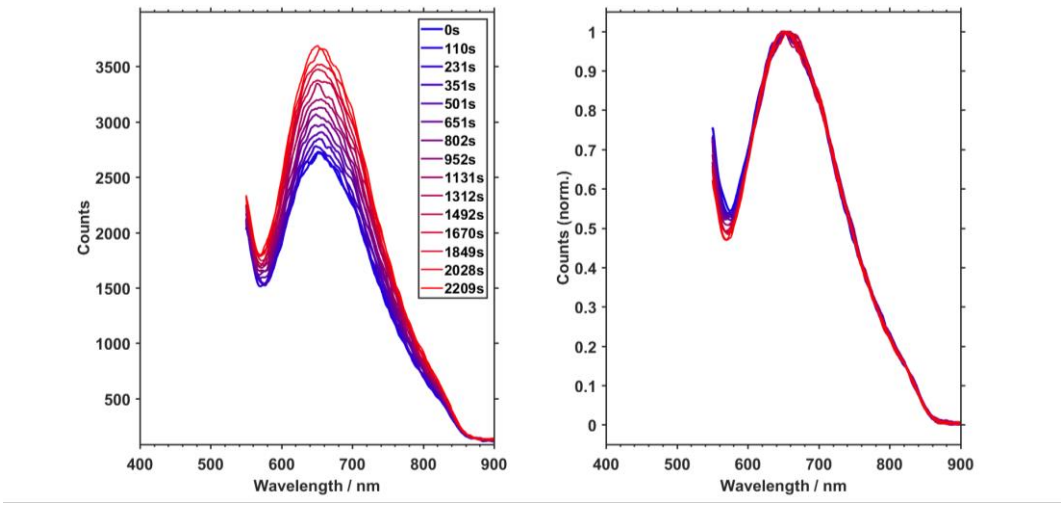

Figure 6-18: Time dependent photoluminescence spectra of solid crystalline Anthra-TAPB-COF with time scale (left) and normalized photoluminescence values (right), illuminated at 510 nm. Here, the PL signal is shown to also increase over time with the different laser.

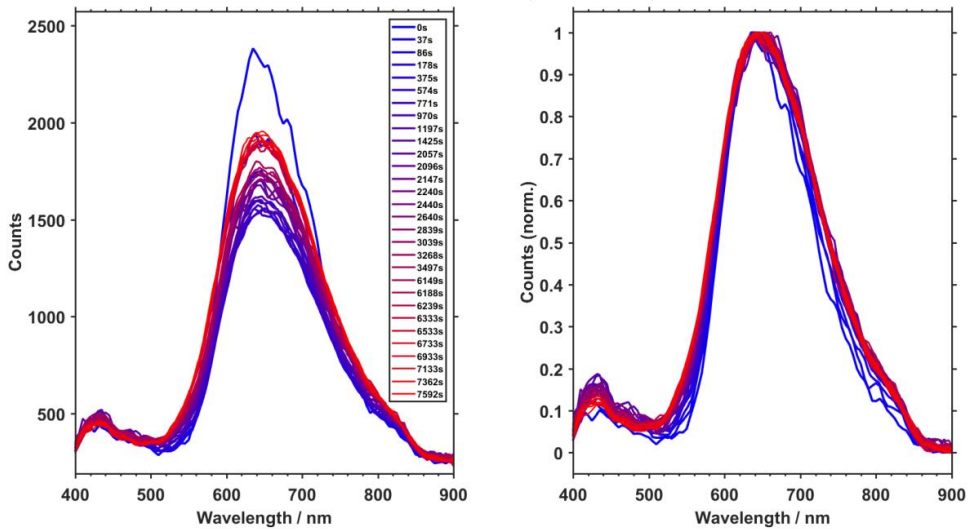

Figure 6-19: Time dependent photoluminescence spectra of solid amorphous Anthra-TAPB-COF with time scale (left) and normalized photoluminescence values (right) illuminated with a 375 nm laser illustrating the degradation of the material over the time.

b) Precursors Anthracenedialdehyde and TAPB

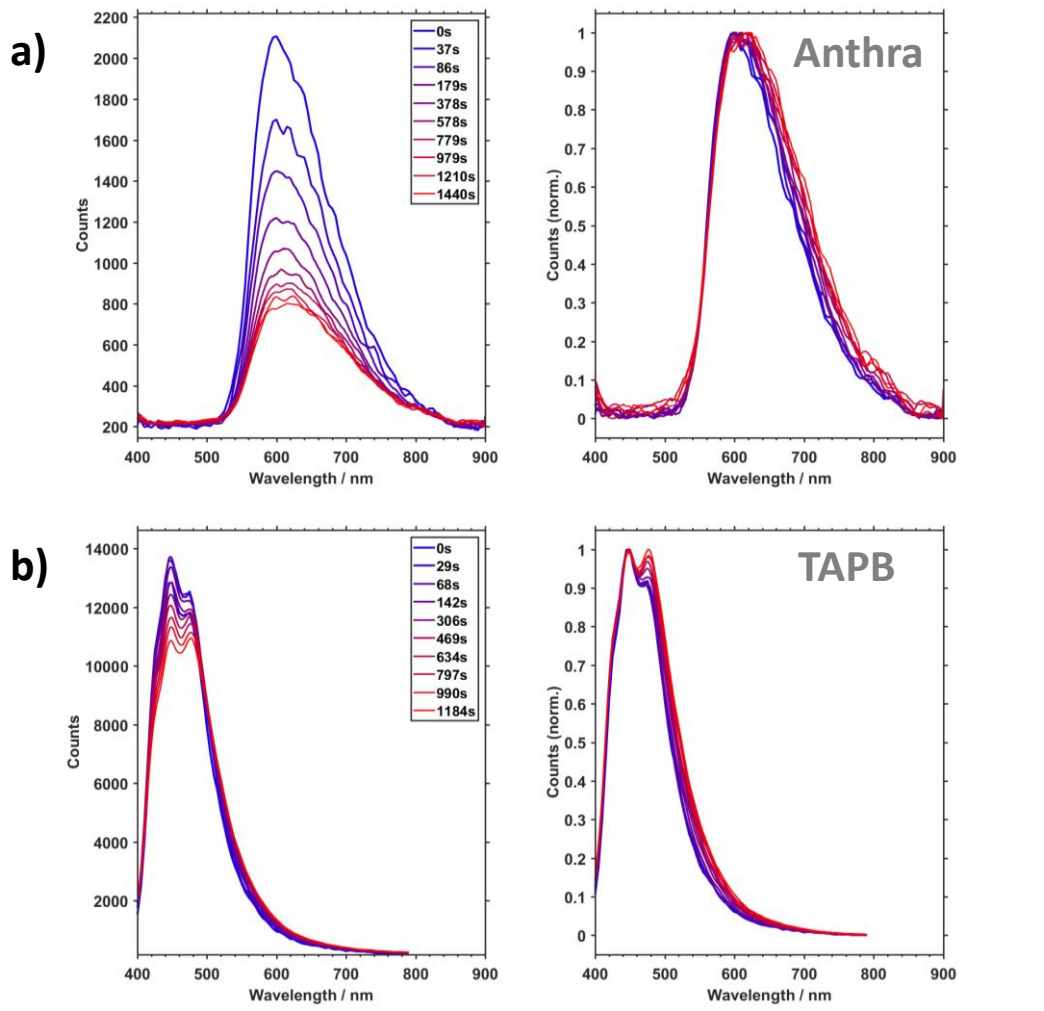

Figure 6-20: Time dependent photoluminescence spectra with time scale (left) and normalized photo-luminescence values (right), illuminated at 375 nm of a) solid Anthra precursor and b) solid TAPB precursor. For both data sets, a degradation of the materials can be observed over time.

To get a deeper insight in the precursor behavior, we also performed the treatment with the 375 nm laser on pure anthracene, which exhibits no functional aldehyde. As visible in Figure 6-21 neither degradation nor increase of the PL signal can be detected.

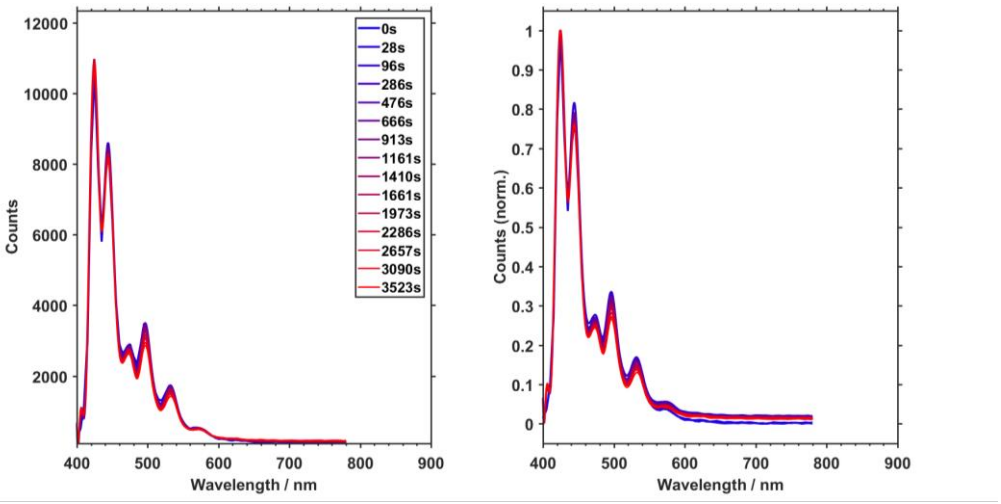

Figure 6-21: Time dependent photoluminescence spectra of solid pure anthracene (without functional groups) with time scale (left) and normalized photoluminescence values (right) illuminated with a 375 nm laser.

c) Mix of Precursors

The influence of the presence of two functional groups, that is, aldehyde and amine was further evaluated by combining both precursor powders in one closed PL sample holder filled with argon. Initially, both precursor signals are visible. During illumination, the two signals are shifted towards each other and the intensity ratios show a significant change.

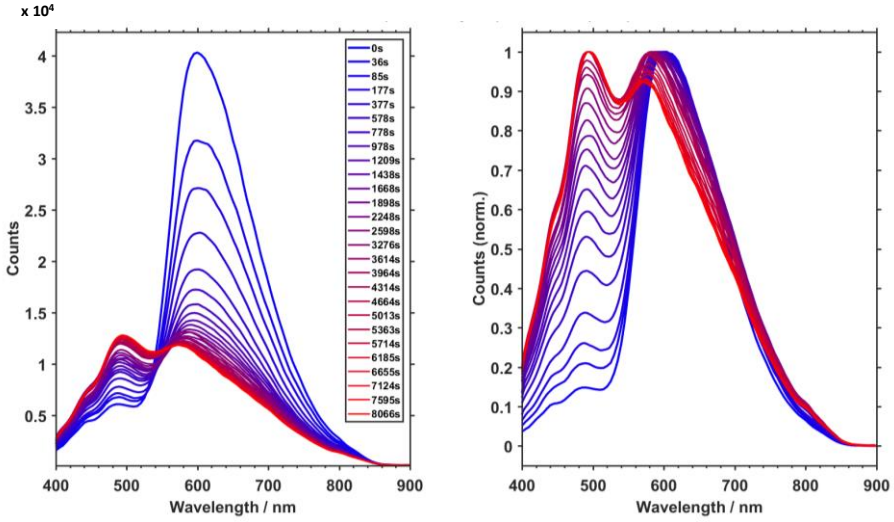

Figure 6-22: Time dependent photoluminescence spectra of the mixture of Anthra and TAPB at a molar ratio as the one used for synthesis with time scale (left) and normalized photoluminescence values (right), illuminated with 375 nm laser.

To further confirm the correlation between the PL changes and the presence of two reactive functional groups on the precursors, we also performed the experiment of

mixing the precursors in an argon filled sample holder with TAPB and non-functionalized pure anthracene. As illustrated in Figure 6-23, the strong anthracene signal decreases upon illumination (similar to the behavior of pure anthracene) and at the same time, the TAPB signal does not change its intensity. We attribute this phenomenon to the fact that no imine bond formation is possible in this case, which implies also no increase in PL.

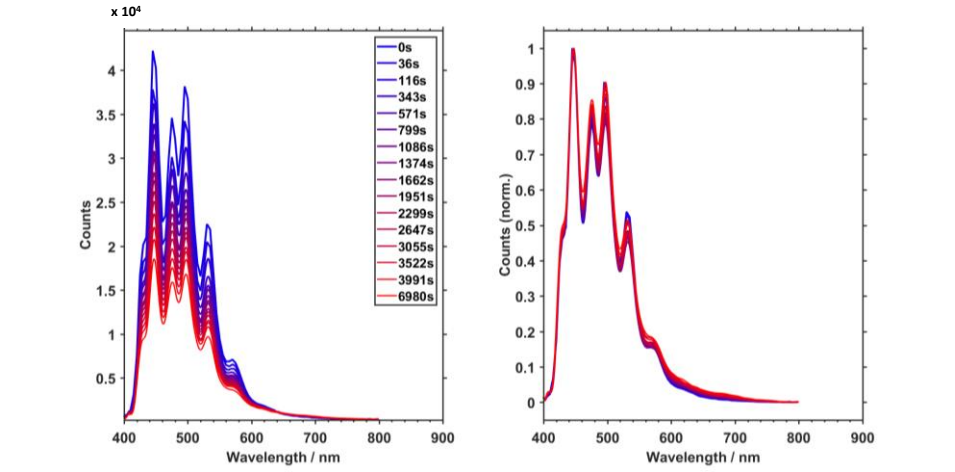

Figure 6-23: Time dependent photoluminescence spectra of the mixture of pure anthracene (without functional groups) and TAPB at the molar ratio used for COF synthesis, with time scale (left) and normalized photoluminescence values (right), illuminated with 375 nm laser.

TA-TAPB-COF and Precursors

a) TA-TAPB-COF

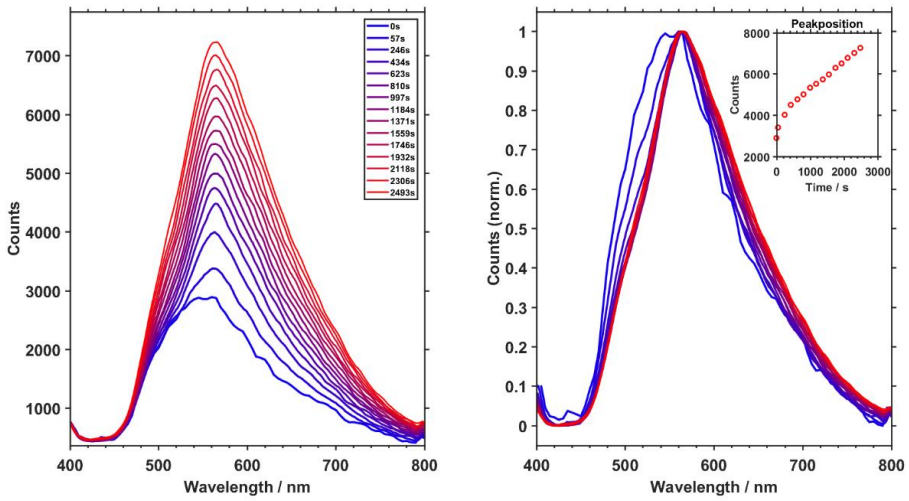

Figure 6-24: Time dependent photoluminescence spectra of solid TA-TAPB-COF with time scale (left) and normalized photoluminescence values (right), illuminated with 375 nm laser, also indicating the increase of the peak intensity given in counts to higher values during reaction time.

b) Mix of Precursors

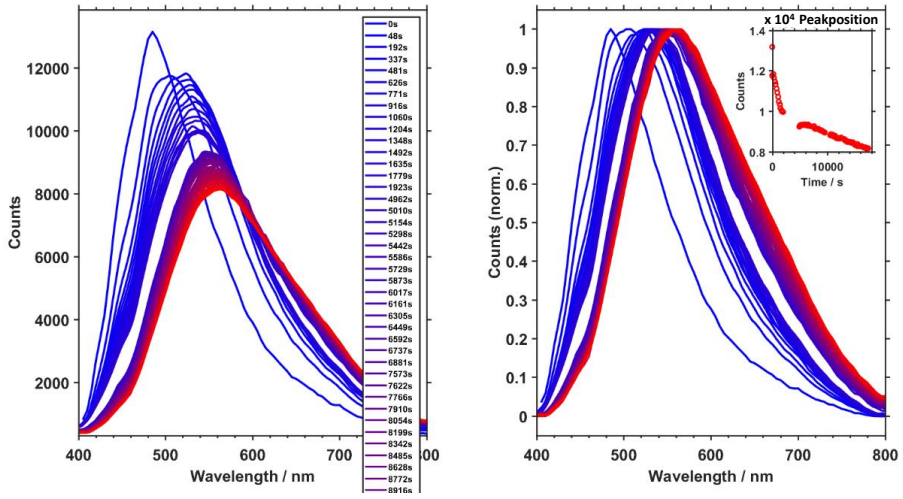

Figure 6-25: Time dependent photoluminescence spectra of solid TA and TAPB precursor mixture with time scale (left) and normalized photoluminescence values (right) illuminated with 375 nm also indicating the change of the peak intensity (given in counts) to lower values.

Anthra-Pyr-COF and Precursors

a) Anthra-Pyr-COF

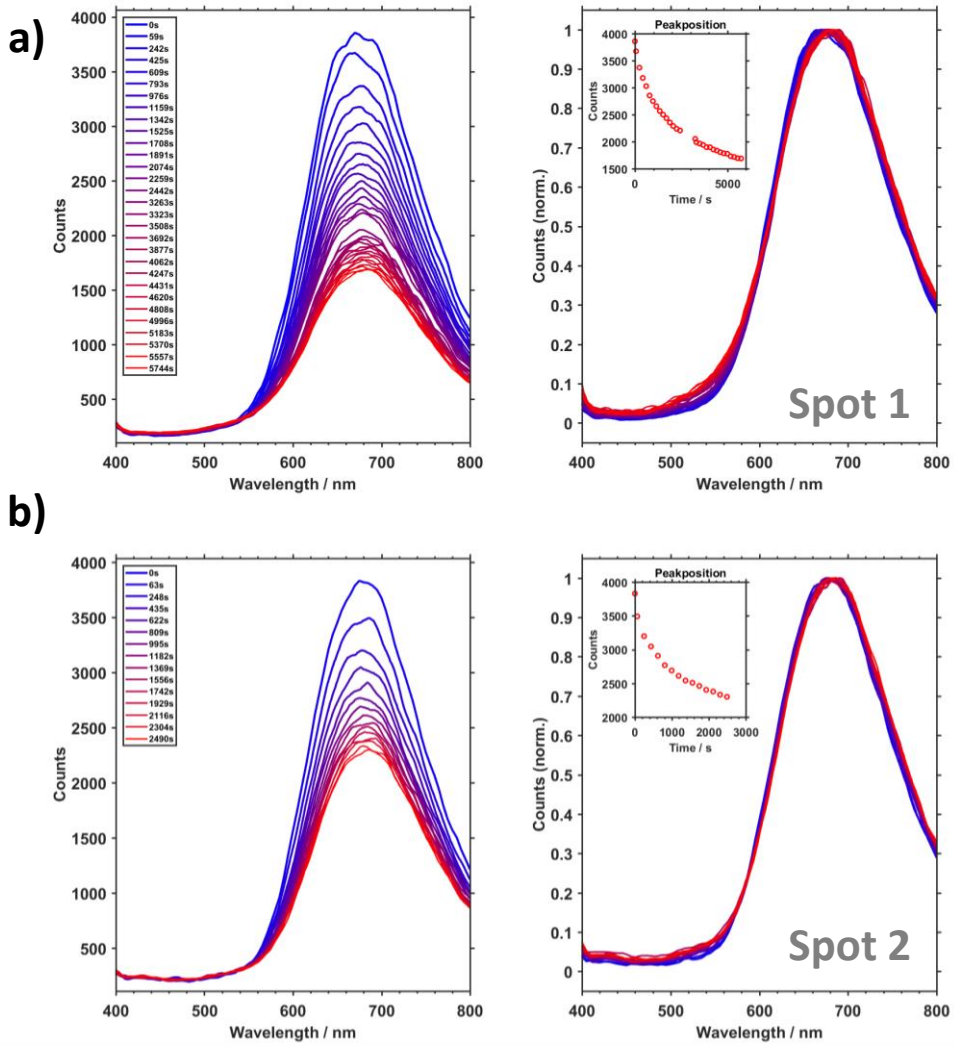

Figure 6-26: Time dependent photoluminescence spectra of solid Anthra-Pyr-COF with time scale (left) and normalized photoluminescence values (right), illuminated with 375 nm laser and measured on two different spots. The change of the peak intensity (given in counts) to lower values is illustrated in the insets on the right. An overall PL intensity decrease can be observed with time.

b) Pyr Precursor

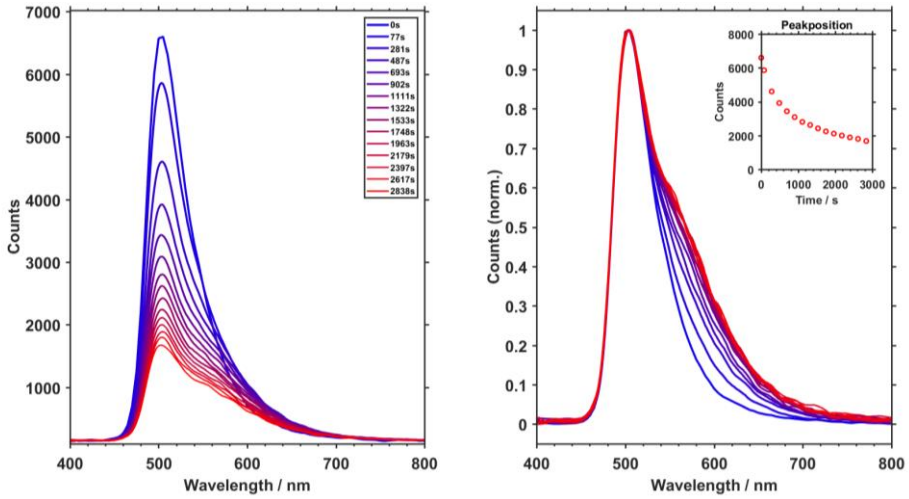

Figure 6-27: Time dependent photoluminescence spectra of solid pyrene precursor with time scale (left) and normalized photoluminescence values (right), illuminated with a 375 nm laser. The change of PL peak intensity (given in counts) is illustrated in the inset. The intensity is reduced with time, indicating a degradation of the precursor material.

c) Mix of Precursors

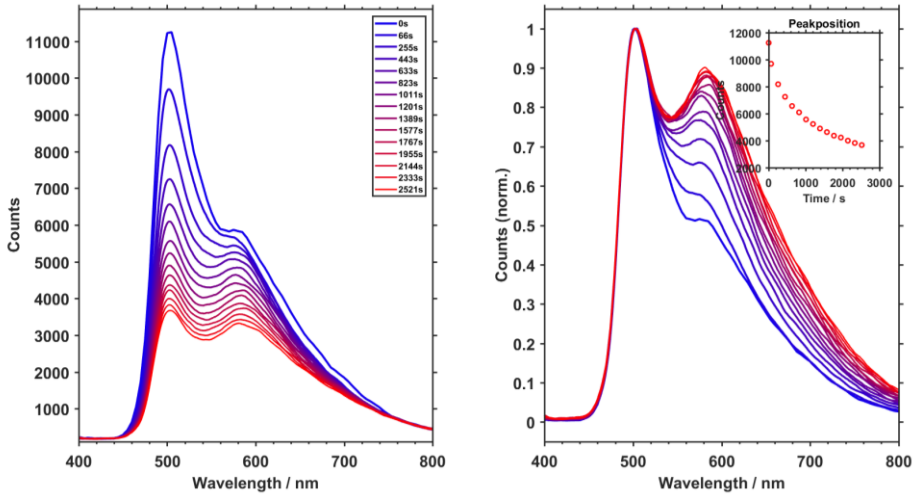

Figure 6-28: Time dependent photoluminescence spectra of the mixture of solid Anthra and pyrene precursors at the molar ratio used for synthesis with time scale (left) and normalized photoluminescence values (right), illuminated with 375 nm laser. The degradation of the materials is illustrated by the change of the peak intensity (given in counts) to lower values.

6.4.2.4 IR Microscope Experiments

IR investigations were performed to further prove and visualize the formation of imine bonds and at the same time the loss of the intensity of free functional groups (aldehyde and amine). The mixture of the solid precursors Anthra and TAPB was redispersed in $CHCl_3$ and a silicon wafer was positioned on a hotplate. The materials were transferred to the silicon substrate *via* dropcasting. The substrate was further placed under argon

and illuminated with a 355 nm laser with around 200 mJ pulses and a diameter of 6 mm. The illumination time was 30 seconds.

The overall IR spectra were extracted from the dataset and demonstrate the change of the sample measured before and after laser treatment (see Figure 6-28). The decrease of the aldehyde vibration at 1682 cm^{-1} is accompanied by a decrease of the amine vibration at 1623 cm^{-1} after the laser treatment. The full range IR spectra of the two samples are depicted in Figure 6-28a and compared to the IR spectrum of the crystalline Anthra-TABP-COF.

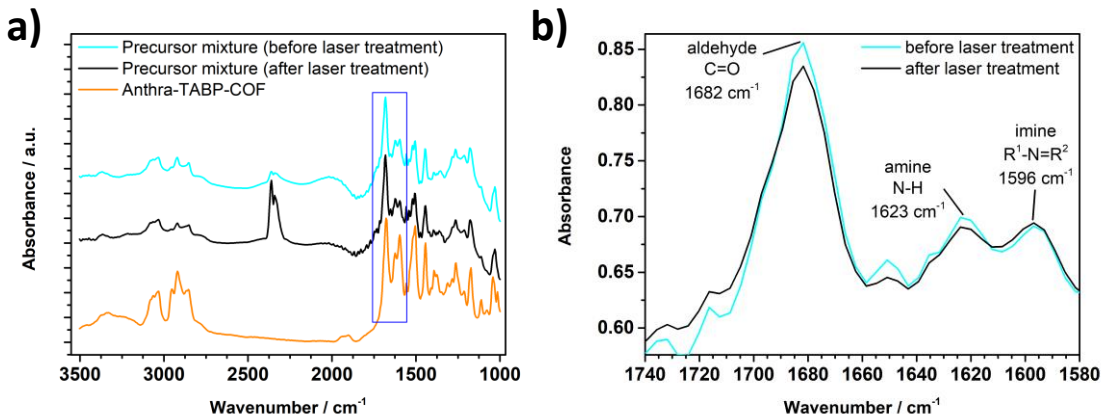

Figure 6-29: a) IR micrograph of the precursor mixtures before laser treatment (blue) and after laser treatment (black) compared to crystalline Anthra-TAPB-COF (orange), the rectangle emphasizes the important vibrations that are related to each other, i.e., aldehyde, amine and imine, b) enlargement of the specific vibrations contributing to the COF formation to visualize the reduction of the aldehyde and the amine vibration and at the same time the increase of the imine vibration. This is in accordance with the measured IR maps.

To further prove the formation of imine bonds, we performed IR microscope experiments also on the mixture of the precursors after an annealing process at 250°C under inert gas without performing a laser treatment (to exclude heat effects). Here, the mixture of the precursors TAPB and Anthra was suspended and transferred to a silicon wafer by dropcasting. The substrate was additionally annealed for 40 minutes (without any laser illumination) and analyzed *via* IR microscope mapping. It is clearly visible that the influence of heat does not change the intensity of the IR vibration activities of every specific vibration, concluding that no imine bond formed while maintaining the aldehyde and amino functional groups.

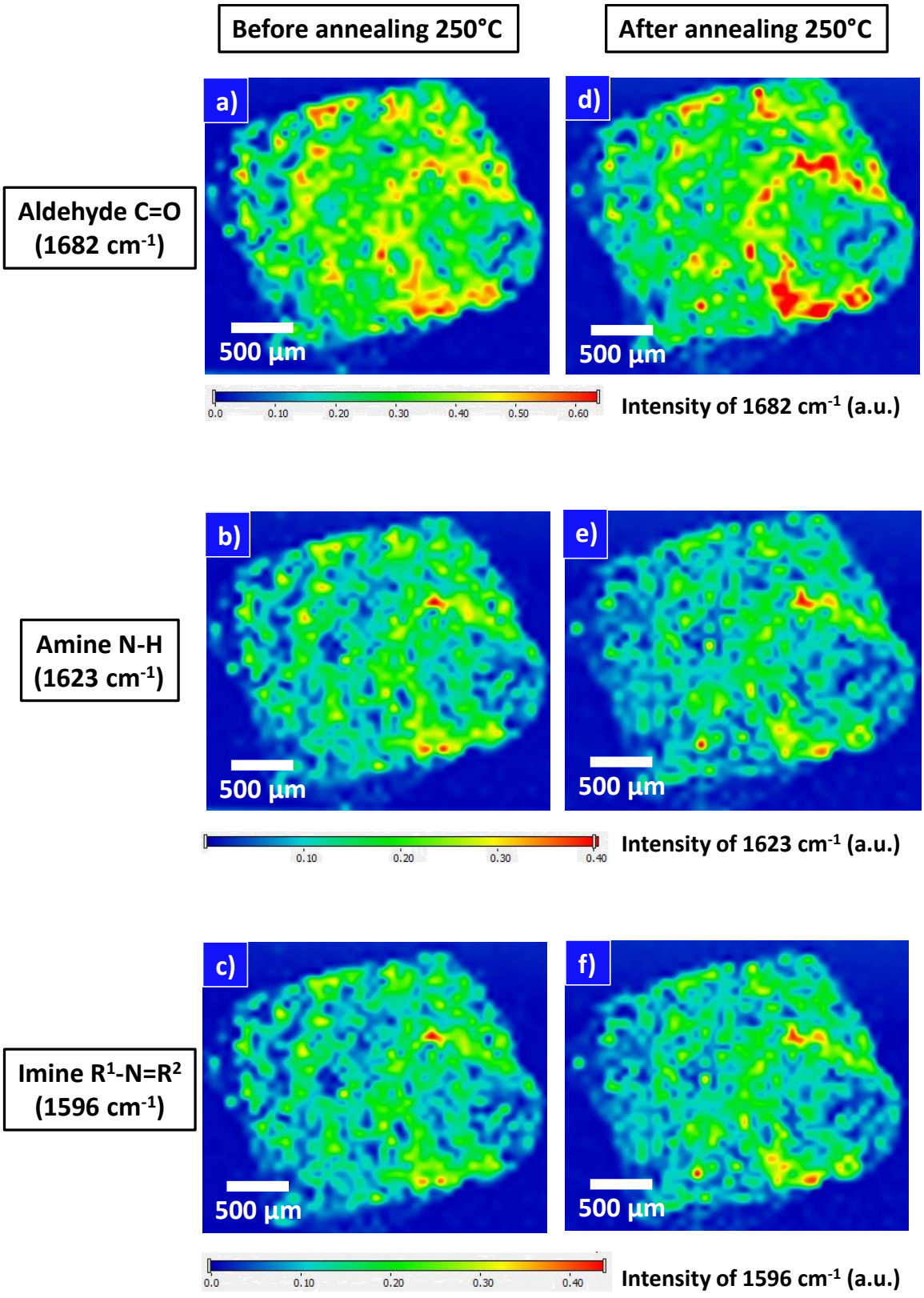

Figure 6-30: Infrared microscopy images of anthracenedialdehyde and TAPB precursors mixed as solid powders. Images of aldehyde (a, d), amine (b, e), and imine (c, f) IR vibration activities, respectively. The given color bars for each vibration are attached below the respective graphics and are given in arbitrary units. The range is displayed from blue (zero activity) to red (higher activity). The measurements were performed before (a, b, c) and after an annealing treatment at 250°C (without any laser illumination) under inert gas (d, e, f), respectively.

6.5 References

1. A. P. Côté, A. I. Benin, N. W. Ockwig, M. O'Keeffe, A. J. Matzger, and O. M. Yaghi, *Science* **2005**, *310*, 1166-1170.
2. H. Xu, J. Gao, and D. Jiang, *Nature Chem.* **2015**, *7*, 905.
3. M. A. Khayum, S. Kandambeth, S. Mitra, S. B. Nair, A. Das, S. S. Nagane, R. Mukherjee, and R. Banerjee, *Angew. Chem. Int. Ed.* **2016**, *128*, 15833-15837.
4. D. N. Bunck and W. R. Dichtel, *Chem. Comm.* **2013**, *49*, 2457-2459.
5. M. S. Lohse and T. Bein, *Adv. Funct. Mater.* **2018**, *28*, 1705553.
6. C. S. Diercks and O. M. Yaghi, *Science* **2017**, *355*.
7. Y. Liu, Y. Ma, Y. Zhao, X. Sun, F. Gándara, H. Furukawa, Z. Liu, H. Zhu, C. Zhu, K. Suenaga, P. Oleynikov, A. S. Alshammari, X. Zhang, O. Terasaki, and O. M. Yaghi, *Science* **2016**, *351*, 365-369.
8. M. Dogru and T. Bein, *Chem. Comm.* **2014**, *50*, 5531-5546.
9. M. L. De Castro and L. Garcıa-Ayuso, *Anal. Chim. Acta* **1998**, *369*, 1-10.
10. M. D. Luque de Castro and L. E. García-Ayuso, *Analytica Chimica Acta* **1998**, *369*, 1-10.
11. Y. Xu, Q. Yu, D. Zhao, W. Zhang, N. Wang, and J. Li, *J Mater Sci* **2018**, *53*, 10534-10542.
12. T. Sick, J. M. Rotter, S. Reuter, S. Kandambeth, N. N. Bach, M. Döblinger, J. Merz, T. B. Marder, T. Bein, and D. D. Medina, **2019**, *submitted*.
13. S. Kim, H. Lim, J. Lee, and H. C. Choi, *Langmuir* **2018**, *34*, 8731-8738.
14. N. Huang, X. Ding, J. Kim, H. Ihee, and D. Jiang, *Angew. Chem. Int. Ed.* **2015**, *54*, 8704-8707.
15. Y. Wu, H. Xu, X. Chen, J. Gao, and D. Jiang, *Chem. Comm.* **2015**, *51*, 10096-10098.
16. M. Dogru, A. Sonnauer, A. Gavryushin, P. Knochel, and T. Bein, *Chem. Comm.* **2011**, *47*, 1707-1709.

7 Pore Wall Fluorescence Labeling of Covalent Organic Frameworks

This chapter is based on the following publication:

Sabrina Rager, Mirjam Dogru, Veronika Werner, Andreij Gavryushin, Maria Götz, Hanna Engelke, Dana D. Medina, Paul Knochel, and Thomas Bein, *CrystEngComm* **2017**, 19, 4886-4891, DOI 10.1039/C7CE00684E.

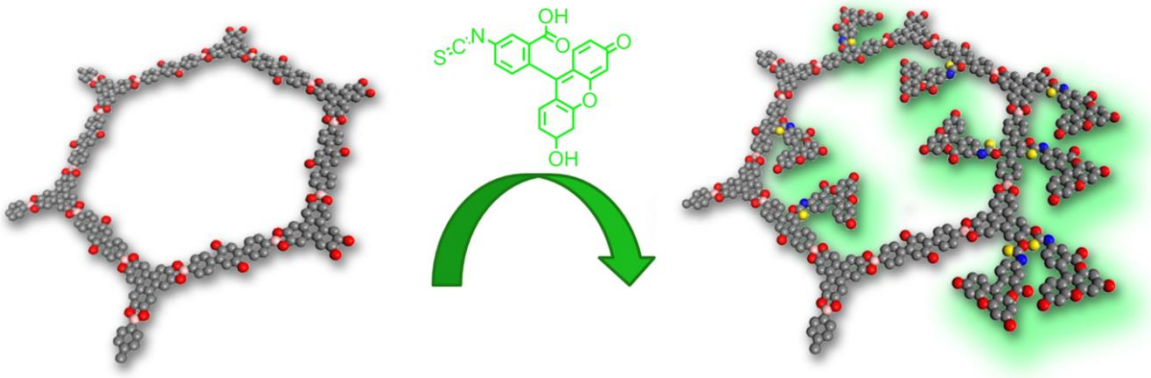

Abstract

The synthesis and characterization of a novel covalent organic framework (COF) based on terphenyldiboronic acid exhibiting open pores of about 4.1 nm is presented in this chapter. The newly created COF features accessible hydroxyl groups at the inner and outer pore walls. These functional groups serve as anchor sites for a fluorescence label installed by a postsynthetic modification approach. By forming *o*-thiocarbamate bonds, fluorescein molecules were immobilized on the inner and outer surfaces of the pore system, respectively. This grafting reaction was also extended to a second COF (COF-5) and to other grafted moieties.

7.1 Introduction

A great challenge in materials research is the synthesis of crystalline porous materials in which the molecular composition as well as physical and chemical properties can be systematically designed. In the past few years, this goal has been realized for a few select inorganic crystalline materials such as zeolites [1, 2], and for inorganic-organic hybrid metal organic frameworks (MOFs) [3-6] through a postsynthetic modification strategy, allowing for structural fine-tuning towards a desired functionality. Covalent organic frameworks (COFs) represent a new class of porous and crystalline materials formed by slightly reversible condensation reactions between molecular building blocks.[7-12] Similar to MOFs, the preselection of organic linkers allows for precisely tunable metrics and composition of the framework. Moreover, due to the great variety of potential organic linkers many different structures with controllable physical and chemical properties can be realized.[13-16] Following a postsynthetic modification approach could grant access to a great variety of covalently attached functionalities. However, it is still considered a challenge to postsynthetically tune the structural and physical properties of a COF while maintaining crystallinity and porosity as its main features.

To date, only a few postsynthetic modification reactions in COF structures have been illustrated. First successful examples were reported by Jiang and co-workers, who introduced azide-decorated building blocks into a boronate ester framework. The azide anchor groups could undergo click reactions with alkynes in postsynthetic reactions yielding a variety of different COF functionalities.[17] Furthermore, the reverse form of this click reaction starts with an alkyne-functionalized linker in the COF framework, which is subsequently reacted with an azide. Using this click reaction, different

functional groups were postsynthetically introduced to tune the storage capacity for carbon dioxide.[18] Later, Dichtel and co-workers demonstrated a postsynthetic thiolene click chemistry reaction in a three-dimensional COF.[19-21]

Hydroxyl groups present another promising functionality that can be used for postsynthetic modification reactions, based on their small size and their great variety in available linker molecules. Furthermore, they present a platform for diverse reactions with other functional groups. For example, succinic anhydride was reacted with hydroxyl groups in a ring opening reaction resulting in a carboxylic acid group functionalization and improving the storage capacity of the investigated COF for carbon dioxide.[22]

The CO_2 uptake was also improved by introducing azobenzene and stilbene units into a hydroxyl-functionalized COF, employing the postsynthetic reaction of carbonyl chloride with the available functional groups.[23] In addition, the first immobilization of an ionic liquid could be reported, obtained by forming covalent ether bonds in the pores of a COF.[24] The first two-step postsynthetic modification of a COF was reported by our group.[25] In a ketoenamine COF with pendant -NO_2 functional groups, the latter were reduced to amines, leading to a pore system decorated with accessible primary amino groups. When amines are used as reactive groups for the condensation reactions leading to the COF lattice, pore-wall functionalization with amino groups is only possible in postsynthetic modification reactions. These pendant amino groups could then be modified with acetyl chloride in a second step.[25]

Efforts aimed at labeling 2D polymer structures with dyes and imaging studies were reported by Schlüter and co-workers. They presented a method for decorating the edges of a 2D polymer by means of Diels-Alder reactions. For this purpose, they chose isotopically enriched dienophiles such as maleic anhydride and maleimide-modified molecules carrying a fluorescent dye.[26]

7.2 Results and Discussion

The new hexagonal COF structure T-COF-OH was synthesized under solvothermal conditions based on a co-condensation reaction of 2',5'-dihydroxy-[1,1';4'1'']terphenyl-4,4''-diboronic acid (DHTBA) and hexahydroxytriphenylene (HHTP). The T-COF-OH exhibits large open pores decorated with hydroxyl groups. In a postsynthetic modification reaction T-COF-OH was labeled with a fluorescence dye by forming *o*-thiocarbamate bonds, resulting in the framework T-COF-OFITC which is

illustrated below in Figure 7-1. The postsynthetic modification process was studied regarding the crystallinity, porosity and the resulting fluorescence properties.

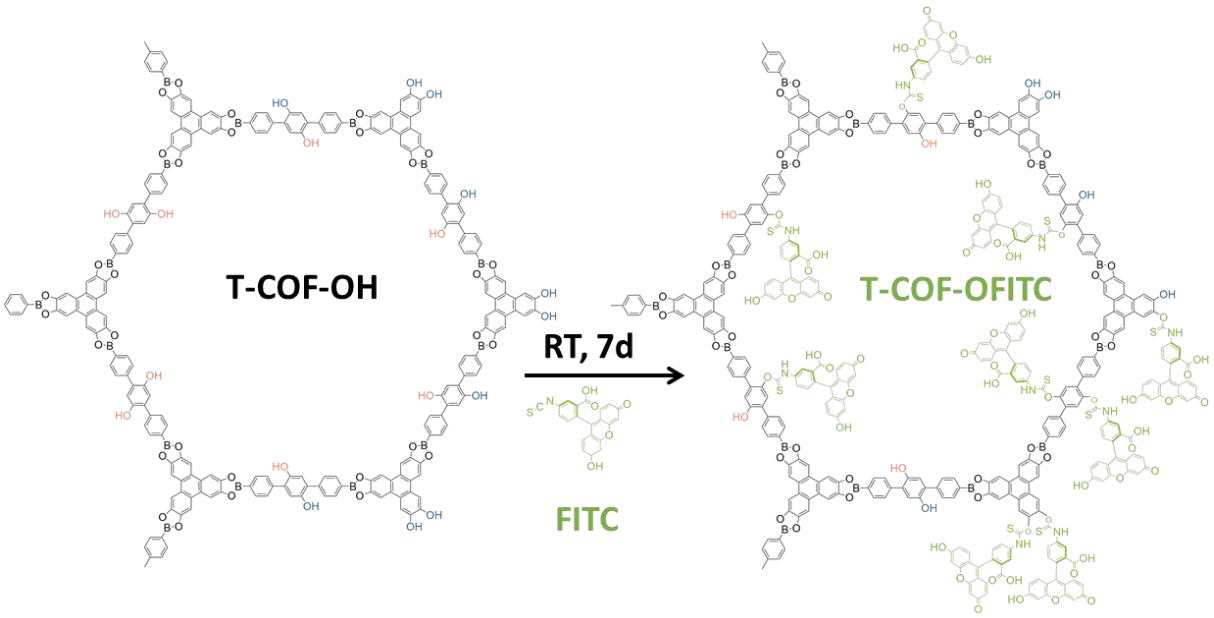

Figure 7-1: Illustration of a hexagonal pore of synthesized T-COF-OH with outer (blue) and inner (orange) standing hydroxyl groups, which is built up from DHTBA and HHTP, undergoing the schematic pathway of postsynthetic modification reaction with FITC by forming *o*-thiocarbamate bonds.

Initially, the synthesis conditions for T-COF-OH were optimized with regard to solvents, solvent ratio, concentration and reagent ratio (see Experimetnal Section). The synthesis was carried out in a 10 mL Schott Duran glass vial. For this purpose, the linker molecules were added to a solvent mixture of toluene and methanol and heated at 120 °C for 3 days. After washing the crude product with dry acetone, a dark-brown powder was obtained.

Powder X-ray diffraction (PXRD) measurements of T-COF-OH indicate the formation of an ordered crystalline framework. Based on the symmetry of the applied building blocks, the expected hexagonal pore system with an eclipsed AA-stacked layer was simulated using the *Materials Studio software* in the *P6* space group and is discussed in the Experimental Section. The resulting simulated X-ray diffraction pattern is in good agreement with the experimental data. We attribute the evident Bragg reflections at 2θ values of 2.31°, 4.07°, 4.62° and 6.17° to the 100, 110, 200 and 210 planes, respectively (see Figure 7-2).

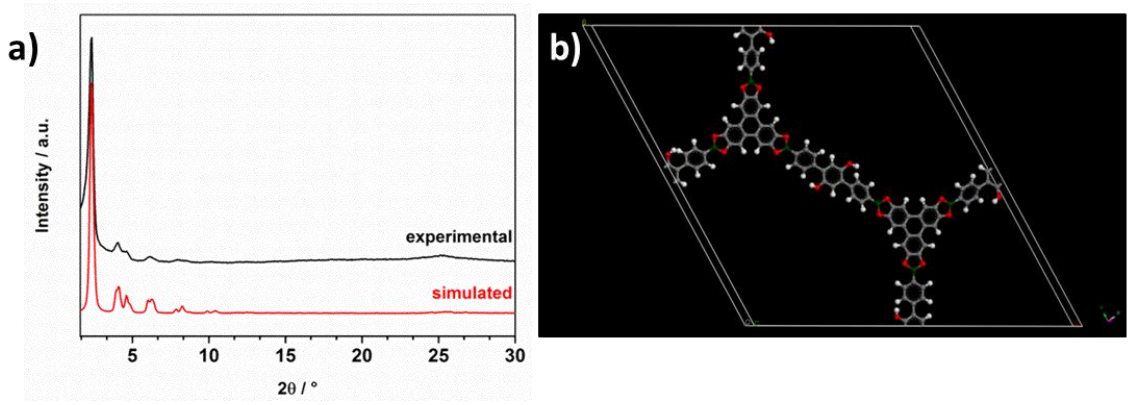

Figure 7-2: a) PXRD of experimentally obtained powder of T-COF-OH (black) compared to the calculated diffraction pattern of the eclipsed 2D layer arrangement (red), b) simulation of crystal lattice of the unit cell in an eclipsed arrangement for T-COF-OH.

The resulted material was analyzed concerning morphology and scanning electron microscpe (SEM) reveals large sheet-like agglomerates consisting of individual particles (Figure 7-3a). Moreover, a TEM micrograph of T-COF-OH (Figure 7-3b) shows crystalline COF domains consisting of well-aligned hexagonal sheets with pore-to-pore distances of about 4.1 nm. The porosity of T-COF-OH was assessed by N_2 sorption measurements at 77 K. Prior to sorption measurements the crude product was treated with anhydrous acetone followed by outgassing for at least 12 hours in vacuum at 120 °C. The obtained isotherm is shown in Figure 7-3c. The COF structure shows a typical type IV isotherm and indicates a mesoporous structure with a calculated BET surface area of more than 2000 m^2g^{-1}. The thermal stability of the COF was examined with thermogravimetry in synthetic air indicating the complete removal of volatile guest molecules at about 150 °C. Degradation of the T-COF-OH starts at 450 °C and the remaining amount of 10 wt% corresponds to approximately 3 mol B_2O_3, related to the sample weight (see Figure 7-3d).

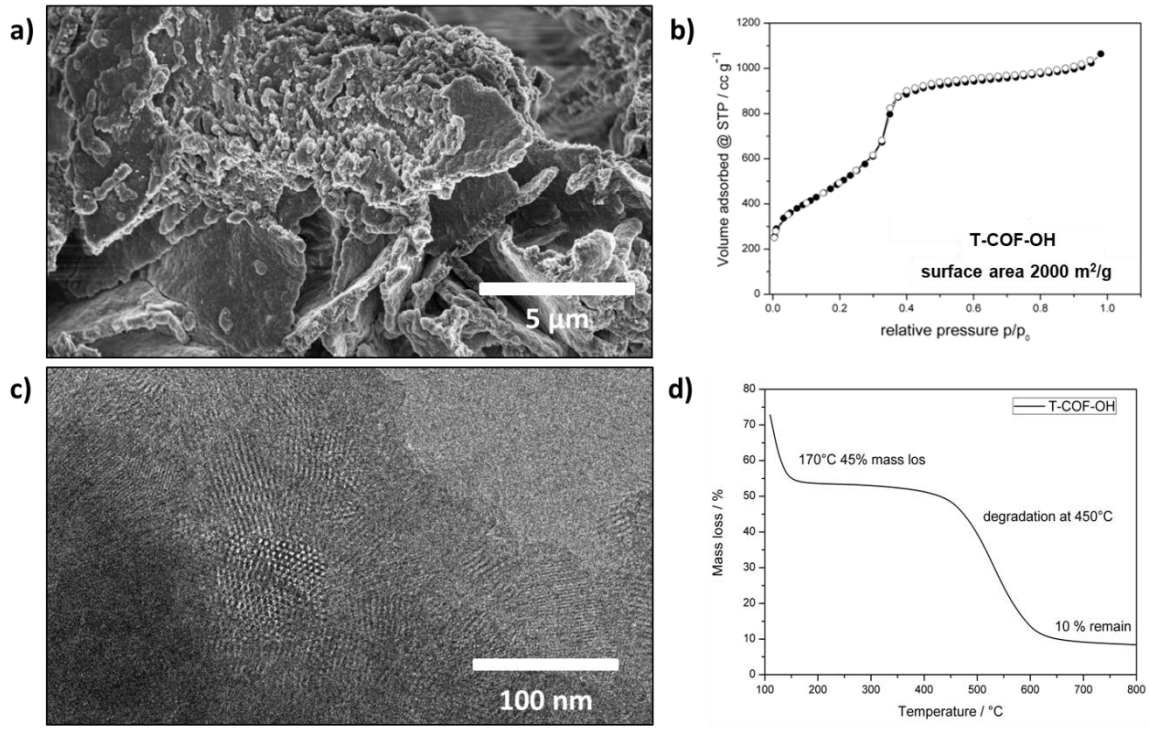

Figure 7-3: a) SEM image of T-COF-OH powder, b) nitrogen sorption isotherm (● adsorption, ○ desorption) of T-COF-OH (black) with calculated BET surface area, c) TEM micrograph of T-COF-OH powder showing the polycrystalline sample with the projection along the *c*-axis illustrating the hexagonal structure d) TGA data of T-COF-OH.

After the successful synthesis and characterization of the hydroxyl-functionalized mesoporous T-COF-OH, a postsynthetic modification reaction with fluorescein-isothiocyanate (FITC) was carried out. In a postsynthetic modification reaction, the outgassed T-COF-OH powder was suspended in a stock solution of FITC in anhydrous acetone for seven days at room temperature (see Experimental Section). Subsequently, the obtained powder was washed with anhydrous acetone to remove the non-reacted FITC molecules from the COF sample, until no fluorescence could be detected in the supernatant.

In a successful modification scenario, the FITC molecules can anchor to the network at different positions. As indicated in Figure 7-1, T-COF-OH exhibits hydroxyl groups facing either the internal pore space (orange) or decorating the external surface of the crystal (blue), and in addition hydroxyl groups arising from the HHTP building blocks, presented on the outer pore surface.

In order to evaluate the crystallinity and stability of the framework after the modification reaction, PXRD measurements were carried out. The powder diffractogram of T-COF-OFITC is in good accordance with the as-synthesized pattern

of T-COF-OH (Figure 7-4a), indicating that the T-COF-OH retained its long range order under the applied reaction conditions.

ATR-IR spectroscopy investigations were carried out for the T-COF-OH, T-COF-OFITC and the free FITC molecules. In the absorption spectra, a strong mode around 2011 cm^{-1} is apparent for the free FITC sample, and attributed to the isothiocyanate functional group. In contrast, in the T-COF-OFITC spectrum the isothiocyanate vibration band is not visible, indicating a successful reaction and the absence of free FITC molecules in the sample (Figure 7-4b).

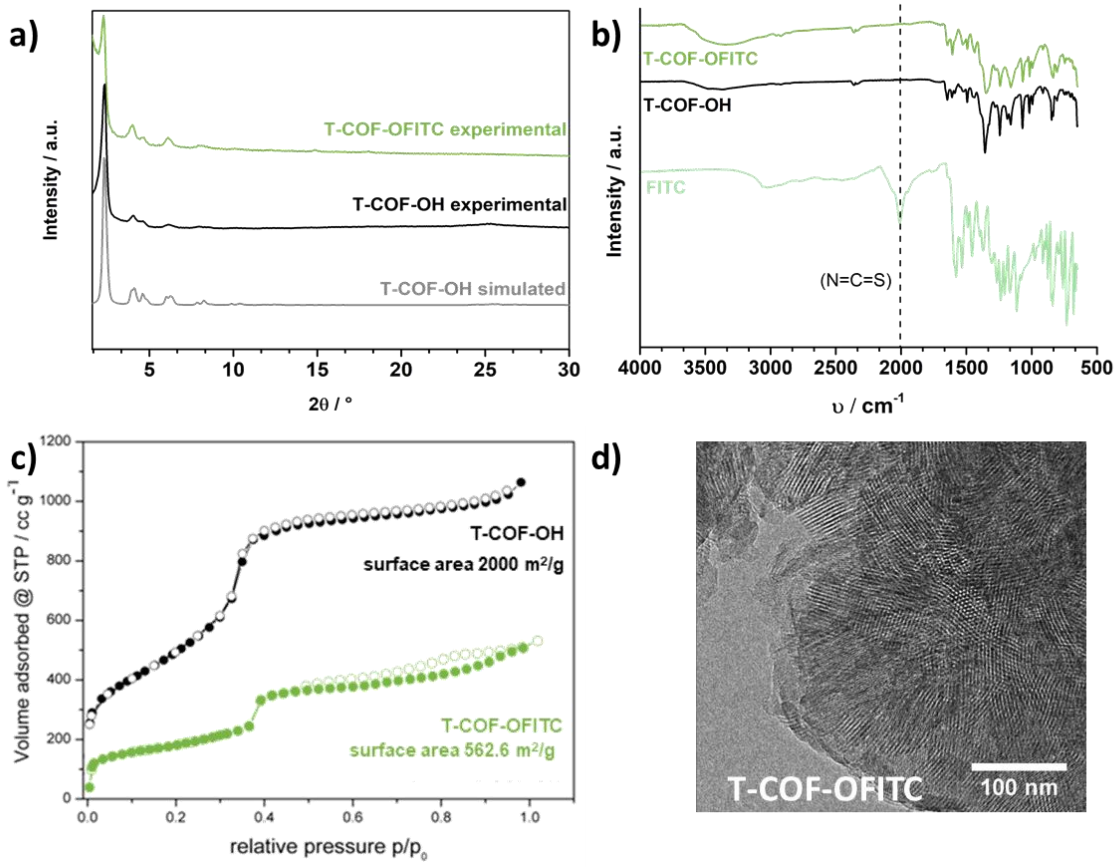

Figure 7-4: a) Experimentally obtained PXRD pattern compared to each other; T-COF-OH calculated diffraction pattern of the eclipsed 2D layer arrangement (grey), T-COF-OH (black), T-COF-OFITC (green); the maintenance of the crystallinity of the framework can be presented, b) comparison of the IR spectra T-COF-OH (black), modified T-COF-OH with FITC after PSM (green), free FITC (lime); the extinction of the free isocyanate vibration clearly indicates the formation of *o*-thiocarbamate bonds within the framework, c) nitrogen sorption isotherm (● adsorption,○ desorption) of T-COF-OH (black) compared to T-COF-OFITC (green) with calculated BET surface area, respectively, d) TEM micrograph viewed along the *c*-axis showing the retained hexagonal structure of T-COF-OFITC.

Nitrogen sorption measurements at 77 K also point towards the presence of grafted FITC guest molecules in the pore system of the COF. As shown in Figure 7-4c, some mesoporosity is retained after the postsynthetic modification reaction compared to the non-treated material. The isotherm still reveals a type IVa shape with a strongly reduced

calculated BET surface area of about 560 m^2g^{-1}. This loss of accessible surface area is attributed to the occupation of the pore system with the grafted FITC molecules. The TEM micrograph of the modified COF (illustrated in Figure 7-4d) confirms that the morphology of the network as well as its crystallinity was conserved. The material still reveals a hexagonal ordered structure, exposing the honeycomb pattern and the periodic channel arrangement.

To extend the covalent attachment concept developed here, we transferred the same reaction conditions to the well-known COF-5. COF-5 consists of HHTP and benzene-1,4-diboronic acid and offers only outer surface hydroxyl groups at the HHTP nodes for subsequent modification reactions. First, we note that the framework of COF-5 also retained its crystallinity after the modification reaction with FITC compared to the non-reacted COF-5 (Figure 7-5a), emphasizing that these reaction conditions are compatible with the boronate ester linking groups. In addition, ATR-IR investigation of the modified COF indicates a successful modification by virtue of the significant weakening of the isothiocyanate vibrations, similar to the observations for T-COF-OFITC (Figure 7-5b).

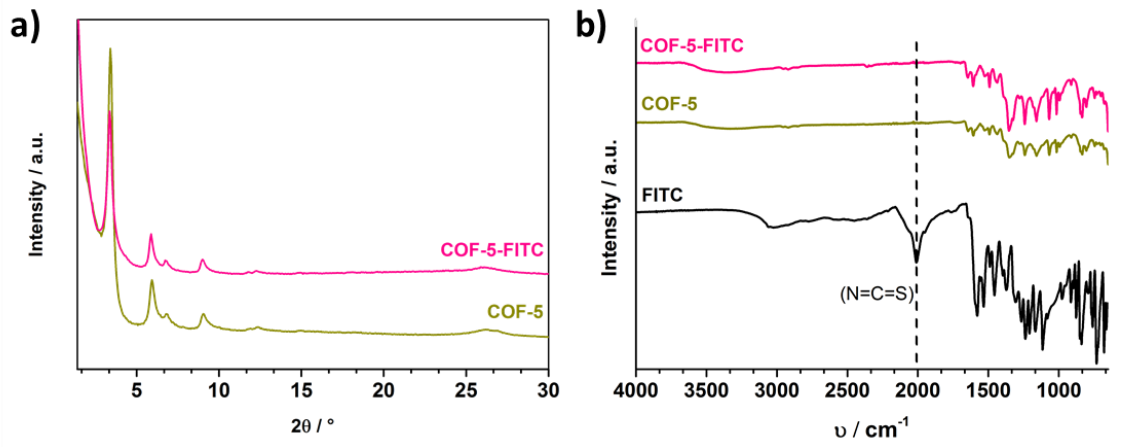

Figure 7-5: a) PXRD of COF-5-FITC (pink) compared to COF-5 (green) to illustrate the maintenance of crystallinity, b) IR spectra of COF-5 (green), modified COF-5 with FITC (pink) and free FITC (black) showing the extinction of the isocyanate vibration.

The fluorescent properties of FITC offer another option to study its presence in the COF samples. Hence, we imaged both the FITC-labeled T-COF-OH and COF-5 after the modification reactions using fluorescence microscopy. Initially, the COFs were washed with anhydrous acetone until the supernatant was no longer fluorescent, confirming that all the non-bound FITC was washed off. Both materials T-COF-OFITC (Figure 7-6a) and COF-5-FITC (Figure 7-6b) showed a strong fluorescence signal, thus establishing

the successful attachment of FITC to the COFs. In the case of FITC grafted to T-COF-OH, fluorescence of rather small particles can be observed which is in good agreement with SEM results (compare Figure 7-6a and Figure 7-6c). Compared to the grafted COF-5 material, T-COF-OFITC reveals smaller particles in solution with strong fluorescence. The fluorescence of the grafted COF-5 sample also indicates the presence of hydroxyl-attached FITC molecules, decorating the periphery of the crystalline COF domains. As seen in Figure 7-6b, the material exhibits fluorescent agglomerated particles that are larger than those observed for the T-COF-OFITC material. As a negative control, we also imaged the non-functionalized COFs, which did not show any significant fluorescence (see Experimental Section). Thus, the fluorescence observed for the FITC labeled COFs truly results from the attached dye.

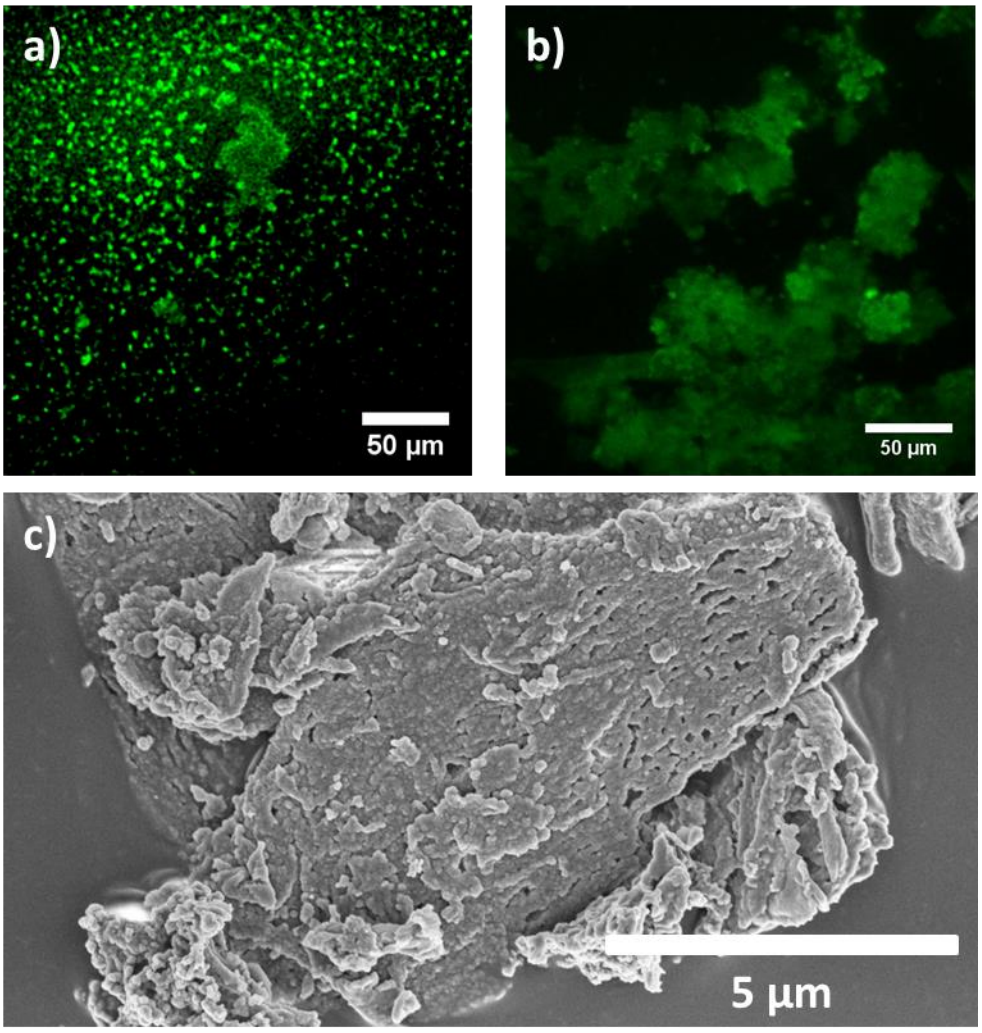

Figure 7-6: a) Fluorescence microscopy image of T-COF-OH and b) COF-5-FITC visualizing the fluorescent behavior of the modified materials, respectively, c) SEM image of T-COF-OFITC powder.

Demonstrating the generality of the above postsynthesis approach, we could also form *o*-thiocarbamate bonds between *n*-octylisothiocyanate and the hydroxyl-functionalized COF instead of using FITC (see Experimental Section). Briefly, these results illustrate that our postsynthetic modification route of COFs pre-functionalized with hydroxyl groups is appropriate even for fragile COF systems such as boronate ester COFs (Figure 7-7).

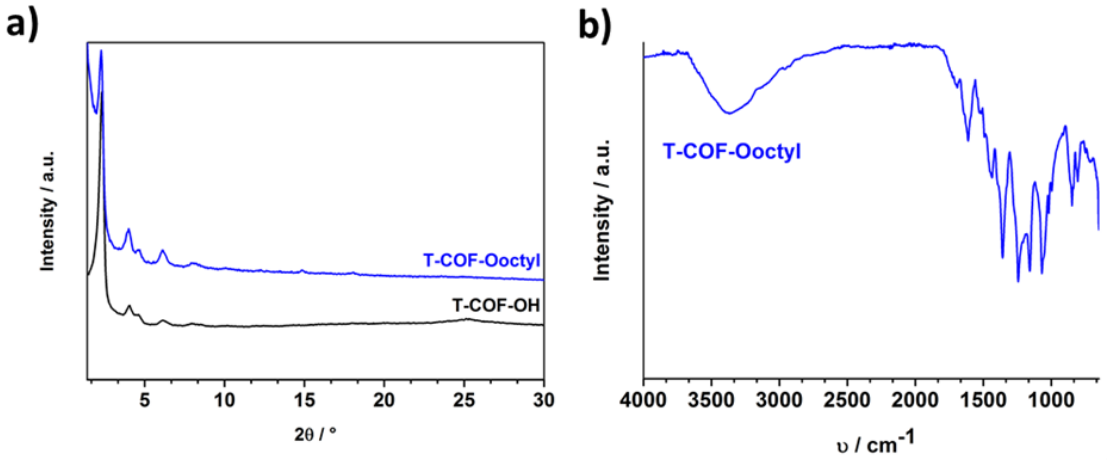

Figure 7-7: a) Comparison of PXRD patterns of T-COF-Ooctyl (blue) and T-COF-OH (black) showing that crystallinity is maintained after the postsynthetic modification reaction with *n*-octylisothiocyanate, b) ATR-IR spectra of T-COF-Ooctyl. The absence of the isothiocyanate vibration band at 2011 cm^{-1} indicates that no free *n*-octylisocyanate molecules are present in the COF sample.

7.3 Conclusion

In conclusion, we could demonstrate the successful integration of a terphenyldiboronic acid-based linker and HHTP into a highly porous COF material *via* boronate ester formation. In addition, it was possible to incorporate small functional groups into the framework by integrating hydroxyl groups into the terphenyl-based COF linker. This linker allows for the subsequent functionalization of the internal and external pore environments, respectively. The incorporation of the hydroxyl groups into the COF leads to the possibility to covalently attach different desired molecules through reactive isothiocyanate moieties. Here we grafted a fluorescent dye that also offered the possibility to demonstrate the successful postsynthetic modification reaction through visualization in a fluorescence microscope. The mild conditions of our newly established postsynthetic modification method also allow for the COF to retain its crystallinity and its porosity as key features. The conversion of small functional groups in COF materials into numerous other functionalities *via* isothiocyanate coupling will

provide access to a large variety of future functional materials with tunable pore properties of interest in areas such as separations, catalysis and optoelectronics.

7.4 Experimental Section

All materials (if not otherwise noted) were purchased from Aldrich or Fluka in the common purities purum and puriss. All materials were used without further purification.

Powder X-ray diffraction (PXRD) measurements were carried out in reflection mode on a Bruker D8 Discover diffractometer with Ni-filtered K_α radiation (λ = 1.54060 Å) and a position-sensitive detector (LynxEye). For visualizing the crystallinity of the resulting COF material, high resolution measurements had to be carried out. For this purpose the material was placed on a silicon wafer and measurements were performed by applying a low scan speed.

The **IR spectra** were recorded on a Perkin Elmer Spectrum BX FTIR device in combination with an attenuated total reflection (ATR) accessory comprising an ATR diamond crystal. All samples were measured at room temperature without further preparation.

Scanning electron microscopy (SEM) was performed on an FEI Helios G3 UC instrument at 2 kV. For this purpose the samples were put on an adhesive graphite film and sputtered with carbon with a BALTEC MED 020 Coating Sytem.

Transmission electron microscopy (TEM) data were obtained with a Tecnai G2 20 STwin at an acceleration voltage of 200 kV.

^{1}H/^{13}C NMR solution spectra were recorded on a Bruker Avance III-400 MHz and a Bruker Avance III-270 MHz spectrometer. Therefore, 4 mg of material and an access of pinacol were put together in DMSO-d_6 to cleave the boronate ester bonds. Proton chemical shifts are expressed in parts per million (δ scale) and are calibrated using residual undeuterated solvent peaks as an internal reference (1H NMR DMSO-d_6: 2.50).

^{11}B and ^{13}C MASnNMR spectra were recorded on a Bruker DSX Avance 500 with a magnetic field of 11.2 Tesla. A 4 mm MAS rotor in a tripleresonance sample head was used. The frequency of the rotors was 10 kHz.

Thermogravimetric (TG) measurements were performed in a stream of synthetic air (25 ml/min) on a Netzsch STA 440 C TG/DSC instrument. The measurements were carried out with a heating rate of 10 °C/min, and a temperature range from 30 °C to 900 °C was covered.

Nitrogen sorption was measured using a Quantachrome AUTOSORB1 station at 77.3 K after degassing the sample for at least 12 h under vacuum at 120 °C. The Brunauer–Emmett–Teller (BET) surface area was calculated from the adsorption branch in the range of p/p_0 = 0.05-0.17. Pore sizes were calculated with a QSDFT adsorption

model of N_2 on carbon (cylindrical, adsorption branch) and a NLDFT adsorption model (slit pore, equilibrium).

Based on the symmetry of the applied building blocks, the final 2D COF structure can be approximately predicted and then confirmed with experimental powder X-ray diffraction (PXRD) data. The **simulation** was carried out with the visualization environment of *Materials Studio software 4.4*, and the geometry of the two dimensional layers was optimized with calculations using forcite methods. Based on the geometry of the precursor molecules, the repeating unit was constructed into a unit cell by directly applying the symmetry operators of the P6 space group. To this end, the repeating fragments were placed in the bare hexagonal unit cell and connected to each other, resulting in the complete unit cell. The geometry of the T-COF-OH layer was optimized in the unit cell using the Dreiding forcefield and the QEq correction for weak interactions. The simulated pattern shows very good agreement with our experimental PXRD data.

The postsynthetically modified fluorescent COFs were imaged using spinning disc **microscopy** (Zeiss Cell Observer SD utilizing a Yokogawa spinning disk unit CSUX1). The objective was a 1.40 NA 63x Plan apochromat oil immersion objective (Zeiss). FITC was imaged with 488 nm laser excitation. Images were acquired using an electron multiplier charge coupled device (EMCCD) camera (Photometrics EvolveTM).

Elementary analysis was performed on a Vario micro cube CHNS analyzer detecting carbon, nitrogen, hydrogen and sulfur. The dried powder of the COF was pyrolized at 1150 °C in an oxygen-enriched He-atmosphere. The resulting gases were detected by thermal conductivity measurements.

The grafting yield of the postsynthetic modification reaction was determined by **fluorescence measurements**. For this purpose, a calibration curve with diverse concentrations of FITC in water was recorded. The two different COF materials were dissolved with excess of pinacol in water and measured under the same conditions. Fluorescence investigations were recorded on a PTI fluorescence system featuring a PTI 814 photomultiplier detector and a PTI A1010B Xenon arc lamp driven by a PTI LPS-220B lamp power supply. Fluorescein was excited with 495 nm and emission was detected at 516 nm (excitation slit 2.0 mm, emission slit 2.0 mm).

7.4.1 Syntheses

7.4.1.1 Synthesis of 2',5'dihydroxy[1,1';4',1'']terphenyl4,4''diboronic acid

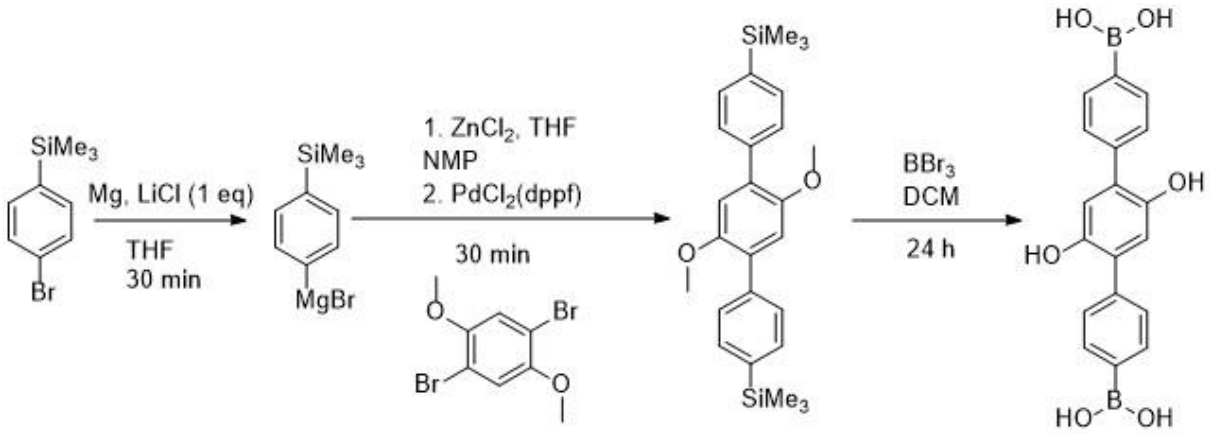

A 500 ml roundbottom flask equipped with a magnetic stirring bar was charged with magnesium turnings (0.645 g, 26.5 mmol, 1.4 eq) and lithium chloride (0.9 g, 21.3 mmol, 90%, 1.0 eq). The reactants were dried under vacuum at 250 °C for 20 min. After cooling to room temperature under nitrogen atmosphere, 15 ml of anhydrous tetrahydrofuran (THF) was added. The reaction solution was stirred for 30 min. Afterwards 1-bromo-4-(trimethylsilyl)-benzene (4.5 g, 18.7 mmol, 1.0 eq) was added dropwise. After 5 min, an exothermic reaction set in. The solution was stirred for another hour and added dropwise to an ice bath-cooled solution of zinc-(II)-chloride (1.28 g, 32 mmol, 0.5 eq) and 0.96 ml (10%) N-methyl-2-pyrrolidone (NMP) in 9.6 ml THF. The mixture was stirred for additional 30 min.

In a 100 ml round-bottom flask, bis(di-tert-butyl)4-dimethylaminophenyl)-phosphine)-dichloropalladium(II) (13.31 mg, 0.019 mmol, 1 mol%) and 1,4dibromo-2,5-dimethoxybenzene (2.22 g, 7.4 mmol, 0.4 eq) were dissolved in THF (6 ml). The mixture was added dropwise to the already produced zinc-(II)-chloride solution and the whole mixture was stirred overnight. The suspension was quenched with 100 ml of a saturated ammonium chloride solution. The amount of 60 ml diethyl ether was added and the mixture was extracted with diethyl ether (4 × 60 ml). Subsequently, the solution was dried over magnesium sulfate and filtered. The solvent was removed by rotary evaporation. Recrystallization in *n*-heptane yielded the product as a grey powder (102.34 mg, 0.23 mmol).

2',5'Dihydroxy[1,1';4',1"]terphenyl4,4"ditrimethylsilane (102.34 mg, 0.23 mmol, 1 eq) was dissolved in 1 ml dichloromethane (DCM). Boron tribromide (0.15 ml, 1.56 mmol, 6.8 eq) was added dropwise and the reaction mixture was stirred at room temperature for 24 h. The amount of 50 g ice was added carefully to the grey reaction suspension and it was stirred until the ice was completely molten. DCM was removed on the rotary evaporator and the product was filtered. The crude product was dissolved in acetone (1.3 ml), and subsequently reduced to half volume by rotary evaporation. Then 1,4dioxane (0.5 ml) was added and the volume was again reduced to half by rotary evaporation. Recrystallization from *n*-heptane yielded a grey powder (101.83 mg, 0.29 mmol).

IR: 3347 (s), 1606 (m), 1556 (w), 1537 (w), 1423 (m), 1395 (m), 1376 (m), 1338 (s), 1290 (w), 1271 (w), 1256 (w), 1202 (w), 1154 (m), 1094 (m), 1024 (m), 1001 (m), 813 (m), 794 (m), 737 (m), 643 (w), 627 (m).
^{13}C-CP-MAS NMR (10 kHz): δ = 146.5 (CO), 139.6 (Cq), 133.2 (CH), 129.0 (Cq), 127.2 (CH), 115.7 (CH) ppm
^{11}B-NMR (10 kHz): δ = 17.44 ppm.
^{1}H-NMR (270 MHz, Methanol-D4, 27 °C, TMS): δ = 7.78 (d, J = 7.7 Hz, 1H), 7.69 – 7.53 (m, 5H), 6.95 (s, 1H), 6.90 (d, J = 3.6 Hz, 1H), 6.86 (s, 1H), 3.65 (s, 2H).
^{13}C NMR (400 MHz, Methanol-D4, 27 °C, TMS): δ = 133.0 (CH), 133.2 (CH), 128.2 (CC), 128.1 (CH), 117.5 (CH) ppm.

7.4.1.2 Synthesis of T-COF-OH

A 10 ml Schott Duran glass was charged with 2',5'-dihydroxy-[1,1';4',1"]terphenyl-4,4"-diboronic acid (9.17 mg, 0.075 mmol, 2.1 eq) and 2,3,6,7,10,11-hexahydroxytriphenylene (HHTP; 10.8 mg, 0.036 mmol, 1.0 eq). The amount of 0.5 ml of a 9:1 v:v mixture of toluene:methanol was added. The reaction mixture was heated at 120 °C for 72 h. The brown solid was isolated by filtration and washed with dry acetone (5 × 1 ml). After washing, T-COF-OH was obtained as brownish powder (69%).

IR: 3307 (w), 1609 (m), 1526 (m), 1491 (m), 1440 (m), 1392 (m), 1353 (s), 1278 (m), 1243 (s), 1164 (m), 1111 (w), 1070 (m), 1039 (w), 1015 (m), 999 (w), 854 (m), 838 (m), 804 (w), 768 (w), 748 (w), 727 (w), 705 (w), 679 (w), 653 (w), 613 (w).

^{13}C NMR (400 MHz, DMSO-d6, 27 °C, TMS): δ = 151.7 (CO), 133.9 (CC), 133.5 (CC), 133.1 (CC), 145.8 (CC), 128.2 (CH), 127.9 (CH), 122.1 (CC), 116.8 (CH), 108.1 (CC), 62.5 (Cq), 26.0 (pinacol) ppm.

Table 7-1: Elemental analysis of T-COF-OH.

N	**C**	**H**	**S**
0	62.35	3.94	0

7.4.1.3 Postsynthetic Modification of T-COF-OH with Fluorescein Isothiocyanate (FITC)

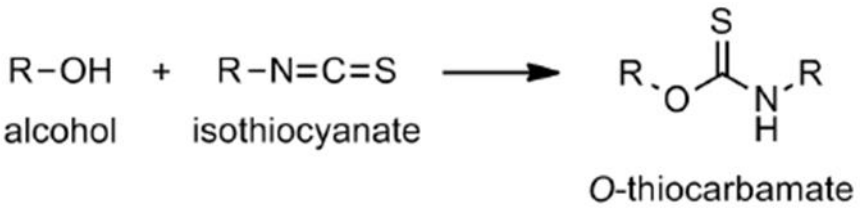

A stock solution of fluorescein isothiocyanate (FITC) (20 mg in 10 ml acetone) was prepared. In a small Eppendorf tube (2 ml size), T-COF-OH (1 mg) and the prepared stock solution (1 ml) of FITC were added together. The reaction suspension was sonicated for ca. 1 min and then left on a shaking plate (600 rpm) at room temperature for seven days. At the end of the reaction, the supernatant was removed by centrifugation (4 min, 14000 rpm). Subsequently, the obtained modified COF material was washed with dry acetone (10 × 1 ml) until the supernatant did not show any fluorescence. Fluorescent T-COF-OH, named T-COF-OFITC, was obtained as brownish powder (0.91 µg FITC/ 1 mg COF; 0.091 wt%).

IR: 3346 (s), 2921 (w), 2351 (w), 1642 (w), 1608 (m), 1519 (w), 1492 (w), 1434 (w), 1399 (w), 1345 (s), 1244 (w), 1159 (w), 1070 (w), 992 (w), 911 (w), 841 (w), 799 (w), 736 (w).

Table 7-2: Elemental analysis of T-COF-OFITC.

N	**C**	**H**	**S**
0	63.11	4.24	0.33

7.4.1.4 Postsynthetic Modification of COF-5 with Fluorescein Isothiocyanate (FITC)

COF-5 was also postsynthetically modified with fluorescein isothiocyanate (FITC). In this case, COF-5 is expected to exhibit available OH-groups belonging to terminating HHTP linker molecules located at the surface of the COF crystals. A stock solution with a large excess of fluorescein isothiocyanate (FITC) (20 mg in 10 ml acetone) was prepared to obtain a virtually constant concentration of the reaction solution as in the reaction procedure for T-COF-OH. In a small Eppendorf tube (2 ml size) COF5 (1 mg) and the prepared stock solution of FITC (1 ml) were added together. The reaction suspension was sonicated for ca. 1 min and later left on a shaking plate (600 rpm) at room temperature for seven days. Subsequently, the supernatant was removed by centrifugation (4 min, 14000 rpm). Thereafter, the obtained modified COF material was washed with dry acetone (10 × 1 ml) until the supernatant did not show any fluorescence. Fluorescent COF-5, named COF-5-FITC, was obtained as brownish powder (0.73 μg FITC/ 1 mg COF; 0.073 wt%).

IR: 3381 (w), 2954 (w), 2905 (w), 1662 (w), 1616 (w), 1515 (m), 1507 (w), 1337 (s), 1240 (m), 1159 (m), 1054 (m), 1004 (m), 829, (m), 741 (m).

7.4.1.4.1 Postsynthetic Modification of T-COF-OH with *n*-Octyl-isothiocyanate (octyl)

To show the generality of the above PSM reaction, the concept was transferred to *n*-octylisothiocarbamate exhibiting the same functional group as FITC bound to an octyl chain. Hence, a stock solution with large excess of *n*-octylisocyanate (octyl) (1.65 mL in 3 ml acetone) was prepared to obtain a virtually constant concentration of the reaction solution as in the reaction procedure for T-COF-OH with FITC. In a small glass vial (10 ml) covered with an aluminum cap, T–COF-OH (40 mg) and the prepared stock solution (3 mL) of octyl were added together. The reaction suspension was sonicated and then shaked at room temperature (600 rpm) for seven days. After the reaction time,

the supernatant was removed by centrifugation (4 min, 14000 rpm). Subsequently, the obtained modified COF material was washed with dry acetone (10 × 1 ml). T-COF-OH functionalized with an octyl chain, named T-COF-Ooctyl, was obtained as brownish powder.

IR: 3363 (vs), 1693 (s), 1617 (m), 1514 (vw), 1491 (vw), 1426 (m), 1400 (vw), 1354 (m), 1239 (s), 1152 (s), 1064 (m), 846 (m).

7.4.2 Characterization Details

7.4.2.1 Simulation of T-COF-OH Crystal Structure

To determine the crystal structure of the obtained product, a powder diffraction pattern was calculated based on a simulated crystal structure.

Table 7-3: Refined crystal data.

	T-COF-OH
Chemical formula	$C_{90}H_{48}O_{15}B_6$
Formula weight	1434.23 g/mol
Crystal system	hexagonal
Space group	P6 (168)
Unit cell dimension	a = b = 45.02 Å c = 3.71 Å α = β = 90° γ = 120°
Cell volume	6528.84 $Å^3$

Table 7-4: Atomic parameters for T-COF-OH.

Atom	**Atom label**	**x/a**	**y/b**	**z/c**
C1	C	-0.01636	-0.47082	-0.26932
C2	C	-0.03846	-0.50847	-0.05036
C3	C	-0.02373	-0.52746	0.15710
C4	C	-0.07662	-0.52784	-0.04127
C5	C	-0.09518	-0.51025	-0.03734
C6	C	-0.13087	-0.52807	-0.03899
C7	C	-0.14863	-0.56379	-0.04416
C8	C	-0.13046	-0.58173	-0.04121
C9	C	-0.09479	-0.56394	-0.03908
O10	O	-0.02670	-0.45565	-0.44154

H11	H	-0.04106	-0.55808	0.33398
H12	H	-0.08085	-0.48122	-0.03278
H13	H	-0.14563	-0.51353	-0.03612
H14	H	-0.14478	-0.61095	-0.04054
H15	H	-0.08017	-0.57869	-0.03553
C16	C	-0.73618	-0.39002	0.09108
C17	C	-0.70509	-0.35971	0.11824
C18	C	-0.70497	-0.32718	0.09772
C19	C	-0.73614	-0.32678	0.05597
C20	C	-0.76553	-0.35720	0.03479
C21	C	-0.76553	-0.38791	0.05099
C22	C	-0.67409	-0.29623	0.11742
C23	C	-0.64274	-0.29710	0.14239
C24	C	-0.64234	-0.32845	0.13838
C25	C	-0.67417	-0.36070	0.15057
C26	C	-0.67369	-0.39296	0.18757
C27	C	-0.64237	-0.39174	0.17832
C28	C	-0.61158	-0.36010	0.13214
C29	C	-0.61069	-0.32850	0.11503
C30	C	-0.61259	-0.26634	0.17671
C31	C	-0.61345	-0.23584	0.16882
C32	C	-0.64283	-0.23450	0.13268
C33	C	-0.67325	-0.26390	0.11081
O34	O	-0.63859	-0.20157	0.12343
O35	O	-0.58587	-0.20421	0.19454
O36	O	-0.58271	-0.36343	0.10250
O37	O	-0.63820	-0.42054	0.19166
B38	B	-0.60230	-0.18272	0.16616
C39	C	-0.58186	-0.14201	0.14807
C40	C	-0.54743	-0.12579	0.20074
C41	C	-0.52869	-0.08901	0.16908
C42	C	-0.54397	-0.06769	0.08166
C43	C	-0.57883	-0.08445	0.03777
C44	C	-0.59760	-0.12126	0.07123
C45	C	-0.52345	-0.02805	0.03044
C46	C	-0.48734	-0.00634	-0.13752
C47	C	-0.53978	-0.01140	0.14296
B48	B	-0.60010	-0.40197	0.13919
O49	O	-0.79694	-0.41514	0.01477
B50	B	-0.81666	-0.39687	-0.02566
O51	O	-0.79707	-0.35998	-0.01002
C52	C	-0.33365	-0.71695	-0.15100
C53	C	-0.33291	-0.68512	-0.13984
C54	C	-0.36471	-0.68489	-0.13824
C55	C	-0.39525	-0.71570	-0.16593
C56	C	-0.39426	-0.74568	-0.17719
C57	C	-0.36440	-0.74645	-0.16543

C58	C	-0.36521	-0.65413	-0.11432
C59	C	-0.33316	-0.62171	-0.13415
C60	C	-0.30167	-0.62194	-0.13227
C61	C	-0.30165	-0.65403	-0.12897
C62	C	-0.26996	-0.65385	-0.11300
C63	C	-0.24013	-0.62323	-0.10156
C64	C	-0.24018	-0.59283	-0.10416
C65	C	-0.27004	-0.59133	-0.11823
C66	C	-0.33405	-0.59014	-0.14622
C67	C	-0.36573	-0.59217	-0.10820
C68	C	-0.39655	-0.62400	-0.05610
C69	C	-0.39718	-0.65493	-0.06153
O70	O	-0.42570	-0.62156	0.00258
O71	O	-0.37018	-0.56409	-0.09698
O72	O	-0.20834	-0.56543	-0.07838
O73	O	-0.20815	-0.62003	-0.07752
B74	B	-0.40846	-0.58335	-0.02193
C75	C	-0.42904	-0.56430	0.01591
C76	C	-0.41142	-0.52594	-0.11119
C77	C	-0.42989	-0.50880	-0.08986
C78	C	-0.46625	-0.52974	0.06802
C79	C	-0.48355	-0.56830	0.20421
C80	C	-0.46519	-0.58541	0.17443
C81	C	-0.48606	-0.51141	0.08256
C82	C	-0.47018	-0.47738	0.13269
C83	C	-0.48849	-0.45978	0.13572
C84	C	-0.52320	-0.47562	0.08754
C85	C	-0.53912	-0.50971	0.03874
C86	C	-0.52082	-0.52732	0.03589
C87	C	-0.54280	-0.45694	0.09422
C88	C	-0.52518	-0.41834	-0.04501
C89	C	-0.54339	-0.40086	-0.02714
C90	C	-0.57970	-0.42158	0.12106
C91	C	-0.59760	-0.45998	0.25237
C92	C	-0.57929	-0.47751	0.24360
B93	B	-0.18832	-0.58324	-0.05979
O94	O	-0.36856	-0.77892	-0.17206
B95	B	-0.40536	-0.79816	-0.19620
O96	O	-0.42215	-0.77730	-0.19912
H97	H	-0.73682	-0.41598	0.10246
H98	H	-0.73678	-0.30137	0.04013
H99	H	-0.69903	-0.41970	0.22471
H100	H	-0.58468	-0.30257	0.08233
H101	H	-0.58778	-0.26688	0.21063
H102	H	-0.69763	-0.26230	0.08754
H103	H	-0.53470	-0.14271	0.26963
H104	H	-0.50075	-0.07600	0.21417

H105	H	-0.59202	-0.06797	-0.02573
H106	H	-0.62585	-0.13455	0.03600
H107	H	-0.47348	-0.01908	-0.23385
O108	O	-0.56738	-0.02733	0.27891
H109	H	-0.30889	-0.71804	-0.14800
H110	H	-0.42045	-0.71559	-0.17876
H111	H	-0.26923	-0.67894	-0.10968
H112	H	-0.26940	-0.56563	-0.11860
H113	H	-0.30870	-0.56327	-0.18716
H114	H	-0.42322	-0.68102	-0.02385
H115	H	-0.38189	-0.50869	-0.23240
H116	H	-0.41554	-0.47756	-0.20090
H117	H	-0.51283	-0.58592	0.34043
H118	H	-0.47963	-0.61664	0.27932
O119	O	-0.44388	-0.46478	0.18151
H120	H	-0.47530	-0.43225	0.17758
O121	O	-0.56535	-0.52227	-0.01138
H122	H	-0.53405	-0.55491	-0.00459
H123	H	-0.49577	-0.40132	-0.17324
H124	H	-0.52870	-0.36961	-0.13340
H125	H	-0.62723	-0.47708	0.36699
H126	H	-0.59387	-0.50877	0.35811
C127	C	-0.46803	-0.96910	-0.18860
C128	C	-0.48433	-0.95245	-0.07498
C129	C	-0.52044	-0.97419	0.09332
C130	C	-0.46380	-0.91286	-0.12400
C131	C	-0.42877	-0.89606	-0.08524
C132	C	-0.40997	-0.85932	-0.11569
C133	C	-0.42586	-0.83873	-0.18280
C134	C	-0.46047	-0.85496	-0.23018
C135	C	-0.47920	-0.89162	-0.20301
O136	O	-0.44050	-0.95318	-0.32623
H137	H	-0.53428	-0.96150	0.19118
H138	H	-0.41577	-0.91274	-0.02846
H139	H	-0.38156	-0.84599	-0.08590
H140	H	-0.47345	-0.83827	-0.29113
H141	H	-0.50724	-0.90461	-0.24495
C142	C	-0.98788	-0.50916	0.14926
C143	C	-0.96579	-0.47148	-0.06905
C144	C	-0.98050	-0.45253	-0.27762
C145	C	-0.92770	-0.45204	-0.07352
C146	C	-0.90910	-0.46971	-0.06792
C147	C	-0.87360	-0.45195	-0.05745
C148	C	-0.85604	-0.41617	-0.05391
C149	C	-0.87419	-0.39808	-0.06824
C150	C	-0.90969	-0.41584	-0.07812
O151	O	-0.97761	-0.52434	0.32262

H152	H	-0.96315	-0.42194	-0.45579
H153	H	-0.92323	-0.49876	-0.07198
H154	H	-0.85882	-0.46657	-0.05176
H155	H	-0.85999	-0.36876	-0.07188
H156	H	-0.92433	-0.40100	-0.09002
H157	H	-0.01326	-0.42751	-0.43359
H158	H	-0.57284	-0.01351	0.45244
H159	H	-0.44073	-0.44688	0.34768
H160	H	-0.58026	-0.51303	0.12106
H161	H	-0.42698	-0.92842	-0.24667
H162	H	-0.95717	-0.50658	0.44899

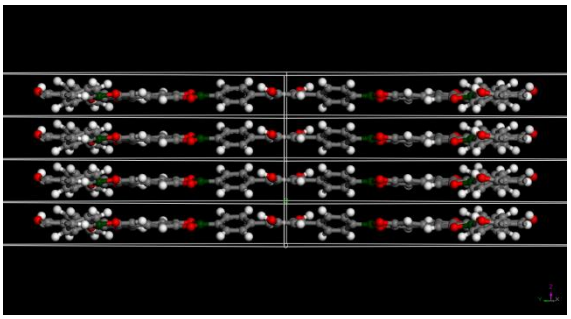

Figure 7-8: Side view at the *c*-axis of 4 unit cells stacked on top of each other with slightly tilted hexagonal layers due to phenyl rings and hydroxyl groups of T-COF-OH rotating out of plane.

7.4.2.2 Nitrogen Sorption Measurements

Evaluation of the pore size distribution shows the retention of the main pores with a pore size of 4.1 nm for non-functionalized as well as functionalized COF material.

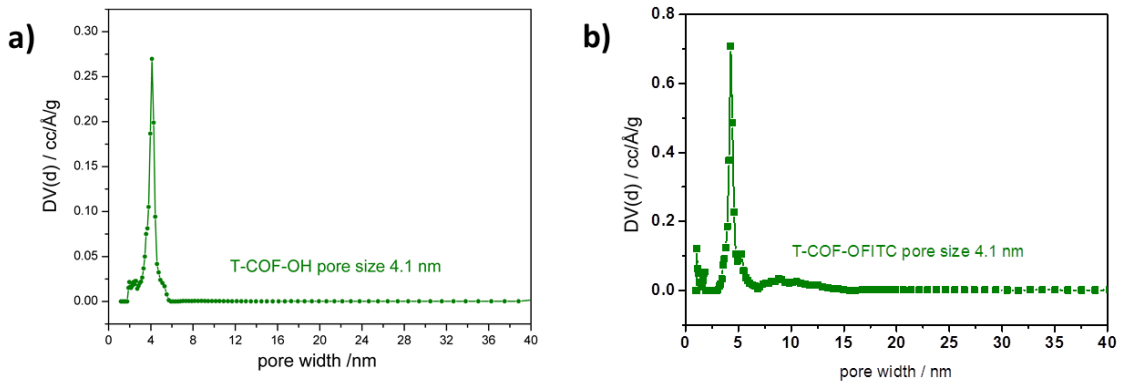

Figure 7-9: Pore size distribution of T-COF-OH, b) pore size distribution of T-COF-OFITC; porosity could have been maintained after pore modification with main pore size of 4.1 nm.

7.4.2.3 Solid State MAS-NMR

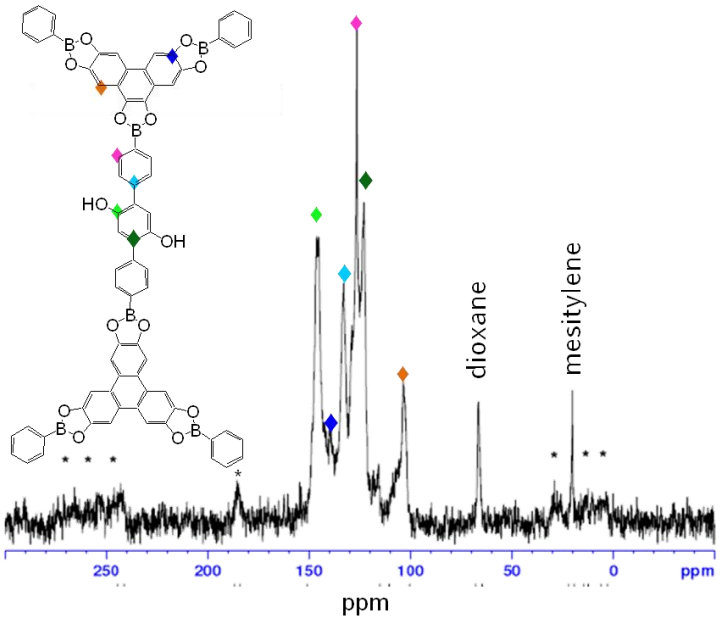

Figure 7-10: ^{13}C NMR spectrum of T-COF-OH with assigned signals for carbon atoms present. Asterisks (*) indicate peaks arising from spinning side bands.

7.4.2.4 IR Spectroscopy

To proof the presence of the isothiocyanate vibration occurring from the free FITC, IR spectroscopy was performed. Therefore, the synthesized COF materials were mixed with 1 wt% of the free FITC material. The visualization of the vibration indicates the presence of free FITC, whereas the postsynthetically modified COF with attached FITC does not show this typical vibrational mode (Figure 7-11).

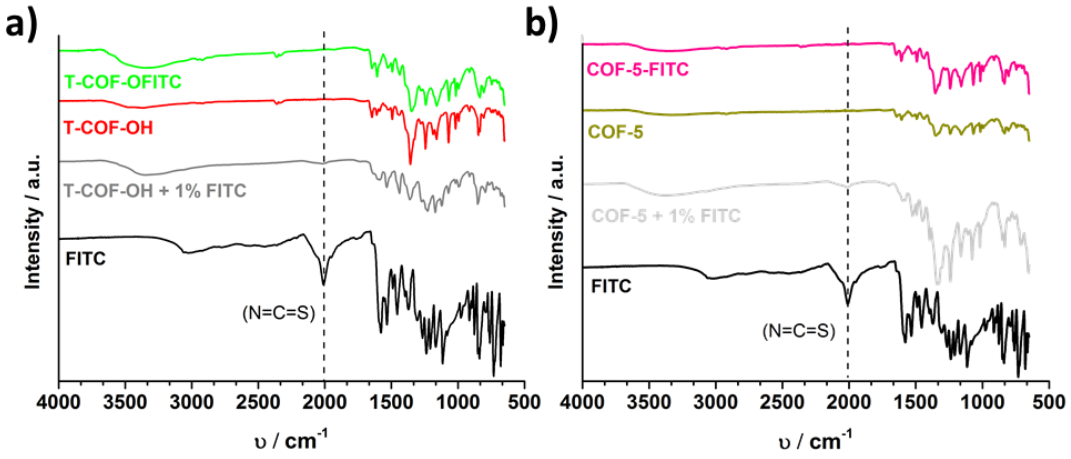

Figure 7-11: Comparison of IR spectra to visualize the extinction of the isothiocyanate specific vibration a) T-COF-OFITC (green), T-COF-OH (red), T-COF-OH + 1% FITC (grey), FITC (black), b) COF-5-FITC (pink), COF-5 (green), COF-5-FITC + 1% FITC (grey), FITC (black).

7.4.2.5 Fluorescence Measurements

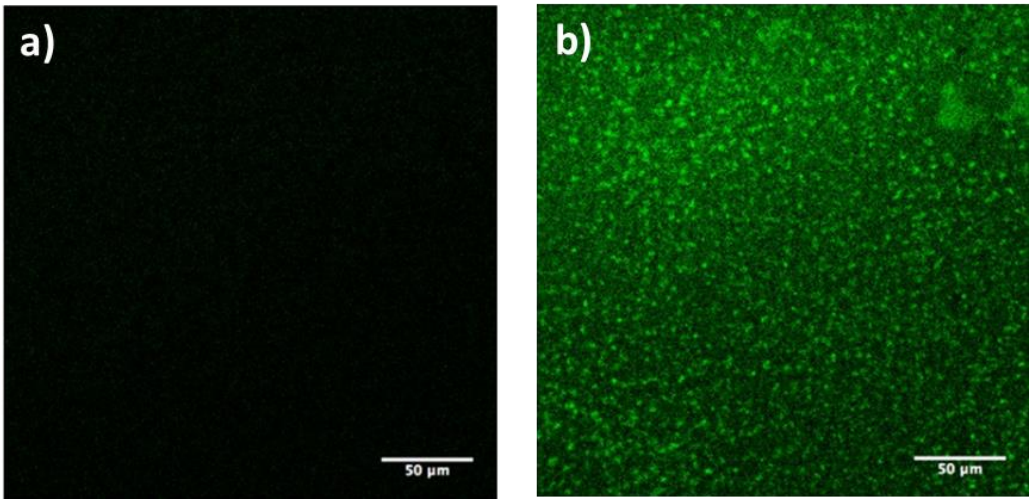

Figure 7-12: a) Fluorescence microscopy image of T-COF-OH illustrating the non-fluorescent behavior of T-COF-OH without covalently bound FITC, and b) fluorescence microscopy image of T-COF-OFITC illustrating the successful postsynthetic modification reaction with FITC.

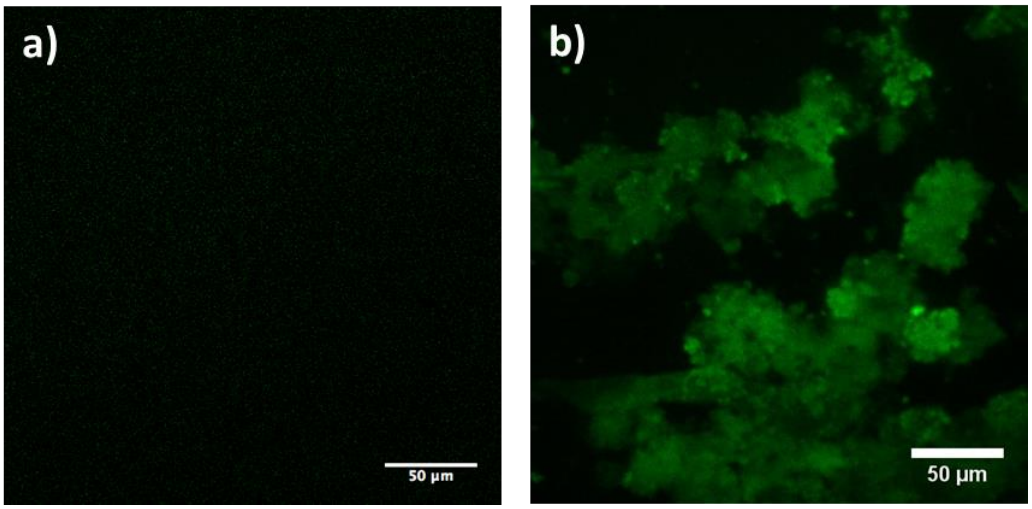

Figure 7-13: a) Fluorescence microscopy image of COF-5 illustrating the non-fluorescent behavior of COF-5 without covalently bound FITC, and b) fluorescence microscopy image of COF-5-FITC illustrating the successful postsynthetic modification reaction with FITC.

The grafting yield of the postsynthetic modification reaction was determined by fluorescence measurements. Here, a very sensitive technique to visualize minor quantities of FITC by florescence microscopy was chosen. To quantify the grafting yield steady-state PL measurements were used. For this purpose, a calibration curve with varied concentrations from free FITC water solutions was constructed. The two different COF materials, namely T-COF-OFITC and COF-5-OFITC, were cleaved with an excess of pinacol in water and measured under the same conditions. The bare COFs were also cleaved and measured under the same conditions revealing a tail of PL

mission in the range of FITC emission. The grafting yield is estimated based on these measurements in the range of 0.1 wt%.

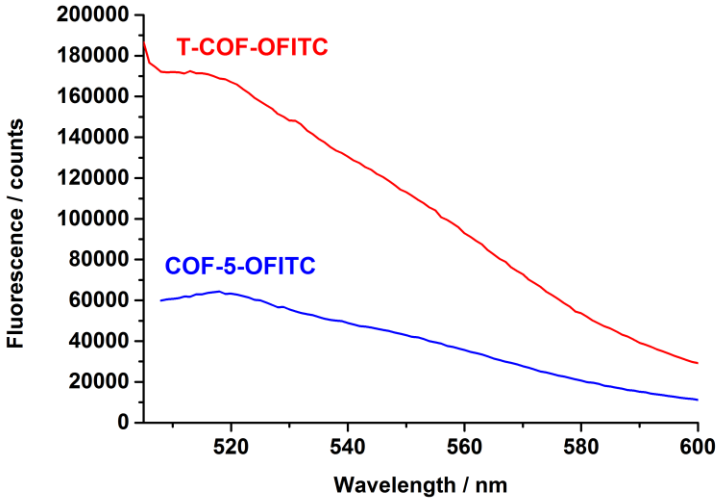

Figure 7-14: Fluorescence measurements of T-COF-OFITC (red) and COF-5-OFITC.

7.5 References

1. V. Valtchev, G. Majano, S. Mintova, and J. Pérez-Ramírez, *Chem. Soc. Rev.* **2013**, *42*, 263-290.
2. J. C. Groen, L. A. Peffer, and J. Pérez-Ramírez, *Microporous Mesoporous Mater.* **2003**, *60*, 1-17.
3. S. M. Cohen, *Chem. Rev.* **2011**, *112*, 970-1000.
4. A. M. Fracaroli, P. Siman, D. A. Nagib, M. Suzuki, H. Furukawa, F. D. Toste, and O. M. Yaghi, *J. Am. Chem. Soc.* **2016**, *138*, 8352-8355.
5. C. V. McGuire and R. S. Forgan, *Chem. Comm.* **2015**, *51*, 5199-5217.
6. C. Dietl, H. Hintz, B. Rühle, J. Schmedt auf der Günne, H. Langhals, and S. Wuttke, *Chem. – Eur. J.* **2015**, *21*, 10714-10720.
7. A. P. Côté, A. I. Benin, N. W. Ockwig, M. O'Keeffe, A. J. Matzger, and O. M. Yaghi, *Science* **2005**, *310*, 1166-1170.
8. H. M. El-Kaderi, J. R. Hunt, J. L. Mendoza-Cortés, A. P. Côté, R. E. Taylor, M. O'Keeffe, and O. M. Yaghi, *Science* **2007**, *316*, 268-272.
9. F. J. Uribe-Romo, C. J. Doonan, H. Furukawa, K. Oisaki, and O. M. Yaghi, *J. Am. Chem. Soc.* **2011**, *133*, 11478-11481.
10. F. J. Uribe-Romo, J. R. Hunt, H. Furukawa, C. Klöck, M. O'Keeffe, and O. M. Yaghi, *J. Am. Chem. Soc.* **2009**, *131*, 4570-4571.
11. S. Kandambeth, A. Mallick, B. Lukose, M. V. Mane, T. Heine, and R. Banerjee, *J. Am. Chem. Soc.* **2012**, *134*, 19524-19527.
12. D. D. Medina, J. M. Rotter, Y. Hu, M. Dogru, V. Werner, F. Auras, J. T. Markiewicz, P. Knochel, and T. Bein, *J. Am. Chem. Soc.* **2015**, *137*, 1016-1019.
13. S. Wan, J. Guo, J. Kim, H. Ihee, and D. Jiang, *Angew. Chem. Int. Ed.* **2008**, *47*, 8826-8830.
14. S. Wan, J. Guo, J. Kim, H. Ihee, and D. Jiang, *Angew. Chem. Int. Ed.* **2009**, *48*, 5439-5442.
15. D. D. Medina, V. Werner, F. Auras, R. Tautz, M. Dogru, J. r. Schuster, S. Linke, M. Döblinger, J. Feldmann, and P. Knochel, *ACS Nano* **2014**, *8*, 4042-4052.
16. M. S. Lohse, J. M. Rotter, J. T. Margraf, V. Werner, M. Becker, S. Herbert, P. Knochel, T. Clark, T. Bein, and D. D. Medina, *CrystEngComm* **2016**, *18*, 4295-4302.
17. A. Nagai, Z. Guo, X. Feng, S. Jin, X. Chen, X. Ding, and D. Jiang, *Nat. Commun.* **2011**, *2*, 536.

18. N. Huang, R. Krishna, and D. Jiang, *J. Am. Chem. Soc.* **2015**, *137*, 7079-7082.
19. J. W. Colson and W. R. Dichtel, *Nat. Chem.* **2013**, *5*, 453-465.
20. C. R. DeBlase, K. E. Silberstein, T.-T. Truong, H. D. Abruña, and W. R. Dichtel, *J. Am. Chem. Soc.* **2013**, *135*, 16821-16824.
21. D. N. Bunck and W. R. Dichtel, *Chem. Comm.* **2013**, *49*, 2457-2459.
22. S. Zhao, B. Dong, R. Ge, C. Wang, X. Song, W. Ma, Y. Wang, C. Hao, X. Guo, and Y. Gao, *RSC Adv.* **2016**, *6*, 38774-38781.
23. N. Huang, X. Chen, R. Krishna, and D. Jiang, *Angew. Chem. Int. Ed.* **2015**, *54*, 2986-2990.
24. B. Dong, L. Wang, S. Zhao, R. Ge, X. Song, Y. Wang, and Y. Gao, *Chem. Comm.* **2016**, *52*, 7082-7085.
25. M. S. Lohse, T. Stassin, G. Naudin, S. Wuttke, R. Ameloot, D. De Vos, D. D. Medina, and T. Bein, *Chem. Mater.* **2016**, *28*, 626-631.
26. Y. Zhao, R. H. M. Bernitzky, M. J. Kory, G. Hofer, J. Hofkens, and A. D. Schlüter, *J. Am. Chem. Soc.* **2016**, *138*, 8976-8981.

8 Conclusion and Outlook

In this work, structural aspects regarding the formation of diverse covalent organic frameworks (COFs) have been investigated. The main focus was the synthetic, structural, and morphological control, also regarding the fabrication of thin film devices as well as structural improvement by different postsynthetic treatments. Furthermore, experimental results supported the suitability and potential of COFs for future applications such as electrically conductive devices and showed new possibilities in the area of tailoring the material properties through the attachment of fluorescent molecules. Chapter 2 delivered an overview and theoretical background of the applied measurement techniques used to fully characterize the different synthesized COF materials.

Chapter 3 summarized the systematic structural control of a diketopyrrolopyrrole (DPP) containing COF. Here, the successful implementation of two chromophores into one single conjugated framework *via* reversible imine bonds was demonstrated. Optical characterization of the material revealed a significant redshift after framework formation, which was attributed to conjugation and delocalization along and across the COF sheets. Structural control was based on a novel type of self-assembly of the COF domains into microtubular aggregates with narrow size distribution, which was observed using electron microscopy. Time-dependent studies supported the hypothesis that the preserved microtubes originated from a roll-up mechanism of the crystallite sheets.

In addition, the implementation of a DPP-based chromophore was extended to a flat and rigid boronate ester binding motif, leading to an improvement of the overall crystalline structure and its characteristics (Chapter 4). This was attributed to the favorable stacking interactions between the adjacent COF layers, leading to extended *J*-type interactions in the stacked DPP columns. Even rather short reaction times resulted in a very crystalline material with excellent optical properties including strong absorption over the whole visible range and a long singlet lifetime. This effect was also associated with the high crystallinity and efficient electronic coupling of the 2D layers and DPP units resulting in efficient stabilization of excitons along the molecular stacks. Besides,

we reported macroscopic conductivity values for boronate ester-based framework powders obtained with van der Pauw measurements. While maintaining the structural characteristics of our COF materials, conductivities of up to 10^{-6} Scm^{-1} were obtained.
Chapter 5 explored the electrical conductivity and mobility features when implementing acene-based building blocks in combination with TAPB into imine-linked COFs. The discussed systems varied in the length of the subunits, influencing the stacking behavior and π-overlap between the COF sheets. The COF was used as a template to induce molecular acene stacks similar to single crystals, in which these molecules show amongst the highest charge carrier mobilities of all organic materials. Therefore, the materials were tested regarding their performance on bulk powder, thin films, and film-based devices. In addition, diverse geometries and setups were compared leading to a better understanding and a more representative evaluation. In a first step, investigations on crystalline and amorphous materials pressed into pellets were performed yielding a distinct limitation through structural defects. Hall mobility values revealed a strong dependency on single crystallite size and can therefore lead to higher values as compared to the macroscopic scale. The van der Pauw measurements on thin films showed an increase in values for the longer anthracene unit as well and similar results were obtained for current-voltage investigations on hole-only devices. The measurements revealed increased charge carrier mobility with longer anthracene backbone by about three orders of magnitude reaching values up to 10^{-3} $cm^2V^{-1}s^{-1}$. Further film devices have to be constructed to get a better statistical distribution of the values. Nevertheless, the presented results strongly indicated on the importance of π-overlap for the mobility behavior of these materials. From these results, further elongation of the backbone towards a pentacene building unit seems a promising pathway due to the even larger π-system and possible overlap. This molecule will be part of future experiments and would complement the study to prove the hypothesis that elongation in the backbone improves the stacking behavior, leading to an enhancement of the charge-carrier mobility.
The third part of this thesis dealt with different postsynthetic treatment approaches. While in the sixth chapter, a postsynthetic treatment without changing the structural characteristics but healing the material from defects was described, the seventh chapter focused on a postsynthetic modification approach, where a functionalization is installed at the inner and outer surface of the pore system. Concerning Chapter 6, a new technique to postsynthetically treat COFs without changing the structural composition

was demonstrated. To illustrate the effect, TAPB and anthracene-based building blocks were successfully implemented into a COF scaffold resulting in a highly crystalline and porous material. When illuminating the as-synthesized (and sc-CO_2-extracted) COF with a high-intensity laser, an auspicious increase in photoluminescence (PL) was observed. This effect was attributed to the removal of defect sites within the system and was also observed for other TAPB-based imine-conjugated COFs. These findings were supported by investigating the influence of the laser illumination on the precursors in a stoichiometric mixture, where the laser light induced the formation of imine bonds between the precursors. This was observed using IR microscopy mapping, revealing a decrease in the vibration activity of the aldehyde and amine vibrations, respectively. While this effect so far seemed to be related to special features of TAPB containing COFs, it might show a new pathway for postsynthetically treating COF materials without the need of solvents or high-temperature conditions. It could be of particular interest for treating thin films, which usually have only limited time to crystallize due to the reaction conditions. Therefore, it might help to improve future thin film applications in the optoelectronic sector.

As mentioned above, Chapter 7 showed the covalent attachment of functional molecules to the pore environment of the framework. As experimental basis, a terphenyldiboronic acid-based COF was synthesized. By integrating hydroxyl groups into the terphenyl-based linker it was possible to incorporate small functional groups into the framework. This synthesized linker allowed for the subsequent functionalization of the internal and external pore environments, respectively, by covalently attaching different desired molecules through reactive isothiocyanate moieties. In this case, a fluorescent dye was installed which allowed for tracking the successful postsynthetic modification reaction through visualization in a fluorescence microscope. This newly-established postsynthetic modification method offers very mild conditions and also allows for the COF to retain crystallinity and porosity as key features.

In summary, the structural impact of diverse linkers with different properties, their implementation into a scaffold, and the resulting characteristics, as well as postsynthetic treatment approaches were investigated in this thesis. The reported morphology and structure control opens the field of investigating and controlling special structures, which might be hard to isolate such as aggregates or crystal segments, while also tailoring the desired overall properties. The described postsynthetic treatment and modification methods further expand this structural control and show key ways how to

even improve already well-defined materials. The results of this thesis provide a new view on COF synthesis and methods, helping to further improve these materials to use their full potential in future applications.

9 Publications and Presentations

PUBLICATIONS

- *Scaffold-Induced Diketopyrrolopyrrole Molecular Stacks in a Covalent Organic Framework*

  Sabrina Rager, Andreas C. Jakowetz, Bappaditya Gole, Florian Beuerle, Dana D. Medina, and Thomas Bein

  Chem. Mater. **2019**, DOI: 10.1021/acs.chemmater.8b02882

- *Enforcing Extended Porphyrin J-Aggregate Stacking in Covalent Organic Frameworks*

  Niklas Keller, Mona Calik, Dmitry Sharapa, Himadri R. Soni, Peter M. Zehetmaier, **Sabrina Rager**, Florian Auras, Andreas C. Jakowetz, Andreas Görling, Timothy Clark, and Thomas Bein

  J. Am. Chem. Soc. **2018**, *140* (48), 16544-16552, DOI 10.1021/jacs.8b08088

- *Microtubular Self-Assembly of Covalent Organic Frameworks*

  Bappaditya Gole, Vladimir Stepanenko, **Sabrina Rager**, Matthias Grüne, Dana D. Medina, Thomas Bein, Frank Würthner, and Florian Beuerle

  Angew. Chem. Int. Ed. **2018**, *57*, 846-850, DOI 10.1002/anie.201708526

- *Pore Wall Fluorescence Labelling of Covalent Organic Frameworks*

  Sabrina Rager, Mirjam Dogru, Veronika Werner, Andreij Gavryushin, Maria Götz, Hanna Engelke, Dana D. Medina, Paul Knochel, and Thomas Bein

  CrystEngComm **2017**, *19*, 4886-4891, DOI 10.1039/C7CE00684E

- *Mobility Studies on Acene-Based Covalent Organic Frameworks*

  Sabrina Rager, Stephan Reuter, Andreas C. Jakowetz, and Thomas Bein

  2019, in preparation

- *A new Postsynthetic Modification Approach for Covalent Organic Frameworks*

  Sabrina Rager, Constantin v. Schirnding, Torben Sick, Dana D. Medina, Andreas C. Jakowetz, and Thomas Bein

  2019, to be submitted

POSTER PRESENTATIONS

- NIM Conference „The Future of Nanoscience“, 2018, Tutzing am Ammersee, Germany.
- 30. Deutsche Zeolith-Tagung (DZT), 2018, Kiel, Germany.
- EuroMOF, 2017, Delft, The Netherlands.
- NIM Conference “Nanostructured functional Materials for sustainable Energy Provision”, 2017, Munich, Germany.
- SolTech Conference, 2017, Munich, Germany.
- NIM Summer School, 2017, Beilngries, Germany.
- CeNS Workshop “Nanosciences: Great Adventures on Small Scales”, 2016, Venice, Italy.
- SolTech Conference, 2016, Munich, Germany
- Inauguration Center for Nanosystems Chemistry (CNC), 2016, Würzburg, Germany.
- NIM Summer Retreat, 2016, Herrsching am Ammersee, Germany.
- EuroMOF, 2015, Potsdam, Germany.
- Summer School Supramolecular Nanosystems”, 2015, Würzburg, Germany.